

DEVELOPMENT AND USE OF  
FAR INFRARED LASERS  
IN STUDIES OF COLLECTIVE  
ELECTRON DENSITY FLUCTUATIONS  
IN A TOKAMAK PLASMA  
BY THOMSON SCATTERING

THESE No 645 (1986)

PRESENTEE AU DEPARTEMENT DE PHYSIQUE

ECOLE POLYTECHNIQUE FEDERALE DE LAUSANNE

POUR L'OBTENTION DU GRADE DE DOCTEUR ES SCIENCES

PAR

IVAR KJELBERG

Ingénieur physicien EPFL  
de nationalité norvégienne

acceptée sur proposition du jury :

Dr M. R. Siegrist, rapporteur  
Dr R. Behn, corapporteur  
Prof. A. Châtelain, corapporteur  
Dr P. D. Morgan, corapporteur



Some books are to bee tasted,  
others to bee swallowed,  
and some few to bee chewed and disgested.

- Francis BACON, Essayes (1579)



TABLE OF CONTENTS.

	<u>TITLE</u>	<u>Page</u>
I.	RESUME. ....	I-1
II.	ABSTRACT. ....	II-1
III.	INTRODUCTION. ....	III-1
	References. ....	III-7
IV.	ACKNOWLEDGMENTS. ....	IV-1
1.	THEORETICAL INTRODUCTION TO THOMSON SCATTERING. .	1-1
1.1.	The principles of Thomson scattering. ....	1-1
1.2.	Scattering from a single particle. ....	1-2
1.3.	Doppler shift due to a moving particle. ....	1-3
1.4.	Scattering from many particles. ....	1-4
1.5.	Incoherent scattering. ....	1-6
1.6.	Coherent scattering. ....	1-7
1.7.	The dynamic form factor. ....	1-8
1.7.1.	Effects of the scattering angle. ....	1-13
1.7.2.	Effects of the electron temperature. ....	1-15
1.7.3.	Effects of the ion temperature. ....	1-15
1.7.4.	Effects of particle drift. ....	1-17
1.7.5.	Effects of plasma microturbulence. ....	1-18
1.7.6.	Effects of impurities. ....	1-19
1.7.7.	Effects of collisions. ....	1-21
1.7.8.	Effects of the magnetic field. ....	1-21
1.8.	Conclusions. ....	1-22
	References. ....	1-24
2.	REQUIREMENTS FOR A COLLECTIVE THOMSON SCATTERING ION TEMPERATURE MEASUREMENT. ....	2-1
2.1.	Choice of the wavelength. ....	2-2

<u>TITLE</u>	<u>Page</u>
2.2. Choice of the scattering angle. ....	2-4
2.3. Estimate of the scattered radiation cross section. ....	2-6
2.4. Plasma background noise. ....	2-6
2.5. The FIR laser. ....	2-10
2.5.1. Power requirement of the FIR laser. ....	2-10
2.5.2. FIR laser bandwidth requirements. ....	2-11
2.5.3. Stray laser light. ....	2-13
2.6. Choice of the detection system. ....	2-14
2.7. Expected precision of the $T_i$ measurement. ....	2-18
2.7.1. The $k$ resolution. ....	2-18
2.7.2. Estimate of the $T_i$ precision by numerical fitting. ....	2-20
2.8. Conclusions. ....	2-23
References. ....	2-26
3. THE OPTICALLY PUMPED FIR LASER. ....	3-1
3.1. The CO <sub>2</sub> laser as a source for optical pumping. ....	3-2
3.1.1. The excited states of the CO <sub>2</sub> molecule. ..	3-3
3.1.2. The excitation process of the CO <sub>2</sub> laser. .	3-4
3.1.3. The CO <sub>2</sub> laser gain width. ....	3-5
3.1.4. A single mode, narrow emission line. ....	3-6
3.1.5. Pulsed, single-pass, amplifier gain calculations. ....	3-7
3.1.6. Limitations of gain length for CO <sub>2</sub> laser amplifiers. ....	3-9
3.2. Description of the CO <sub>2</sub> laser system. ....	3-10
3.2.1. The performance of the CO <sub>2</sub> hybride oscillator. ....	3-15
3.2.2. The double pass CO <sub>2</sub> preamplifier. ....	3-19
3.2.3. The gas isolation cell. ....	3-21
3.2.4. The two CO <sub>2</sub> amplifier chains. ....	3-21

<u>TITLE</u>	<u>Page</u>
3.2.5. The CO <sub>2</sub> laser power supplies. ....	3-22
3.2.6. Timing and triggering of the laser modules. ....	3-22
3.2.7. Alignment procedure of the CO <sub>2</sub> lasers. ...	3-29
3.2.8. Overview of the experimental layout. ....	3-29
3.3. The FIR D <sub>2</sub> O laser. ....	3-34
3.3.1. The D <sub>2</sub> O laser design criteria. ....	3-40
3.3.2. Performance of the D <sub>2</sub> O laser. ....	3-45
3.3.3. The buffer gas. ....	3-45
3.3.4. The D <sub>2</sub> O laser line width and pulse shape.	3-47
3.3.5. Comparison of D <sub>2</sub> O lasers. ....	3-50
3.4. Conclusions. ....	3-53
References. ....	3-55
 4. THE FAR INFRARED OPTICS ON TCA. ....	 4-1
4.1. The constraints for the design of the optical system. ....	4-4
4.2. The FIR laser beam profile. ....	4-4
4.3. General calculations of the FIR beam size. ..	4-5
4.4. The spatial filter and the laser vacuum window. ....	4-9
4.5. The beam transport to the first focusing mirror. ....	4-12
4.6. The ellipsoidal mirrors. ....	4-12
4.7. Measured FIR beam profile of the scattering volume. ....	4-16
4.8. The TCA tokamak vacuum windows. ....	4-16
4.9. The beam and viewing dumps. ....	4-21
4.10. The collecting optics. ....	4-28
4.11. The removable target. ....	4-28
4.12. The alignment procedure. ....	4-31
4.13. Measured FIR beam profiles at W3. ....	4-32

<u>TITLE</u>	<u>Page</u>
4.14. Mechanical stability of the FIR optics. ....	4.34
4.15. Conclusions. ....	4-37
References. ....	4-38
5.    THE HETERODYNE DETECTION SYSTEM. ....	5-1
5.1    Introduction to heterodyne detection. ....	5-1
5.2.    The elements of the detection system. ....	5-9
5.3.    The local oscillator. ....	5-9
5.4.    The optical diplexer. ....	5-16
5.5.    The Schottky barrier diode mixer. ....	5-22
5.5.1.    Contacting the Schottky diode. ....	5-22
5.5.2.    Operating the Schottky diode. ....	5-28
5.6.    The IF amplifiers, filters and square law detectors. ....	5-31
5.6.1.    Measurement of the IF amplifier noise figure. ....	5-34
5.7.    Impedance matching of the Schottky diode to the IF amplifiers. ....	5-37
5.8.    Measurement of the total detection system NEP. ....	5-39
5.9.    Estimate of the mixer conversion loss. ....	5-42
5.10.    The video amplifiers. ....	5-45
5.11.    The CAMAC integrators - digitizers. ....	5-47
5.12.    The CAMAC timer and trigger system. ....	5-49
5.13.    The CAMAC controller and the data transfer. .	5-52
5.14.    Possible improvements of the detection system. ....	5-53
5.15.    Conclusions. ....	5-56
References. ....	5-57
6.    THE OBSERVED SCATTERED SIGNALS. ....	6-1
6.1.    Choice of the spectral channels. ....	6-1
6.2.    The tokamak parameters. ....	6-2
6.3.    Measurement procedure. ....	6-2



<u>TITLE</u>	<u>Page</u>
6.4. Relative calibration of the spectral channels.	6-5
6.5. Measured spectra. ....	6-7
6.5.1. Discussion. ....	6-8
6.5.2. Comparison with results from MIT. ....	6-12
6.6. Estimate of the global system NEP. ....	6-12
6.7. Requirements for a single shot Ti measurement.	6-14
6.8. Conclusions. ....	6-15
References. ....	6-16
7. CONCLUSION. ....	7-1
APPENDIX: A. THE TCA TOKAMAK AT LAUSANNE. ....	A-1
A.1. Typical plasma parameters for the scattering experiment. ....	A-2
References. ....	A-3
APPENDIX: B. MICROWAVE DEFINITIONS AND FORMULAS. ....	B-1
References. ....	B-12
APPENDIX: C. A COMPARATIVE STUDY OF D <sub>2</sub> O OSCILLATORS EMITTING AT 385 $\mu$ m. ....	C-1
M.R. Green, I. Kjelberg, R. Behn, P.D. Morgan, and R. Siegrist. IEEE-Journal of Quantum Electronics, QE- <u>19</u> , pp. 222-232, (1983).	
APPENDIX: D. BUFFER GASES TO INCREASE THE EFFICIENCY OF AN OPTICALLY PUMPED FAR INFRARED D <sub>2</sub> O LASER. ....	D-1
R. Behn, M.A. Dupertuis, I. Kjelberg, P.A. Krug, S.A. Salito, and M.R. Siegrist. IEEE-Journal of Quantum Electronics, QE- <u>21</u> , pp. 1278-1285, (1985).	
APPENDIX: E. TABLE OF SYMBOLS. ....	E-1
CURRICULUM VITAE. ....	F-1
Publications. ....	F-2



## I. RESUME.

La mesure de la température ionique d'un plasma de tokamak peut être obtenue au moyen de la diffusion Thomson collective d'un faisceau laser émettant dans l'infrarouge lointain. La très faible section efficace de la diffusion Thomson ( $10^{-28} \text{ m}^2$ ) nécessite un rayonnement laser incident d'une puissance d'environ 1 MW pour une durée de l'impulsion d'au moins 1  $\mu\text{s}$ . Avec un système de détection hétérodyne performant, d'une puissance équivalente de bruit d'au moins  $10^{-13} \text{ W/Hz}$ , il serait possible de mesurer la température ionique locale d'un plasma avec une précision de l'ordre de 20 %.

Cette thèse présente le développement d'un laser infrarouge lointain et d'un système de détection hétérodyne utilisés pour prouver la possibilité d'une mesure de température ionique par diffusion Thomson collective sur le plasma du tokamak TCA, tokamak qui est situé au Centre de Recherches en Physique des Plasmas (CRPP) à Lausanne.

L'expérience de faisabilité fut effectuée avec un laser  $\text{D}_2\text{O}$  pulsé, d'une puissance de 150 kW pour durée de 1  $\mu\text{s}$  et émettant à une longueur d'onde de 385  $\mu\text{m}$ . Le signal diffusé est mesuré par un système de détection hétérodyne à diode Schottky au moyen d'un oscillateur local comprenant un laser quasi continu émettant à 383  $\mu\text{m}$ . Le spectre diffusé est analysé à travers un banc de filtre dans la bande S des micro-ondes, dont le signal de chaque canal est intégré puis digitalisé.

La puissance du laser  $\text{D}_2\text{O}$  n'est pas suffisante pour une mesure instantanée de la température ionique. Elle permet néanmoins d'observer la lumière diffusée. L'expérience contribue ainsi à l'obtention d'une expertise pratique qui devrait faciliter la connaissance des problèmes d'une mesure réelle.

Il a été observé que les perturbations dues aux microturbulences du plasma ne couvrent pas la partie utile du spectre diffusé pour l'évaluation de la température ionique. Ainsi, une augmentation de la puissance totale du laser infrarouge lointain, par rapport au système décrit ici, devrait être suffisante pour permettre une mesure de la température ionique d'un tokamak.

Cette expérience a montré la nécessité d'améliorer encore la sensibilité de notre système de détection. Celui-ci présente une trop grande perte de conversion pour la diode détectrice. Diverses améliorations sont proposées, qui devraient avec l'installation d'un nouveau laser  $D_2O$  dix fois plus puissant permettre la mesure future de la température ionique par la diffusion Thomson collective en une seule décharge tokamak.

## II. ABSTRACT.

The measurement of the tokamak plasma ion temperature can be obtained by collective Thomson scattering. This method requires a far infrared laser to achieve useful spatial resolution for typical tokamak plasma parameters. The very low Thomson scattering cross section ( $10^{-28} \text{ m}^2$ ) implies the use of a pulsed far infrared laser with 1 MW power and 1  $\mu\text{s}$  pulse duration. With the best technology of far infrared heterodyne receivers available today, with a noise equivalent power (NEP) below  $10^{-18} \text{ W/Hz}$ , it should be possible to measure the ion temperature with 20 % precision.

This thesis describes the development of a far infrared laser and a detection system to prove the feasibility of the ion temperature measurement by collective Thomson scattering on the TCA tokamak. This tokamak is situated at the Centre de Recherches en Physique des Plasmas (CRPP) of the Ecole Polytechnique Fédérale in Lausanne.

The aim was to observe a scattered signal from the plasma and to obtain the required practical knowledge for the design of a large Thomson scattering system to measure the ion temperature in TCA.

For the experiment, an optically pumped  $\text{D}_2\text{O}$  laser is used to produce pulses of 1  $\mu\text{s}$  duration and 150 kW of power, at the far infrared wavelength of 385  $\mu\text{m}$ . The scattered signal is observed with a heterodyne Schottky diode detection system using a quasi continuous  $\text{CD}_3\text{Cl}$  far infrared laser as local oscillator. The scattered spectrum is resolved through a multichannel S band microwave filter bank, after which the signals are integrated and digitized.

Although the laser power is not sufficient to permit an instantaneous ion temperature measurement, a scattered signal correlated with the presence of the plasma was observed when averaging over ten tokamak discharges.

It has been found that perturbations from microturbulence in the plasma are not significant within the useful bandwidth of the scattered spectrum. Hence an increase in the available far infrared laser power and a better sensitivity of the detection system should be sufficient to allow for a single discharge ion temperature measurement.

The experiment also showed the necessity to reduce the NEP of the detection system, which currently presents an excessively high mixer conversion loss. This is being improved for the future installation of a multi-megawatt far infrared laser. With this new laser it should be possible to obtain the first direct measurement of the tokamak ion temperature by collective Thomson scattering on a tokamak.

### III. INTRODUCTION.

The main goal of FIR Thomson scattering from collective electron fluctuations in a tokamak plasma is to measure the plasma ion temperature ( $T_i$ ) [1,2]. An ion temperature measurement by collective (also called coherent) Thomson scattering has several advantages over current methods: it is non-perturbing and can provide a direct measurement with good spatial and temporal resolution. If a sufficiently large signal to noise ratio can be obtained, other plasma parameters like the magnetic field direction and the effective charge could also be measured [2].

At present, most measurements of  $T_i$  [3] are obtained from a spectral analysis of charge-exchange neutrals [4]. This method is, however, less suitable for the new tokamak generation with machines like TFTR and JET. The spatial resolution of this technique is poor. It gives a line integrated measurement and requires assumptions about the processes inside the plasma. In addition, the mean free path of the neutrals in these new tokamaks is smaller than the plasma radius. The study of  $T_i$  with this method is mainly limited to the plasma edge.

Another method to measure  $T_i$  is the spectroscopic analysis of Doppler line broadening in the ultraviolet [5] of the radiation of light impurities. This technique fails, however, on the highly stripped atoms of the hottest plasmas obtained today. With the plasma purity currently achieved the method is also limited to studies of the plasma edge where the main concentration of cooler impurity atoms is located. This method also requires assumptions about temperatures and density distributions of the impurities.

A third method to measure the ion temperature is by studying the neutron flux (at 2.5 and 14 MeV) escaping from the plasma [6]. This method is limited to hot deuterium-deuterium or deuterium-tritium plasmas. An independent verification to check whether the neutrons are of thermonuclear origin would be necessary. The method requires neutron detectors with a resolution at the limit of current technology.

An experimental proof that Thomson scattering is suitable for an ion temperature measurement can be found in scattering from the ionosphere [7]. Incoherent Thomson scattering, at visible wavelengths, (with a scattering scale length smaller than the plasma Debye length) is a common method for measurements of the electron temperature in tokamak plasmas [8].

At the time of commencement of this project, ion temperature measurements by collective Thomson scattering had to be demonstrated on a tokamak plasma, and the necessary radiation source and detection system had to be developed.

The choice of the laser frequency is limited [1,2]. It must be sufficiently low to allow scattering in the collective regime at a practical scattering angle, and high enough to avoid refractive effects due to the plasma. The plasma becomes opaque and reflects waves of frequency lower than the plasma electron frequency. The laser frequency should also be higher than the second harmonic of the electron cyclotron frequency, which is the main source to consider of background noise from the tokamak plasma. With current Tokamak plasmas this restricts us to the far infrared (FIR) wavelength region, more precisely to wavelengths between 200  $\mu\text{m}$  and 2 mm.

The main problem of Thomson scattering is the extremely low cross section ( $10^{-28} \text{ m}^2$ ) which implies the use of at least 1 MW of FIR laser power for a pulse duration of 1  $\mu\text{s}$ , and a heterodyne detection system with a noise equivalent power  $\text{NEP} \leq 10^{18} \text{ W/Hz}$  to achieve the necessary detection signal to noise ratio [1,2]. This low cross section has also some



advantages: the radiation does not disturb the plasma and the scattered light does not interact with the plasma on its way out.

The first problem to solve was the development of a powerful FIR radiation source. Since the first optically pumped FIR molecular gas laser was discovered in 1970 by Chang and Bridges [9], thousands of new FIR laser lines have been reported but no system delivered 1 MW of pulsed FIR power when we started our studies [10].

There also exist other FIR sources but they were not developed to a stage to compete with molecular FIR lasers for high power generation. These include: the carcinotrons [11], which were side benefits of the microwave development carried out since the last world war; recently, free electron lasers [12] and gyrotrons [13] have shown a potential to emit powerful FIR radiation; and even a semiconductor FIR laser [14] has been reported with the advantage of being tunable over a wavelength of several  $\mu\text{m}$ , but with only some mJ of FIR energy.

The second requirement for Thomson scattering was a very sensitive detection system. New detectors for the FIR radiation have appeared during the last few years. Since the early Golay cell [15], the first FIR detector, pyroelectric and photoconductive detectors [16] have been developed, and more recently, thin film bolometers and semiconductor point contact diodes of the Schottky, Josephson or metal-insulator-metal types [17]. Today, specifications like high sensitivity, fast response time or large bandwidth can be met in the FIR wavelength region.

We have taken advantage of research and development of FIR technology in many fields. The early applications of FIR radiation were spectroscopic studies of solids and molecular gases by chemists and astrophysicists [18]. With the increasing power of newer FIR lasers and the improvement of the detector sensitivity these lasers soon became an important

diagnostic tool in laboratory plasma physics [19]. Today, the electron density in most tokamak plasmas is obtained by FIR interferometry [20]. Magnetic fields inside the plasma are measured by FIR Faraday rotation [21], and the study of synchrotron emission (ECE) is done in the far infrared [22]. Even FIR holographic imaging of a plasma is under investigation [19].

Several groups working in Europe, the USA and Japan have been involved in the study of powerful pulsed FIR lasers in the 50 to 500  $\mu\text{m}$  wavelength region, these lasers are frequently based on the  $\text{D}_2\text{O}$  molecule. Most of these groups are attached to institutes performing tokamak research. Highly sensitive FIR detectors are also being developed in Europe and the USA mainly for astrophysical applications. Most effort has been concentrated on heterodyne detection with Schottky barrier diode mixers, using a molecular FIR laser as the local oscillator.

Only the groups at MIT and at the CRPP in Lausanne have actually mounted a collective Thomson scattering experiment on a tokamak, with the aim of performing a  $T_i$  measurement. The effort has been abandoned by other teams even after the successful achievement of sufficiently high power FIR lasers [23].

At MIT [24] the experiment was mounted on Alcator C from 1982 to 1984. Scattered light from thermal fluctuations was observed but the signal to noise ratio was not sufficient for a measurement of the ion temperature. The main problems were stray light from the FIR laser, diffraction from the small port size on the tokamak, and emission at harmonics of the ECE frequency which, due to the high magnetic fields of ALCATOR C, reached the level of the scattered signal.

At CRPP, investigations of FIR lasers started in 1977. In 1981 the work was subdivided: a first pulsed FIR laser was mounted on the TCA tokamak to investigate the feasibility of the technique, while the group continued to develop a higher power pulsed FIR laser for the final  $T_i$  measurement [25].

The FIR laser used for the feasibility study was in many ways comparable to the one used at MIT. However, on TCA there is a better access to the torus and the lower magnetic field of the tokamak does not produce any noticeable background ECE perturbations at the wavelength range of interest. On TCA, the scattering angle of 90 degrees is unfavourable for reasons of signal level, but gives optimum spatial resolution and stray light rejection.

This thesis reports the construction of the feasibility experiment carried out on the TCA tokamak up to and including the observation of a scattered signal. It concentrates on the experimental part. Theoretical investigations of optically pumped FIR lasers are described in detail in the thesis of M.A. Dupertuis [26]. The final  $T_i$  measurement and diagnostic investigation on TCA with the new multi-megawatt FIR laser, currently being installed, will be the theme of another thesis.

This thesis is subdivided in the following way:

Chapter one gives a short introduction to the theory of Thomson scattering. It discusses the effect of the scattering angle and of different plasma parameters including particle temperatures, impurities and the effect of the magnetic field on the scattered spectrum distribution.

Chapter two discusses the power requirement and wavelength limitations of the FIR laser and the characteristics of the detection system, to allow an ion temperature measurement under typical TCA tokamak plasma conditions.

Chapter three contains the description of the optically pumped FIR laser developed for the feasibility experiment. It includes a presentation of the multi-megawatt  $\text{CO}_2$  pump laser.

Chapter four presents the optical system used to focus the FIR laser beam into the plasma of the TCA tokamak, and the collection optics relaying the scattered signal to the detection system.

Chapter five describes the FIR heterodyne detection system and the data acquisition system. It includes a discussion of possible future improvements of the detection system.

The final chapter presents the observed scattered signal and the data analysis technique used. Numerically simulated spectra for similar plasma conditions are also shown.

Finally a brief presentation of the TCA tokamak and some microwave formulas and definitions can be found in the appendices A and B. Two articles describing  $D_2O$  lasers developed at CRPP are included in the appendices C and D.

REFERENCES.

- [1] "Laser light scattering in laboratory plasmas", D.E. Evans and J. Katzenstein, Rep. Prog. Phys., 32, 207, (1969).
- "Thomson scattering of FIR radiation", D.E. Evans, Invited lecture, 2nd Int. Conf. Sub-MM Waves and Applications, Porto Rico, (1976).
  - "To the question of ion temperature measurements with far infrared lasers", G. Magyar, EUR-CEA-FC-815, Fontenay-aux-Roses, (1976).
  - "The development of FIR lasers for Thomson scattering measurements on Tokamak plasmas", P.D. Morgan, M.R. Green, M.R. Siegrist and R.L. Watterson, Comments Plasm. Phys. Cont. Fusion, 5, 141, (1979).
- [2] "A study of the feasibility of measuring the plasma ion temperature in JET by Thomson scattering using a FIR laser", M.R. Green, P.D. Morgan, M.R. Siegrist and R.L. Watterson, CRPP-EPFL Lausanne report LRP-168, (1980).
- "Simulation of magnetic field and ion temperature measurement in a tokamak by thomson scattering", M.R. Siegrist, M.A. Dupertuis, R. Behn and P.D. Morgan, Plasm. Phys., 24, 1449 (1982).
- [3] "Instrumentation for magnetic confined fusion plasma diagnostics", N.C. Luhmann, Jr., and W.A. Peebles., Rev. Sci. Instr., 55, 279 (1984).
- "Plasma physics for nuclear fusion", K. Miyamoto, Chap. 15: "Plasma diagnostics", MIT Press, (1980).
- [4] "Multichannel neutral-particle analyzer system", W.E. Nexsen Jr., W.C. Turner and W.F. Cummins, Rev. Sci. Instrum., 50, 1227 (1979).
- "Low energy H atom analyzer using a cesium heat pipe", D. Brisson, F.W. Baity, B.H. Quon, J.A. Ray and C.F. Barnett, Rev. Sci. Instrum., 51, 511 (1980).
  - "Charge exchange recombination spectroscopy measurements of ion temperature and plasma rotation in PBX", K.P. Jaehning, R.J. Fonck, F. Ida and E.T. Powell, Rev., Sci, Instr., 56, 1096 (1985).
- [5] "Spectral line broadening by plasmas", H.R. Griem, Academic Press, (1974).

- [6] "Selective fast neutron detector", R.E. Chrien and J.D. Strachan, Rev. Sci. Instrum., 51, 1638 (1980).
- "Approaches to ultrafast neutron detectors", C.L. Wang et al., Rev. Sci. Instr., 56, 1096 (1985).
- [7] "Observation of vertical-incidence scatter from the ionosphere at 41 MHz", K.L. Bowles, Phys. Rev. Ltr., 1, 454, (1958).
- [8] "Plasmas and laser light", T.P. Hughes, Chap. 3: "Incoherent scattering of light by plasmas", Adam Hilger, (1975).
- [9] "Laser action at 452, 496, and 541 micron in optically pumped CH<sub>3</sub>F", T.Y. Chang and T.J. Bridges, Opt. Com., 1, 423 (1970).
- [10] "Present status of FIR optically pumped lasers", F. Strumia, Proc. Int. Conf. Infr. MM Waves, paper J6.2, Marseille, (1983).
- "CRC handbook of laser science and technology, Volume II Gas lasers", M. J. Weber, CRC Press., (1982).
- [11] "Backward wave oscillators", G. Kantorowicz and P. Palluel, Infrared and millimeter waves, Vol. 1, Chap. 4, Academic Press, (1979).
- [12] "Stimulated emission of Bremsstrahlung in a periodic magnetic field", Appl. Phys., Vol. 42, (1971).
- "Free electron lasers and stimulated scattering from relativistic electron beams", P. Sprangle et al., Infrared and millimeter waves, Vol. 1, Chap. 7, Academic Press, (1979).
- "Free electron lasers", Vol. 18, European Physical Society, Ed. S. Martellucci and A.N. Chester, (1983).
- [13] "Gyrotrons", J.L. Hirshfield, Infrared and millimeter waves, Vol. 1, Chap. 1, Academic Press, (1979).
- "High-frequency gyrotrons and their application to tokamak plasma heating", K.E. Kreisler and R.J. Temkin, Infrared and millimeter waves, Vol. 7, Chap. 8, Academic Press, (1983).
- [14] "Semiconductor Raman and Brillouin lasers for FIR generation", J. Nishizawa, K. Suto, Infrared and millimeter waves, Vol. 7, Chap. 6, Academic Press, (1983).

- [15] "A pneumatic infrared detector", M.J.E. Golay, Rev. Sci. Instr., 18, 357 (1947).
- [16] "Pyroelectricity and pyroelectric detectors", J. Hadni, Infrared and millimeter waves, Vol. 3, Chap. 4, Academic Press, (1980).
- [17] "Far-infrared techniques", M. F. Kimmitt, Chap. 4: "Detectors", Pion Ltd. (1970).
- "Detection techniques at short millimeter and submillimeter wavelengths: An overview", T.G. Blaney, Infrared and millimeter waves, Vol. 3, Chap. 1, Academic Press, (1980).
  - "Optimization of Schottky barrier diodes for low-noise, low-conversion loss operation at near-millimeter wavelengths", W.M. Kelly and G.T. Wrixon, Infrared and mm waves, Vol. 3, Chap. 2, Academic Press, (1980).
  - "Metal-semiconductor junctions as frequency converters," M.V. Schneider, Infrared and millimeter waves, Vol. 6, Chap. 4, Academic Press, (1982).
- [18] "Dispersive Fourier Transform Spectroscopy", J.R. Birch and T.J. Parker, Infrared and millimeter waves, Vol. 2, Chap. 3, Academic Press, (1979).
- "Far infrared submillimeter spectroscopy with an optically pumped laser", B.L. Bean and S. Perkowitz, Infrared and millimeter waves, Vol. 2, Chap. 4, Academic Press, (1979).
  - "Molecular spectroscopy by far infrared laser emission", J.O. Henningsen, Infrared and millimeter waves, Vol. 5, Chap. 2, Academic Press, (1982).
  - "Electromagnetic waves in matter, Part I", Editor K.J. Button, Infrared and millimeter waves, Vol. 8, Academic Press, (1983).
  - "Infrared and submillimeter spectroscopy of the atmosphere", J.E. Harries, Infrared and millimeter waves, Vol. 6, Chap. 1, Academic Press, (1982).
  - "Infrared detectors for low-background astronomy: Incoherent and coherent devices from one micrometer to one millimeter", P.L. Richards and L.T. Greenberg, Infrared and millimeter waves, Vol. 6, Chap. 3, Academic Press, (1982).
- [19] "Instrumentation and techniques for plasma diagnostics: an overview", N.C. Luhmann, Jr., Infrared and millimeter waves, Vol. 2, Chap. 1, Academic Press, (1979).

- [20] "Submillimeter interferometry of high-density plasmas", D. Véron, Infrared and millimeter waves, Vol. 2, Chap. 2, Academic Press, (1979).
- [21] "Theoretical considerations and preparatory experiments for poloidal field measurements in tokamaks by FIR polarimetry", W. Kunz and G. Dodel, Infr. Phys., 18, 769 (1978).
- "A FIR polari-interferometer for simultaneous electron density and magnetic field measurements in plasmas", G. Dodel and W. Kunz, Infr. Phys., 18, 773 (1978).
- [22] "Measurement of the spectrum of tokamak electron cyclotron emission on a submillisecond time-scale", D.V. Bartlett, A.E. Costley and L.C. Robinson, Infr. Phys., 18, 749 (1978).
- "Fourier transform spectral analysis of the cyclotron radiation from the PLT tokamak", J.F. Stauffer and D.A. Boyd, Infr. Phys., 18, 755 (1978).
  - "Submillimeter emission in Alcator tokamak", I.H. Hutchinson, Infr. Phys., 18, 763 (1978).
- [23] "A high energy D<sub>2</sub>O submillimeter laser for plasma diagnostics", A. Semet L.C. Johnson and D.K. Mansfield, Int. J. Inf. MM Waves, 4, 231 (1983).
- [24] "385 micron D<sub>2</sub>O laser Thomson scattering plasma diagnostic", P. Woskoboinikow et al., 7th Int. Conf. Infr. MM Waves, paper V10-5, Marseille, (1983).
- "385 micron D<sub>2</sub>O laser collective Thomson scattering ion temperature diagnostic", P. Woskoboinikow et al., 11th. EPS Conf. Contr. Fusion Plasma Phys., Aachen, paper E21, (1983).
- [25] "The measurement of plasma parameters by Thomson scattering of FIR laser radiation", M.R. Siegrist, P.D. Morgan, R. Behn, M.A. Dupertuis, I. Kjelberg, T. Okada, Helv. Phys. Acta, 55, 227 (1982).
- "A system to measure plasma ion temperature on the TCA tokamak by Thomson scattering at 385 microns", I. Kjelberg, R. Behn, M.A. Dupertuis, P.D. Morgan, T. Okada, M.R. Siegrist, Helv. Phys. Acta, 55, 227 (1982).



- "Erste Ergebnisse zur kollektiven Thomson Streuung an einem Tokamak Plasma mit Hilfe eines D<sub>2</sub>O Ferninfrarot Lasers", R. Behn, M.A. Dupertuis, I. Kjølberg, P.A. Krug, S.A. Salito, M.R. Siegrist, *Helv. Phys. Acta*, 58, 895 (1985).
  - "Measurement of FIR D<sub>2</sub>O laser radiation collectively scattered by thermal fluctuations in a tokamak plasma", R. Behn, M.A. Dupertuis, I. Kjølberg, P.A. Krug, S.A. Salito, M.R. Siegrist, *EPS Conf. Trends in Quant. Electr.*, Bucharest, (1985).
- [26] "Etude théorique des lasers infrarouge lointains pulsés et de leur comportement multimode", M.A. Dupertuis, Thèse No. 558, EPFL Lausanne, (1985).



#### IV. ACKNOWLEDGMENTS.

My deep gratitude goes to Dr. P.D. Morgan and the "laser group", which in 1979, at the commencement of this work, also comprised Dr. M.G. Green, Dr. M.R. Siegrist and Dr. R.L. Watterson. They offered me the opportunity to start my Ph. D. studies on the laser group's main subject of research. In 1983, P.D. Morgan left for JET and M.R. Siegrist took over as my thesis supervisor until the completion of this work. The group was partly diminished in 1981 by the tragic loss of M. Green in a mountaineering accident, and later by the departure of R.L. Watterson to MIT. However, the arrival of Dr. R. Behn and Dr. P. Krug have greatly assisted the completion of this work. S.A. Salito has taken the challenge to continue the Thomson scattering experiment on TCA, hopefully for a successful Ph. D. thesis.

Special thanks also go to the late Professor E.S. Weibel and Professor F. Troyon, directors of the CRPP during my stay at the institute, and to Dr. A. Heym the vice-director. The experimental part of this work could not have been achieved without the close collaboration of the TCA Tokamak team. They have provided access, operator and machine time, as well as numerous discussions during the build up of the experiment on TCA. Discussions with Dr. H. Van den Bergh (of the Ecole Polytechnique Fédérale de Lausanne) on FIR lasers and with Dr. H.P. Röser (of the Max Planck Institute für Radioastronomie, Bonn) on the Schottky diode receivers have also contributed to the success of the experiment.

I must not forget the people who have been engaged in the construction and maintenance of the equipment: G. Bochy and the electricians: J.P. Denereaz, C. Guillemin and R. Serex; the mechanics shop: J.P. Bärtschi, F. Besançon, P. Bise, A. Botta, J.L. Curty, A. Dubrit, R. Dussault, A. Gorgérat, R. Lassueur, R. Niclaus, P. Pagnoni, J. Richon and

J.P. Rudaz; the draftsmen and designers: J.L. Beney, P. Gogerat, K. Hruska, J.C. Magnin and J.M. Mayor; the electronics shop: P.L. Aubert, J.M. Baur, G. Besson, A. Garcia, R. Gribi, T. Köhli, J.P. Perotti, C. Rizzo and A. Simik; the vacuum technicians: E. Bader, P. Conti and H. Ripper; and the TCA technicians: S. Berthouzoz, Y. Deillon, P. Marmillod, C. Raggi and M. Ries.

Our secretaries during these years: F. Bariatti, C. Antille-Fiore, E. Grüter, P. Halter, B. Schwab and R. Vincent where lucky, I saved them from typing this text, nevertheless I wish to thank them for there help.

And finally, I am very grateful to all my fellow physicists, and to those who do not find their names mentioned here, for the many discussions and fights which have, in some way or another, contributed to this thesis.

This work has been supported by the Ecole Polytechnique Fédérale de Lausanne, the Swiss National Science Foundation, and the Association Euratom-Suisse.

What we have to learn to do  
we learn by doing.

- ARISTOTLE, *Ethica Nicomachea* (c. 325 B.C.)



## CHAPTER 1 .

### THEORETICAL INTRODUCTION TO THOMSON SCATTERING.

The basic theory of Thomson scattering, as a means to measure plasma parameters, is well established and will not be repeated in detail here. For a complete description the reader is referred to J. Sheffield's book: "Plasma scattering of electromagnetic radiation" [1]. Only a short discussion of the influence of plasma parameters on the coherently scattered spectrum will be given here.

#### 1.1. The principles of Thomson scattering.

In the field of an electromagnetic wave charged particles undergo forced oscillations. Since accelerated particles re-emit radiation in a dipole pattern, a fraction of the incident power will reappear in directions which are different from that of the incident wave. This effect is called scattering.

Scattering from a large number of free charged particles, as in a plasma, is generally referred to as Thomson scattering. It implies sufficiently low frequencies such that the photon energy  $h\nu$  is negligible compared to the rest mass energy  $mc^2$  of the scattering particles. Thomson scattering is usually treated classically and can be considered as a limiting case of Compton scattering [1].

The electromagnetic wave incident on the electrons of a plasma is reemitted with a Doppler shifted frequency. The magnitude of this shift depends on the velocity and direction of motion of the electrons, which may be thermal, turbulent or caused by plasma wave phenomena.

1.2. Scattering from a single particle.

When a plane electromagnetic wave of intensity  $I$  is incident on an electron at rest, the scattered power  $dP_s$  reemitted per solid angle element  $d\Omega$  in the direction  $\theta$  can be expressed as a dipole emission [1,2,3]:

$$dP_s = I r_e^2 \sin^2\theta d\Omega \quad (1.1)$$

where

$$r_e = \frac{e^2}{4\pi \epsilon_0 m_e c^2} = 2.82 \cdot 10^{-15} \quad [\text{m}] \quad (1.2)$$

is the classical electron radius. Integrated over all possible directions for an unpolarized incident wave, the total scattered power can be expressed as:

$$P_s = \frac{8\pi}{3} r_e^2 I = \sigma_t I \quad (1.3)$$

where

$$\sigma_t = \frac{8\pi}{3} r_e^2 = 6.65 \cdot 10^{-29} \quad [\text{m}^2] \quad (1.4)$$

is called the total Thomson scattering cross section.

The very low value of  $\sigma_t$  offers the advantage that the incident wave does not disturb the plasma and the scattered light does not rescatter significantly on its way out. It is, however, the cause of the major difficulty of a Thomson scattering experiment: the amount of scattered radiation is extremely small. Thomson scattering requires a high power laser source and a very sensitive detection system.

Scattering from ions can be neglected since the cross section is inversely proportional to the square of the particle mass. While the influence of partially stripped atoms with high polarizability could be an important source of



Rayleigh scattering, this process is proportional to the fourth power of the incident frequency, and thus can be neglected for far infrared wavelengths [4].

### 1.3. Doppler shift due to a moving particle.

If a scattering particle is moving with a velocity  $v$  with respect to a stationary source of angular frequency  $\omega_0$  or wavelength  $\lambda_0$ , the frequency seen by the particle is Doppler shifted by the velocity component of the particle along the direction of the incident wave. This new frequency is given by:

$$\omega_d = \omega_0 - k_0 \cdot v \quad (1.5)$$

where

$$|k_0| = \frac{2\pi}{\lambda_0} \quad (1.6)$$

is the propagation vector of the incident wave. The frequency of the scattered wave, reemitted by the particle, as seen by an immobile observer, is also Doppler shifted by the velocity component of the particle along the direction of observation, hence:

$$\omega_s = \omega_d + k_s \cdot v \quad (1.7)$$

which combined with (1.5) gives:

$$\omega_s = \omega_0 - k \cdot v \quad (1.8)$$

where

$$k = k_0 - k_s \quad (1.9)$$

The observed scattered frequency shift is now:

$$\omega = \omega_0 - \omega_s \quad (1.10)$$

and is due to the component of the particle velocity along the wave vector  $\mathbf{k}$ . It has the magnitude  $\mathbf{k} \cdot \mathbf{v}$ . The two last equations are in fact the statements of the conservation of momentum and energy.

As already mentioned, Thomson scattering is treated classically. The momentum transfer between the incident photon and the particle is negligible, hence:

$$|\mathbf{k}_s| = |\mathbf{k}_0| \quad (1.11)$$

From geometrical considerations outlined in figure 1.1, one obtains:

$$|\mathbf{k}| = 2 |\mathbf{k}_0| \sin(\theta/2) = \frac{4\pi}{\lambda_0} \sin(\theta/2) \quad (1.12)$$

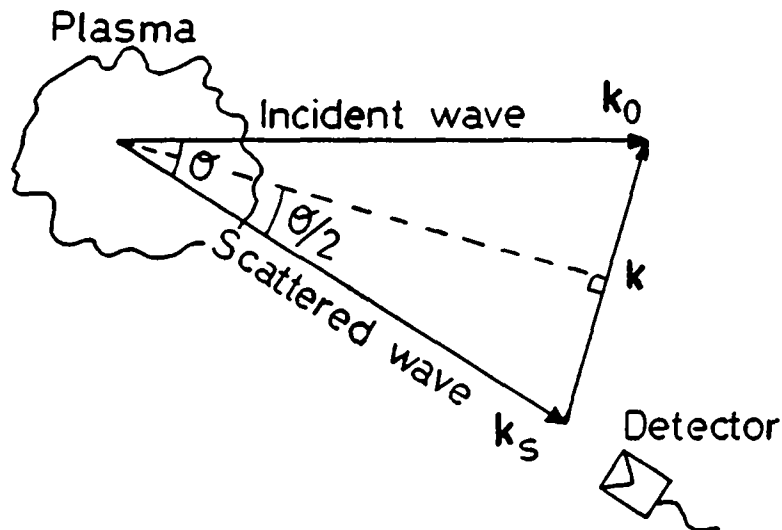


FIGURE 1.1. Vector diagram of the scattering process.

#### 1.4. Scattering from many particles.

The result of scattering from many particles is obtained by summing up the components from the individual electrons

whilst taking into account the phase terms. If the plasma were composed of charges with a uniform distribution, the total scattered power would cancel out due to interference between the contributions of opposite phase. A plasma, however, contains local electron density variations due to thermal fluctuations and collective motion. Such collective density variations lead to constructive interference for particular combinations of the  $k$  vector (Bragg conditions).

In order to characterize the fluctuations in a plasma their scale length  $\Lambda = 2\pi/k$  is compared to the Debye length:

$$\lambda_D = \frac{\sqrt{2}\omega_{pe}}{v_e} = \sqrt{\frac{\epsilon_0 \kappa T_e}{e^2 n_e}} = 7.4 \cdot 10^3 \sqrt{T_e/n_e} \quad [\text{m}] \quad (1.13)$$

where

- $\omega_{pe}$  is the plasma frequency,
- $v_e$  is the mean plasma electron thermal speed,
- $T_e$  is the mean plasma electron temperature, in eV,
- $n_e$  is the mean plasma electron density, in  $\text{m}^{-3}$ ,
- $\kappa$  is the Boltzmann constant,
- $e$  is the electron charge.

The Debye length represents the characteristic distance beyond which the potential of a charge is shielded by neighboring charges. Fluctuations of scale lengths shorter than the Debye length are due to the incoherent thermal electron motion, while the collective behavior of the plasma causes fluctuations of scale lengths longer than  $\lambda_D$ .

The different regimes of Thomson scattering are characterized by a parameter  $\alpha$  defined as:

$$\alpha = \frac{1}{|k| \lambda_D} = \frac{\lambda_0}{4\pi \lambda_D \sin(\Theta/2)} \quad (1.14)$$

1.5. Incoherent scattering.

For  $\alpha \ll 1$ , the characteristic length of the density fluctuations observed is short compared to the Debye shielding distance. Scattering is due to the uncorrelated thermal motion of the individual electrons. This is called incoherent Thomson scattering.

For a Maxwellian electron velocity distribution, the scattered spectrum is a Gaussian of half-width proportional to the electron thermal velocity. This is in turn proportional to the square root of the electron temperature (see figure 1.2). In this regime Thomson scattering is commonly used to measure the electron temperature in tokamaks. For typical tokamak plasma parameters, the emission of the laser needed is in the visible or the near infrared part of the spectrum.

For the case of a scattering angle of 90 degrees, a laser wavelength of 694.3 nm (Ruby laser) and a plasma electron temperature of 400 electron volts, the full width at half maximum (FWHM) of the scattered spectrum would be 73 nm, while the line width of the laser is typically less than 0.05 nm.

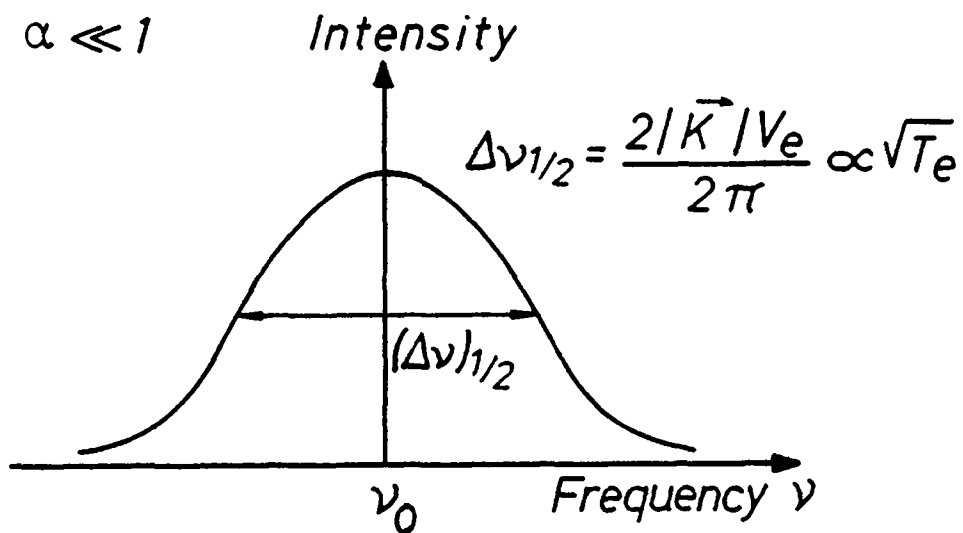


FIGURE 1.2. Incoherent scattering spectrum for a plasma in thermal equilibrium.  $\nu_0$  is the incident laser frequency.

1.6. Coherent scattering.

When  $\alpha \gg 1$  we observe the correlated motion of the electrons, e.g. the motion of electron clouds Debye-shielding the ions or density fluctuations associated with plasma waves. This is called coherent or collective Thomson scattering.

For a thermal plasma with equal electron and ion temperatures, a typical scattered spectrum is represented in figure 1.3. The width of the central feature is proportional to the square root of the plasma ion temperature. The two detached peaks result from scattering off electron plasma waves (of frequency  $\nu_e$ ) and the shoulders on the central peak are due to ion acoustic waves of frequency  $\nu_i$ .

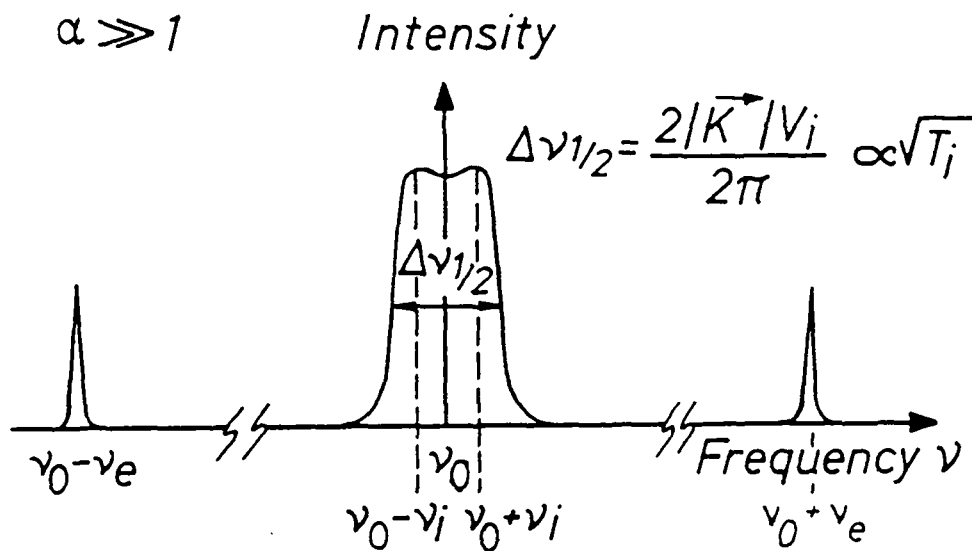


FIGURE 1.3. Coherent scattering spectrum for a thermal plasma with  $\alpha \gg 1$  and  $T_e \approx T_i$ .

1.7. The dynamic form factor.

The total scattered power from a plasma with a mean electron density  $n_e$  into a solid angle  $d\Omega$  can be written as [5]:

$$P_s(\mathbf{k}, \omega) = P_0 r_e^2 L d\Omega n_e S(\mathbf{k}, \omega) \quad (1.15)$$

where  $P_0$  is the incident power. The scattering volume  $V$  is defined by the intersection of the incident laser beam and the cone within which the scattered light is collected. Its dimension along the incident beam is given by  $L$ .

$S(\mathbf{k}, \omega)$  is the dynamic form factor, which describes the shape of the scattered spectrum. It is proportional to the Fourier transform in space and time  $\tau$  of the electron density [1,5]:

$$S(\mathbf{k}, \omega) = \lim_{\tau, V \rightarrow \infty} \frac{1}{V \tau} \left\langle \frac{|n_e(\mathbf{k}, \omega)|^2}{n_0} \right\rangle \quad (1.16)$$

The dynamic form factor contains the information about the plasma behavior.

For a collisionless plasma, with only one ion species, the form factor is generally written as [1,5]:

$$S(\mathbf{k}, \omega) = \left| 1 - \frac{\Gamma_e(\mathbf{k}, \omega)}{\epsilon(\mathbf{k}, \omega)} \right|^2 F_{e0}(\mathbf{k}, \omega) + Z \left| \frac{\Gamma_e(\mathbf{k}, \omega)}{\epsilon(\mathbf{k}, \omega)} \right|^2 F_{i0}(\mathbf{k}, \omega) \quad (1.17)$$

where  $Z$  is the charge of the ions,  $F_{e0}$  and  $F_{i0}$  are the normalized velocity distributions and  $\Gamma_e$ ,  $\Gamma_i$  are the screening integrals for the electrons and ions respectively. The plasma dielectric function  $\epsilon$  is defined as [1]:

$$\epsilon(\mathbf{k}, \omega) = 1 + \Gamma_e(\mathbf{k}, \omega) + \Gamma_i(\mathbf{k}, \omega) \quad (1.18)$$

For a plasma in thermal equilibrium the velocity distributions are Maxwellian and the screening functions can be expressed by [1,5]:

$$\Gamma_e = \alpha^2 W(x_e) \quad (1.19)$$

$$\Gamma_i = Z (T_e/T_i) \alpha^2 W(x_i) \quad (1.20)$$

where

$$x_e = \omega / (k \cdot v_e) : \text{normalized frequency of the electron term.} \quad (1.21)$$

$$x_i = \omega / (k \cdot v_i) : \text{normalized frequency of the ion term.} \quad (1.22)$$

$$v_e^2 = \frac{2k T_e}{m_e} : \text{mean electron velocity} \quad (1.23)$$

$$v_i^2 = \frac{2k T_i}{m_i} : \text{mean ion velocity} \quad (1.24)$$

The plasma dispersion function  $W(x)$  is defined as [1.5]:

$$W(x) = 1 - 2x e^{-x^2} \int_0^x e^{t^2} dt - i \sqrt{\pi} x e^{-x^2} \quad (1.25)$$

The first term in the form factor (1.17) represents the electron feature and becomes dominant when  $\alpha \ll 1$  (incoherent scattering). The second term is the ion feature and is superimposed on the broader electron feature. The ion feature is dominant when  $\alpha > 1$  (coherent scattering).

This can be seen when the Salpeter approximation is applied to equation (1.17). This approximation assumes  $T_e \simeq T_i$  and separates the form factor (using Maxwellian velocity distributions) into two independent functions depending only on the variables  $x_e$  and  $x_i$ . It makes use of the large disparity in scale between the variables  $x_e$  and  $x_i$  [1.5]:

$$a_e = \frac{x_e}{x_i} = \frac{v_i}{v_e} = \left( \frac{m_i T_e}{m_e T_i} \right)^{1/2} \simeq 60 \text{ on TCA.} \quad (1.26)$$

The form factor can now be expressed as:

$$S(k, \omega) = \Gamma_{\alpha}(x_e) + Z \left\{ \frac{\alpha^2}{1+\alpha^2} \right\} \Gamma_{\beta}(x_i) \quad (1.27)$$

where

$$\Gamma_{\alpha}(x_e) = \frac{\exp(-x_e^2)}{|1 + \alpha^2 W(x_e)|} \quad (1.28)$$

and

$$\Gamma_{\beta}(x_i) = \frac{\exp(-x_i^2)}{|1 + \beta^2 W(x_i)|} \quad (1.29)$$

and

$$\beta^2 = Z \left( \frac{\alpha^2}{1+\alpha^2} \right) \frac{T_e}{T_i} \quad (1.30)$$

For a 90° Thomson scattering experiment at a wavelength of 385  $\mu\text{m}$  on TCA with typical  $D^+$  plasma parameters (see appendix A) we would have:

$$\alpha = 1.5 \quad \text{and} \quad \beta = 1.7 \quad (1.31)$$

Figure 1.4 shows the shape of  $\Gamma_{\alpha}(x)$  for various values of  $\alpha$ . The shape of  $\Gamma_{\beta}(x)$  would be the same except for the large difference in the horizontal scale due to the differences between  $x_e$  and  $x_i$ .

By integrating over all frequencies, we may calculate  $S(k)$ , the integrated form factor incorporating electron and ion features. The result is [5]:

$$S(k) = \frac{1}{1+\alpha^2} + \frac{Z \alpha^4}{(1+\alpha^2)^2 \cdot (1+\beta^2)} \quad (1.32)$$

The contributions of both the electrons and ions to the integrated form factor are shown in figure 1.5. For  $\alpha \gg 1$ , as is the case for the experiment on TCA, the total scattered spectrum would have a shape as illustrated in figure 1.6. The narrow central peak is the ion feature while the broad, weaker pedestal is the electron feature.



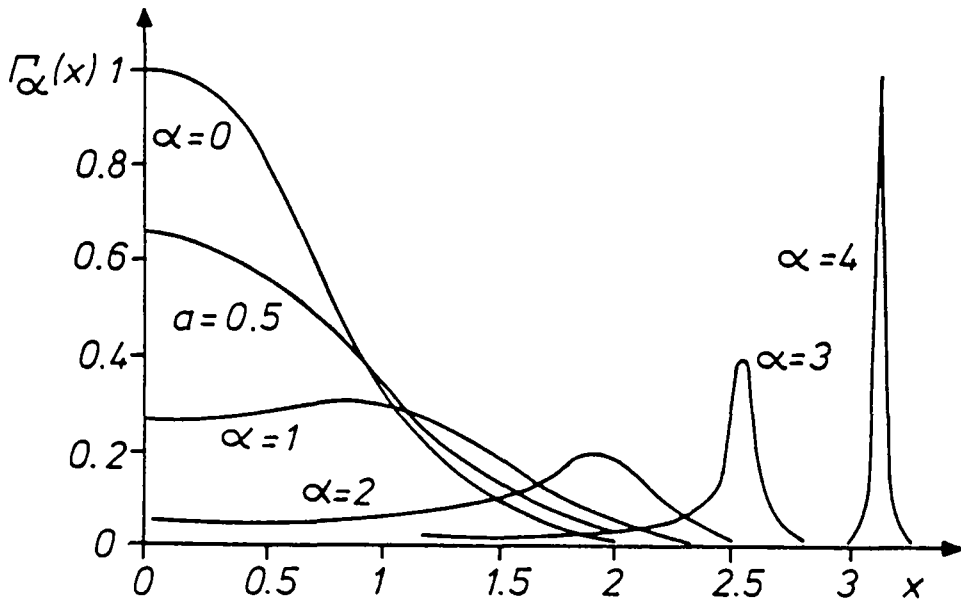


FIGURE 1.4. Variation of  $\Gamma_\alpha(x)$  with  $\alpha = 1/(k\lambda_D)$  [5].

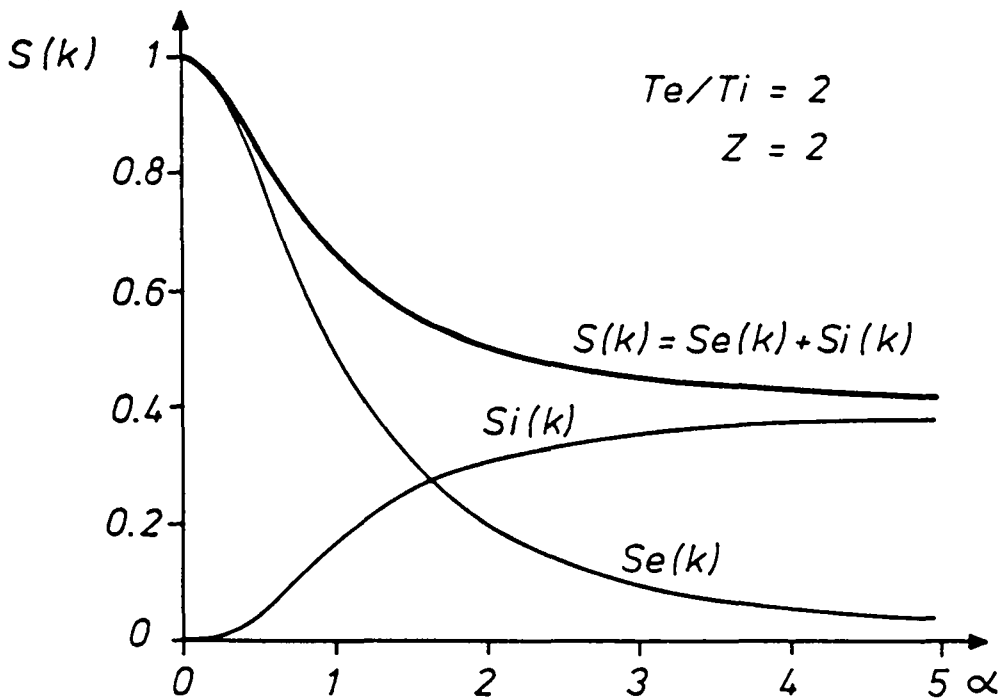


FIGURE 1.5. Contribution of electron and ion terms to  $S(k)$  the integrated form factor (see equation 1.32).

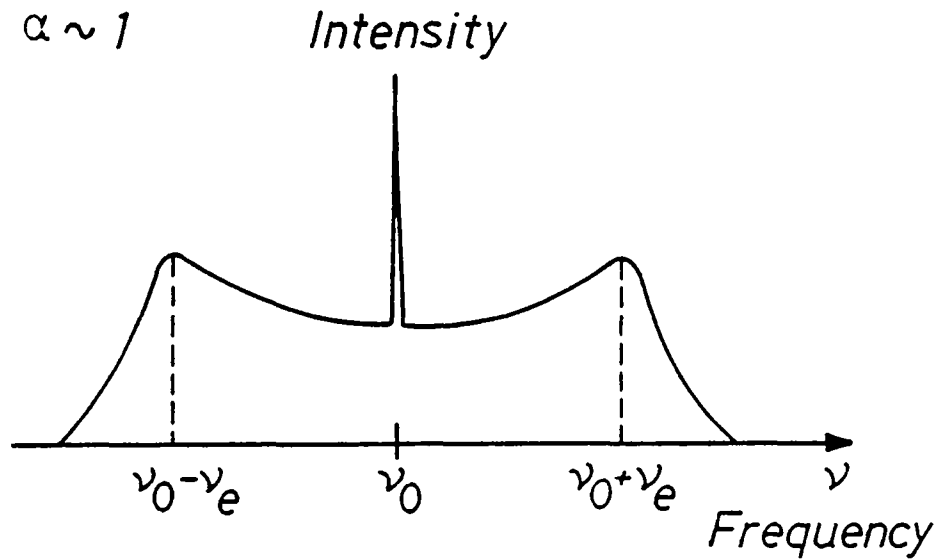


FIGURE 1.6. Coherent scattering spectrum for a thermal plasma with  $\alpha \sim 1$ , shown on a logarithmic intensity scale.

The form of  $S(k, \omega)$  for various plasma conditions has been studied extensively by several authors [1,2,4-9,11-14]. These studies show the influence of various plasma parameters on the precision of an ion temperature measurement and the possibilities to measure other plasma parameters by collective Thomson scattering. In the remaining part of this introduction we will discuss the results of numerical calculations which show the influence on the dynamic form factor of different parameters of the plasma and the scattering experiment. The more generalized form factor used for these calculations (see equation 1 from M.R. Siegrist et al. [6], and M.A. Dupertuis [6]) is derived from D.E. Evans [4] and T.J.M. Boyd et al. [7]. It includes the effect of impurities, particle drift and the magnetic field. The ion and electron velocity distributions are assumed to be Maxwellian to use a classical definition of the temperature.

For typical TCA conditions, both the electron and ion features influence equally the integrated form factor (see figure 1.5). The electron spectrum is, however, about 40 times broader

(square root of the mass ratio) than the ion spectrum, and thus contributes only by 2.5% to the total scattered signal within the spectral width of the ion feature. Therefore, the spectra presented in the following sections will represent mainly the ion feature of the scattered signal.

If not specifically stated, all figures presented in the following sections are derived for a  $90^\circ$  Thomson scattering experiment with a laser wavelength of  $385 \mu\text{m}$  on a  $D^+$  plasma (see appendix A for typical TCA plasma parameters). For clarity, to show the effect of the individual terms on the scattered spectral shape, we will only alter one variable at a time. For the same reason, effects due to the magnetic field and the impurities, which are always present in a real plasma, are not included in the calculations before §1.7.6.

#### 1.7.1. Effects of the scattering angle.

For a given incident wavelength, the effect of varying the scattering angle  $\Theta$  will be to modify the magnitude of the scattering vector  $|k|$ , hence the  $\alpha$  parameter. The angle  $\Theta$  directly influences the mean bandwidth and the shape of the scattered spectrum [8] as illustrated in figure 1.7.

A smaller angle will increase the  $\alpha$  parameter. The ion contribution to the scattered power will be more intense (see figure 1.5), and it will be concentrated into a narrower spectrum. An increase of  $\alpha$ , keeping the plasma parameters constant, results in an increase of  $\beta$ . The peak appearing for large  $\beta$  corresponds to the point  $x_i \approx \beta$  of figure 1.4. With some algebra this is equivalent to  $\omega^2 = 2\omega_{pi}^2 / (1 + \alpha^2)$  [8], where  $\omega_{pi}$  is the ion plasma frequency. This resonance peak is more pronounced for larger  $\beta$  because the Landau damping (the imaginary part of equation 1.25) decreases for large values of  $x$  [1,5].

There are many reasons for a particular choice of the scattering angle in a coherent Thomson scattering experiment. These are, among others:

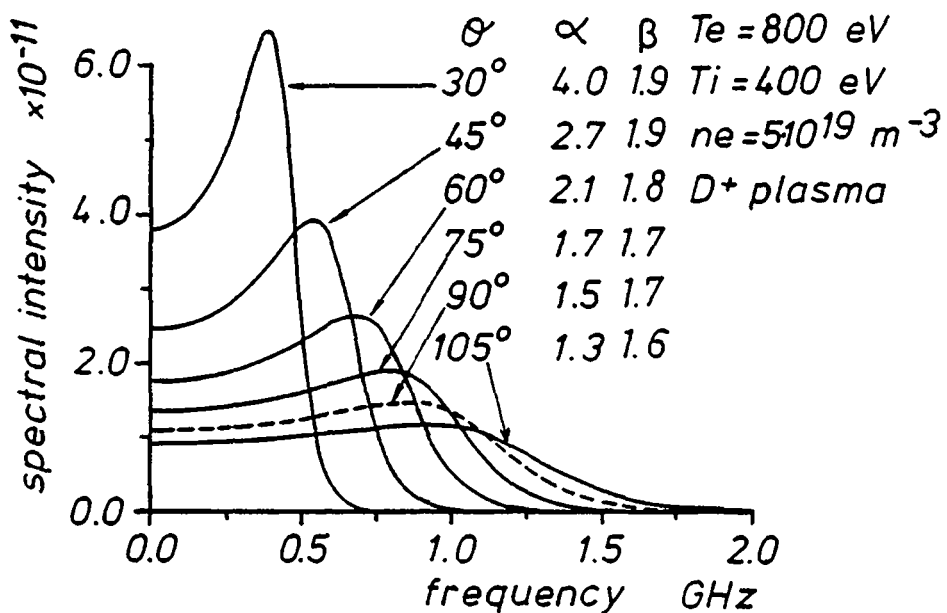


FIGURE 1.7. Effect of the scattering angle on the scattered spectrum.

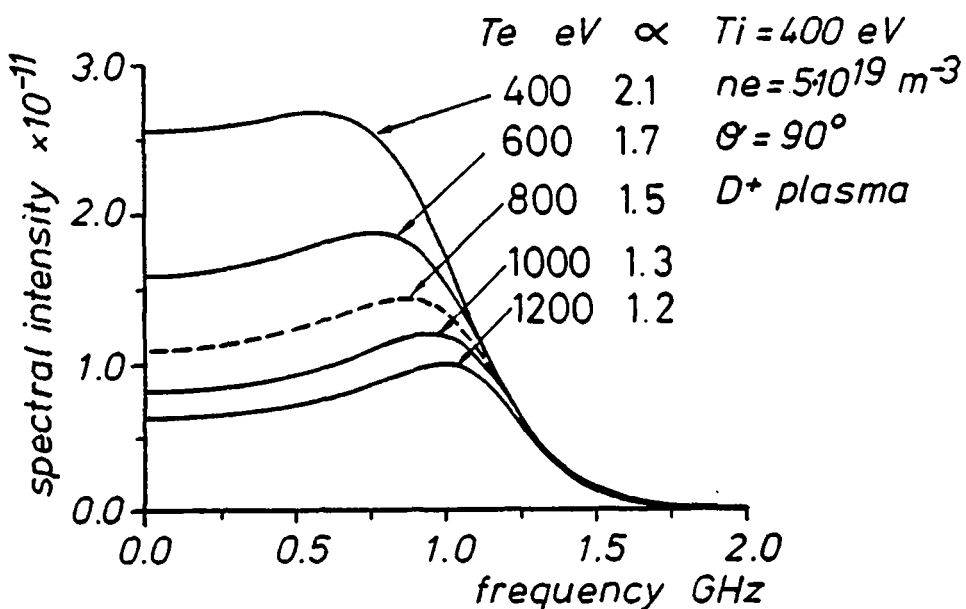


FIGURE 1.8. Effect of the electron temperature on the scattered spectrum.

- the choice of a particular  $\alpha$  regime for a given wavelength of the laser source,
- the adjustment of the spatial resolution,
- the improvement of the stray light rejection,
- the adaption of the spectral width to the bandwidth of the detection system,
- the limitations imposed by the access on the tokamak.

### 1.7.2. Effects of the electron temperature.

Figure 1.8 illustrates the effect of changing the electron temperature and maintaining the other parameters fixed.

Changing the electron temperature alone affects the Debye length, hence the  $\alpha$  parameter. The total power in the ion feature of the spectrum varies roughly as  $\alpha^2$  (equation 1.32). We observe that the total scattered power over the ion feature bandwidth is reduced with increasing electron temperature.

The ion acoustic resonance hardly changes between  $\alpha=2.1$  and  $\alpha=1.2$ , this could seem surprising if we compare it with figure 1.7. It is explained, however, by the fact that Landau damping is strong for  $T_e \simeq T_i$  and decreases with the increasing electron to ion temperature ratio. This change in the Landau damping cancels the effect from the corresponding increase of  $\alpha$  [1,5].

### 1.7.3. Effects of the ion temperature.

The main influence of the ion temperature on the scattered spectrum is illustrated in figure 1.9 and 1.10. In contrast with the case of incoherent scattering, where the electron temperature can be simply evaluated from the half width of a Gaussian spectrum, both the width and the shape of the spectrum from coherent scattering varies significantly with several plasma parameters. For a precise evaluation of the ion temperature numerical fitting routines have to be applied which make use of the general shape of the scattered spectrum.

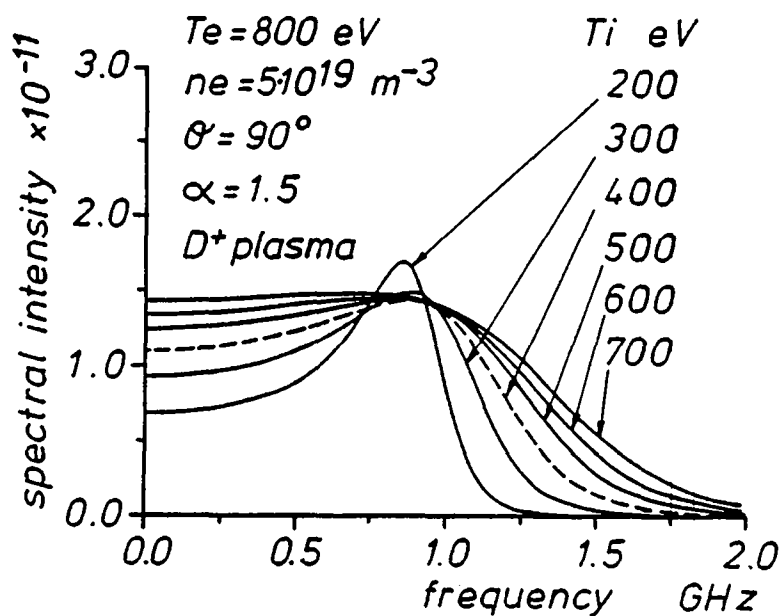


FIGURE 1.9. Effect of the ion temperature on the scattered spectrum.

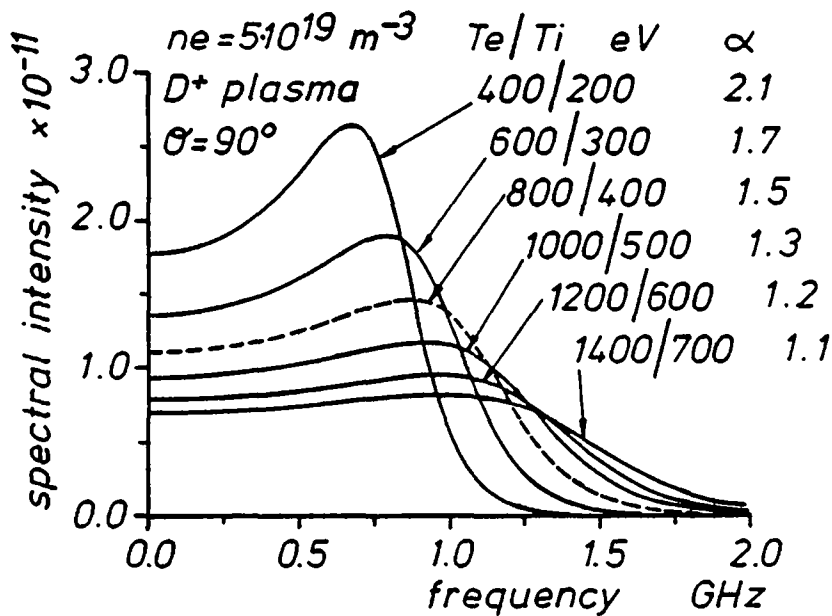


FIGURE 1.10. Effect of the ion temperature on the scattered spectrum, keeping  $T_e/T_i$  fixed.

We show in §2.7.2 the result of numerical simulations used to estimate the influence of the plasma parameters on the precision of an ion temperature measurement.

Figure 1.9 shows the scattered spectrum for different ion temperatures, keeping all other plasma parameters constant. The enhancement of the ion acoustic resonance for low ion temperatures illustrates the decrease of the Landau damping for the increasing electron to ion temperature ratio.

It is generally found that on axis of an ohmically heated TCA plasma, and for a given density, the electron to ion temperature ratio stays roughly constant. On TCA, the electron temperature is usually twice the ion temperature. This case is illustrated in figure 1.10, where the ion temperature is changed together with the electron temperature. The combined variation of the ion and electron temperatures affects not only the spectral width but also the spectral intensity of the ion feature through the variations of  $\alpha$  via the electron temperature.

#### 1.7.4. Effects of particle drift.

In a tokamak the plasma current causes particle drift in the toroidal direction. Turbulences over a scale greater than the scattering volume can also produce the effect of a local drift. The influence of a drift velocity on the scattered spectrum is illustrated in figure 1.11.

The particle drift mainly influences the symmetry of the spectrum [1,5]. The Landau damping of the forward and backward traveling ion acoustic waves is different due to the shift of the velocity distributions.

The particle drift velocity due to the plasma current is typically below 1% of the thermal velocity, and in any case, on TCA, the toroidal velocity vector is perpendicular to the scattering vector, hence the plasma current will have no effect.

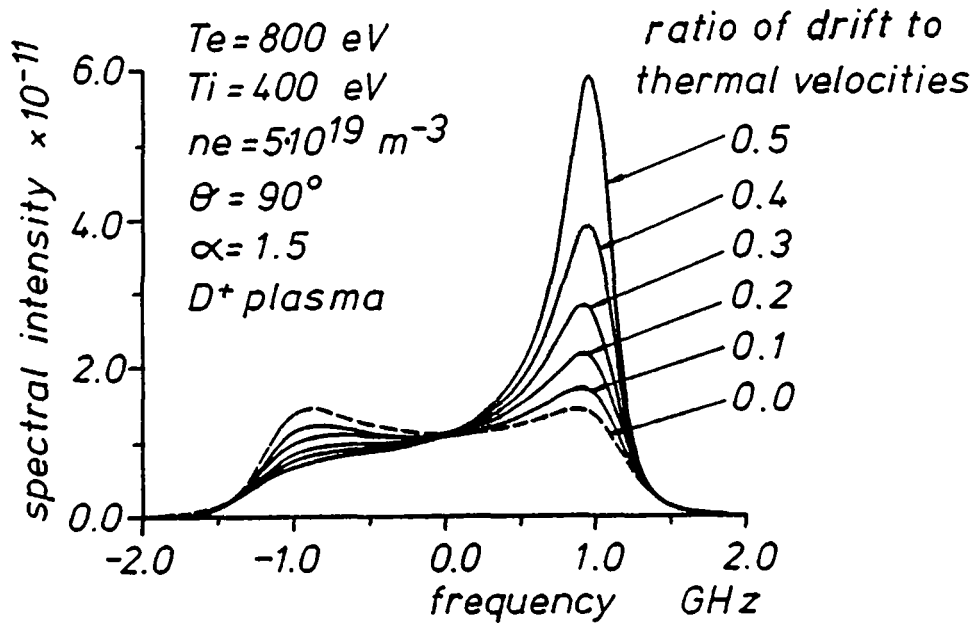


FIGURE 1.11. Effect of the particle drift on the scattered spectrum.

To measure particle drift velocities, both sides of the scattered spectrum must be observed. The detection system must have a bandwidth twice as large as the minimum necessary for an ion temperature measurement.

#### 1.7.5. Effects of plasma microturbulence.

Microturbulence leads to density fluctuations  $\Delta n_e$  well above the thermal level. In the collective regime the intensity of the scattered radiation is proportional to  $\Delta n_e^2$  (see equation 1.16). Therefore turbulent density fluctuations will cause significant contributions, which are difficult to predict. No theory is currently available to describe tokamak plasma microturbulence such that it could be included successfully in our numerical simulations.

Up to now, no direct experimental observations of microturbulence covering the full frequency spread of a thermal



spectrum have been reported [10]. Scattering from slow density fluctuations below 100 kHz in frequency and with scattering vectors of  $\sim 50 \lambda_D$  has been measured with CW far infrared lasers [15]. The observed scattered intensity varies as  $\omega^{-2.5}$  and  $k^{-3.5}$  [2]. Scaling from these results, for  $k \sim 1/\lambda_D$  and  $\nu \geq 0.5$  GHz, leads to negligible power levels of microturbulence.

#### 1.7.6. Effects of impurities.

Tokamak plasmas always contain small amounts of impurities. In the TCA tokamak these are mainly oxygen and metals from the torus walls. With the use of coated carbon limiters, carbon and coating materials have also been observed [16].

Even if these impurities are of low relative densities they will scatter strongly due to their high  $Z$ , which will attract a cloud of shielding electrons. Calculated spectra including impurities are shown in figure 1.12.

The impurities produce a peak around the central laser frequency [4]. The width of this peak is proportional to the thermal velocity of each species and is narrower than the majority ion feature due to their higher masses. The height is related to the charge and abundance of the impurity ions.

Only the central part of the Thomson scattered spectrum is affected, as shown in figure 1.12, hence the presence of a known amount of impurities (e.g. measured by UV spectroscopy) would have a minor influence on the measurement of the ion temperature if only the outer part of the spectrum is considered.

A numerical fit to the effective charge of the plasma, which is defined as:

$$Z_{\text{eff}} = \frac{\sum Z_j^2 N_j}{\sum Z_j N_j} \quad (1.33)$$

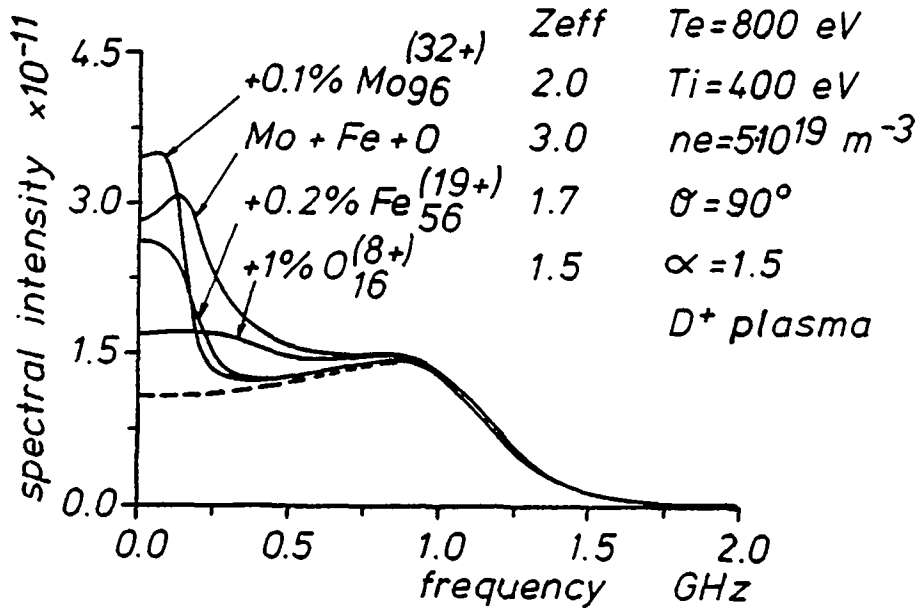


FIGURE 1.12. Effect of impurities on the scattered spectrum.

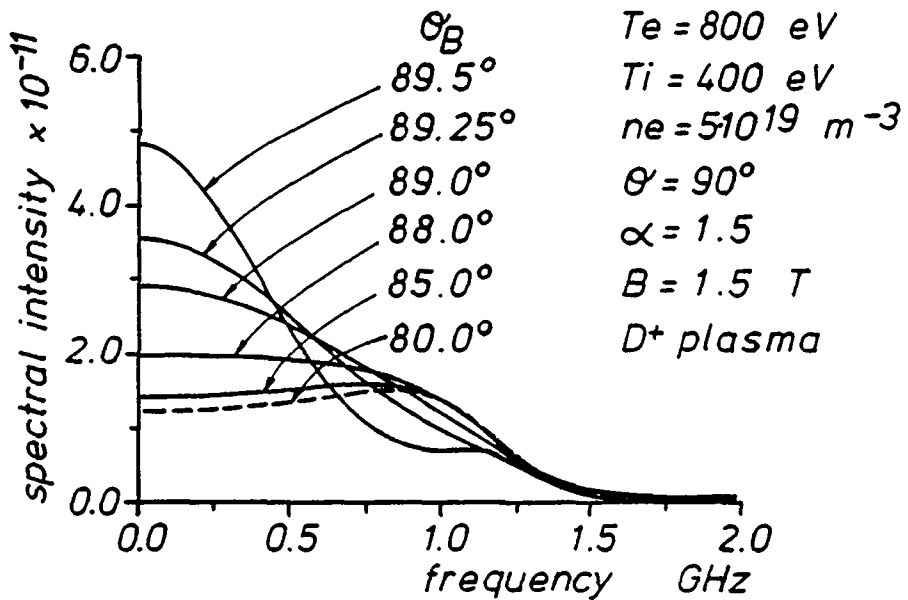


FIGURE 1.13. Effect of the magnetic field on the scattered spectrum.

where

$Z_j$  is the charge of the  $j$ 'th ion species

$N_j$  is the density of the  $j$ 'th ion species,

could be attempted if this central feature were measured with sufficient accuracy [4,6]. This would imply a scattering experiment with negligible stray light from the laser, which is practically impossible to achieve. Effects from microturbulence and the magnetic field in the tokamak would also affect the same central part of the scattered spectrum.

In the analytic expression of the form factor the impurities enter as a sum over the ion screening terms and over the velocity distribution term weighted by their relative charges. One assumes that each velocity distribution function satisfies its own collisionless Boltzmann equation, and that the electron and ion terms are coupled by Poisson's equations [4]. This modifies the numerator and the common denominator of the form factor expression, hence the final spectrum is not a simple linear superposition of the spectrum of each species. This is also illustrated in figure 1.12.

#### 1.7.7. Effects of collisions.

Collisions will affect the spectrum when the collisional frequency becomes comparable to the width of the scattered spectrum. In the TCA tokamak plasma, this collisional frequency is too low ( $< 1$  MHz) to influence significantly the global spectrum, thus we will ignore this term [6,10].

#### 1.7.8. Effects of the magnetic field.

For the current experiment on TCA, apart from the impurities, the main perturbation of the scattered spectrum comes from the magnetic field, as illustrated in figure 1.13.

The magnetic field introduces a modulation of the electron and ion scattered spectra. The periodicity of this modulation is given by the respective cyclotron frequencies. This modulation only influences the scattered spectrum when the scattering vector  $k$  is almost perpendicular to the magnetic field vector  $B$ . This condition is often satisfied in Thomson scattering experiments on tokamaks where port access generally defines the scattering geometry [6,10,12-14].

For the calculations of figure 1.13 it has been assumed that only the electrons are magnetized ( $kp_e \ll 1$ , where  $\rho_e$  is the electron Larmor radius). For a B-field of 12 kG (typical TCA conditions) a modulation of the electron feature at a frequency of 34 GHz is to be expected. The electron cyclotron motion also affects the central part of the electron feature, which is strongly enhanced in this case.

The ion cyclotron frequency, on the other hand, modulates the ion feature at 18 MHz and will not be resolved by the 80 MHz wide channels of the detection filter bank [6].

Additionally, for the effect of the gyration to be observed, the charges must gyrate within the scattering volume and during the time of the measurement [1]. On TCA the Larmor radius of the electrons and ions are about 35  $\mu\text{m}$  and 3.8 mm respectively. The linear dimension of the scattering volume is about 2 mm and the laser pulse duration is about 1  $\mu\text{s}$ . Therefore, only the effect of the electrons need to be considered.

### 1.8. Conclusions.

If a sufficient signal to noise ratio is achieved in a given scattering configuration, several plasma parameters could be measured by collective Thomson scattering [9].

Except for a scattering geometry with an angle of  $90^\circ \pm 1^\circ$  between the scattering  $k$ -vector and the magnet field vector,

the ion temperature can be unequivocally extracted from the scattered spectrum by applying numerical routines to fit the measured coherent scattered spectrum [6,8,10].

Depending on the direction of the scattering vector with respect to the magnetic field vector, it would be possible to measure the magnetic field direction by carefully analysing the shape of the scattered spectrum [6,13,14].

An attempt to measure the level of impurities ( $Z_{\text{eff}}$ ) is theoretically possible [6], but it implies a very low level of stray laser light around the central laser line which is difficult to achieve in practice.

Whereas the influence of impurity ions and of the magnetic field orientation are well described by the theory, strong microturbulence could disturb the spectrum in an unpredictable way. Up to now there is no experimental evidence that for the  $k$ -vectors considered here the contribution from microturbulence extends in to the frequency range of a thermal spectrum [10].

The next chapter discusses why we are limited in practice to measuring only the ion temperature of the plasma in the TCA tokamak.

REFERENCES.

- [1] "Plasma scattering of electromagnetic radiation", J. Sheffield, Academic Press, (1975).
- [2] "Plasmas and laser light", T.P. Hughes, Chap. 3, Adam Hilger, (1975).
- [3] "Classical electrodynamics", Sect. 9.2, J.D. Jackson, John Wiley, N.Y. (1975).
- [4] "The effect of impurities on the spectrum of laser light scattered by a plasma", D.E. Evans, Plas. Phys. 12, 573 (1970).
- [5] "Laser light scattering in laboratory plasmas", D.E. Evans and J. Katzenstein, Rep. Prog. Phys., 32, 207 (1969).
- [6] "Mesure de  $T_i$  et de  $Z_{eff}$  par diffusion Thomson dans un tokamak", M.A. Dupertuis, CRPP report LRP-185/81, (1981).
- "Simulation of a magnetic field and ion temperature measurement in a tokamak by Thomson scattering", M.R. Siegrist, M.A. Dupertuis, R. Behn, P.D. Morgan, Plasm. Phys. 24, 1449 (1982).
- "Etude théorique des lasers infrarouges lointains pulsés et de leur comportement multimode", M.A. Dupertuis, Ecole Polytechnique Fédérale de Lausanne, Thèse no. 558, (1985).
- [7] "Numerical calculations of the frequency spectrum of light scattered by a magnetized plasma", T.J.M. Boyd, D.E. Evans, G.A. Gardner, contr. 5.3.2, p. 42, Int. Conf. Phenom. in ionized gases, (1971).
- [8] "To the question of ion temperature measurements with far infrared lasers", G. Magyar, EUR-CEA-FC-815, Fontenay-aux-Roses, (1976).
- "Guide de la diffusion cohérente dans l'I.R. lointain", J. Olivain, EUR-CEA-FC-1024, Fontenay-aux-Roses, (1979).
- [9] "Thomson scattering of FIR radiation", D.E. Evans, Inv. Lect. 2nd. Int. Conf. Sub-MM Waves and their Appl., Puerto Rico, (1976).

- [10] "A study of measuring the plasma ion temperature in JET by Thomson scattering using a far infrared laser", M.R. Green, P.D. Morgan, M.R. Siegrist, R.L. Watterson, CRPP report LRP-168/80, (1980).
- [11] "Light scattering from plasmas with a non-Maxwellian velocity distribution", W.H. Kegel, *Plasm. Phys.*, 12, 295 (1970).
- [12] "Influence of symmetry about the magnetic vector on the spectrum of light scattered by a magnetized plasma", P.G. Carolan and D.E. Evans, *Plasm. Phys.*, 13, 947 (1971).
- [13] "Measurement of the magnetic field in a laboratory plasma by Thomson scattering of laser light", D.E. Evans and P.G. Carolan, *Phys. Rev. Lettr.*, 25, 1605 (1970).
- [14] "Laser light scattering as a method for measuring the magnetic field direction in a plasma", P.G. Carolan, *Plasm. Phys.*, 19, 757 (1977).
- [15] "FIR collective scattering from the UCLA Microtor Tokamak", A. Semet, A. Mase, W.A. Peebles, N.C. Luhmann, Jr., 4. Int. Conf. IR and MM Waves, Miami, p. 42 (1979).
- "Study of density fluctuations in plasmas by small-angle CO<sub>2</sub> laser scattering", R.E. Slusher and C.M. Surko, *Phys. Fluid*, 23, 472 (1980).
  - "Study of plasma density fluctuations by the correlation of crossed CO<sub>2</sub> laser beams", C.M. Surko and R.E. Slusher, *Phys. Fluid*, 23, 2425 (1980).
- [16] "Plasma target conditions in TCA", A. de Chambrier et al., CRPP report LRP-241/84, (1984).
- [17] "Principles of optics", M. Born and E. Wolf, Pergamon press, 1970.





## CHAPTER 2 .

### REQUIREMENTS FOR A COLLECTIVE THOMSON SCATTERING ION TEMPERATURE MEASUREMENT.

In this chapter we will specify the parameters of the radiation source (laser wavelength, bandwidth and power) and the detection system (sensitivity and bandwidth) to fulfil the requirements of a collective Thomson scattering experiment on the TCA tokamak. To be able to measure, simultaneously with  $T_i$ , other plasma parameters (e.g. the effective charge of the plasma or the magnetic field direction), the measurement of the scattered spectrum must be obtained with a higher accuracy. This means a higher signal to noise ratio and a better frequency resolution of the scattered signal would be required. The values needed for a  $T_i$  measurement alone are already at the limit of current technology of pulsed FIR lasers and heterodyne detection systems. This is the main reason why in the present chapter we will concentrate only on the ion temperature and will not consider the case of a multiparameter measurement on TCA.

For this study, and if not specifically mentioned, we use the following typical plasma parameters of the TCA tokamak (referred to later in the text as standard TCA conditions, see appendix A):

$$\begin{aligned} n_e &= 5 \cdot 10^{19} & \text{m}^{-3} & \text{the plasma density,} \\ T_e &= 800 & \text{eV} & \text{the electron temperature,} \\ T_i &= 400 & \text{eV} & \text{the ion temperature,} \\ Z_{\text{eff}} &= 2.5 & & \text{the effective charge of the plasma,} \\ B_T &= 1.2 & \text{T} & \text{the toroidal magnetic field,} \\ \theta &= 90^\circ & & \text{the scattering angle,} \end{aligned} \tag{2.1}$$

which gives a Debye length (see equation 1.13) of:

$$\lambda_D = 30 \cdot 10^{-6} \quad [\text{m}], \text{ and}$$

$$N_D = 4\pi/3 n_e \lambda_D^3 = 5.6 \cdot 10^6 \quad \text{particles in the Debye cloud.}$$

### 2.1. Choice of the wavelength.

The ion temperature measurement is performed by collective scattering and therefore requires  $\alpha \geq 1$ . The formula (1.14), from chapter 1, can be rearranged such that a lower limit of the laser wavelength is obtained by:

$$\lambda_0 > 4\pi \alpha \sin(\Theta/2) \lambda_D \quad (2.2)$$

$$\lambda_0 > 93400 \alpha \sin(\Theta/2) \sqrt{T_e/n_e} \quad [(\text{eV} \cdot \text{m})^{-1/2}]$$

$$\lambda_0 > 265 \quad [\mu\text{m}] \quad \text{for scattering at } \Theta = 90^\circ \text{ on TCA.}$$

The limit of  $\alpha = 1$  is illustrated in figure 2.1 for different laser wavelengths and scattering angles. The scattering parameter  $\alpha$  increases above one to the right of each curve.

An upper wavelength limit is given by the electron plasma frequency  $\omega_{pe}$ . The electrons of the plasma will follow, and cancel out, any electric field that varies slower than  $\omega_{pe}$ , hence the plasma will reflect these frequencies. This limit is expressed by:

$$\lambda_0 < 2\pi c / \omega_{pe} = \lambda_{\text{crit}} \quad (2.3)$$

$$\lambda_0 < 33.4 \cdot 10^6 / \sqrt{n_e}$$

$$\lambda_0 < 4.7 \quad [\text{mm}] \quad \text{for standard TCA conditions.}$$

where  $n_e$  is the electron density in  $\text{m}^{-3}$ .

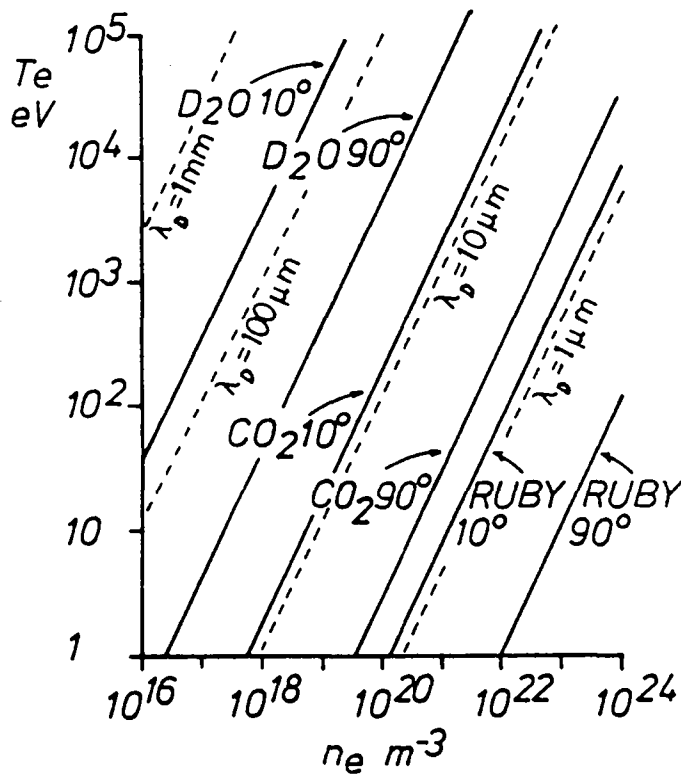


FIGURE 2.1. Wavelength limits for  $\alpha = 1$  (solid lines), and plasma Debye lengths (broken lines).

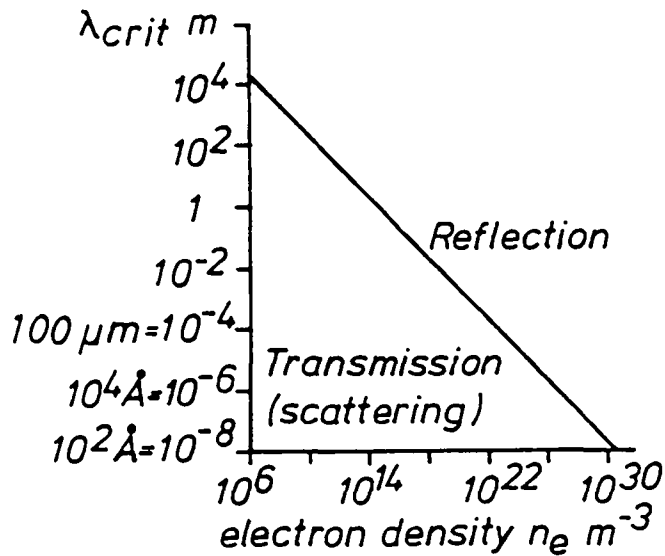


FIGURE 2.2. The critical wavelength for a plasma as a function of the plasma density.

A more restrictive limit on the wavelength is caused by background plasma emission at the harmonics of the electron cyclotron (ECE) frequency. For present tokamaks like TCA the incident wavelength should be shorter than the third harmonic of the ECE frequency  $\omega_{ece}$  [1,2,3]. The expression for this limit is:

$$\lambda_0 < 2\pi c / (\ell\omega_{ece}) \quad (2.4)$$

$$\lambda_0 < 10.7 \cdot 10^{-3} / (\ell B)$$

$$\lambda_0 < 7.1 \cdot 10^{-3} / \ell \quad [\text{cm}] \quad \text{for TCA.}$$

where  $B$  is the magnetic field in Tesla, and  $\ell > 3$  is the harmonic number.

The power of the ECE received by the detection system depends on the plasma temperature, the solid angle of the collection optics and the quality of the viewing dump. Extensive measurements have been done by the MIT group on the ALCATOR A tokamak [1]. They show that only the third (and lower) harmonics can interfere with the expected level of Thomson scattered signals. However on new generation machines like JET a lower limit of  $\omega_0 \geq 5\omega_{ece}$  would be required [2,4,5].

Combining these conditions, in the case of TCA, we find that the wavelength of the laser source to be used with a collective Thomson scattering experiment has to be chosen within the following limits:

$$2.35 \text{ [mm]} > \lambda_0 > 265 \text{ [\mu m]} \quad (2.5)$$

This is within the far infrared (FIR) wavelength region.

## 2.2. Choice of the scattering angle.

On TCA the scattering angle is imposed by technical constraints. The axis defined by the input port and the opposed

beam dump port on the TCA torus intercepts the plasma at its center. Scattering from a point situated on an axis passing through the plasma center has the advantage of minimizing the displacement of the scattering volume due to beam refraction from density gradients in the plasma. The position of the observation port in the same poloidal plane fixes the scattering angle to about  $90^\circ$ , which gives an optimum spatial resolution of the scattering volume.

A small change of the scattering angle of  $\pm 5$  degrees can be obtained by shifting the scattering volume 25 mm above or below the plasma center (see chapter 4).

Scattering from the plasma center, where  $B = B_T$ , with the scattering vector in the poloidal plane, means that the vector  $k$  is perpendicular to the magnetic field vector  $B$ . As discussed in chapter 1, at this angle, the magnetic field will strongly influence the spectral shape of the scattered signal. This effect must be considered when analysing the experimental data to extract the ion temperature.

The scattering angle determines the mean spectral width of the scattered signal. From the results presented in chapter 1 (figures 1.9 and 1.10) the half width at half maximum (HWHM) of the spectrum for  $90^\circ$  scattering with standard TCA parameters is approximately:

$$\begin{aligned} \Delta\nu &\approx 1250 \text{ [MHz]} \quad \text{for a } D^+ \text{ plasma, and} \\ \Delta\nu &\approx 1700 \text{ [MHz]} \quad \text{for a } H^+ \text{ plasma.} \end{aligned} \quad (2.6)$$

This is only a rough estimate but it tells us that the bandwidth of the detection system must be of the order of 2 GHz to resolve half the spectrum of a hydrogen plasma. Except for the effect due to particle drift (see chapter 1), the scattered spectrum is symmetric with respect to the incident laser frequency, hence the information on  $T_i$  is fully contained in both halves of the spectral width.

### 2.3. Estimate of the scattered radiation cross section.

A general formula (1.15) was given in chapter 1 for the total scattered power from a plasma into given solid angle. By rearranging this expression we obtain the total scattered cross section (ratio of scattered to incident power) of the ion feature, where  $S_i(\alpha)$  is taken from equation 1.32:

$$\frac{P_s(\alpha)}{P_0} = r_e^2 n_e L d\Omega S_i(\alpha) \quad (2.7)$$

A coherent scattering experiment on TCA with standard deuterium plasma conditions and a  $90^\circ$  scattering angle can be achieved with an incident laser wavelength of  $385 \mu\text{m}$ . In this case we obtain  $\alpha = 1.5$  and  $S_i(\alpha) = 0.25$ . The length  $L$  of the volume is typically  $3 \text{ mm}$  on TCA, and the collecting solid angle  $d\Omega$  is about  $2 \cdot 10^{-2}$  str (see §2.7.1), which corresponds to the solid angle of a diffraction limited  $F/6$  optical element. By introducing these values into equation 2.7 we obtain:

$$\frac{P_s}{P_0} \approx 6 \cdot 10^{-15} \quad (2.8)$$

If we assume furthermore that the incident laser power is  $1 \text{ MW}$ , we obtain an average scattered power density of  $2 \cdot 10^{-18} \text{ W/Hz}$  over the full  $3 \text{ GHz}$  bandwidth of the scattered spectrum. The main difficulty of the Thomson scattering experiment lies in this very low efficiency.

### 2.4. Plasma background noise.

If the plasma radiated like a blackbody in the FIR, emitting a power of  $\kappa T_e \text{ W/Hz}$  into the detector of etendue  $\leq \lambda_0^2$ , the scattered signal would not be observable. Fortunately this is not the case. Among the different plasma radiation sources only the Bremsstrahlung will have an effect comparable to the level of scattered radiation on TCA. Line radiation and recombination radiation are negligible in the FIR wavelength

region ( $h\nu/e \approx 3 \cdot 10^{-3}$  eV). Even ECE can be ignored as will be shown later.

The electron-ion Bremsstrahlung power emitted by the plasma into the solid angle  $\Delta\Omega$ , and into the frequency interval  $\Delta\nu$ , can be estimated by [2.6,7]:

$$P_B = \frac{32\pi e^6}{3(4\pi\epsilon_0 c)^3 m_e} \left(\frac{2\pi}{3m_e e}\right)^{1/2} g Z^2 \left(\frac{n_e n_i}{T_e^{3/2}}\right) \exp\left(\frac{-h\nu}{eT_e}\right) V \frac{\Delta\Omega}{4\pi} \Delta\nu \quad (2.9)$$

$$P_B = 5 \cdot 10^{-54} g Z^2 \left(\frac{n_e n_i}{T_e^{3/2}}\right) \exp\left(\frac{-1.24 \cdot 10^{-6}}{\lambda_0 T_e}\right) V \Delta\Omega \Delta\nu$$

where

- c is the speed of light,
- $m_e$  is the mass of the electron,
- $\epsilon_0$  is the permittivity of free space,
- e is the charge of the electron,
- g is the Gaunt factor,  $g \approx 5$  in the FIR see [6],
- $\lambda_0$  is the incident laser wavelength,
- Z is the main plasma ion charge,
- V is the plasma volume seen by the detector,
- $\Delta\Omega$  is the solid angle of the detection optics,
- $\Delta\nu$  is the scattered bandwidth,
- $\exp(\dots) \approx 1$  in the FIR.

For a gaussian beam the product of observed plasma volume and solid angle can be expressed by:

$$V\Delta\Omega = 2/3 a^3 d\Omega^2 \approx 1.5 \cdot 10^{-6} [\text{m}^3 \cdot \text{str}] \text{ on TCA, } (2.10)$$

where a is the minor plasma radius (0.18 m, see appendix A) and the solid angle of the collecting optics  $d\Omega$  is set to  $2 \cdot 10^{-2}$  str (see §2.7.1).

Introducing the standard TCA deuterium plasma parameters, and assuming a FIR radiation wavelength of 385  $\mu\text{m}$ , the total power density due to Bremsstrahlung collected by the detection system is:

$$P_B = 1.3 \cdot 10^{-20} \text{ [W/Hz]} \quad (2.11)$$

This power level would increase if no viewing dump is used to avoid reflections from the inner torus wall, but could be reduced if a polarizer is introduced between the plasma and the detector. The polarizer will have no effect on the horizontally polarized scattered signal.

The power level of the ECE has been studied extensively on ALCATOR A using the heterodyne detection system designed for the  $T_i$  measurement by Thomson scattering at MIT [1]. Measurements up to the fifth harmonic were made and showed reasonable agreement with theoretical estimates [1]. On ALCATOR, because of its high magnetic field, the ECE of the harmonics  $\lambda = 2, 3, 4$  are in the FIR region used for the Thomson scattering. This is not the case on TCA as will be shown here.

The ECE power level is calculated with the following formula valid in the high frequency limit such that  $\omega_{pe}/\omega \ll 1$  is satisfied [1,7]:

$$P_{ECE} = P_{BB} (1 - \exp(-\tau_\lambda)) \quad \text{[W/(Hz} \cdot \text{m}^2)] \quad (2.12)$$

where  $P_{BB}$  is the blackbody radiation intensity and  $\tau_\lambda$  is the optical depth of the  $\lambda$ 'th ECE harmonic defined as [1,7]:

$$P_{BB} = \frac{e T_e}{2\pi\lambda_0^2} \quad \text{[W/(Hz} \cdot \text{m}^2)] \quad (2.13)$$

$$\tau_\lambda \approx \tau_\lambda^e = \frac{\pi e}{2c \epsilon_0} \frac{\lambda^{2\lambda-2}}{(\lambda-1)!} \left(\frac{R}{B}\right) n_e \left(\frac{e T_e}{2m_e c^2}\right)^{\lambda-1} \quad (2.14)$$

$$\tau_\lambda \approx 9.5 \cdot 10^{-17} \frac{\lambda^{2\lambda-2}}{(\lambda-1)!} \left(\frac{R}{B}\right) n_e (9.8 \cdot 10^{-7} T_e)^{\lambda-1} \quad (2.15)$$

where

R is the radial coordinate from the center of the torus to the observation point in the plasma, (major plasma radius on TCA), in meters,

B is the toroidal magnetic field, in Tesla, and



$$\lambda = \frac{\omega}{\Omega_{ce}} = \frac{2\pi c m_e}{\lambda_0 eB} = \frac{1.1 \cdot 10^{-2}}{\lambda_0 B} \tag{2.16}$$

Only the extraordinary mode is considered here. The ordinary mode, although having its initial polarization parallel to the polarization of the scattered radiation, is several orders of magnitude weaker:

$$\tau_{\lambda}^o = \left( \frac{eT_e}{2m_e c^2} \right) (1 - \omega_{pe}^2/\omega^2)^{\lambda - \frac{1}{2}} \cdot \tau_{\lambda}^e \tag{2.17}$$

$$\tau_{\lambda}^o = 9.8 \cdot 10^{-7} T_e (1 - 8 \cdot 10^{-16} n_e \lambda_0^2)^{\lambda - \frac{1}{2}} \cdot \tau_{\lambda}^e \tag{2.18}$$

where  $\omega_{pe}^2 = n_e e^2 / (m_e \epsilon_0)$  is the plasma frequency.

The polarization of the extraordinary radiation is initially perpendicular to the polarization of the scattered radiation. By the time the radiation gets to the detection system, however, the polarization is totally scrambled [1,2] due to multiple reflection off the torus walls. For the toroidal field strength of TCA (12 to 15 kG) a laser source emitting at 800 GHz corresponds to the 23rd harmonic of the ECE. The stray power level is therefore negligible. This is illustrated in table 2.1:

$$T_e = 800 \text{ eV} , \quad n_e = 5 \cdot 10^{19} \text{ m}^{-3} , \quad \nu_{pe} = 64 \text{ GHz} ,$$

$$B = 1.2 \text{ T} , \quad R = 0.6 \text{ m} , \quad \nu_{ce} = 34 \text{ GHz} .$$

$\lambda$	$\tau_{\lambda}^e$	$P_{ECE}^e$ $\times 10^{-18} \text{ [W/Hz]}$	$\tau_{\lambda}^o$	$P_{ECE}^o$ $\times 10^{-18} \text{ [W/Hz]}$
2	7.42	$2.04 \cdot 10^1$	$5.75 \cdot 10^{-3}$	$1.17 \cdot 10^{-1}$
3	$5.88 \cdot 10^{-2}$	1.16	$4.52 \cdot 10^{-5}$	$9.23 \cdot 10^{-4}$
4	$7.76 \cdot 10^{-4}$	$1.58 \cdot 10^{-2}$	$5.93 \cdot 10^{-7}$	$1.21 \cdot 10^{-5}$
5	$1.45 \cdot 10^{-5}$	$2.95 \cdot 10^{-4}$	$1.10 \cdot 10^{-8}$	$2.24 \cdot 10^{-7}$
6	$3.51 \cdot 10^{-7}$	$7.15 \cdot 10^{-6}$	$2.64 \cdot 10^{-10}$	$5.39 \cdot 10^{-9}$

TABLE 2.1. Calculated ECE powers for TCA.

### 2.5. The FIR laser.

There are numerous lasers which emit in the FIR wavelength region as required for collective Thomson scattering on TCA. Most of these are continuous wave (CW), molecular gas lasers of low output power. Because of the extremely low cross section of Thomson scattering (see §2.3), a high power laser is needed. The minimum power and bandwidth requirements, for such a laser are established in the next sections.

#### 2.5.1. Power requirements of the FIR laser.

The minimum power required of the FIR laser is to produce a detectable scattered signal in the solid angle of the detection optics. This is achieved when  $P_s$  (from equation 2.7) is greater or equal to the detection system noise equivalent power (NEP) over a given frequency range [2,3].

$$P_s(\alpha) = P_0 r_e^2 L d\Omega n_e S_i(\alpha) \geq \text{NEP} \Delta\nu \quad (2.19)$$

where the frequency range  $\Delta\nu$  (HWHM) is given by the bandwidth of the scattered signal. In a first order approximation the signal bandwidth can be derived from:

$$\Delta\nu = 2 v_i \cdot k = \sqrt{\frac{2eT_i}{m_i}} \frac{2}{\alpha \lambda_D} \quad (2.20)$$

where

$v_i$  is the ion thermal velocity,  
 $k$  is the scattering wave number.

With (2.20) equation (2.19) can be rearranged to:

$$s = \frac{P_s(\alpha)}{\text{NEP} \Delta\nu} = C \frac{P_0 n_e L d\Omega S_i(\alpha) \lambda_D \alpha}{\text{NEP} (T_i)^{3/2}} \left[ C \frac{\text{W} \cdot \text{m}^{-3} \cdot \text{m} \cdot \text{m}}{\text{W}/\text{Hz} \cdot (\text{eV})^{3/2}} \right] \quad (2.21)$$

where the constant  $C$  for a hydrogen plasma is given by:

$$C = \frac{r_e^2}{2} \sqrt{\frac{m_i}{2e}} = 2.87 \cdot 10^{-34} \left[ \frac{m \cdot (eV)^{1/2}}{Hz} \right] \quad (2.22)$$

and  $s$  is the signal to noise ratio.

Table 2.2 presents the minimum incident power  $P_0$ , needed to achieve  $s=1$  for different plasma conditions on TCA. It is assumed that the scattered light is integrated over the whole ion feature.

The values presented in table 2.2 do not take into account any losses in the optical system between the FIR laser and the plasma (window absorption and diffraction losses) neither do they include losses in the path from the plasma to the detector system. Total losses of the order of 6 to 10 dB (see §6.6) are expected, requiring a corresponding increase of the power  $P_0$ .

At present, the most suitable high power laser source is the optically pumped  $D_2O$  laser. Laser powers of several megawatts, for pulse lengths exceeding 1  $\mu s$ , have been reported for the 385  $\mu m$   $D_2O$  wavelength transition (see chapter 3, table 3.3). A 90° scattering experiment on TCA with a  $D_2O$  laser will allow coherent Thomson scattering since the related  $\alpha$  value is 1.5. Chapter 3 gives a detailed description of the  $D_2O$  laser chosen for the Thomson scattering feasibility experiment on TCA.

### 2.5.2. FIR laser bandwidth requirements.

The spectra presented in chapter one have been calculated assuming a perfectly monochromatic laser pulse. Experimentally observed spectra are convolved with the line profile of the laser emission. If the laser line width is not negligible with respect to the spectral width then this effect can be corrected by numerical treatments as long as the laser line profile is known and stable. In practice, the spectral resolution is already limited by the width of the receiver channels,

$$S_i(\alpha) = 0.25, \quad Ld\Omega = 6 \cdot 10^{-5} \text{ m}\cdot\text{str}, \quad \lambda_0 = 385 \text{ }\mu\text{m}.$$

NEP	$n_e$	$T_i$	$P_o$	$P_o$
[W/Hz]	[ $\text{m}^{-3}$ ]	[eV]	[kW]	[kW]
$\times 10^{-18}$	$\times 10^{19}$		H <sup>+</sup> plasma	D <sup>+</sup> plasma
0.3	1	200	310	220
0.3	1	400	440	310
0.3	1	600	540	380
0.3	5	200	65	45
0.3	5	400	90	65
0.3	5	600	110	80
0.3	10	200	30	20
0.3	10	400	45	30
0.3	10	600	55	40
1	1	200	1050	740
1	1	400	1480	1050
1	1	600	1810	1280
1	5	200	210	150
1	5	400	300	210
1	5	600	360	260
1	10	200	110	75
1	10	400	150	110
1	10	600	180	130
3	1	200	3140	2220
3	1	400	4440	3140
3	1	600	5440	3840
3	5	200	630	440
3	5	400	890	630
3	5	600	1090	770
3	10	200	310	220
3	10	400	440	310
3	10	600	540	380

TABLE 2.2. Minimum incident FIR power for H<sup>+</sup> and D<sup>+</sup> plasmas to obtain  $s=1$ , losses not taken into account. The FIR laser presented in chapter 3 has average power of 150 kW, and the detection system presented in chapter 5 has a typical NEP of  $10^{-18}$  W/Hz.

which has been chosen to be 80 MHz. The finite width of the laser emission must not further degrade this resolution. Therefore single mode emission of the FIR laser would be desirable.

Because of the high level of stray light expected, the laser line width must stay narrow to several orders of magnitude below the central line intensity. This is particularly difficult with FIR lasers because of the presence of a large-band pedestal of amplified stimulated emission inherent to the high gain of this type of lasers. Filtering the laser emission or blocking unwanted radiation with molecular gas filters is possible, but at the cost of increasing complexity of the pump laser (frequency tuning).

### 2.5.3. Stray laser light.

Because of the very low Thomson scattering cross section the dominant parasitic radiation will be stray laser light, even in a well-designed experiment. The level of stray light depends on the efficiency of the beam and viewing dumps, on the scattering angle, on the quality of the optical elements used (windows and mirrors) and on the size and quantity of dust particles encountered by the laser beam on its way to the tokamak. It is not possible to make any general prediction about the total level of stray light. The contribution of each element must be minimized.

The dumps used on the tokamak must be as large as possible (150 mm on TCA) and composed of highly absorbing materials. This is in conflict with the limited access to the torus, and the problems of keeping the plasma free from impurities. Metals and graphite are highly reflecting in the FIR wavelength region, whereas Pyrex glass, Macor glass ceramic and alumina are good absorbers.

Assuming that the incident laser beam has a gaussian intensity profile and the beam dump has a diameter of six beam waists (as on TCA, see chapter 4), then the fraction of the

beam missing the dump is still greater than  $7 \cdot 10^{-9}$  of the total incident power. Fortunately, only a fraction of this power will, after multiple reflections in the torus, enter the limited solid angle of the collecting optics.

The scattering cross section of microscopic particles (dust) or scratches on the optics is orders of magnitude stronger than Thomson scattering. We use a set of absorbing baffles in the torus to limit the solid angle of the incident and scattered beam. In addition, the full beam path between the FIR laser and the tokamak is covered with thick rubber foam to alleviate this problem (for details see chapter 4).

For comparison, the Thomson scattering experiment on ALCATOR C suffered from stray light six orders of magnitude higher than the expected scattered signal [8]. This was the reason for the use, at MIT, of an optical notch filter in the detection beam path.

### 2.6. Choice of the detection system.

The detection system must extract the weak scattered signal ( $\sim 10^{-18}$  W/Hz, see §2.3) from the surrounding noise at the FIR laser frequency of approximately 800 GHz. It must further allow to measure the spectral distribution of the scattered signal. Two techniques exist: video (or direct) detection of the scattered signal at the laser frequency, or heterodyne detection.

Video detection requires spectral filtering of the scattered signal at the laser frequency. This implies the use of a Michelson or a Fabry-Perrot interferometer. Several detectors are then required to detect the optical signal within each of the desired number of spectral channels. Assuming the need for 10 spectral channels of 100 MHz width, we can only expect a power level of  $10^{-10}$  W per channel (see §2.3). A standard Fabry-Perrot interferometer used as the optical filter will further reduce this signal power since each spectral channel only collects radiation from a fraction of the total

scattered volume. The NEP of the video detector must then be of at least  $10^{-14}$  W/Hz<sup>1/2</sup> with a bandpass of about 1 MHz to observe a microsecond long scattered pulse. Only the best liquid He cooled micro-bolometer and the cooled Josephson junctions have reached such a video NEP [9]. These detectors are also sensitive to a large wavelength range, and thus thermal emission from the collecting optics would be an important source of parasitic radiation.

Heterodyne detection consists of coherently mixing the scattered signal with a narrow bandwidth local oscillator signal, thus converting the spectrum of the scattered radiation to a lower and more accessible intermediate frequency (IF). The sensitivity of heterodyne detection is generally higher than that of video detection, due to the mixing process. The frequency resolution is also better, but heterodyne detection needs a stable local oscillator, emitting at a frequency close to the main laser frequency. The heterodyne mixer with a polarized local oscillator is only sensitive to one spatial radiation mode (see §5.1 and [9]) and to the wavelength range defined by the IF circuit bandwidth, hence thermal emission from the optical elements collecting the scattered signal can be ignored.

We have chosen to use a heterodyne detection system because it requires only one mixer and the spectral filtering of the scattered signal is obtained by a commercially available microwave filter bank at the IF frequency. For such an arrangement, it can be shown (see §5.1) that the post integration signal to noise ratio in each of the spectral channels is (see equation 5.9) proportional to:

$$S/N = \frac{s}{s+1} \sqrt{1+B\tau} \quad (2.23)$$

where  $s$  is the pre integration signal to noise ratio as defined by equation (2.21),  $B$  is the spectral channel bandwidth and  $\tau$  is the integration time which corresponds to the scattered signal pulse length. Equation (2.23) has implications on the requirements of the FIR laser power and pulse length. From the moment the scattered power is such that  $s=1$

(see table 2.2) there is no point continuing to increase the FIR laser power, an increase in laser pulse length  $\tau$  (integration time) would give a better improvement of the final signal to noise ratio.

With the heterodyne detection we had to choose the type of mixer to use to obtain an NEP of at least  $10^{-18}$  W/Hz (see §2.3). At the time of purchase (1979-1980) there were three types of detectors available for the 50 to 400  $\mu\text{m}$  wavelength region [2,9,10]. These were the GaAs point contact Schottky diode, the Nb-Nb superconductor Josephson junction and photoconducting detectors such as the Ga:Ge detector. Thermal detectors, (radiation absorbers attached to a thermometer) have typical response times of some milliseconds and cannot be used as a mixer for the 2 GHz wide signal required for the  $T_i$  measurement.

Photoconductive detectors [2,9,10], which depend on the change of electrical conductivity of certain doped semiconductor materials when subjected to radiation, require a minimum incident quantum energy resulting in a long-wavelength cut-off ( $\lambda < 100 - 200 \mu\text{m}$ ) for the detection process. To detect FIR wavelengths they require cryogenic operation at liquid helium temperatures. These devices have excellent NEP (close to the quantum limit) but usually a compromise has to be made between fast response time (200-800 MHz) and high sensitivity. In low signal power conditions the quantum type detectors have a high intrinsic impedance, which introduces matching problems to the available low impedance high speed amplifiers [9]. The photoconductive detector did not meet our bandwidth and responsivity requirements at the wavelength of 385  $\mu\text{m}$ .

Josephson effect diodes [2,9] are based on quantum mechanical effects occurring when two superconductors are weakly coupled together allowing a flow of superconducting electrons. The junction in such a diode can take the form of a thin insulating layer, such as oxide, or a metal point contact. The latter has been used for the most successful FIR mixers. Contrary to Schottky diodes, the Josephson diodes are active devices, hence they have low conversion losses. A heterodyne



mixer with a Josephson diode requires low local oscillator power ( $< 10 \mu\text{W}$ ), which is a great advantage when an optically pumped FIR laser is to be used as local oscillator. The Josephson effect diodes have an excellent NEP ( $< 10^{-19} \text{ W/Hz}$ ) at wavelengths of 300 to 500  $\mu\text{m}$  [9]. Impedance matching problems to the 50 ohms high speed IF amplifiers will increase the effective conversion losses. These devices have shown to be very fragile and difficult to recontact. They also need cryogenic cooling to liquid helium temperatures. Thermal recycling often results in contact failures. Mainly because of these technical problems we finally decided to use a Schottky diode mixer, although the detection properties of the Josephson junctions are somewhat better.

The point contact Schottky diode [2,9,11] consists of an electrical contact between a sharply pointed metal whisker and a semiconductor (mostly GaAs). This type of diode is the most promising for detection at 800 GHz where these devices show the highest ruggedness with an acceptable NEP and signal bandwidth. The whisker acts as an antenna for the incident radiation which is detected through the nonlinear resistance in the Schottky barrier. The Schottky diode can be operated at room temperatures, however, the NEP can be lowered by a factor of 2 by cryogenic techniques. Noise equivalent powers of  $2 \cdot 10^{-19} \text{ W/Hz}$  have been achieved for a mixer at 760 GHz but only for bandwidths of some hundreds of megahertz [9]. One weakness is the high conversion loss which lowers the NEP for large bandwidth applications. When used as a mixer the Schottky diode needs about 10 mW local oscillator power to achieve an optimum NEP.

New types of FIR detectors are currently being developed [12]. They allow quantum detection of electromagnetic fields in the far infrared. These devices are based on electron tunneling through a superconductor-insulator-superconductor (SIS) barrier. They show more than two orders of magnitude better NEP than Schottky diodes, and necessitate three orders of magnitude less local oscillator powers. SIS mixers have been operated below 300 GHz and research and development of these devices is extending to higher frequencies.

For the Thomson scattering experiment on TCA we have chosen a heterodyne detection system with a Schottky diode mixer. The IF frequency is 3.6 GHz (see chapter 5). The detectable bandwidth extends from 2.2 to 3.8 GHz. This bandwidth is not limited by the mixer itself but by the IF amplifiers and filter bank used to resolve the scattered spectrum. The measured NEP is better than  $10^{-18}$  W/Hz (for details see chapter 5).

### 2.7. Expected precision of the $T_i$ measurement.

Assuming that the scattered spectrum can be detected with a sufficient signal to noise ratio, then, as discussed in chapter 1, the ion temperature cannot be simply extracted from the scattered spectrum width. It is not possible to unequivocally define a width of the scattered spectrum since several plasma and scattering parameters strongly influences its shape. The first order approximation represented by equation 2.20 indicates, however, that the precision of  $T_i$  is strongly related to the precision of the scattering vector  $k$ . The relation between the errors of  $k$  and  $T_i$  from equation 2.20 is [3]:

$$2 \Delta|k|/|k| = \Delta T_i/T_i \quad (2.24)$$

The effect of the magnetic field on the scattered spectrum is the most sensitive parameter influencing the  $k$  vector (see §1.7.8) but it is not included in the previous approximation.

To include the effect of all plasma and scattering parameters on the precision of the  $T_i$  measurement, a numerical simulation code has been developed [13,14].

#### 2.7.1. The $k$ resolution.

The desired resolution in  $k$  space leads to a condition for the size of the scattering volume: it must contain several wavelengths of the plasma fluctuations to reduce the dispersion of the scattering vector [15]. This is because the resolution

in  $k$  space is related by the Fourier transform to the spatial resolution of the fluctuations in the scattering volume (see equation 1.16). On TCA with a  $90^\circ$  scattering angle and symmetric incoming and scattered beams the  $k$  space resolution is given by [3,15,16]:

$$\Delta k_x = \Delta k_y = \Delta k_z / \sqrt{2} = 2/w \quad (2.25)$$

where  $w$  represents a gaussian beam waist radius,  $x$  the direction along the scattered beam,  $y$  the direction along the incident beam, and  $z$  represents the axis perpendicular to the scattering plane, see figure 2.3.

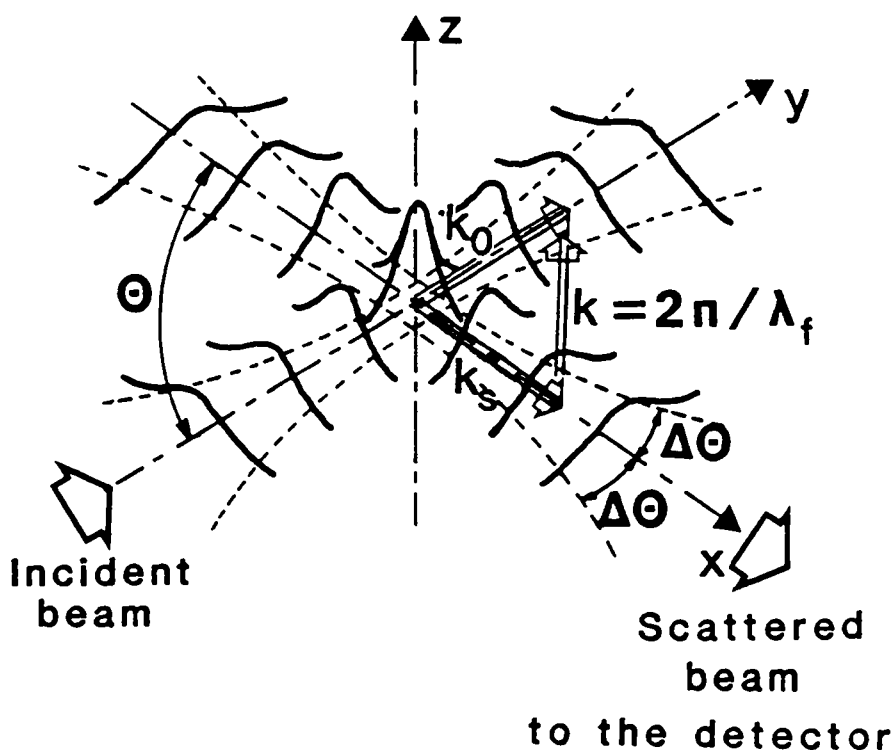


FIGURE 2.3. The scattering volume presented as the intersection of two gaussian beams.

The resolution parameter  $r$  can be introduced as:

$$r = \frac{L}{\lambda_f} = \frac{2w}{\lambda_f \sin(\theta)} = \frac{4w \sin(\theta/2)}{\lambda_0 \sin(\theta)} = \frac{2\sqrt{2} w}{\lambda_0} \quad (2.26)$$

where  $L = 2w/\sin(\theta)$  is the linear extent of the scattering volume and  $\lambda_f$  is the wavelength of the scattering vector  $k$ .

A reasonable value for  $r$  would be around ten. The influence of  $r$  on the final shape of the scattered power spectrum has been discussed by Holzhauser et al. [15]. A noticeable deleterious influence on the signal to noise ratio has been found for  $r < 4$ .

The expression  $L\Delta\Omega$  from equation 2.7 and 2.19, assuming the use of gaussian beams, can now be approximated by:

$$L \Delta\Omega = \frac{2w\pi\Delta\Theta^2}{\sin(\Theta)} = \frac{2\lambda_0^2}{\pi w \sin(\Theta)} = \frac{8\sin(\Theta/2) \lambda_0}{\pi r} = \frac{4\sqrt{2} \lambda_0}{\pi r} \quad (2.27)$$

where  $\Delta\Theta$  is the gaussian far field divergence. For small angles ( $< 15^\circ$ ) the divergence and the solid angle are related by  $\Delta\Omega \simeq \pi \Delta\Theta^2$ .

By using gaussian beams for imaging the scattered volume on the detector we are sure to satisfy the heterodyne detection antenna theorem (see §5.1).

### 2.7.2. Estimate of the $T_i$ precision by numerical fitting.

Estimate of the precision of the ion temperature measurement by a single shot Thomson scattering experiment can be obtained by numerical simulations. Several cases, for JET and TCA conditions have been studied. The main conclusions are reported here, further details are to be found in references [2,3,13,14].

The simulation program calculates a theoretical spectrum  $S(k, \omega, T_i, T_e, n_e, B, Z_{eff})$  for given plasma parameters, which is divided into a fixed number of spectral channels. To each channel is added a noise value chosen randomly from a  $\chi^2$  distribution. The level of noise is determined by the specific NEP of the detection system. The results are treated as "experimental data", and a theoretical curve, with  $T_i$  as the free parameter, is fitted to these data. The central part of the spectra (within a specific cut-off frequency) is ignored in the fitting routine, as would be done in the real experiment, in order to minimize the influence of stray light, mag-

netic field and plasma impurities. This procedure is repeated to obtain statistically relevant results (usually 31 times). For each repetition, fixed parameters like  $T_e$ ,  $n_e$  and  $B$  are allowed to vary randomly within a specified range given by  $\Delta T_i$ ,  $\Delta n_e$  etc. These ranges represent the accuracy with which the plasma parameters are known. Finally, the precision of the ion temperature measurement is described by the statistical variations of the "measured" values of  $T_i$ .

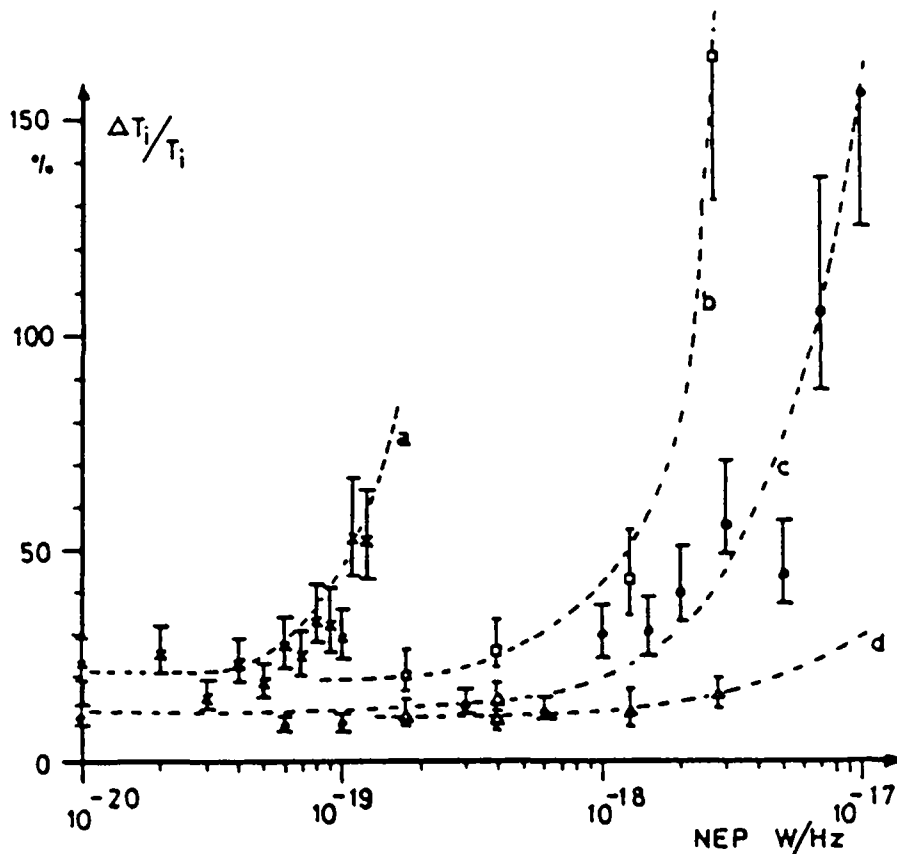


FIGURE 2.4. Relative error of the  $T_i$  measurement versus the detection system NEP for typical TCA tokamak parameters. The error bars represent the 67% interval of confidence. No beam transport losses are assumed. Courtesy S.A. Salito, [17].

For all curves: Deuterium plasma with  $T_i=400 \pm 10\%$  eV,  $T_e=800 \pm 10\%$  eV,  $Z_{eff}=2.5$ , scattering angle  $90^\circ$ , laser wavelength  $385 \mu\text{m}$ , spectral resolution: 10 spectral channels of 80 MHz, starting 440 MHz from line center.

Curve #	Incident power kW	Pulse length $\mu\text{s}$	Plasma density $\text{m}^{-3}$	Magnetic field strength T
a	27	0.8	$5 \cdot 10^{19}$	1.2
b	100	1.0	$8 \cdot 10^{19}$	1.5
c	460	0.8	$5 \cdot 10^{19}$	1.2
d	1400	1.0	$8 \cdot 10^{19}$	1.5

From curve c of figure 2.4, we can conclude that for an NEP  $< 10^{-18}$  W/Hz and an estimate of  $T_e$  and  $n_e$  within  $\pm 10\%$ , the relative error on the ion temperature  $\Delta T_i/T_i$  is  $< \pm 20\%$ .

The relative error on  $T_i$  increases rapidly if the signal to noise ratio  $s < 1$  (equation 2.21), which for curve c, figure 2.4, corresponds to a NEP  $> 2 \cdot 10^{-18}$  (see table 2.2), and a post integration signal to noise ratio  $S/N < 4$ , (equation 2.23).

The knowledge of the electron temperature and density to within  $\pm 10\%$  is important [13]. For a multiparameter fit without this knowledge, the relative error of the ion temperature is approximatively twice that of a single parameter fit [13]. The accuracies of simultaneous estimates of the other parameters ( $T_e$ ,  $n_e$ ) are also too poor to be of practical interest. This can be explained by the fact that the electron density and temperature do not only change the spectral shape but rather the absolute intensity. An absolute calibration of the system is needed to improve a multiparameter fitting [13]. Absolute calibration of a collective Thomson scattering experiment in the FIR is difficult, because of lack of a well known scattering source like Rayleigh scattering which is used successfully in the visible wavelengths with incoherent Ruby laser scattering. Rayleigh scattering in the FIR is impractical because the scattering cross section is proportional to the fourth power of the laser frequency.

The influence of the impurities is also important. In chapter 1 we showed that the impurities strongly influence the central part of the spectrum. Since it is considered unlikely that the impurity concentration and charge would be accurately known, the central part of the spectrum up to a cutoff frequency of 400 to 600 MHz for a deuterium plasma, is ignored. In this way the effect of impurities, together with the effect of stray light, magnetic field and microturbulence, which cover the same frequency region around the central laser frequency, will be reduced. The total incident laser power must, however, be increased by a factor of about two to compensate for the lower scattering efficiency in the wings of the spectrum.

The results in figure 2.4 are obtained by fitting an impurity free spectrum to the frequency range beyond the cut-off limit. A study is presently under way to include the effect of the impurities in the fitted theoretical spectrum.

The attempt to measure the effective charge through the study of the deformations of the spectrum by the impurities would necessitate an order of magnitude increase in the required laser power and a laser pulse duration of about 5  $\mu$ s [13, 14]. A second detection system might even be required to analyse simultaneously the scattered signal from another angle. This is far beyond the capabilities of the current FIR lasers used for this feasibility experiment or currently available for a  $T_i$  measurement.

In chapter 1 it was shown that the magnetic field strongly influences the spectral shape when the angle between the magnetic field vector and the scattering vector  $k$  is close to  $90^\circ$ . Since this is the case for the experiment on the TCA tokamak, the effect would be noticeable. In fact, no acceptable estimate of  $T_i$  is possible for scattering from an angle of  $90^\circ \pm 1^\circ$  between  $k$  and  $B$ . Avoiding direct scattering at  $90^\circ$  to the magnetic field vector may be necessary for a true  $T_i$  measurement.

It has been observed that the relative error of the ion temperature increases linearly with the relative error of the magnitude of the magnetic field, when the latter increases above 10% [14].

## 2.8. Conclusions.

For typical TCA conditions (see appendix A) an attempt to measure the plasma ion temperature by collective Thomson scattering requires the following parameters:

(1) The laser wavelength can be chosen in the range 265  $\mu\text{m}$  to 2.3 mm. In practice, the optically pumped  $\text{D}_2\text{O}$  laser, emitting at 385 microns, offers the best possibilities.

(2) Because of access geometry on TCA, the scattering angle is fixed to  $90 \pm 5$  degrees. This implies  $\alpha=1.5$  and gives a scattered spectral width of 2 GHz for a hydrogen plasma.

(3) The detection system chosen is a heterodyne receiver with a Schottky diode mixer.

(4) With a detector NEP of  $10^{-18}$  W/Hz and for a deuterium plasma density of  $5 \cdot 10^{19} \text{ m}^{-3}$ , 0.8 MW of FIR laser power is necessary, considering 6 dB beam transport losses, to achieve a signal to noise ratio of  $s = 1$  at the detector. Dividing the scattered spectrum into typically 10 channels of  $B=80$  MHz each, and assuming  $\tau=1 \mu\text{s}$  long laser pulses, the post integration signal to noise ratio would be about 4, scaling according to a  $0.5\sqrt{B \cdot \tau}$  law.

(5) The incident laser linewidth should not exceed one spectral channel width, which is 80 MHz in our case.

(6) A high level of stray light is to be expected. This will perturb the measurements close to the central frequency.

(7) Noise caused by plasma radiation due to ECE and Bremsstrahlung is below the expected scattering signal power and can be neglected on TCA.

(8) The expected precision of an ion temperature measurement on TCA with 0.8 MW of FIR power, 1  $\mu\text{s}$  long laser pulses and a detection NEP of  $10^{-18}$  W/Hz would be about  $\pm 20\%$ . This value has been derived from numerical simulations.

The FIR laser available for the feasibility study presented in chapter 3 delivers 150 kW in a 1  $\mu\text{s}$  long pulse. The detection NEP is about  $10^{-18}$  W/Hz, so that it will not be possible to obtain a precise measurement of the ion tempera-



ture with this system. Nevertheless, the power and detectivity of the feasibility experiment allow us to:

- show correlations with gross changes in the plasma parameters e.g. changes from hydrogen to deuterium plasmas,
- check our prediction that scattering from non-thermal fluctuations (e.g. microturbulence) does not cover the full spectral width used to determine the ion temperature,
- obtain a first measurement of the cut-off frequency required by the  $T_i$  measurement fitting routines to limit the disturbance due to stray laser light, the magnetic field and scattering from plasma impurity ions,
- gain experience in several practical problems of implementing a Thomson scattering experiment on a tokamak.

The insufficient performance of the system can be partially compensated by averaging over several tokamak shots, if plasma and laser conditions are kept constant over all shots. The final signal to noise ratio increases with the square root of the number of shots.

REFERENCES.

- [1] "Measured sub-millimeter synchrotron background in Alcator A, - Implications for D<sub>2</sub>O laser Thomson scattering", P. Woskoboinikow, H.C. Praddaude, I.S. Falconer, W.J. Mulligan, Nuclear Fusion, 21, 1028 (1981).
- "Heterodyne measurements of electron cyclotron emission from Alcator A and absolute submillimeter receiver calibration", P. Woskoboinikow, H.C. Praddaude, I.S. Falconer, W.J. Mulligan, J. Appl. Phys., 52, 7099 (1981).
- "2nd-5th electron cyclotron harmonic emission from thermal plasmas in Alcator A", P. Woskoboinikow, H.C. Praddaude, I.S. Falconer, W.J. Mulligan, Appl. Phys. Ltr., 39, 548 (1981).
- [2] "A study of the feasibility of measuring the plasma ion temperature in Jet by Thomson scattering using FIR lasers", M.R. Green, P.D. Morgan, M.R. Siegrist, R.L. Watterson, CRPP report LRP-168/80, (1980).
- [3] "Signal to noise requirements for interpreting submillimetre laser scattering experiments in a Tokamak plasma", L.E. Sharp, A.D. Sanderson, Plasm. Phys., 23, 357 (1981).
- [4] "Application of advanced millimeter-FIR sources to collective Thomson scattering plasma diagnostics.", P. Woskoboinikow, D.R. Cohn, R.J. Temkin, MIT report, PFC/JA-82-9, (1982).
- [5] "Electron cyclotron emission from magnetically confined plasmas, I - Diagnostic potential", Course on diagnostics for fusion reactor conditions, Vol. 1, Varenna, (1982).
- [6] "Plasma scattering of electromagnetic radiation", J. Sheffield, Academic Press, (1975).
- [7] "Cyclotron radiation from a rarefied inhomogeneous magnetoplasma", F. Engelmann and M. Curatolo, Nucl. Fus., 13, 497 (1973).

- [8] "High power submillimeter wave Thomson scattering diagnostic", P. Woskoboinikow, W.J. Mulligan, D.R. Cohn, R.J. Temkin, H.R. Fetterman, R. Erickson, Poster, IEEE Int. Conf. Plasma Sci., Ottawa, (1982).
- "385  $\mu\text{m}$  D<sub>2</sub>O laser collective Thomson scattering ion temperature measurement", P. Woskoboinikow, W.J. Mulligan, J. Machuzak, D.R. Cohn, R.J. Temkin, T.C.L.G. Sollner, R. Lax, Poster E21, EPS Contr. Fusion and Plasma Phys. Conf., Aachen, (1983).
- [9] "Detection techniques at short millimeter and submillimeter wavelengths: An overview", T.G. Blaney, Infrared and millimeter waves, Vol. 3 Chap. 1, Academic Press, (1980).
- [10] "Radiation detection at submillimeter wavelengths", T.G. Blaney, J. Phys. E: 11, 856 (1978).
- [11] "Detection of Optical and Infrared Radiation", R.H. Kingston, Springer Series in Optical Science, Vol. 10, (1978).
- [12] "Quantum detection at millimeter wavelengths", J.R. Tucker Reviews of Modern Phys, 57, 1055 (1985).
- [13] "Numerical simulations of a system for ion temperature measurement by Thomson scattering in a tokamak", R.L. Watterson, M.R. Siegrist, M.A. Dupertuis, P.D. Morgan, M.R. Green, J. Appl. Phys., 52, 3249 (1981).
- "Simulations of a magnetic field and ion temperature measurement in a tokamak by Thomson scattering", M.R. Siegrist, M.A. Dupertuis, R. Behn, P.D. Morgan, Plasm. Phys., 24, 1449 (1982).
- "Mesure de  $T_i$  et Zeff par diffusion Thomson dans un Tokamak", M.A. Dupertuis, CRPP-EPFL report: LRP-185-81, (1981).
- [14] "Etude théorique des lasers infrarouge lointains pulsés et de leur comportement multimode", M.A. Dupertuis, Thèse No. 558, EPFL Lausanne, (1985).
- [15] "An analysis of optical mixing in plasma scattering experiments", E. Holzhauser, J.H. Massig, Plasm. Phys., 20, 867 (1978).

- [16] "Lichtstreuung an kollektiven, thermischen Fluktuationen, der Electronendichte in Plasmen mit mehreren Ionenkomponenten", W. Kasperek, Institut für Plasmaforschung der Universität Stuttgart, IPF-84-8, (1984).
- [17] "Progress towards ion temperature measurements in the TCA Tokamak by collective Thomson scattering of FIR laser radiation", S.A. Salito, R. Behn, I. Kjelberg, P.A. Krug, M.R. Siegrist, Swiss Physical Society, Spring 1986 symposium in Neuchâtel, (1986).

## CHAPTER 3 .

### THE OPTICALLY PUMPED FIR LASER.

Coherent far infrared (FIR) radiation can be produced by transitions between adjacent rotational levels of molecules. Since the rotational levels are separated by energies less than  $kT$  (a quantum of thermal energy) only a selective excitation mechanism can populate a particular rotational energy level [1,2]. Excitation by electron collisions in an electric discharge [3] as in the case of the  $CO_2$  laser, where the infrared (IR) radiation is produced by transitions between different vibrational energy levels is no longer sufficient. Optical pumping using the emission of a  $CO_2$  laser is currently the most frequently used method to excite molecules from the vibrational ground state to a particular rotational level in a higher vibrational state [1,2].

In chapter 2 we have estimated the values of the parameters of a FIR laser for a single shot  $T_i$  measurement on the TCA tokamak. The required power is about 1 MW with a pulse duration of 1  $\mu s$  for a wavelength between 265  $\mu m$  and 2.3 mm. The system described here does not reach this power level. Using a  $CO_2$  laser available at the beginning of this study, a FIR  $D_2O$  laser has been assembled which produces typically a power of 150 kW. The development of a new, multi-megawatt, optically pumped FIR laser was simultaneously undertaken with the first observation of scattered FIR radiation on TCA. The latter system is currently being installed on TCA and will not be presented here.

The first part of the following description introduces the  $\text{CO}_2$  laser used for optically pumping the FIR laser. The second section describes and justifies the choice of the  $\text{D}_2\text{O}$  laser configuration used for the coherent Thomson scattering experiment.

### 3.1. The $\text{CO}_2$ laser as a source for optical pumping.

The  $\text{CO}_2$  laser is today one of the most common and well known IR laser. A number of publications (among others [3 to 6]) describe in detail the processes and behavior of this laser, so we will only summarize here some of the most important points.

The laser action needs a population inversion between the upper and the lower energy levels of the active medium. It is therefore important to know the natural rates of decay for the different types of transitions which will compete with the laser transition.

The spontaneous emission between two energy levels is given by the Einstein A coefficient:

$$A \propto \nu^3 \rho^2 \quad (3.1)$$

where:

$\nu$  is the transition frequency.

$\rho$  is the molecular dipole moment.

Thus the importance of spontaneous emission, as a relaxation process, is much smaller for the IR than for the visible, and is mostly negligible for the FIR wavelengths. For the  $\text{CO}_2$  molecule, the relevant Einstein A coefficients have been calculated [3,6] and are of the order of  $1 \text{ s}^{-1}$ . At typical operating pressures of a  $\text{CO}_2$  laser the dominant deexcitation process apart from the laser transition is due to collisional induced vibrational relaxations.

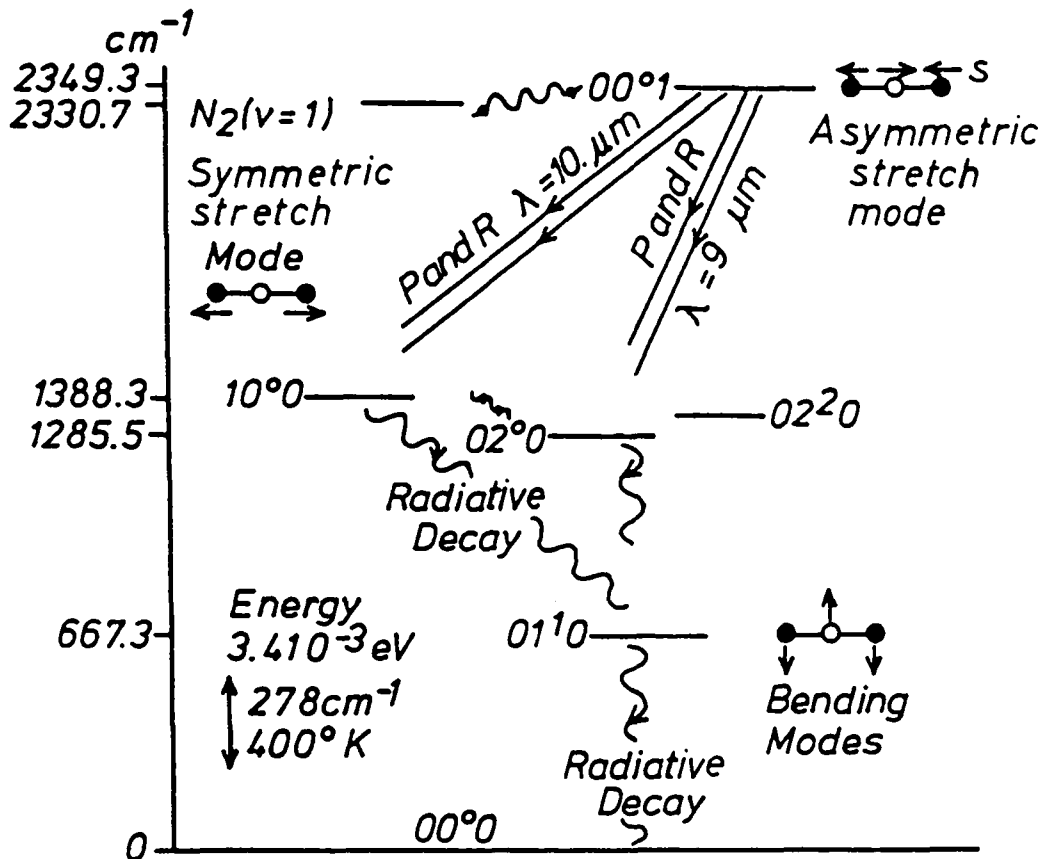


FIGURE 3.1. Partial energy level diagram for the CO<sub>2</sub> molecule. The individual energy levels are designed by the standard notation  $(\nu_1 \nu_2 \nu_3)$ , where the  $\nu$ 's represent the quantum number for the vibrational excitation levels and  $\ell$  represents the quantum number for vibrational angular momentum caused by rotation about the axis of symmetry of the CO<sub>2</sub> molecule [3,7].  
Reminder:  $\Delta T = 1 \text{ K} \leftrightarrow 8.6 \cdot 10^{-5} \text{ eV} \leftrightarrow 0.7 \text{ cm}^{-1}$ .

### 3.1.1. The excited states of the CO<sub>2</sub> molecule.

The linear CO<sub>2</sub> molecule has 5 degrees of freedom, resulting in 4 normal vibrational modes. These are generally described as the symmetric (stretch) mode  $\nu_1$ , the doubly degenerate bending mode  $\nu_2$  and the asymmetric (stretch) mode  $\nu_3$  (see figure 3.1). The laser action occurs between a rotational energy level of the first asymmetric excited state (00°1) and a rotational level of either the first symmetric mode (10°0, 10.6 μm band), or the second excited state of the bending mode (02°0, 9.6 μm band).

The quantum selection rules require that the rotational quantum number ( $J$ ) differ by  $\pm 1$  forming the two families of possible transitions designated  $P(J)$  and  $R(J)$  (see figure 3.5), where  $J$  is the quantum number of the final rotational level.

At room temperature (300 K), essentially only the fundamental state ( $00^{\circ}0$ ) is populated, since the first excited state ( $01^{\circ}0$ ) is approximately  $3kT$  above the fundamental energy level.

### 3.1.2. The excitation process of the CO<sub>2</sub> laser.

To achieve the population inversion necessary for laser action to take place, the CO<sub>2</sub> molecule must be excited efficiently to the ( $00^{\circ}1$ ) level (see figure 3.1). This is achieved by molecular collisions with typical 0.5 to 1 eV electrons [3].

Excitation of the ( $00^{\circ}1$ ) level has the largest collisional cross section. It has been noted, however, that the efficiency of the CO<sub>2</sub> laser greatly increased when N<sub>2</sub> is added to the active medium. This is due to the fact that the N<sub>2</sub> molecule has an even larger electron collisional cross section (between 2 and 3 eV electron energy), and near-resonant energy transfer takes place from a level of the excited N<sub>2</sub> molecule to the ( $00^{\circ}1$ ) level of the CO<sub>2</sub> molecules. The two relevant energy levels differ by only  $18.6 \text{ cm}^{-1}$  [3].

Since the symmetric N<sub>2</sub> molecule does not have any dipole moment, it can only be deexcited by collisions. Therefore the excitation energy can be temporarily stored in the N<sub>2</sub> molecule. By adapting the relative pressures of CO<sub>2</sub> to N<sub>2</sub> the laser pulse length can be varied. For long pulse operation of the CO<sub>2</sub> laser we use a gas mixtures with a high content of N<sub>2</sub>. The values measured for this N<sub>2</sub>-CO<sub>2</sub> energy transfer rate is  $14.4 \mu\text{s}^{-1} \cdot \text{atm}^{-1}$  at 300 K [6].



Compared to vibrational energy exchange, the relaxation rates between the different rotational levels of a given vibrational state are higher by orders of magnitude,  $\sim 10 \text{ ns}^{-1} \cdot \text{atm}^{-1}$ . This allows us to assume that thermal equilibrium is established within each vibrational state.

The laser process will quickly stop if the population of the final state builds up such that there is no longer a population inversion (bottleneck effect). For the  $\text{CO}_2$  molecule, the  $(10^0)$  and  $(02^0)$  states are in near resonance (Fermi resonance) and radiative decay brings the  $\text{CO}_2$  molecule down from the  $02^0$  level to the ground state  $(00^0)$ . This decay is increased by adding He gas to enhance the collisional deexcitation. These energy transfer rates have been measured [6] to be of the order of  $10^7 \text{ s}^{-1} \cdot \text{atm}^{-1}$ .

### 3.1.3. The $\text{CO}_2$ laser gain width.

At low gas pressures (typically below 5 Torr) the  $\text{CO}_2$  laser gain width is mainly due to the inhomogeneous Doppler broadening which leads to a gaussian profile [3]:

$$\Delta\nu = 7.15 \cdot 10^{-7} \nu \sqrt{T/M} \quad (3.2)$$

where:

- $\Delta\nu$  is the FWHM of the gain profile in Hz.
- $\nu$  is the line emission frequency in Hz.
- T is the temperature of the gas molecules in K.
- M is the gas molecular weight in amu.

At higher pressures, the gain width is dominated by the homogeneous pressure broadening (or collisional broadening) due to the fast rotational exchange rate for the asymmetric excited level (which presents a Lorentzian gain distribution). The full line-width at half maximum (FWHM) for the  $00^0 1$  to  $10^0$  transition can be estimated by the following formula [5,8]:

$$\Delta\nu = 5.76 \cdot 10^9 (F_{\text{CO}_2} + 0.73 F_{\text{N}_2} + 0.64 F_{\text{He}}) P \sqrt{300/T} \quad (3.3)$$

where

$\Delta\nu$  is the FWHM of the gain profile in Hz.

$F_{\text{CO}_2}$ ,  $F_{\text{N}_2}$ ,

$F_{\text{He}}$  are the mole fractions of the three gas species.

$P$  is the total gas pressure in atm.

Typically, for a TEA (Transverse Excited Atmospheric pressure) laser with a gas mix of 50% He, 25%  $\text{CO}_2$  and 25%  $\text{N}_2$  at 300 K, the pressure broadened gain width is approximately 4 GHz. Pressure broadening is the dominant effect under these conditions. The contribution of Doppler broadening is only 60 MHz.

#### 3.1.4. A single mode, narrow emission line.

For the generation of narrow band FIR laser emission by optical pumping, a  $\text{CO}_2$  laser operated on a single longitudinal mode is required. The 4 GHz gain width of the TEA  $\text{CO}_2$  laser implies that the laser, when operated as an oscillator, will generate multimode emission if no special measures of mode selection are taken. For a 1.5 m long cavity the longitudinal mode spacing would be  $\Delta\nu_1 = c/(2L) = 100$  MHz, where  $c$  is the speed of light and  $L$  the cavity length. A single longitudinal mode can only be achieved by adding extra frequency selective elements to the oscillator cavity [9-14]. Among common techniques are: the intracavity etalon, to add extra loss to the longitudinal cavity modes falling outside the etalon transmission curve; the intracavity saturable absorber cell, which forces the laser to oscillate on the saturated absorption line of a given gas; and the hybrid gain medium.

We have chosen to use a hybrid gain medium [12,13], comprising a low pressure section (5 to 15 Torr, hence low power) with a 60 to 120 MHz gain width. Within the same oscillator cavity is a TEA  $\text{CO}_2$  laser to provide high gain. Mode competition in the oscillator cavity will favor the few modes falling within the low pressure gain width (see figure 3.2).

This approach fixes the emission frequency to the CO<sub>2</sub> line center. The mechanical stability of the hybrid oscillator is less critical than in alternative schemes.

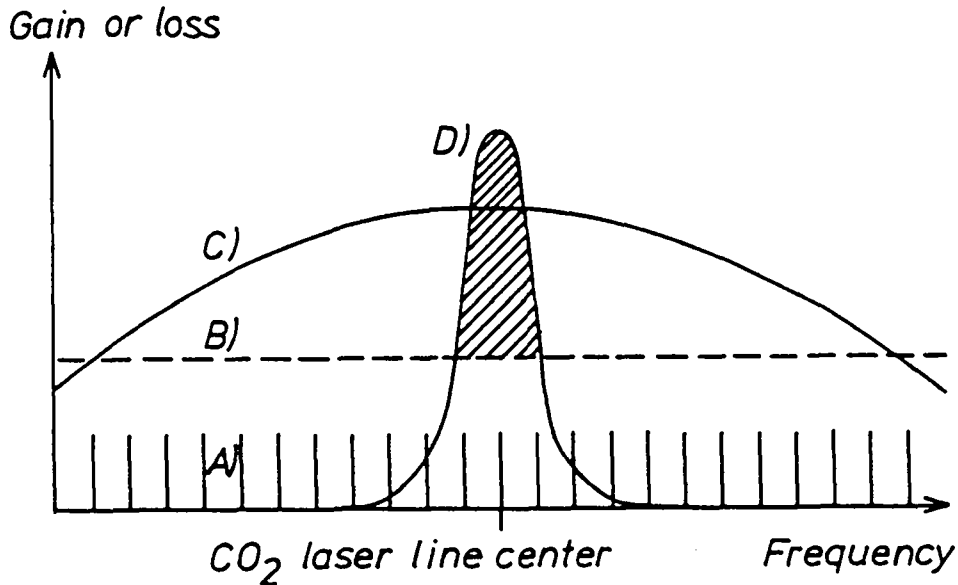


FIGURE 3.2. The hybrid CO<sub>2</sub> laser gain width. A) the longitudinal cavity modes, B) the cavity losses, C) the CO<sub>2</sub> gain curve and D) the low pressure section gain curve.

### 3.1.5. Pulsed, single-pass, amplifier gain calculations.

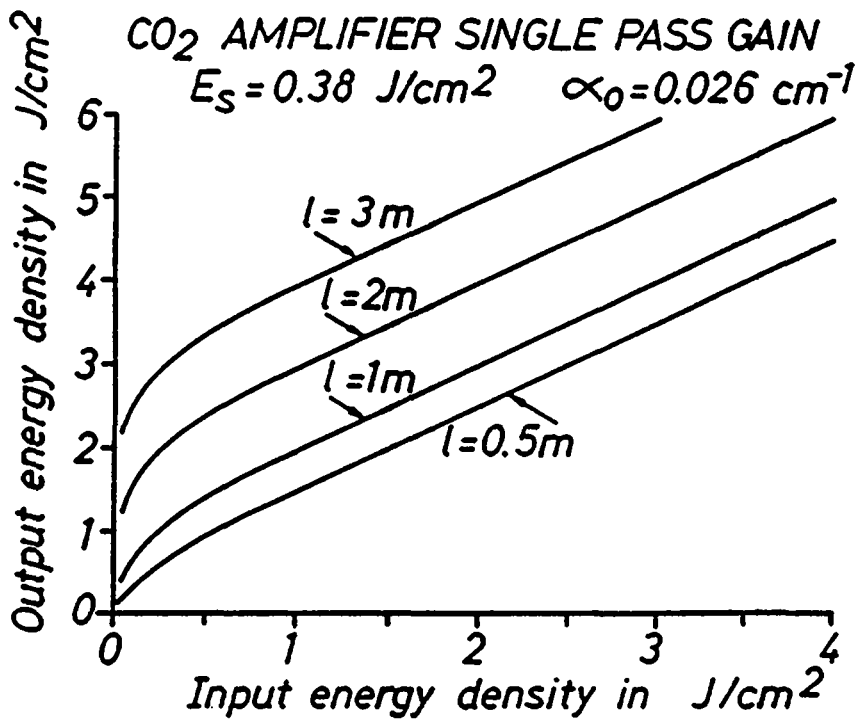
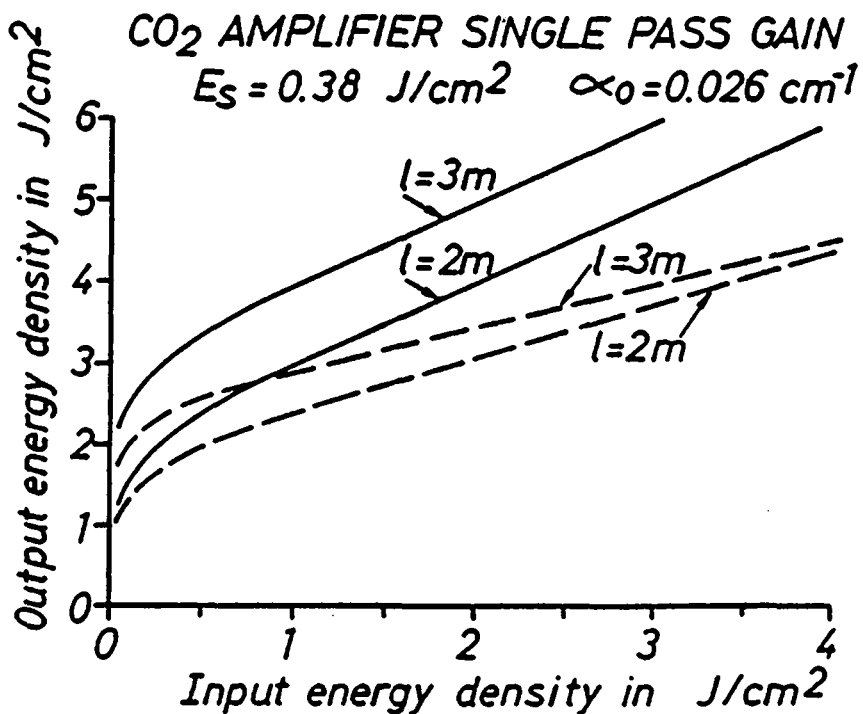
The weak single mode laser emission from the oscillator has to be amplified to reach the power levels required for optical pumping of a D<sub>2</sub>O laser. A simple approach to calculate the gain factor for a pulsed single pass amplifier makes use of the Frantz-Nodvik equation [5,15]. This equation describes laser amplification for a simple two level system with a square pulse of finite duration. The energy density  $dE(z)$  at any position  $z$ , along the path of the beam through the gain medium can be expressed as:

$$dE(z) = dE_s \ln(1 + \exp(\alpha_0 z) (\exp(dE_i/dE_s) - 1)) \quad (3.4)$$

or, with some algebra:

$$(3.5)$$

$$dE(z) = dE_i + \alpha_0 z dE_s + dE_s \ln(1 - \exp(-dE_i/dE_s) (1 - \exp(-\alpha_0 z)))$$

FIGURE 3.3. Single pass gain of a CO<sub>2</sub> amplifier.FIGURE 3.4. Single pass gain of several short CO<sub>2</sub> amplifiers. The broken lines represents the case when a 20% absorption cell is inserted between each module of 1 m gain length.

where

- $dE_i$  is the input energy density  $J/cm^2$ ,
- $dE_s$  is the saturation energy density  $J/cm^2$ ,
- $\alpha_0$  is the small signal gain  $cm^{-1}$ .

Typical values are [15]:

- $dE_s = 0.25 J/cm^2$  for the 10P(20) line,
- $dE_s = 0.38 J/cm^2$  for the 9R(22) line,
- $\alpha_0 = 0.04 cm^{-1}$  for the 10P(20) line.

For  $dE_i > 2.5 dE_s$  the above equation reduces to [5]:

$$dE(z) = dE_i + \alpha_0 z dE_s \quad (3.6)$$

In a first approximation we can consider that the total extractable energy  $E_{tot}$  in the gain medium is independent of the  $CO_2$  line, so that:

$$E_{tot} = (dE(L) - dE_i) A = \alpha_0 L dE_s A \quad (3.7)$$

where

- L is the total gain length.
- A is the beam area.

This enables us to estimate the small signal gain for the 9R(22) laser line to be about  $0.026 cm^{-1}$  from the data of the 10P(20) line (we have not measured the small signal gain for the 9R(22) line in our modules).

Applying the formula 3.4 to 3.7 we can calculate the total output energy density as a function of the input energy density. This is illustrated in figures 3.3 and 3.4 which show the output energy density after a single pass through an amplifier of 0.5, 1, 2 and 3 m total gain length.

### 3.1.6. Limitations of gain length for $CO_2$ laser amplifiers.

It has been observed [16 to 18] that  $CO_2$  laser amplifier systems with  $\alpha_0 L > N$  (with  $N = 10$  to  $15$ ) have the tendency

to produce amplified spontaneous emission or start self oscillation on the higher gain lines. For example, for a 3 m long gain section, the 10P(20) line has  $\alpha_0 L = 12$ , while for the 9R(22) line the value of  $\alpha_0 L$  is 8. This can be overcome by use of selective absorbers to reduce the gain only on the 10P and 10R lines. Figure 3.5 shows some transmission spectra for different gases for wavelengths from 9 to 11  $\mu\text{m}$  (see also fig. 2 of ref. [19], appendix C). For these reasons we have considered to divide the total gain length into several sections separated by frequency selective absorption cells (see §3.2.3).

Figure 3.4 compares the gain of a 2 and 3 m section with a laser system composed of 2 or 3 sections of 1 m gain length each, but with an element of 20% loss (e.g. a gas cell) in front of each section. For input energy densities above  $1 \text{ J/cm}^2$  the single 2 m gain section has a higher output energy than a system of three times 1 m sections with gas isolation cells.

### 3.2. Description of the CO<sub>2</sub> laser system.

In the mid seventies, a TEA CO<sub>2</sub> laser module was developed at the CRPP (see figures 3.6 and table 3.1) [20]. The amplifying volume of this module has a length of 1 m and a cross section of 20 cm<sup>2</sup>. Two Chang profile electrodes with UV preionisation from fifty capacitively coupled side arcs ensure a uniform glow discharge in the gas mixture kept at atmospheric pressure [21].

The discharge circuit consists of a two stage Marx-bank with two 0.22  $\mu\text{F}$ , 60 kV capacitors (see figure 3.6). The charging voltage can be varied between 40 and 60 kV (350 to 790 J stored electric energy), and is typically set to 50 kV.

The maximum repetition rate is one shot per minute for reproducible operation. Since we use six of these modules in our laser chain, reproducible operation of each module is important.

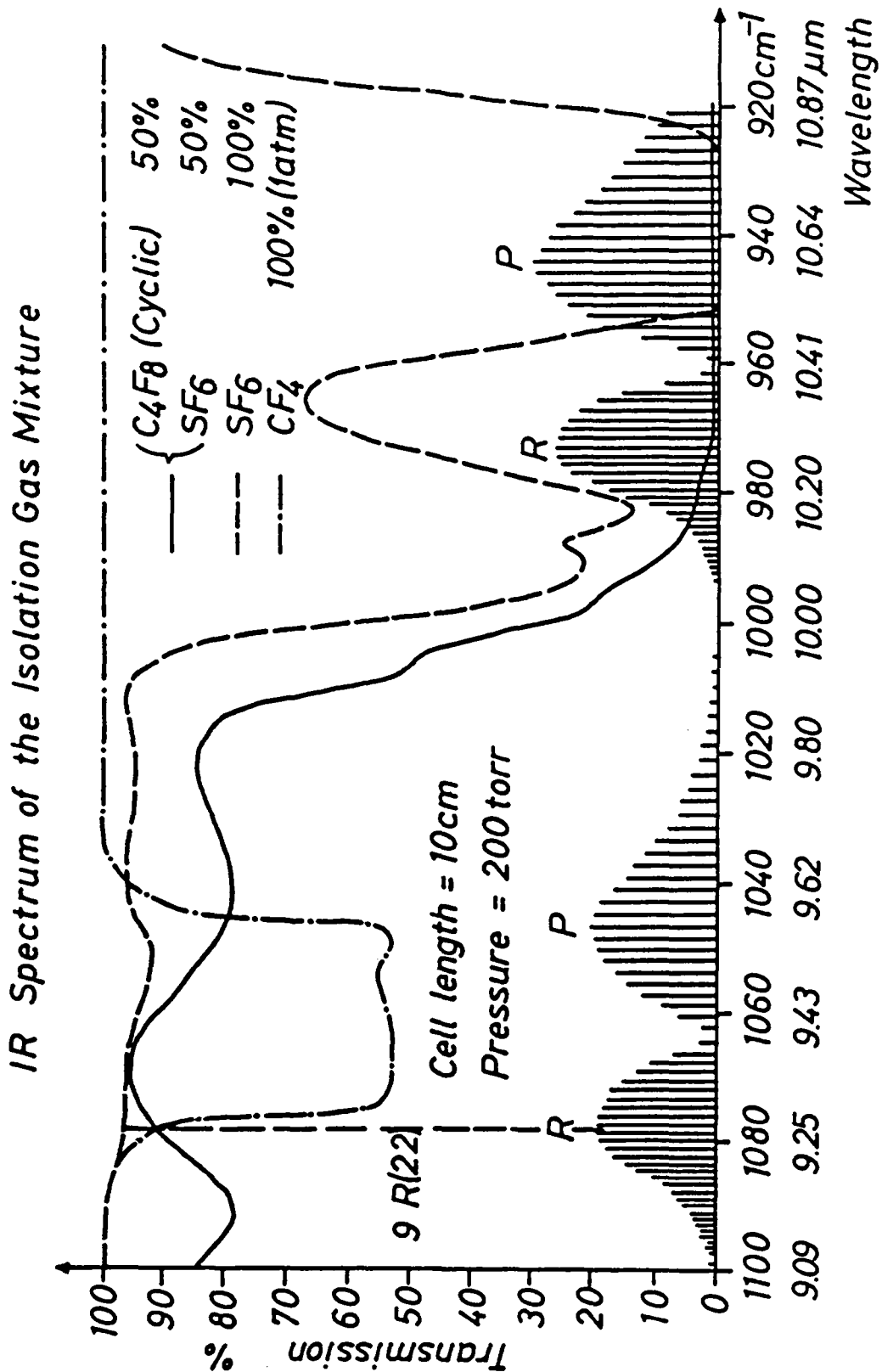


FIGURE 3.5. IR spectra of isolation gas mixtures. The bottom "comb" lines represent the most common CO<sub>2</sub> laser lines with their relative gains. See also figure 2 of reference [22] in Appendix C.

**THE TEA CO<sub>2</sub> LASER MODULE**

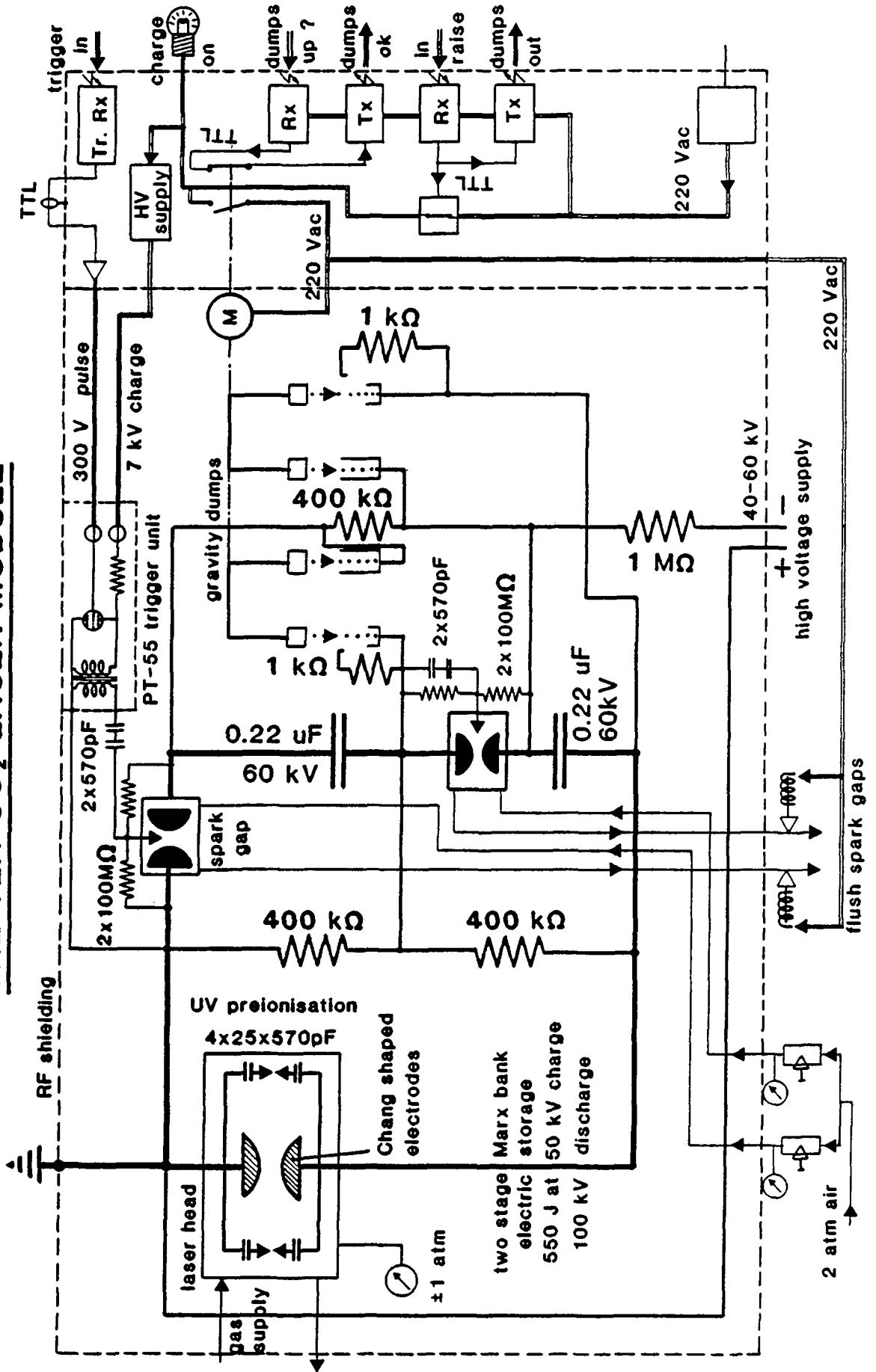


FIGURE 3.6. The CO<sub>2</sub> TEA laser module [20].



Laser head characteristics.

Electrode type	.....	Chang profile
Electrode dimension	.....	1145 × 145 × 28 mm <sup>3</sup>
Electrode gap	.....	50 mm
Gas chamber volume	.....	260 liters
Beam area	.....	20 cm <sup>2</sup>
Useful discharge volume	.....	2 liters
Peak current density	.....	37 A/cm <sup>2</sup>
Average electric field at peak current	.....	√ 11 kV/cm
Ionisation method	.....	Self-synchronizing side arcs
Input energy density	.....	300 J/liter
Output energy / Discharge volume	.....	25 J/liter
Pulse repetition rate	.....	1 shot / minute

Electrical characteristics.

Stored energy (at 60 kV)	.....	792	J
Total capacitance	.....	0.44	μF
Maximum charging voltage	.....	60	kV
Typical operating voltage	.....	50-55	kV
Total peak current at 55 kV	.....	18.6	kA
Total circuit inductance	.....	630	nH
Current rise time	.....	280	ns
Current pulse duration	.....	600	ns

TABLE 3.1. Characteristics of the TEA CO<sub>2</sub> laser module [20].

To avoid electric interference between the different modules, all commands and trigger signals are passed to the modules by optical fibers.

These TEA lasers have shown reliable operation over a range of gas mixtures. For operation under standard conditions a gas mixture with 50% He, 25% N<sub>2</sub> and 25% CO<sub>2</sub> with flow rates of 1 to 3 liters per minute was used. The capacity of the full gas chamber surrounding the electrodes is 260 liters.

When operated regularly (each day) no additive (tri-n-propylamine) is necessary to achieve a uniform glow discharge [20,23]. The additive improves the UV preionisation of the active gas [24]. Care has to be taken to avoid oxygen from the surrounding air to enter the discharge area which leads to severe arcing.

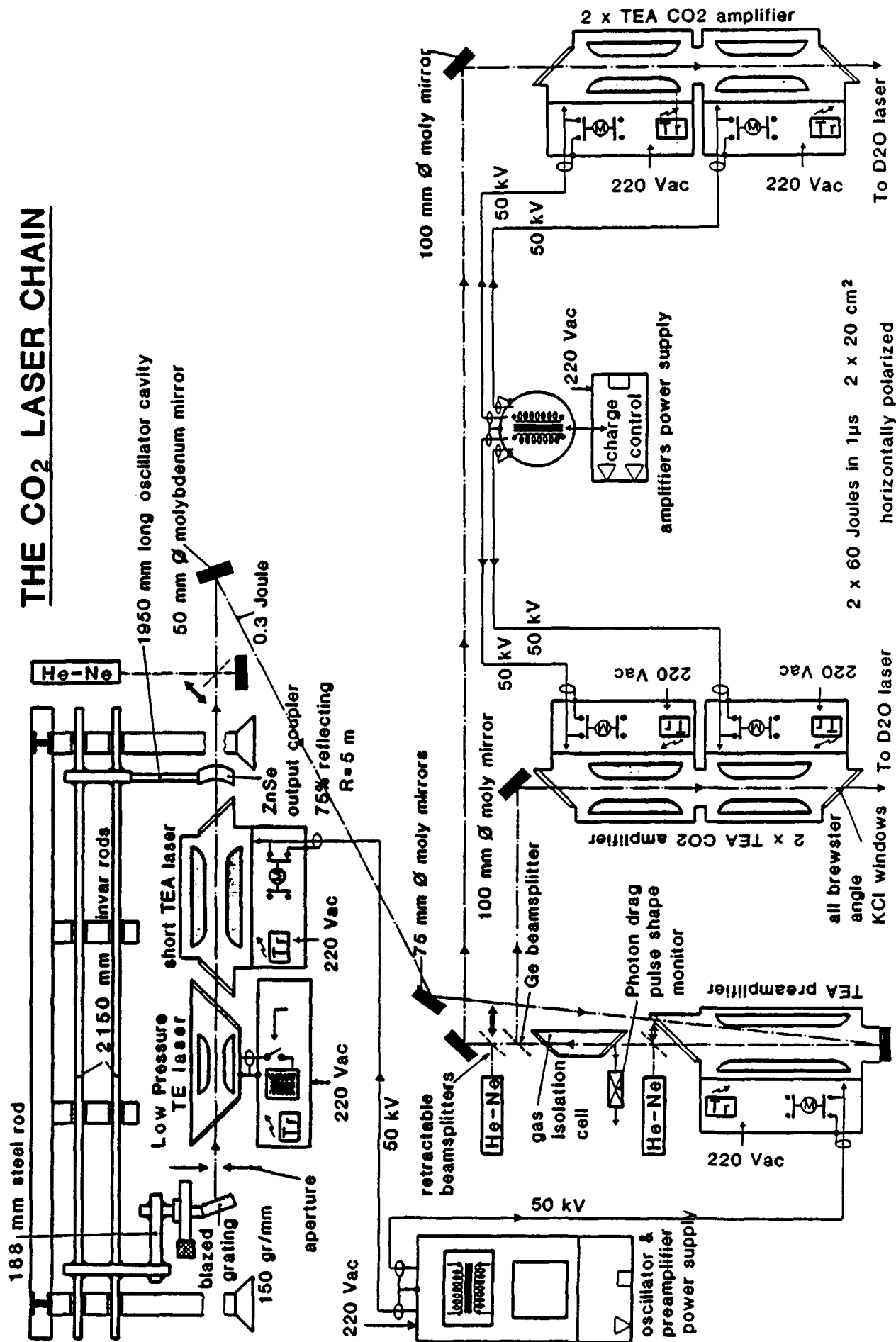


FIGURE 3.7. The CO<sub>2</sub> laser chain, including the hybrid oscillator, the double pass preamplifier and the two double stage amplifier arms.

When operated as an oscillator, with a resonator formed by a flat mirror and a flat KCl output coupler, each of these modules is capable of producing a multimode laser pulse of typically 50 J (35 ns spike followed by a 1 us tail) [20].

One module has been specially built to be used in the short oscillator cavity. The length of the electrodes is only 500 mm and the two stage Marx-bank uses two 0.11  $\mu$ F capacitors.

### 3.2.1. The performance of the CO<sub>2</sub> hybrid oscillator.

The CO<sub>2</sub> oscillator cavity (see figure 3.7. [22]) is formed by a grating, with 150 grooves per mm and blazed at 8  $\mu$ m opposed to a 45% reflecting ZnSe output coupler with a 5 m radius of curvature.

The 1.96 m long cavity has longitudinal mode spacing of  $\Delta\nu_l = 76.5$  MHz and transverse mode spacing of  $\Delta\nu_a = 16.5$  MHz. This is obtained from:

$$\Delta\nu_a = \Delta\nu_l \cos^{-1}(\sqrt{g_1 g_2}) / \pi \quad (3.8)$$

$$g_i = 1 - L/R_i$$

where

- $\Delta\nu_l$  is the longitudinal mode spacing,
- $\Delta\nu_a$  is the transverse mode spacing,
- L is the total cavity length,
- $R_i$  is the radius of curvature, of the optical element i forming the cavity.

The radial waist ( $e^{-2}$  of the power profile) is about 2.7 mm at the grating and 3.5 mm at the output coupler [14].

The thermal stability of the cavity length is obtained using a supporting structure where four 2.15 meters long invar rods are opposed to two steel rods, 0.188 meter long. The relative length of the two types of rods are arranged so that their linear thermal expansion cancels.

**THE CO<sub>2</sub> LASER CHAIN**

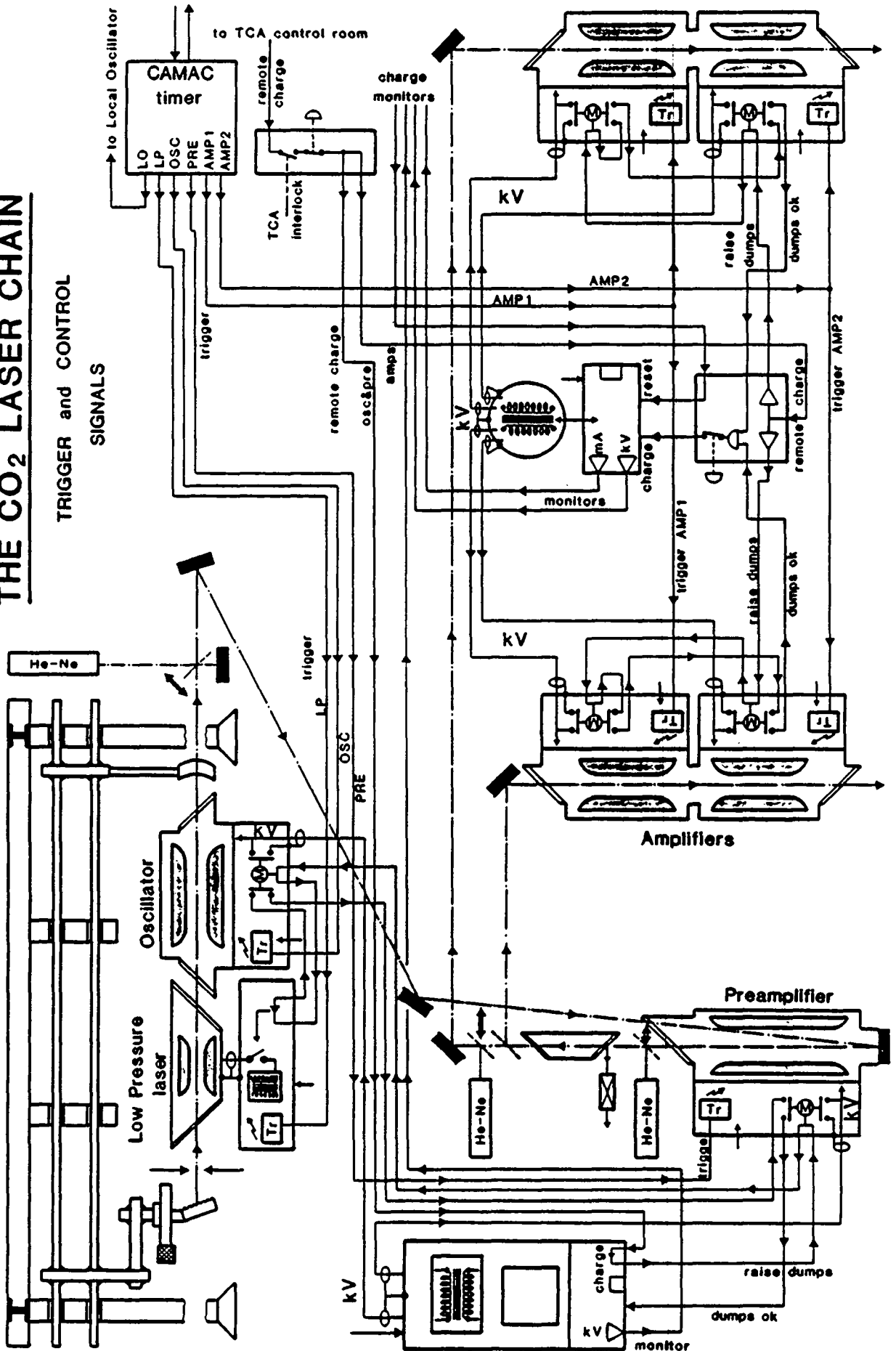


FIGURE 3.8. The CO<sub>2</sub> laser chain, including the electric and trigger connections.

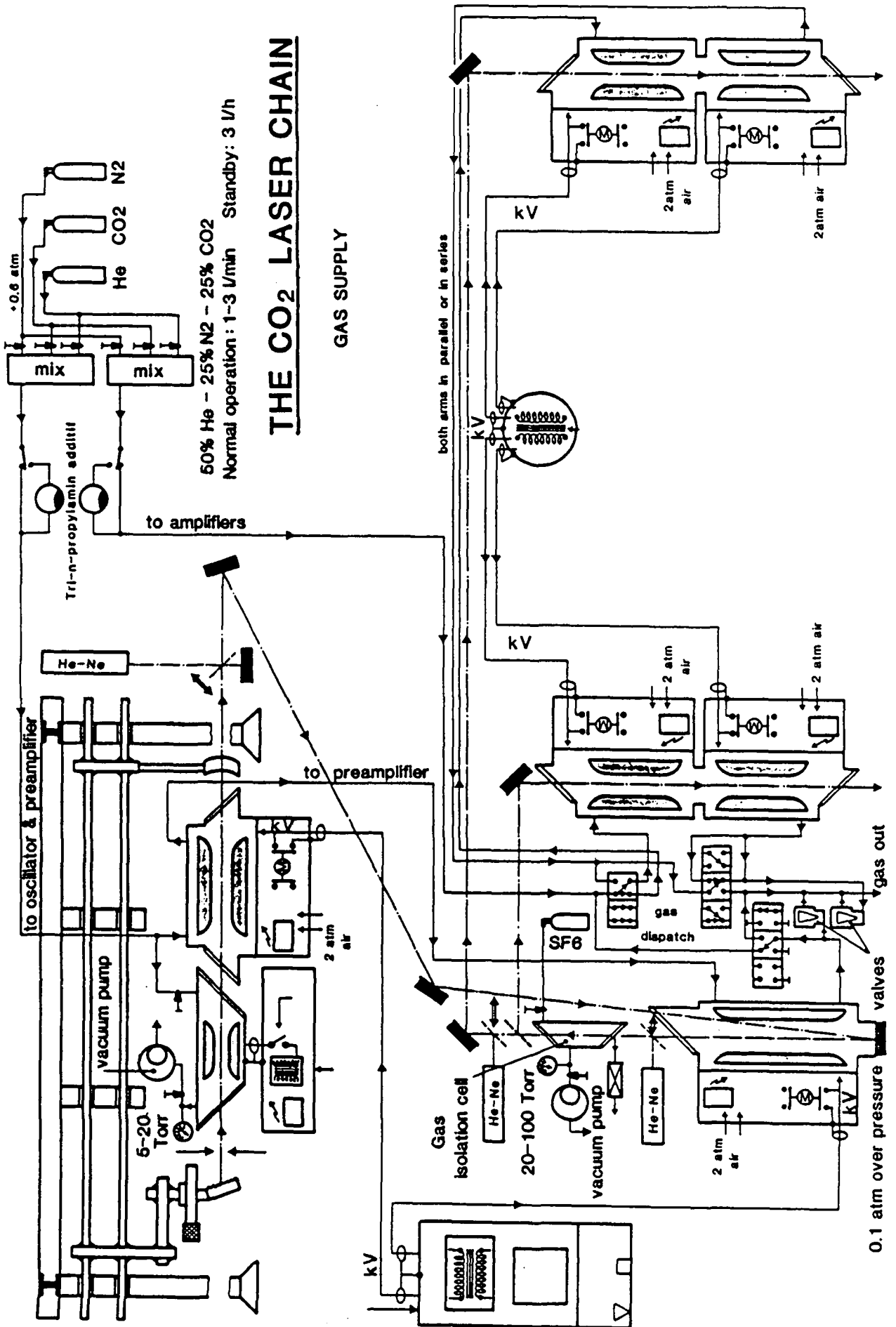


FIGURE 3.9. The CO<sub>2</sub> laser chain, including the gas supply lines.

The grating is mounted on a translation stage with  $2 \mu\text{m}$  resolution for fine tuning of the resonator length. Length tuning has been found to be necessary to ensure single mode operation of the hybrid oscillator.

To avoid stability problems due to the pulsed stray magnetic fields of the tokamak, non magnetic materials such as stainless steel and glass fiber composites have been used as often as possible in the different laser structures.

The hybrid oscillator is composed of a short TEA laser module (1 liter active volume for a  $20 \text{ cm}^2$  full area) and a low pressure transversely excited (TE) laser from Pulsed Systems California. It operates at typically 15 Torr gas pressure and has a  $200 \times 20 \times 20 \text{ mm}^3$  gain volume. A 6 mm diaphragm, situated in front of the grating limits the beam to a single tranverse mode.

With four Brewster angle windows situated inside the oscillator cavity (two KCl windows on the TEA section, two ZnSe windows on the low pressure section) the laser beam is linearly polarized with the electric vector in the vertical plane.

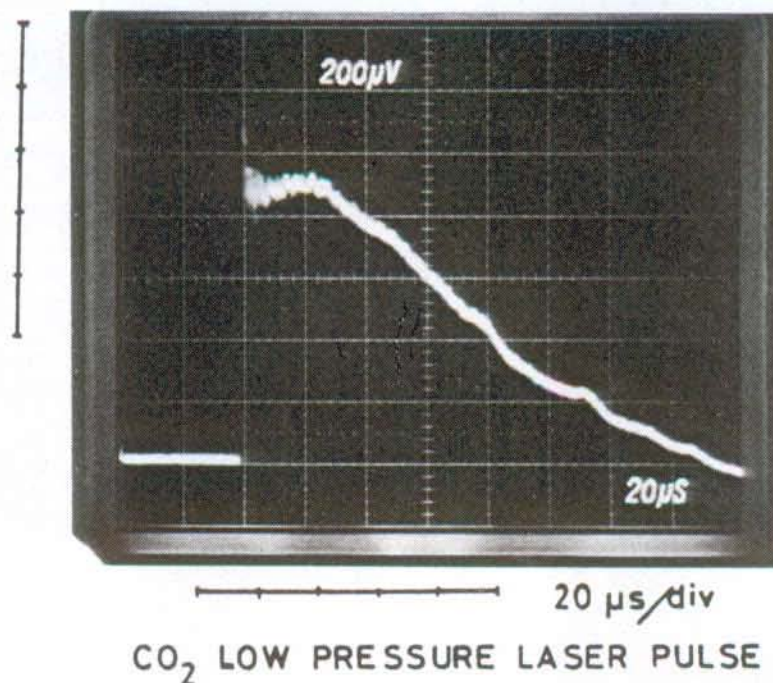


FIGURE 3.10. The low pressure TE laser pulse shape.

When only the low pressure module is fired it produces approximately 2 mJ of energy on the 9R(22) line, in a 80  $\mu$ s pulse (see figure 3.10).

The pulse energy of the low pressure section in addition to the cavity tuning is sufficient to force single mode operation of the oscillator. The presence of gain in the cavity before the build up of the gain in the TEA section reduces the gain switched spike of the oscillator pulse shape.

The oscillator (the low pressure section and the TEA section) delivers pulses of typically 0.3 J. The beam diameter is about 6 mm see figure 3.11 which corresponds to an energy density of 1 J/cm<sup>2</sup>. The laser radiation is linearly polarized with a single transverse and axial mode at the 9R(22) wavelength of 9.26  $\mu$ m. Since only a small fraction of the active volume is used in this oscillator configuration, the beam energy is clearly below the maximum extractable energy of the laser module.

### 3.2.2. The double pass CO<sub>2</sub> preamplifier.

After a 4 m path in air, and two reflections off molybdenum steering mirrors, the beam enters the preamplifier with roughly the same energy but a diameter of 13 mm, or an energy density of 0.2 J/cm<sup>2</sup>.

The average energy density of the oscillator output is well below the saturation value of a TEA laser amplifier (see figure 3.3). Therefore a double pass preamplifier is used in order to extract the stored energy more efficiently. For this purpose one of our standard TEA laser modules has been equipped with a mirror on one end. In a first approximation this is equivalent to passing through a gain medium of twice the single module length ( $L = 2$  m in figure 3.3).

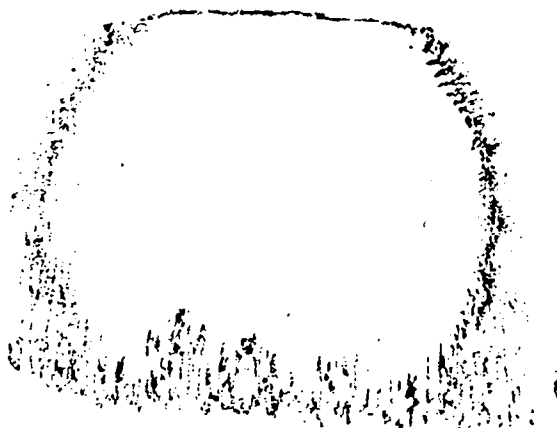
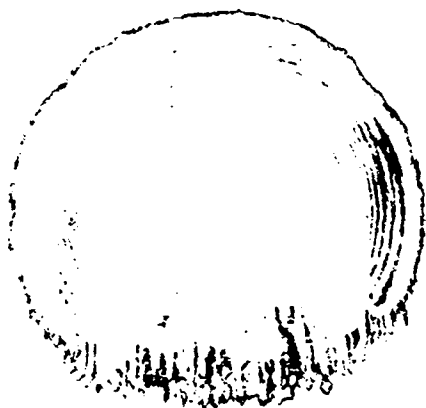
Earlier experiments with a triple pass [17] have shown that it is almost impossible to avoid feedback from the mirror supports and parasitic amplification from a 3 m gain length.



Two burn marks from the hybride oscillator  
( $\sim 0.3$  J).



Burn mark from the preamplifier ( $\sim 12$  J).



Burn marks from the amplifiers, at the laser output (left) and just in front of the  $D_2O$  laser (right), ( $\sim 50$  J).

FIGURE 3.11. Burn marks on heat sensitive paper from the oscillator, the preamplifier and one of the amplifier chains. The scale is 1:1 .



The losses from the extra gas-isolation cells needed in that case cancel the gain obtained by the third passage (see figure 3.4).

A single KCl window (120 mm in diameter) at the Brewster angle transmits the incoming and outgoing CO<sub>2</sub> beams, which are separated in the horizontal plane by an angle of about 2°. The beam is folded back by a flat molybdenum mirror situated at the far end of the laser module (see figure 3.7).

After the preamplifier, typically 12 J of CO<sub>2</sub> power is obtained in a linearly polarized, of 40 mm diameter beam (see figure 3.11, 9R(22) line, 0.95 J/cm<sup>2</sup>).

### 3.2.3. The gas isolation cell.

At the output of the preamplifier module, a 250 mm long and 55 mm in diameter gas isolation cell filled with 10 to 40 Torr of SF<sub>6</sub> or CF<sub>4</sub> (see figures 3.4 and 3.5) [17,18] prevents build up of parasitic oscillations from the 10P and 10R bands, and introduces losses for unwanted parts of the 9P and 9R bands. The reflection off one of the two tilted KCl windows of the gas cell is used to monitor the preamplifier pulse shape with a Rofin Photon Drag detector.

### 3.2.4. The two CO<sub>2</sub> amplifier chains.

Just after the gas cell, the beam is divided by a 50%-50% Ge beamsplitter and sent to the two CO<sub>2</sub> amplifier chains (see figure 3.7). Each amplifier chain consists of two of our standard TEA laser modules installed in series without windows in between. Both the input and output KCl windows are at the Brewster angle to reduce losses and to conserve the linear polarisation of the beams. In this configuration the CO<sub>2</sub> laser system produces two beams of 20 cm<sup>2</sup> cross section (see figure 3.11) with a pulse energy of typically 60 J (maximum 80 J) each and a pulse length of 1 μs. The beams are linearly

polarized to better than 95% with the electric field in the vertical plane. The spectral purity corresponds to a single longitudinal mode at the wavelength of  $9.26 \mu\text{m}$ .

We use two Gen-Tec ED-500 pyroelectric detectors for energy recordings and a Photon Drag (Rofin,  $20 \text{ mm}^2$  sensitive area) to resolve the pulse shape of the output beam of one amplifier chain. The Gen-Tec detectors are calibrated against a Scientec series 116 energy meter ( $\leq 4 \text{ J/cm}^2$ ,  $314 \text{ cm}^2$  area).

### 3.2.5. The CO<sub>2</sub> laser power supplies.

The oscillator and the preamplifier modules are charged by the same electric high power supply (adjustable from 40 to 60 kV with a current of 10 mA [20]) whereas a separate power unit (40 to 60 kV with a current of 5.5 mA) is used for the amplifier modules. For safety purpose, all laser modules have a gravity dump circuit to short out the capacitors (see figure 3.6). The dumps are raised just before charging by a control signal sent by the power supply to each laser module (see figure 3.8).

Both power supplies are remotely controlled from the TCA control room. All control signals transmitted between the control room and the power supplies, as well as between the power supplies and the laser modules, are carried by fiber-optical links, using frequency encoded signals, thus ensuring electric isolation between the different units.

### 3.2.6. Timing and triggering of the laser modules.

Each CO<sub>2</sub> laser module is triggered independently (see figure 3.8). The 50 kV pulse needed to switch one of the low-inductance three-electrode spark gaps [20] in the laser modules is provided by a krytron (high voltage discharge

tube) followed by a pulse transformer (model PT-55 from PATCO Inc. California US). The krytron is controlled by a pulse amplifier accepting ordinary TTL pulses (see figure 3.6).

The overall delay between the TTL trigger pulse and the occurrence of the gain switched CO<sub>2</sub> laser pulse is about 1  $\mu$ s. The overall jitter, when the krytrons are new, is less than 200 ns, but it can increase to 1  $\mu$ s when a tube at the end of its lifetime can no longer trigger properly the spark gaps (for the electric circuit diagram see figure 3.6). The main drawback with this trigger system is the limited lifetime (2000-5000 shots) of the EG&G KN-6B krytrons.

The triggering of each laser module is controlled by a programmable 20 MHz counter mounted in the CAMAC crate associated with the detection system (see § 5.8). The signals to the different modules are relayed by about 50 meters of 200  $\mu$ m core glass fiber (type Pifax S-120) to ensure electrical isolation between each laser module and from the detection electronics. The TTL pulses generated by the timer unit are sent to the circuit given in figure 3.12. The laser diodes used here emit in the near IR, at a wavelength of 904 nm. A PIN diode detects the light pulses and a voltage comparator transforms them back to TTL signals again (see figure 3.13).

The overall jitter in these fiber-optical links is typically less than 10 ns while the constant delay introduced by both the transmitter and receiver is 40 ns plus 5 ns per meter of optical fiber.

A typical timing sequence (see figure 5.25) is performed by first triggering the low pressure section of the oscillator. About 80  $\mu$ s later the oscillator TEA section is triggered, followed by the preamplifier and the four amplifier modules within about 1  $\mu$ s. Two separate trigger pulses are sent to the amplifier modules so that the two first and the two last modules of each arm are triggered together.

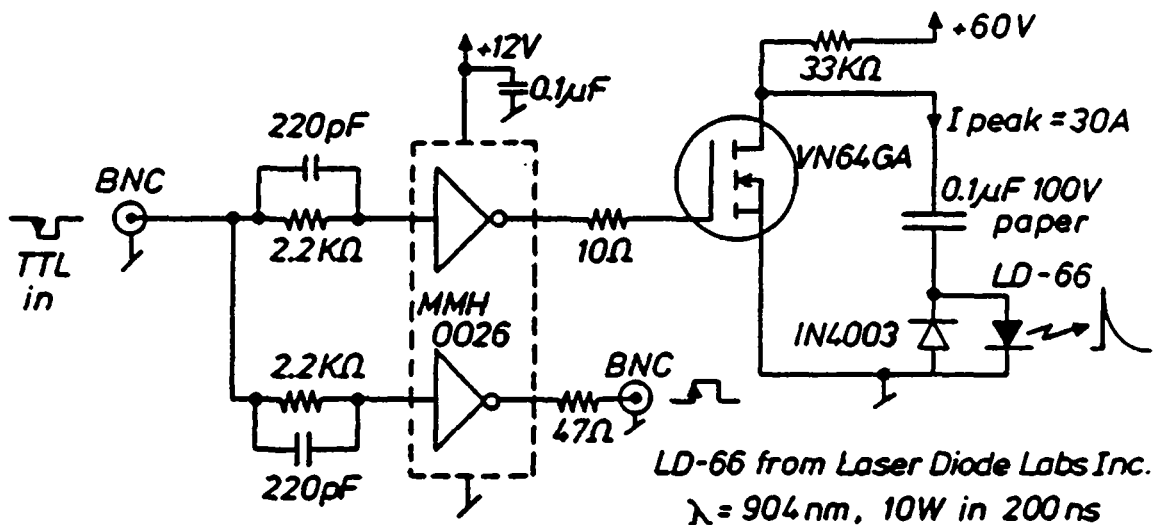


FIGURE 3.12. The optical fiber trigger transmitter.

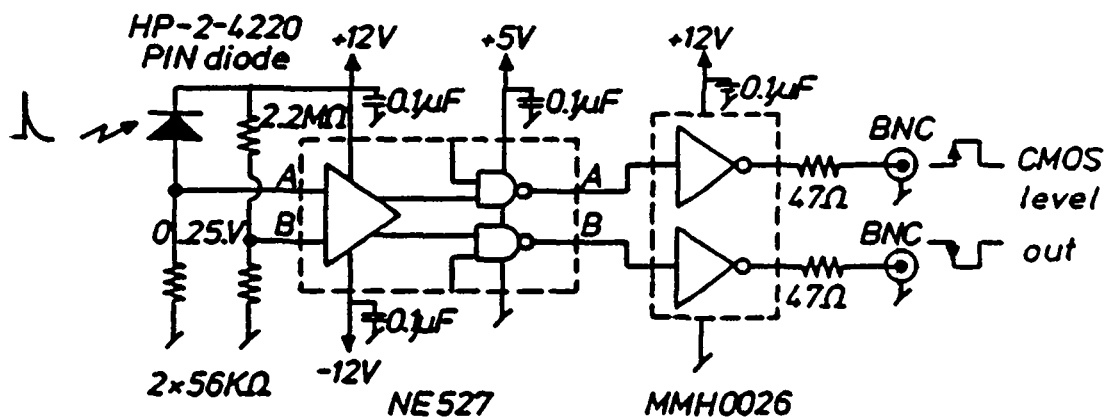


FIGURE 3.13. The optical fiber trigger receiver system.

The length of the  $\text{CO}_2$  laser pulse can be adjusted by varying the timing between the different laser modules, see figures 3.14 and 3.15 [16,25] and figure 3 in appendix C [22]. Figure 3.14 shows a typical short pulse which approaches the ordinary gain switched pulse shape of  $\text{CO}_2$  lasers. The timing of the preamplifier and all four amplifier modules are set to a delay of 500 ns with respect to the oscillator. Figure 3.15 shows a typical long pulse obtained by delaying the triggering of the amplifiers by another 500 ns.

Too short a pulse produces high power densities which damages the KCl windows. For optimum long pulse operation both the timing and the gas mixture have to be adjusted. Stable discharges are only obtained with at least 50% He in the gas mix. The increase of  $\text{N}_2$  partial pressure lengthens the pulse but also reduces the total power because of the lower  $\text{CO}_2$  concentration.

In figure 3.16 typical time resolved laser pulses are presented, measured after the preamplifier (but with the full  $\text{CO}_2$  laser chain fired into the  $\text{D}_2\text{O}$  laser). The upper trace shows a typical single mode pulse, preceded by some electric noise due to electrical pick up from the discharge in the spark-gaps of the laser modules.

The triangular shape without a gain switched spike is typical of a system that uses a hybrid TEA oscillator where the low pressure section provides gain before and during the build-up of gain in the TEA section.

The second trace shows longitudinal mode beating in the oscillator, at 76.5 [MHz], due to an improper cavity length tuning of the oscillator. The gain width of the hybrid oscillator is still sufficiently large to allow two cavity modes to develop if the cavity length happens to be such that both modes have about an equal gain (see figure 3.2).

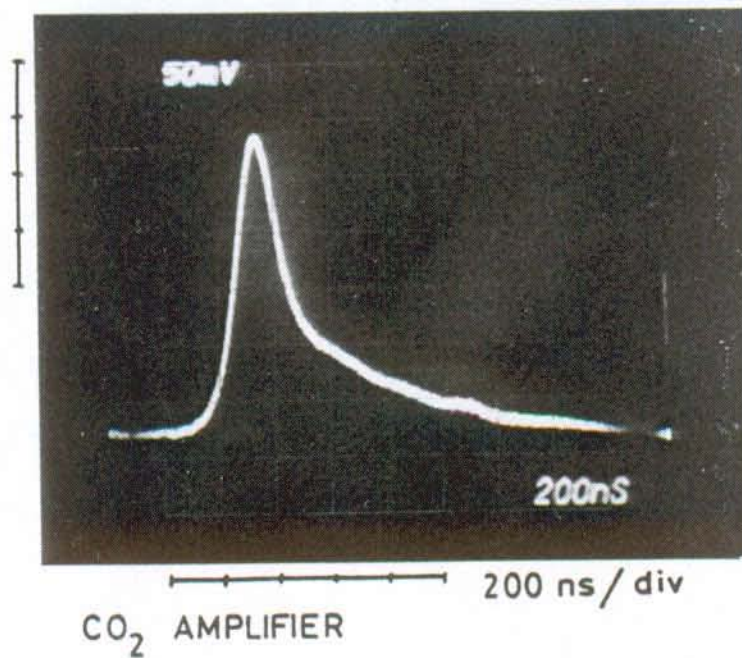
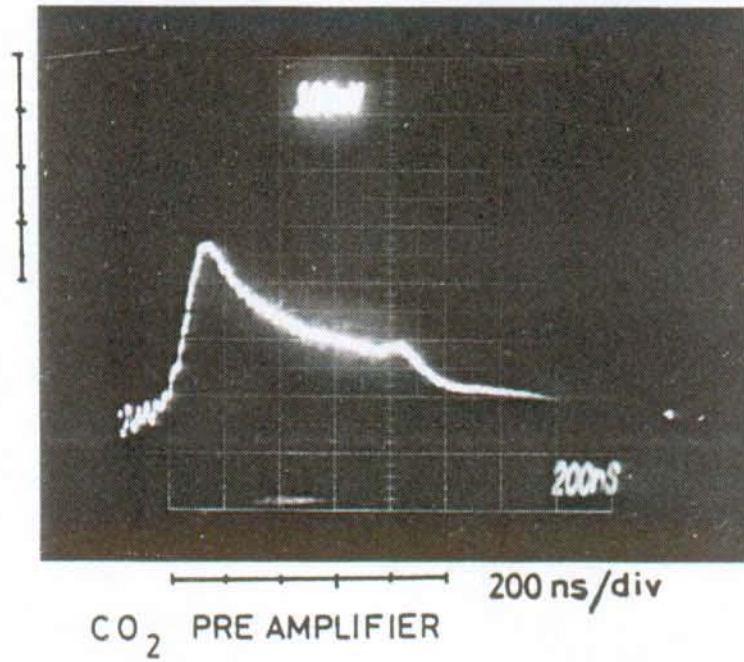


FIGURE 3.14. Pulse shape of the CO<sub>2</sub> preamplifier and one amplifier arm for short pulses. The amplifiers and the preamplifier are triggered at the same time, 500 ns after the oscillator.

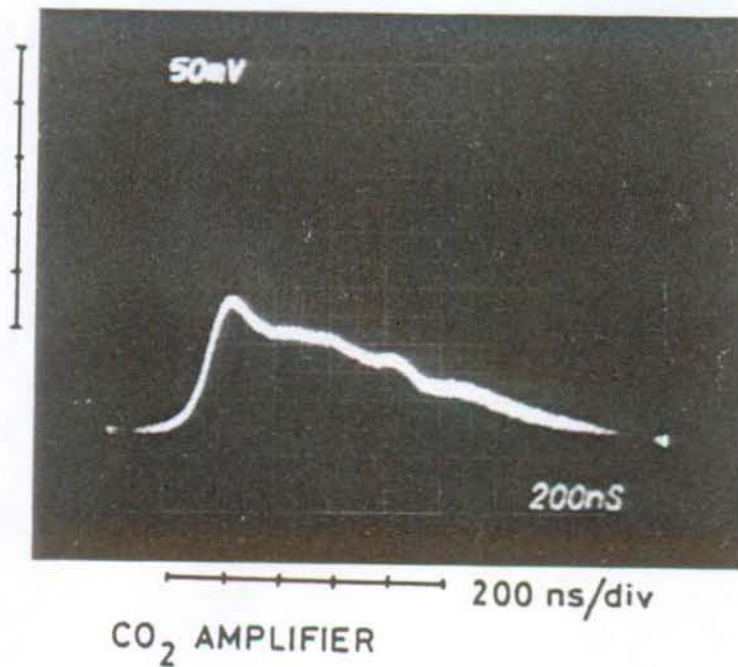
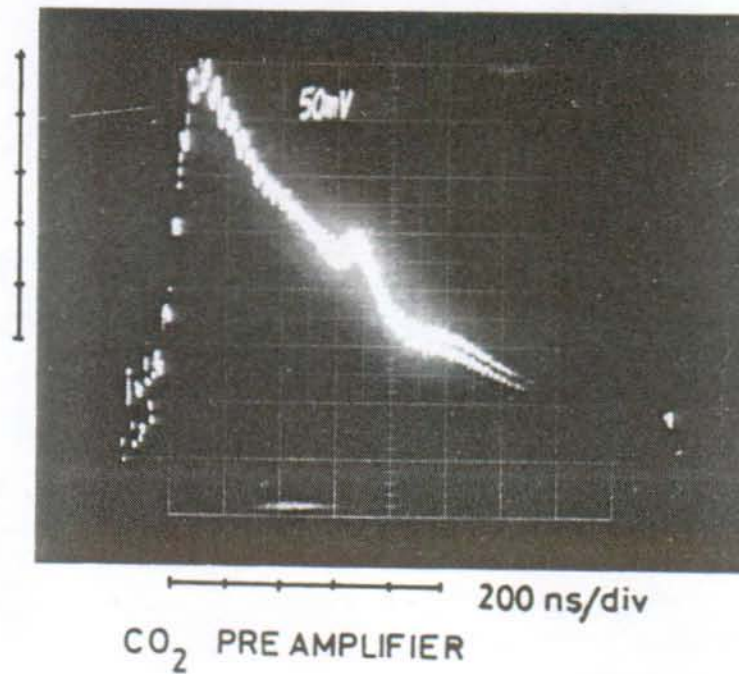


FIGURE 3.15. Pulse shape of the CO<sub>2</sub> preamplifier and one amplifier arm for long pulses. The oscillator is triggered first, followed after 500 ns by the preamplifier and then again 500 ns later by the two amplifier chains.

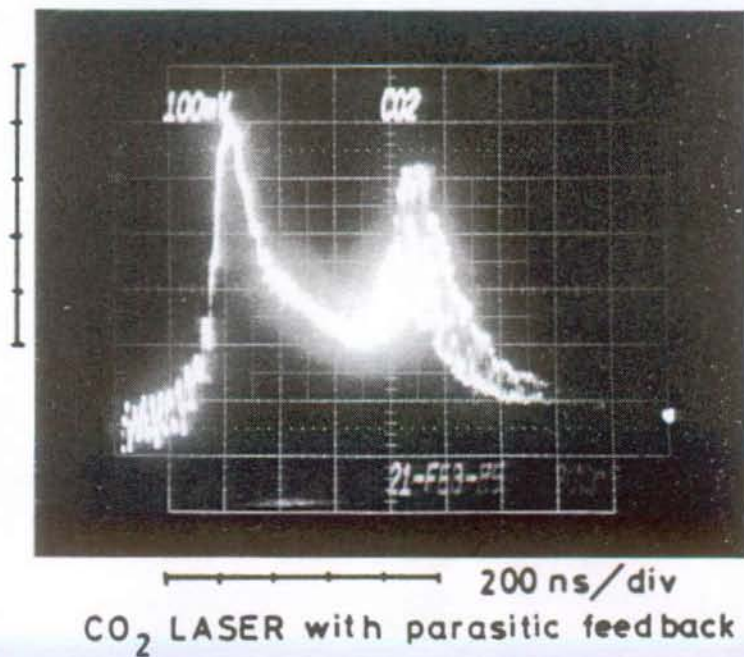
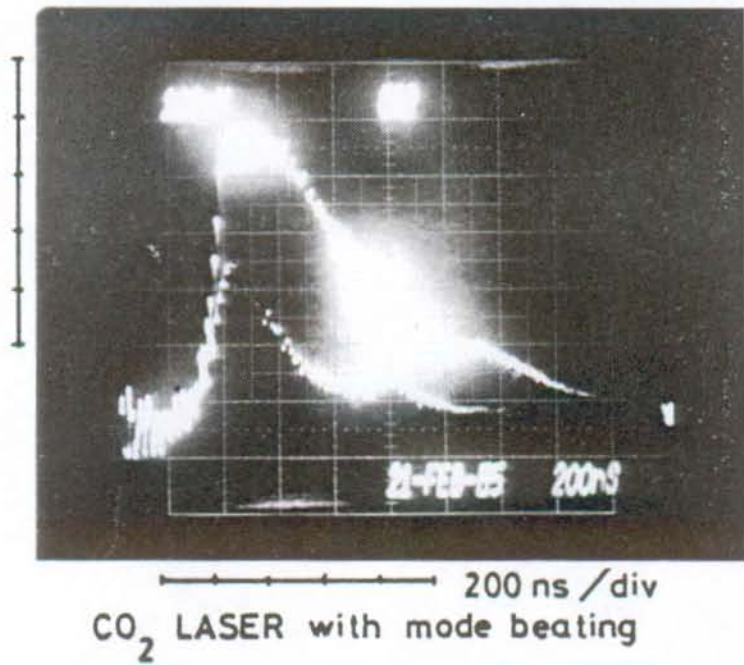
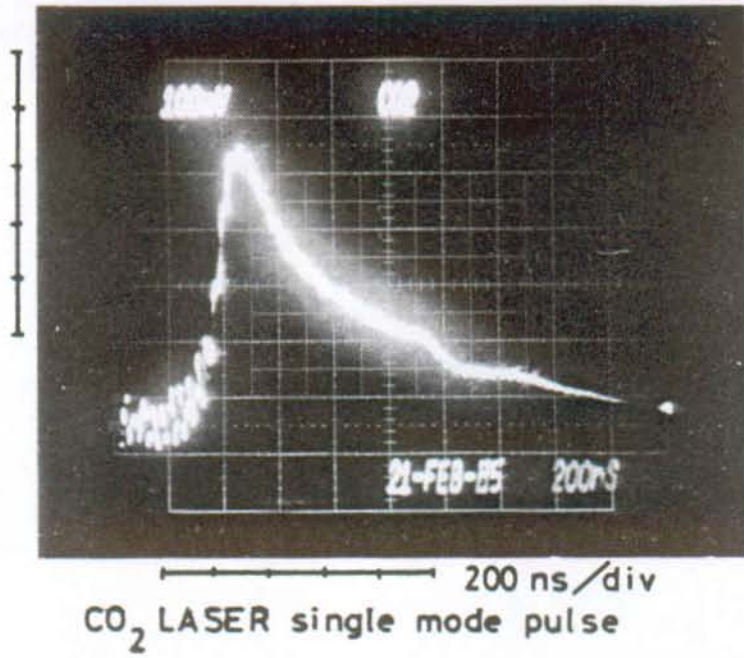


FIGURE 3.16. CO<sub>2</sub> laser pulse shapes, measured after the preamplifier.



The bottom trace shows the effect of typical parasitic feed-back due to spurious reflections in the  $D_2O$  laser. This feed-back appears generally during the second half of the long laser pulse. It presents one of the difficulties introduced by long pulse generation in the  $CO_2$  laser. At the oscillator powers greater than 10 J have been measured, for a parasitic beam travelling backwards through the laser chain.

### 3.2.7. Alignment procedure of the $CO_2$ lasers.

The alignment of the  $CO_2$  laser chain is achieved with three He-Ne lasers, one is placed between the oscillator and the preamplifier, and two others, one for each amplifier arm, are positioned after the preamplifier (see figure 3.7). The first He-Ne beam is centered with respect to burn marks from the  $CO_2$  oscillator beam, while the two other He-Ne beams are aligned on the optical axes defined by the  $CO_2$  amplifier modules. The  $CO_2$  amplifier beams are brought colinear with the alignment lasers by adjusting the different steering mirrors such that the burn marks from the  $CO_2$  beams are centered with respect to the He-Ne laser beams.

Finally, the He-Ne beams defining the optical axis of the  $CO_2$  amplifiers are made coincident with the He-Ne beam defining the optical axis of the  $D_2O$  laser by adjusting the steering mirrors situated between the  $CO_2$  and the  $D_2O$  laser.

$CO_2$  laser burn marks are recorded on "pencil blackened" paper for energy densities of about  $0.1 \text{ J/cm}^2$ , on carbon paper for energy densities up to  $0.3 \text{ J/cm}^2$  and on 3M thermal sensitive paper for higher energy densities.

### 3.2.8. Overview of the experimental layout.

Figures 3.17 to 3.20 show the general layout of the laser system on the TCA Tokamak. The photos 3.18 and 3.19 show the  $CO_2$  and  $D_2O$  lasers seen from two different sides, while

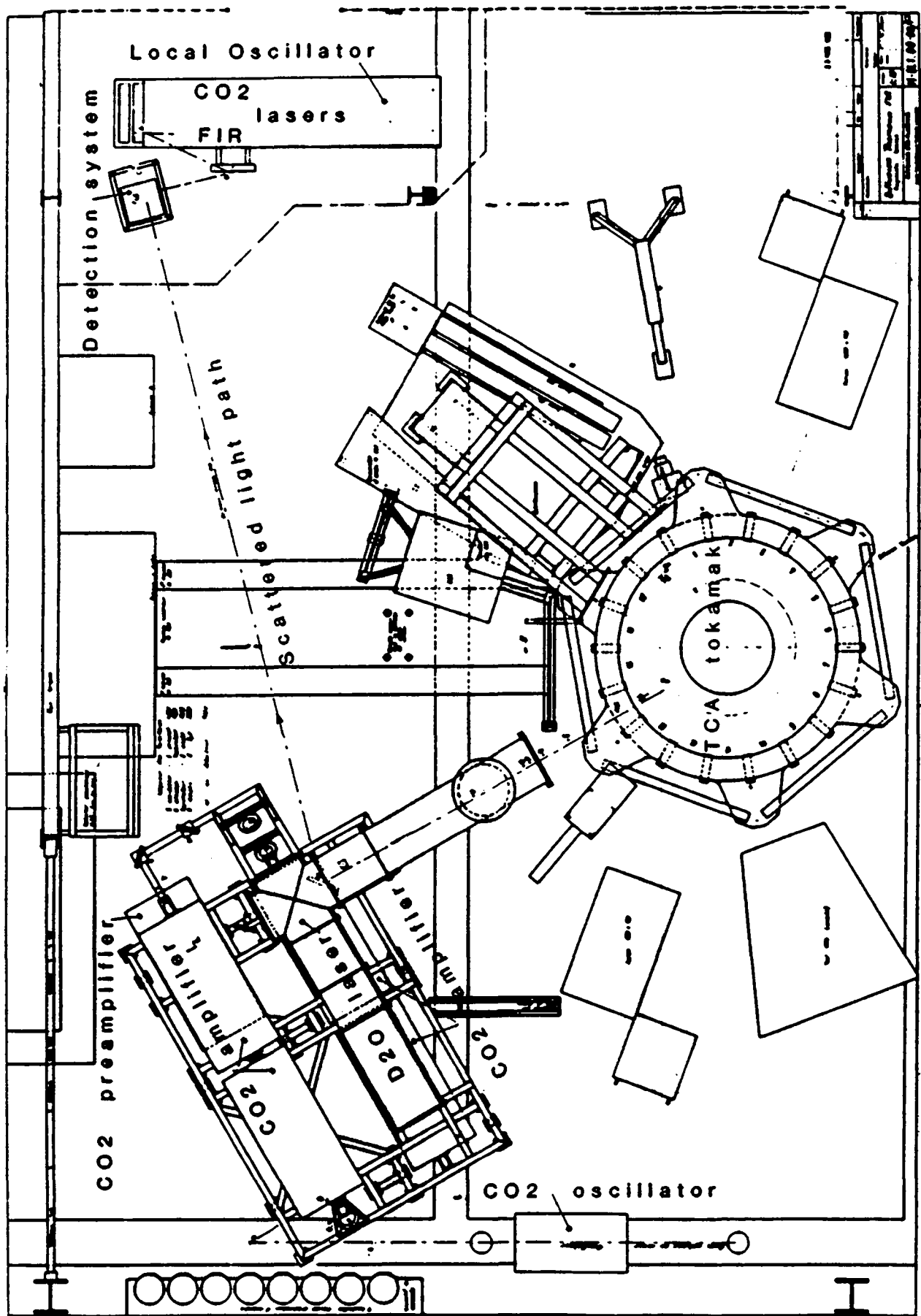


Figure 3.17. The CO<sub>2</sub> and D<sub>2</sub>O laser layout around the TCA tokamak.

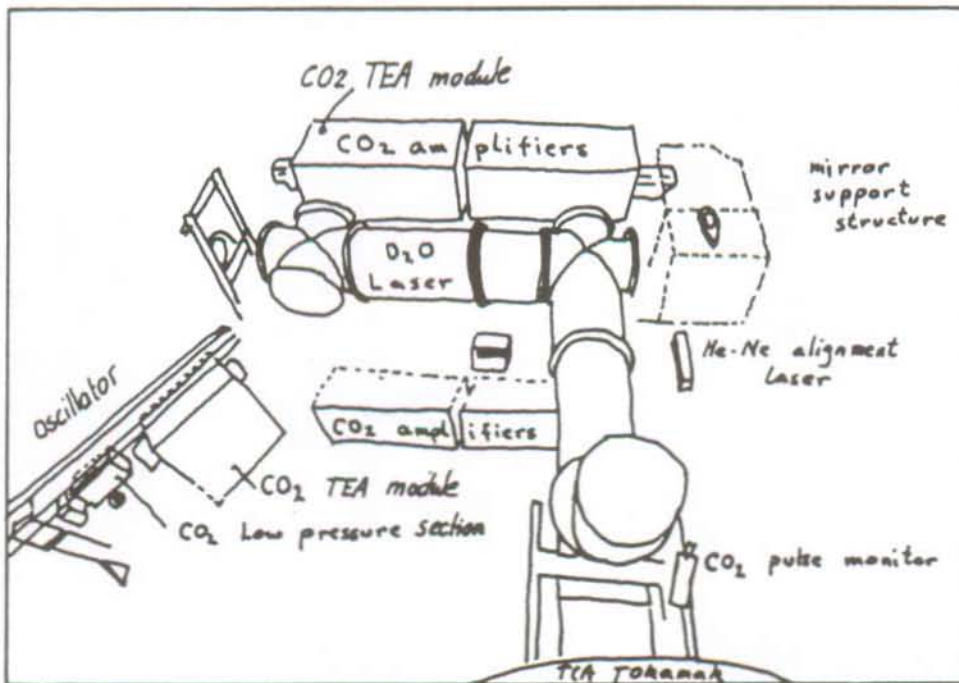
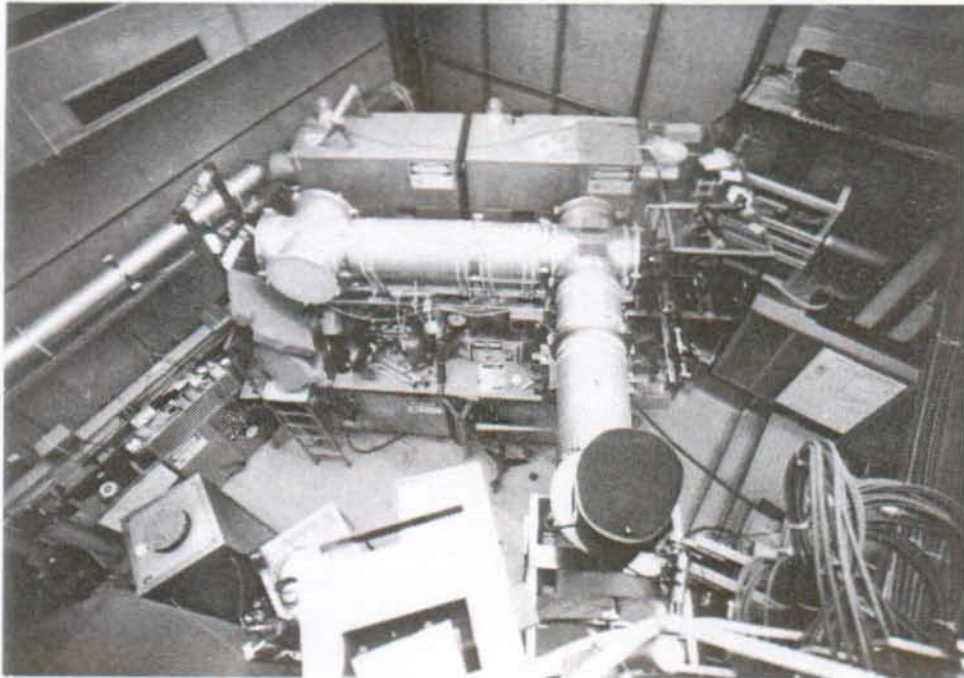


Figure 3.18. Bird's eye view of the CO<sub>2</sub> - D<sub>2</sub>O laser system.

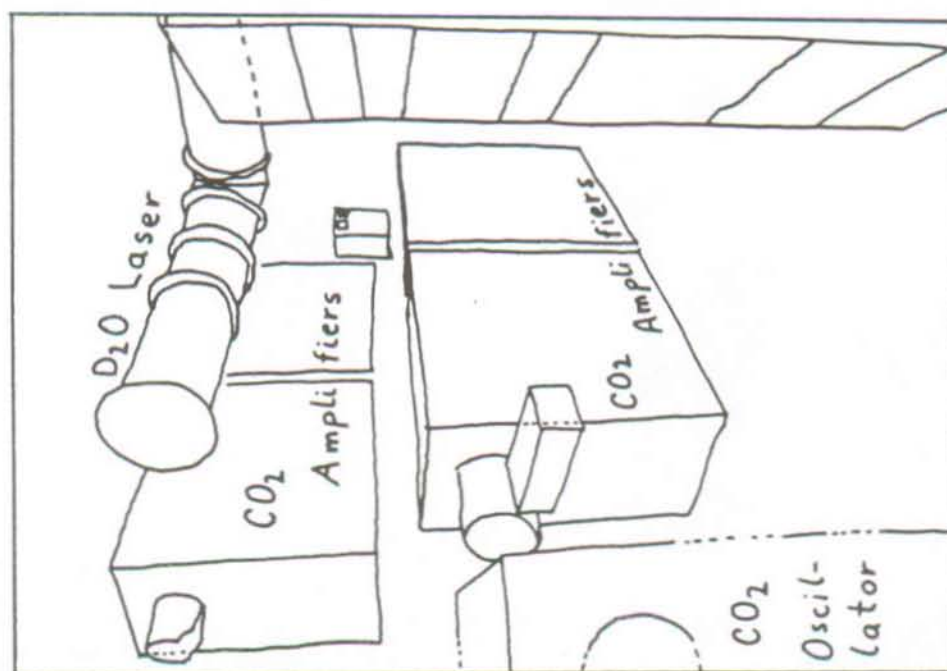
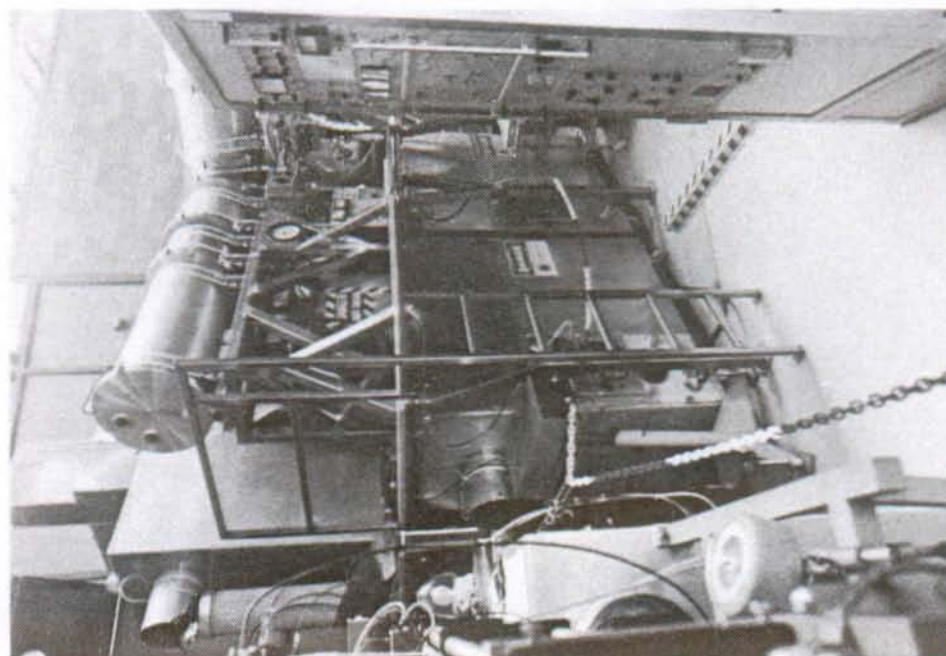


Figure 3.19. The CO<sub>2</sub> laser system seen from the oscillator.

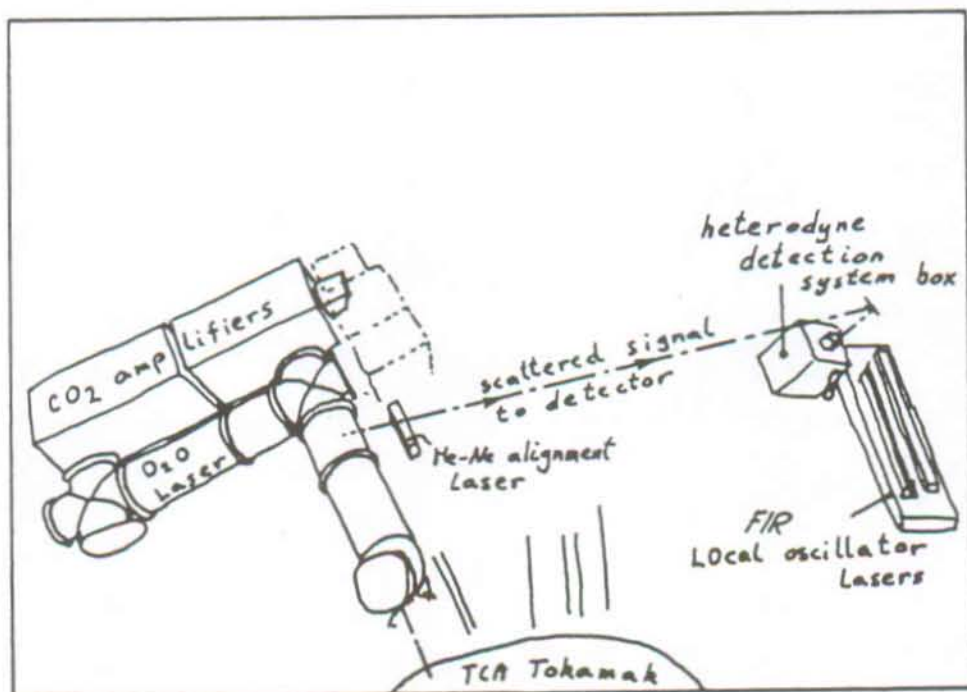
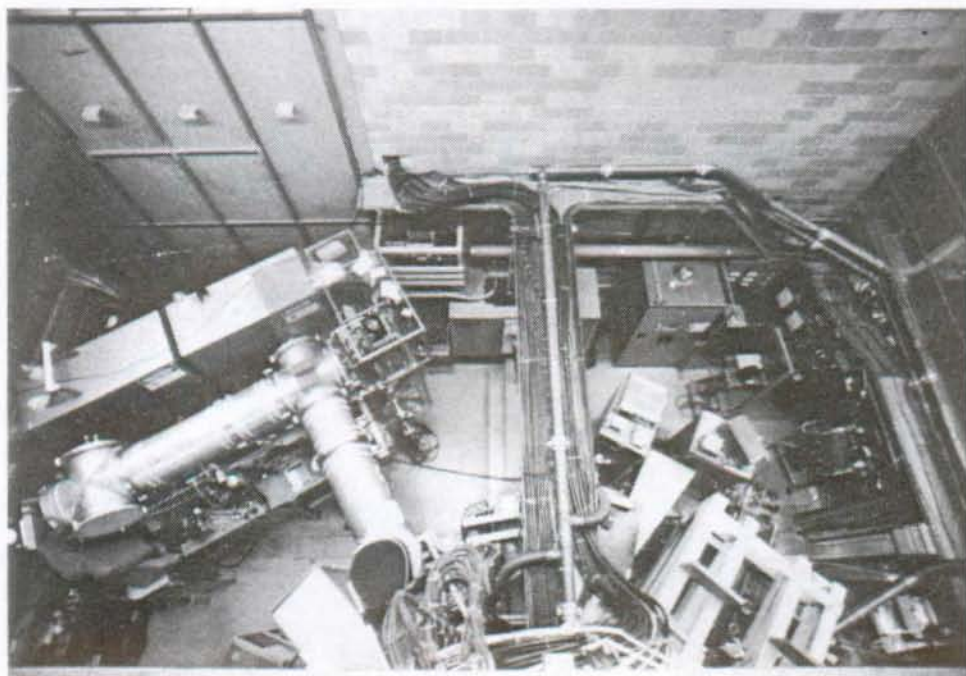


Figure 3.20. Bird's eye view of the lasers and the detection system with the local oscillator.

photo 3.20 also shows the detection system situated at the east side of the hall, outside the restricted area so that it is accessible at any time during tokamak operation.

Because of the limited space, the two  $\text{CO}_2$  amplifier arms were mounted one above the other on a stainless steel structure, where the  $\text{D}_2\text{O}$  laser was also mounted. The axis of the  $\text{D}_2\text{O}$  laser beam is situated 2.35 m above the floor level.

### 3.3. The FIR $\text{D}_2\text{O}$ laser.

Figure 3.21 shows a partial energy level diagram for the  $\text{D}_2\text{O}$  molecule, in particular the  $\nu_2$  symmetric bending mode levels. We use the standard spectroscopic notation for the rotational energy levels of an asymmetric top molecule which are defined by the  $J_{K-K+}$  quantum numbers, where  $J$  is the total angular momentum quantum number and  $K$  the projection of  $J$  onto the principal axis of symmetry of the molecule in the case of a prolate ( $K-$ ) and oblate ( $K+$ ) asymmetric top molecule, for details see [7,26].

The  $9R(22)$  transition of the  $\text{CO}_2$  laser ((1) in figure 3.21) pumps the  $\text{D}_2\text{O}$  molecule between the rotational level  $5_{33}$  of the vibrational ground state and the rotational level  $4_{23}$  in the first excited vibrational state. The change of angular momentum is  $\Delta J_p = -1$ .

The FIR emission at the wavelength of 385  $\mu\text{m}$  occurs between the  $4_{23}$  and the  $4_{13}$  rotational level ((1') in figure 3.21). The quantum number  $J$  stays constant for the FIR transition ( $\Delta J_1 = 0$ ). When  $\Delta J_p + \Delta J_1$  is an odd number the polarization of the FIR beam is perpendicular to the polarization of the pump beam [1,7,27,28,29].

Refill (276  $\mu\text{m}$ :  $6_{33} - 6_{24}$ , 239  $\mu\text{m}$ :  $6_{24} - 5_{33}$ ) and cascade lines (358  $\mu\text{m}$ :  $4_{13} - 4_{04}$ ) have been reported [28], the strongest

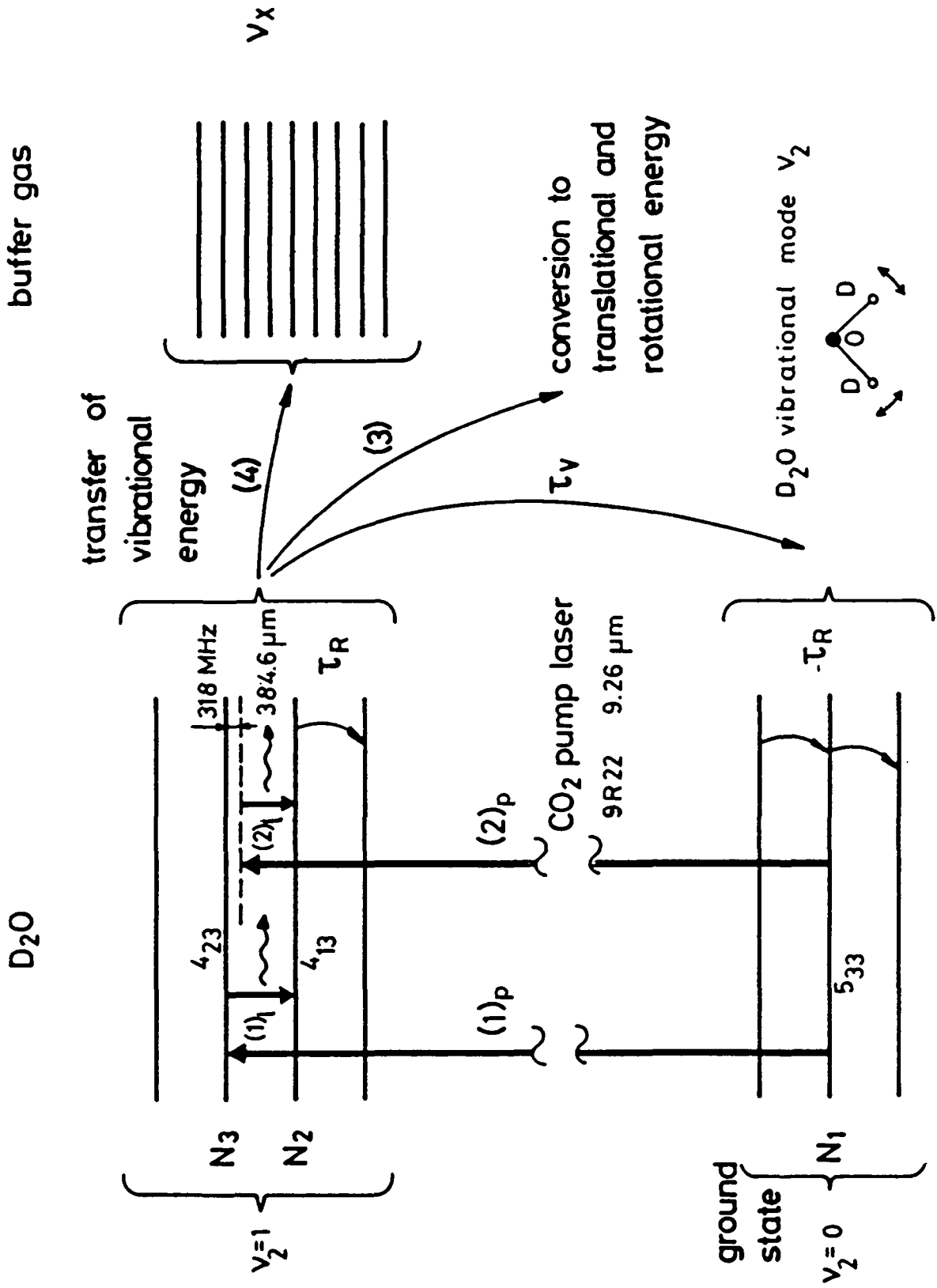


FIGURE 3.21. The  $D_2O$  molecule energy levels for  $385 \mu m$  emission.

being the 358  $\mu\text{m}$  cascade line with a measured output energy of one tenth of the 385  $\mu\text{m}$  output energy [22]. The short rotational relaxation time  $\tau_r$  in figure 3.21 thermalizes the rotational sublevels within each vibrational state rapidly compared to the slower vibrational deexcitation time  $\tau_v$ .

In 1977 there was a significant advance in the understanding of the mechanism of optically pumped FIR lasers with the demonstration that the 66  $\mu\text{m}$ , like the 385  $\mu\text{m}$  emission [27,30] of  $\text{D}_2\text{O}$  is produced by the stimulated Raman effect [1]. Raman emission is a two photon process and is theoretically twice as efficient as normal laser emission. A population inversion is not required, unlike in a laser process [16]. If the pump frequency in the Raman process is offset by  $\Delta\nu_p$  from the  $\text{D}_2\text{O}$  absorption line center frequency ((2) in figure 3.21) it gives rise to a FIR output frequency offset by  $\Delta\nu_p$  from the FIR laser line center frequency ((2') in figure 3.21). For the case of the 385  $\mu\text{m}$  transition in  $\text{D}_2\text{O}$  the detuning  $\Delta\nu_p$  is -318 MHz [28,31]. The fact that the FIR emission is generated by stimulated Raman emission has implications on the FIR line width, pulse length and power.

A narrow line width FIR emission can only be obtained with a narrow width pump laser. The actual Raman line width of the  $\text{D}_2\text{O}$  laser depends also strongly on the pump intensity as described in details in the thesis of M.A. Dupertuis [2].

As long as there are sufficient molecules in the ground state to excite, the pulse lengths of the pump and FIR lasers are usually comparable. A bottleneck effect occurs when the excited molecules are not recycled at a sufficient rate. The recycling rate depends strongly on the vibrational relaxation rate which is  $\tau_v \approx 1 \mu\text{s} \cdot \text{Torr}$  for the  $\text{D}_2\text{O}$  molecule [31]. It has been shown [19] that the addition of certain buffer gases to the  $\text{D}_2\text{O}$  laser enhances the vibrational deexcitation, and thus the laser efficiency for long pulses ( $> 500 \text{ ns}$ ), without adversely affecting the emission line width. The buffer gas study is shortly described in §3.3.3, see also appendix D.



The power efficiency of the optical pumping scheme is low. In the ideal case it will reach the Manley-Rowe limit:

$$\lambda_{\text{CO}_2} / \lambda_{\text{FIR}} = 9.26 \text{ } \mu\text{m} / 385 \text{ } \mu\text{m} = 24 \text{ mJ(FIR) / J(IR)} = 2.4\% \quad (3.9)$$

assuming the generation of a FIR photon for each pump photon [1,16,2]. Under the conditions of saturating pump and FIR intensities, the power emitted from the FIR laser is proportional to the rate of pump absorption from the ground-state. The laser process is limited by collisional refilling of the ground state and the depletion of the excited state, both of which occur at a rate characterized by  $\tau_r \approx 8 \text{ ns} \cdot \text{Torr}$ . In a first approximation the maximum pump rate can be expressed as [1,16]:

$$\rho_p = N_{10} / \tau_r \approx 80 \cdot 10^{24} \text{ [s}^{-1} \cdot \text{liter}^{-1} \cdot \text{Torr}^{-2}] \quad (3.10)$$

where  $N_{10}$  is the molecular density of the ground state at equilibrium (see table 3.2). This leads to an extractable, or saturated power density at the FIR frequency  $\nu_{\text{FIR}} = 778.58 \text{ GHz}$  of [1,16]:

$$P_{\text{FIR}} = h \nu_{\text{FIR}} \rho_p \approx 40 \text{ [kW} \cdot \text{liter}^{-1} \cdot \text{Torr}^{-2}] \quad (3.11)$$

assuming that each pump photon generate a FIR photon (Manley-Rowe limit). Experimental values typically 20 times lower are reported [1,22]. It is clear that in order to reach power levels of a megawatt or more, a very high power IR laser pumping a FIR laser of several liters active volume is needed.

Some physical constants and calculated parameters of the  $\text{D}_2\text{O}$  molecule for emission at  $385 \text{ } \mu\text{m}$  are given in table 3.2 [25,28]. Although the spontaneous emission  $\tau_s$  is large, the power density from spontaneous emission is low. It is comparable to the background thermal emission which is about  $10^{-15} \text{ W/cm}^2$  for a wavelength of  $500 \text{ } \mu\text{m}$ . As a consequence of the high gain of FIR lasers these low power levels are amplified to the saturation power level within a short distance [1].

$p$	=	3 to 6	Torr	typical D <sub>2</sub> O laser gas pressure.
$\lambda_f$	=	$384.6 \cdot 10^{-6}$	m	D <sub>2</sub> O laser line wavelength.
$\nu_{lf}$	=	$778.90 \cdot 10^9$	Hz	D <sub>2</sub> O laser line frequency.
$\nu_{rf}$	=	$778.58 \cdot 10^9$	Hz	D <sub>2</sub> O Raman line frequency.
$\sigma_{13}$	=	$(6.7/p) \cdot 10^{-20}$	m <sup>2</sup>	Line centre absorption
$\sigma_{32}$	=	$(6.9/p) \cdot 10^{-19}$	m <sup>2</sup>	cross-sections.
$N_{10}$	=	$(63.5 p) \cdot 10^{19}$	m <sup>-3</sup>	= 1.8 % of total molecules.
$N_{20}$	=	$N_{10} \cdot 6.25 \cdot 10^{-3}$	m <sup>-3</sup>	Equilibrium level populations
$N_{30}$	=	$N_{10} \cdot 5.5 \cdot 10^{-3}$	m <sup>-3</sup>	in the absence of a pump.
$\tau_r$	=	$(7.9/p) \cdot 10^{-9}$	s	Rotational relaxation time.
$\tau_v$	=	$(1/p) \cdot 10^{-6}$	s	Vibrational relaxation time.
$\tau_s$	=	52	s	Spontaneous emission lifetime (1/A).
$\mu_{13}$	=	0.12	D	Transition dipole moments.
$\mu_{32}$	=	1.87	D	(1 D = $3.33564 \cdot 10^{-30}$ C·m)
$\Delta\nu_p$	=	$(40 p) \cdot 10^6$	Hz	Pressure line broadening.
$\Delta\nu_D$	=	$3 \cdot 10^6$	Hz	Doppler line broadening.
$g_f$	=	0.21	cm <sup>-1</sup>	Measured FIR small signal gain [34].

Calculated values based on rate equations [1]:

$G_f$	=	2.2	cm <sup>-1</sup>	FIR laser gain ( $\sigma_{32} \cdot N_{10}/2$ ).
$G_r$	=	0.43	cm <sup>-1</sup>	FIR Raman gain.
$G_p$	=	-0.45	cm <sup>-1</sup>	Pump absorption ( $\sigma_{13} \cdot N_{10}$ ).
$U_{sf}$	=	$(10 p^2) \cdot 10^6$	Wm <sup>-3</sup>	FIR laser saturation power density.
$U_{sp}$	=	$(650 p^2) \cdot 10^6$	Wm <sup>-3</sup>	Pump saturation power density.

TABLE 3.2. Typical parameters for the D<sub>2</sub>O 385  $\mu$ m line emission, from [1,2,32,33,34].

For the  $D_2O$  laser a gain length of 85 cm is sufficient to amplify thermal noise to the saturation power density (values obtained from table 3.2). This results in an amplified spontaneous emission (ASE) background which covers a large frequency band compared to the line width of a cavity mode.

Other experimental studies of the  $D_2O$  385  $\mu m$  line have shown:

- The line width is reduced when pumping with a single mode  $CO_2$  line [27].
- Maximum output of the  $D_2O$  laser occurs for a frequency offset from the  $D_2O$  absorption line centre [27]. This offset value strongly depends on gas pressure and pump intensity.
- The conversion efficiency of  $CO_2$  laser energy to  $D_2O$  laser energy is larger when pumping with a single mode line than with a multimode line [27,28].
- Due to the high gain, a  $D_2O$  resonator emits maximum FIR power with a low cavity feed-back. The optimum is around an output coupler reflectivity of 5% [22,33,35].

Different numerical simulations have been undertaken in order to study the dynamic behavior of FIR lasers. The theoretical treatment of multiple coherent waves interacting with the molecular system of the FIR lasers has been extensively studied in the thesis of M.A. Dupertuis [2]. For FIR lasers, the standard rate equation approach is not general enough to treat multiphoton effects such as the stimulated Raman emission, or the competition between laser and Raman emission. Semi-classical treatment using the density matrix equation is necessary to describe the large number of processes interacting in the FIR laser [1,2,36,37]. The reader is referred to reference [2] for further details. In the following paragraphs, we will discuss the design of the FIR laser.

### 3.3.1. The D<sub>2</sub>O laser design criteria.

We have tested different D<sub>2</sub>O laser cavities, as described in the enclosed article [22] (see appendix C) and references [35,38]. The following observations govern the design of a FIR laser providing 1 μs long pulses of high power and a high spectral purity, both temporal and spatial, the latter to allow focusing of the FIR beam in the plasma with the full energy in the main lobe.

- To obtain high pulse energy a large volume is required (equation 3.11). The pump saturation sets a limit for the minimum cross section of the active volume. A typical value for the pump energy density is  $< 1 \text{ J/cm}^2$ . These requirements, and the demand for low divergence would favor an unstable resonator configuration.
- The cavity length should be long to efficiently absorb the pump beam. The cavity length should not, however, exceed about 4 m to limit the number of longitudinal modes within the homogeneously broadened emission line.
- The increased complexity of the pump laser to allow for tuning of the pump frequency is not paid back by a significant improvement of the FIR laser efficiency.
- The use of SF<sub>6</sub>, CF<sub>4</sub> or C<sub>6</sub>H<sub>14</sub> as a means to enhance the deexcitation of the D<sub>2</sub>O molecules increases the total output energy by up to 40% for long pulse operation [19] (see §3.3.3 and appendix D).

The pump laser described in §3.2 delivers typically 2 beams of 60 J for a pulse duration of about 1 μs. The pump beam diameter is 60 mm at the D<sub>2</sub>O laser. This corresponds to a pump energy density of  $2 \text{ J/cm}^2$ , and a pump power density of  $2 \text{ MW/cm}^2$ .

We have chosen not to expand the pump beams to lower the pump density. The cost and complexity to install a set of

THE D<sub>2</sub>O LASER

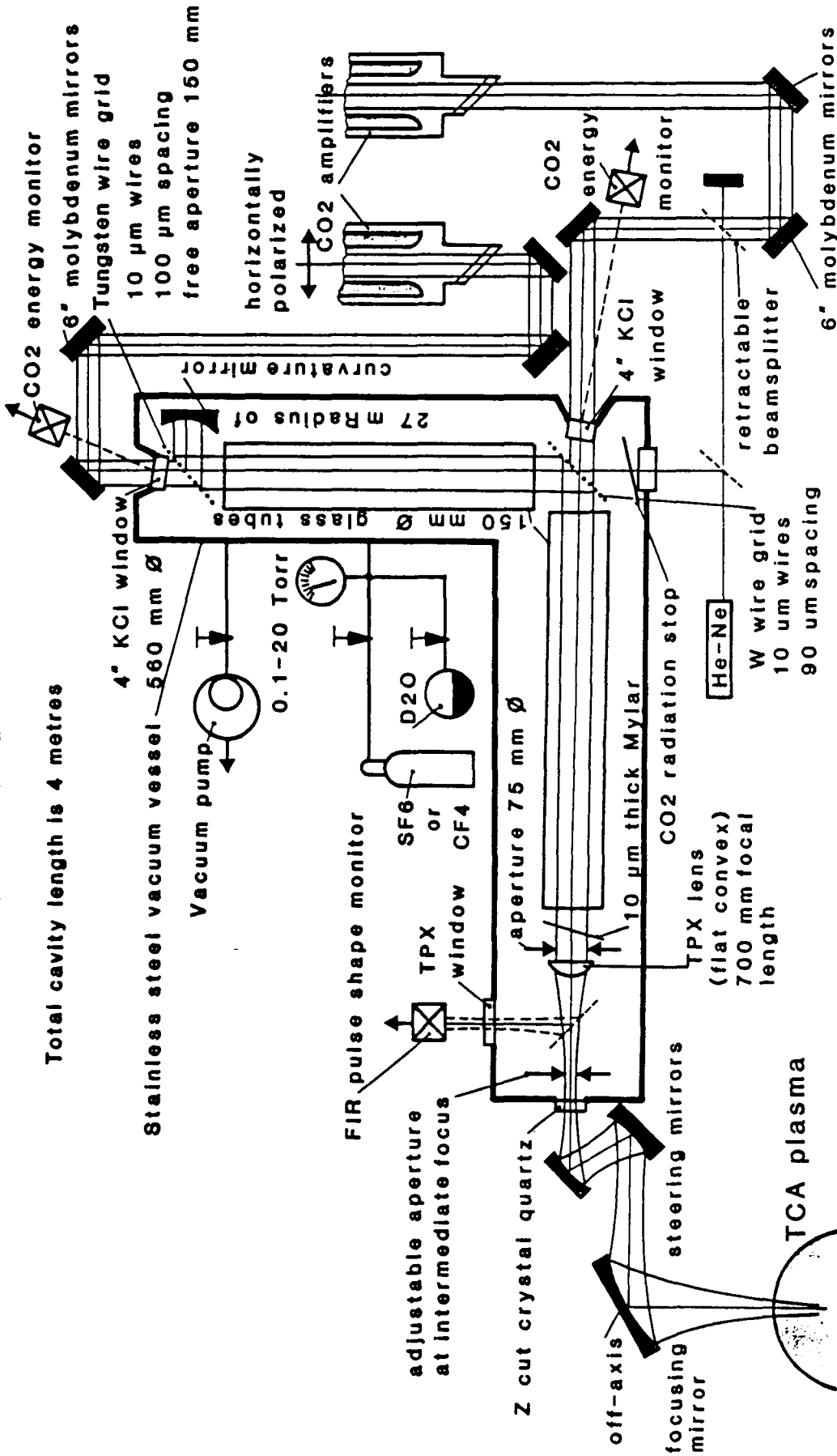


FIGURE 3.22. The D<sub>2</sub>O laser configuration.

larger mirrors, KCl windows and wire grids for the  $D_2O$  laser were considered to be too high. By keeping the pump beam diameter at 60 mm, a stable FIR cavity can be used. The fundamental cavity mode of a flat-flat mirror cavity has a gaussian waist of 35 mm which matches well the pump beam area. By choosing a total FIR cavity length of 4 m we have an active volume of 11 liters. Each of the two IR beams is pumping one half of the total cavity length.

The present  $D_2O$  laser set-up is given in figure 3.22. Two free standing grids are used to fold the cavity and to couple the  $CO_2$  laser beams into the FIR resonator. These grids transmit 90% of the incident pump beams, while they reflect more than 75% of the FIR radiation at 385  $\mu m$  wavelength. The pump beams are polarized perpendicular to the wires, while the FIR emission is polarized parallel to the wires of the grids. The cavity is formed by an aluminium coated glass mirror of 27 m radius of curvature and 250 mm in diameter opposed to a plano-convex TPX lens of 75 mm in diameter. Only the flat surface of the TPX lens acts as a 4.5% reflecting output coupler, while the reflection from the curved surface (330 mm radius of curvature) forms a highly unstable cavity and the radiation is lost rapidly. The TPX lens is used to form an intermediate focus which is imaged into the plasma by an off-axis elliptical mirror (see chapter 4). Combining the output coupler and the lens into one element reduces the losses from extra optical surfaces, since optical antireflection coatings are not yet readily available in the FIR for a wavelength of 385  $\mu m$ .

The longitudinal mode spacing for the 4 m long cavity is 37.5 MHz, while the homogeneous gain width is about 150 MHz at 4 Torr. The transverse mode spacing is only 4.7 MHz, but the diameter of the TPX lens output coupler acts as an aperture limiting the emission to the lowest order transverse mode.

Two glass tubes of 150 mm in diameter are used as light guides to improve the confinement of the pump radiation. The improvement due to the tubes for this particular laser confi-

uration has not been measured, but previous observations [19, 22,27] have shown a 10% to 20% increase of the FIR energy.

To avoid spurious reflections of  $\text{CO}_2$  radiation back into the amplifiers we use two 10  $\mu\text{m}$  thick Mylar sheets to absorb the  $\text{CO}_2$  energy which is not absorbed by the  $\text{D}_2\text{O}$  gas (about 25% at 4 Torr pressure and 10% at 6 Torr).

The reflections from the two wedged KCl windows, acting as input ports on the  $\text{D}_2\text{O}$  laser, are used to monitor the pump beam energy and pulse shape. The free aperture of these windows is 85 mm which is sufficient to avoid diffraction and spurious reflections of the pump pulse.

The FIR pulse shape is monitored by a Molectron P3-01 fast response ( $< 1$  ns) pyroelectric detector. A thin Mylar sheet beam splitter is used to couple approximately 5% of the FIR beam onto the detector.

The FIR laser beam leaves the  $\text{D}_2\text{O}$  vessel via a Z-cut crystal quartz window. The quartz window is machined as an etalon for maximum transmission, it has a diameter of only 50 mm since the FIR beam is focused just 100 mm before exiting the  $\text{D}_2\text{O}$  laser vessel. The Raman emission from the  $\text{D}_2\text{O}$  laser is not significantly absorbed on the 700 mm path from the TPX output coupler to the quartz window. This short path after the output coupler is not pumped. To avoid an air-breakdown which scatters and absorbs the FIR radiation the focal spot must be inside the vacuum vessel.

The stainless steel vacuum chamber of the  $\text{D}_2\text{O}$  laser forms a rigid frame to which the optical elements of the FIR resonator are attached. The system is modular so that we can easily change the resonator configuration. This large tube has the drawback that the vacuum vessel has a total volume of 1355 liters (100 times the active laser volume). The leak rate is of the order of one Torr per day which is acceptable.

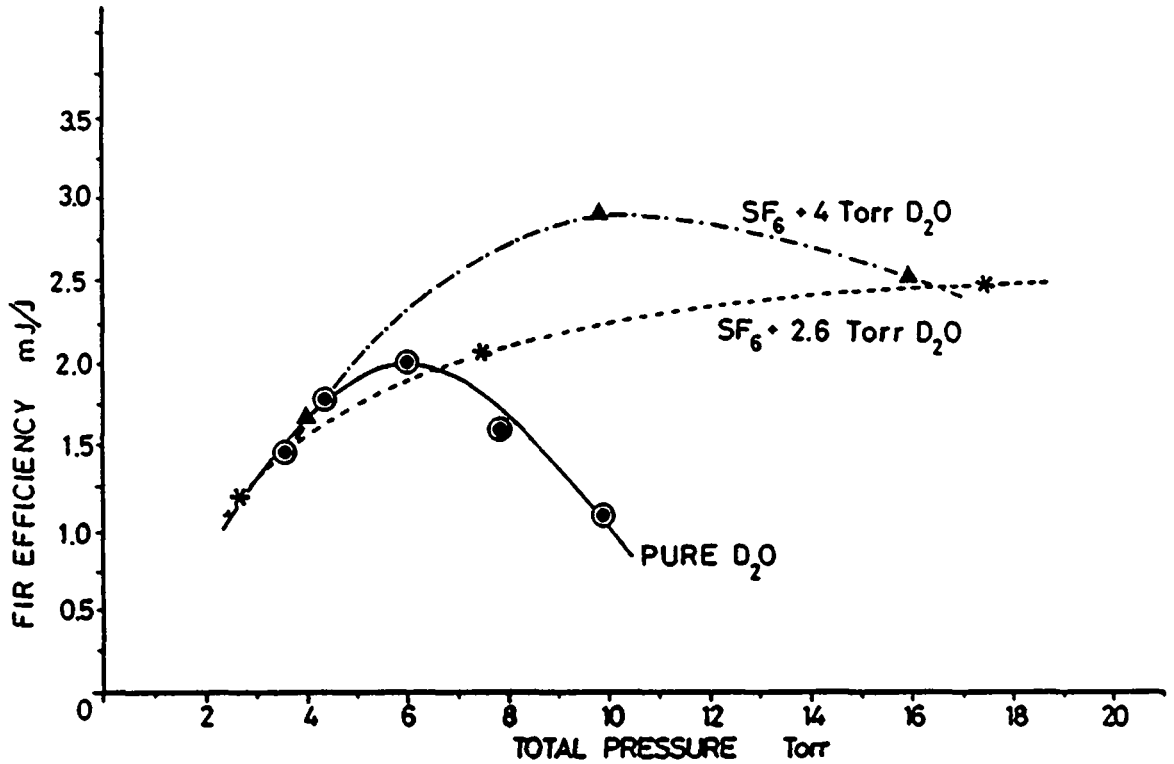


FIGURE 3.23. Laser energy conversion versus gas pressure, each point is the average of 3 measurements.

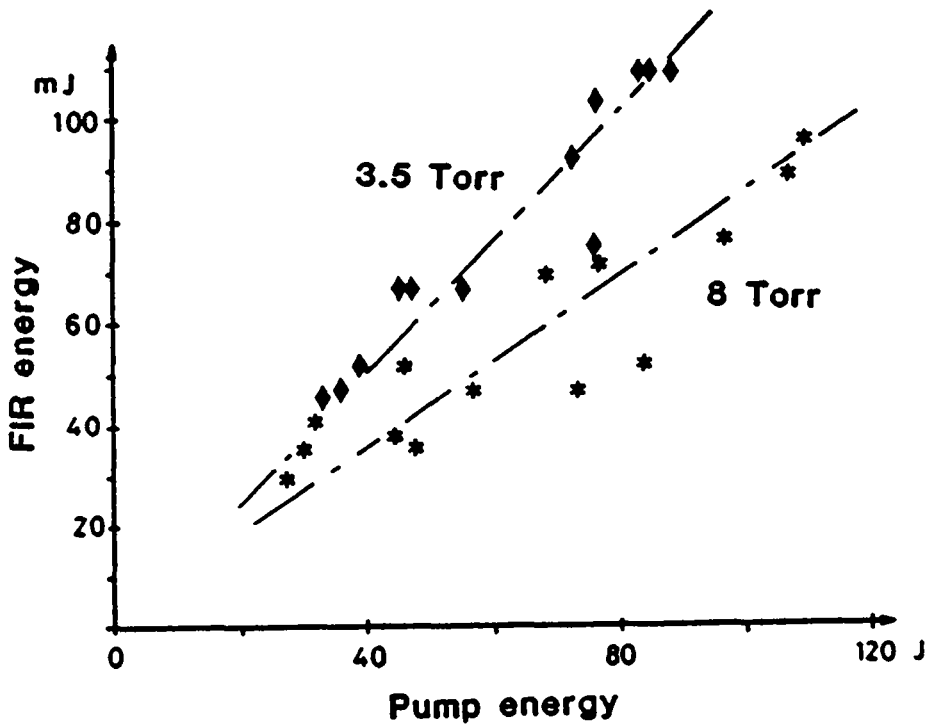


FIGURE 3.24. FIR pulse energy as a function of the pump pulse energy for pure D<sub>2</sub>O (see also appendices C and D).



### 3.3.2. Performance of the D<sub>2</sub>O laser.

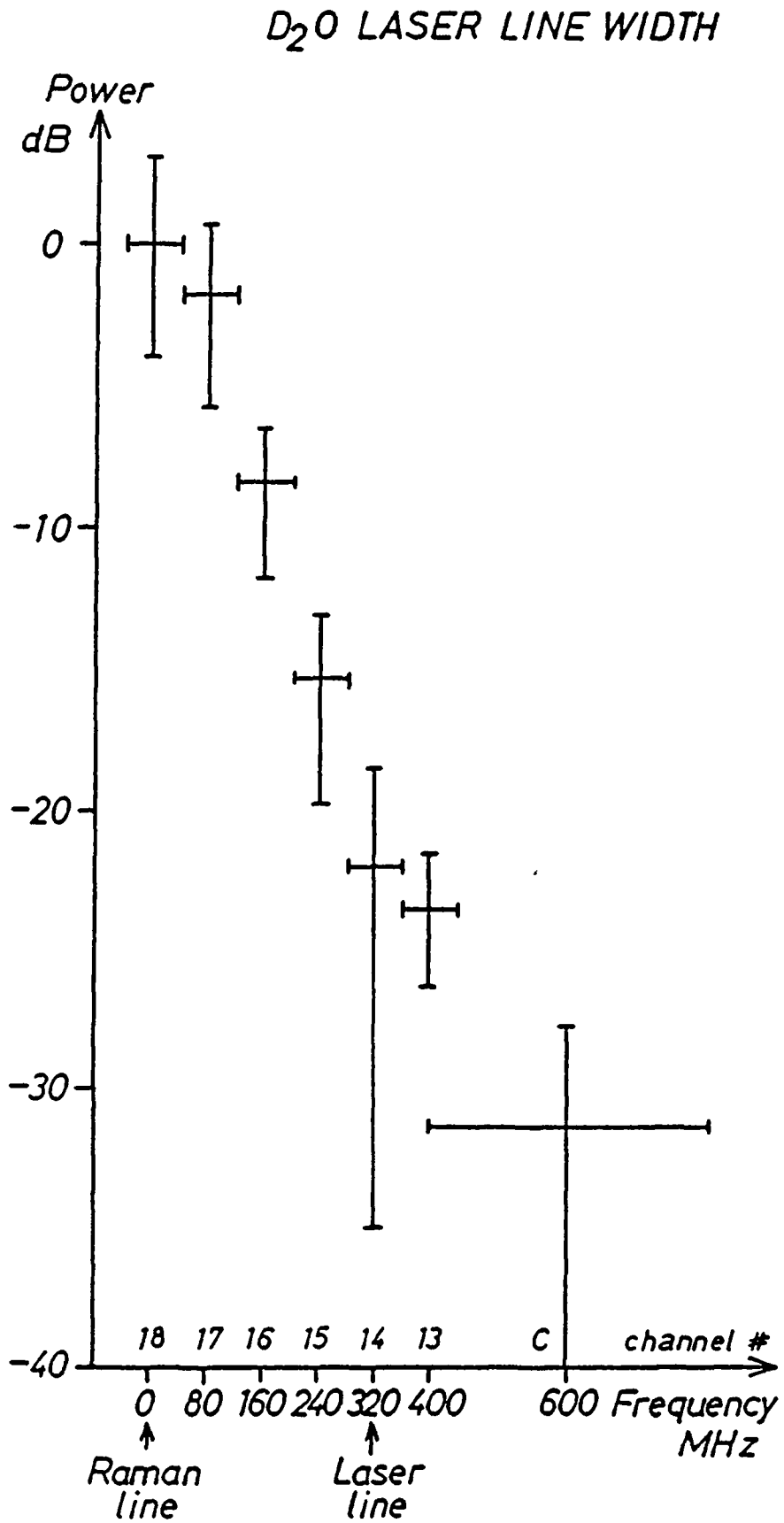
Figure 3.23 shows the D<sub>2</sub>O laser energy efficiency as a function of D<sub>2</sub>O gas pressure. Each point represents a mean of 3 laser shots. This curve is obtained for typical pump beam energies and is to compare with the figure 6 of the enclosed article [22] (see appendix C) and figure 8a of reference [19] (see appendix D). Taking into account the 18% losses from the KCL windows and the wire grids the CO<sub>2</sub> laser delivers a net energy of 2x50 J, which corresponds to a net energy density of 1.75 J/cm<sup>2</sup> for each of the two beams.

### 3.3.3. The buffer gas.

With the pump energy density of the present laser figure 3.24 does not show a saturation effect as can be observed in figure 6 of the enclosed article (reference [19] appendix D). The saturation is due to the bottleneck introduced by the slow vibrational decay from the final excited state down to the ground level ((3) in figure 3.21). Figure 3.23 shows, however, that addition of SF<sub>6</sub> to the D<sub>2</sub>O gas increases the net energy conversion. This effect has been described in detail in reference [19] (see appendix D).

The role of the buffer gas is to enhance the decay from the excited vibrational state of the D<sub>2</sub>O molecule to the ground state via intermolecular collisions without affecting the rotational lifetime, which would lower the FIR gain. The decrease of the FIR conversion efficiency for pure D<sub>2</sub>O at pressures above 4 Torr, as observed in figure 3.23, is mainly due to the increasing collisional broadening of the rotational levels. The guidelines for selecting a buffer gas molecule are [19]:

- Vibrational energy levels near 1079 cm<sup>-1</sup> allowing resonant energy transfer from the  $\nu_2$  level of the D<sub>2</sub>O molecule.
- Negligible absorption of the pump radiation at 9.26  $\mu\text{m}$ .

FIGURE 3.25. The FIR line width at 4 Torr  $D_2O$  pressure.

- Negligible absorption of the FIR radiation at 385  $\mu\text{m}$ .
- Minimum collisional broadening of the  $\text{D}_2\text{O}$  rotational levels.

Resonant energy transfer only requires coincidence of the levels to within thermal energy  $kT$ . This will avoid a conflict between the first two requirements. A buffer gas molecule without a permanent dipole moment satisfies the two last requirements, since it does not have any far infrared active rotational transition.

Only the use of  $\text{SF}_6$  is shown in figure 3.23, although we have used the other gases  $\text{CF}_4$  and n-hexane ( $\text{C}_6\text{H}_{14}$ ) with success [19].

#### 3.3.4. The $\text{D}_2\text{O}$ laser line width and pulse shape.

The  $\text{D}_2\text{O}$  laser line width, at a working pressure of 4 Torr pure  $\text{D}_2\text{O}$ , is shown in figure 3.25. It was measured by the heterodyne detection system (see chapter 5). The FIR beam, focused into the TCA vacuum vessel, was scattered by the alignment target (see chapter 4). A set of calibrated cardboard attenuators was used to bring the observed signal within the limited 20 db dynamic range of the detection system. Attenuators were inserted in the IF circuit (see figure 5.21) to balance the signal power of the different channels. Each point is a mean of three or more laser shots, with one standard deviation represented by the vertical error bars. The horizontal bars are the width of each of the spectral channels (80 MHz and 400 MHz for the last channel).

Because of the steep rolloff of the stray laser light, if we ignore the four spectral channels adjacent to the FIR Raman line, we could tolerate a stray light signal at the Raman frequency 26 dB above the level of the average scattered signal. Our measurement is in good agreement with the  $\text{D}_2\text{O}$  laser line-width measurement performed at MIT [39].

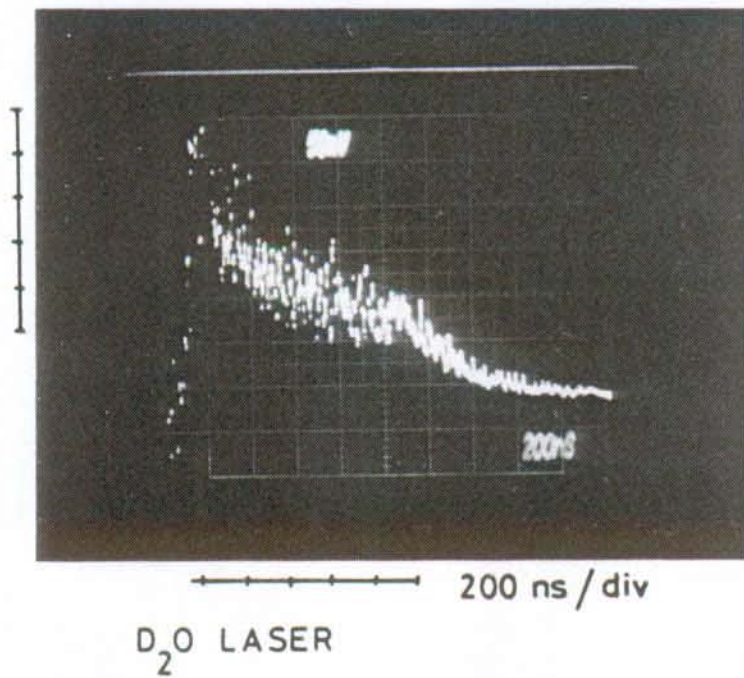
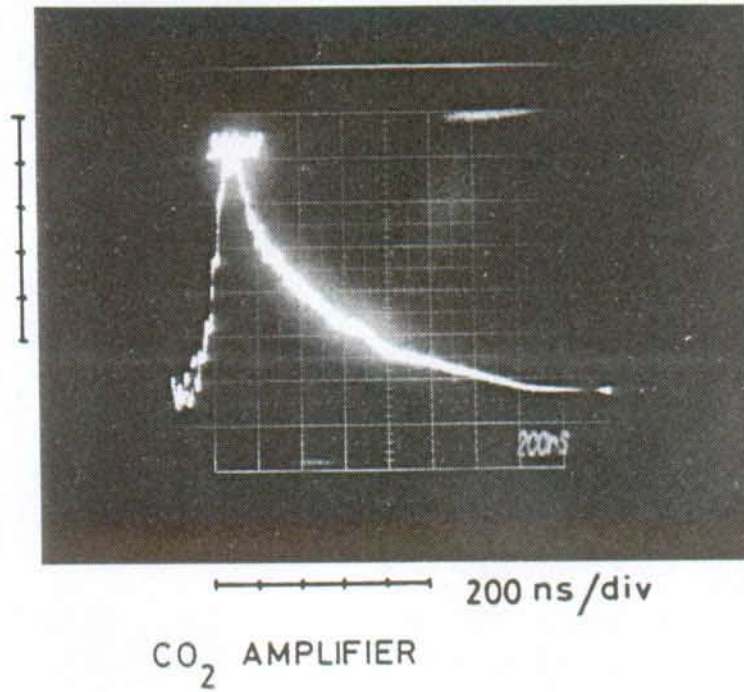


FIGURE 3.26. Typical CO<sub>2</sub> (upper trace) and D<sub>2</sub>O laser pulse shapes.

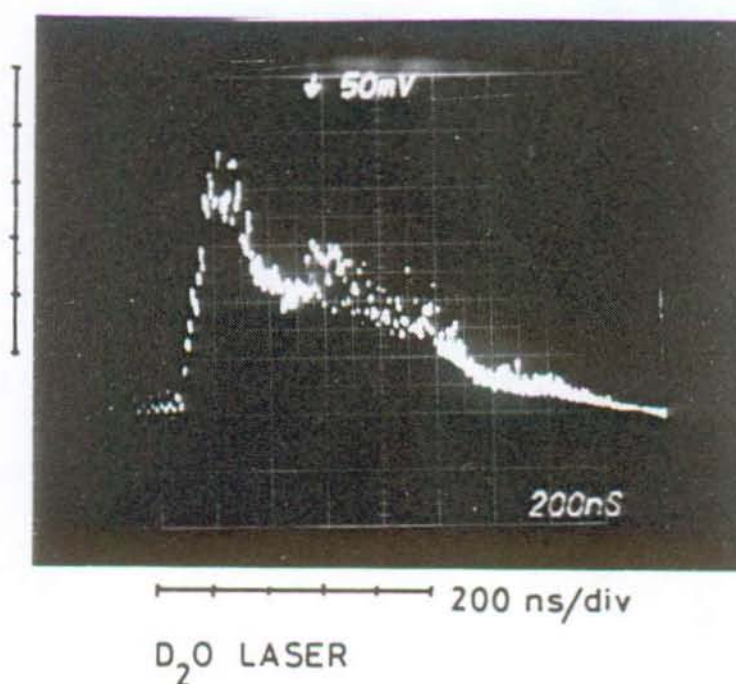
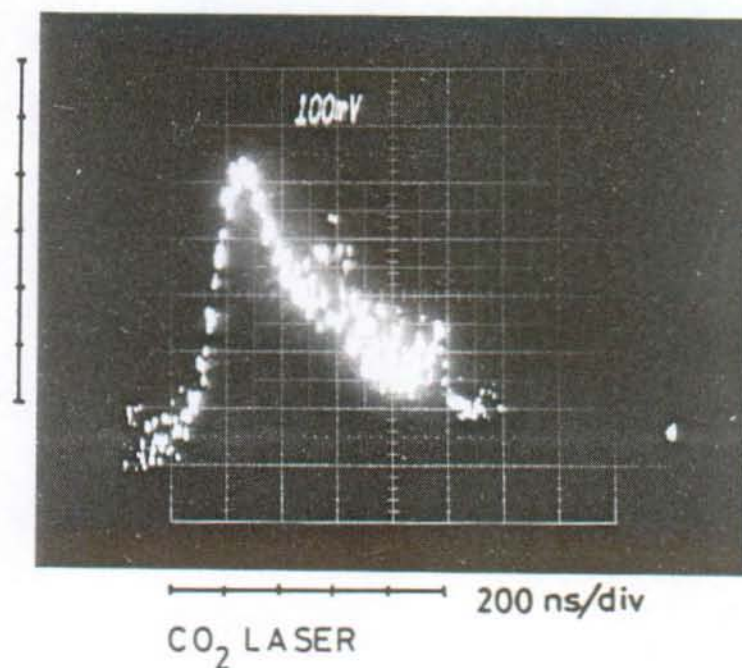


FIGURE 3.27. The CO<sub>2</sub> (upper trace) and D<sub>2</sub>O laser pulse shapes with modulation from parasitic feed-back appearing 400 ns after the beginning of the pulse. Modulations before the laser pulse are due to electric pick-up from the spark-gaps in the laser modules. FIR energy 195 mJ with 4 Torr D<sub>2</sub>O and 7 Torr CF<sub>4</sub>.

Typical FIR pulse shapes are given in figure 3.26 and 3.27 (see also figures 8 to 11 of [22] appendix C). We observe that the FIR laser pulse shape closely follows the shape of the CO<sub>2</sub> pump pulse even for amplitude modulations due to mode beating or spurious feedback in the pump laser (figure 3.27).

The influence of the buffer gas on the bottleneck of the FIR pulse is illustrated in [19] by figure 9 (appendix D). In long pulse operation the FIR laser pulse length is significantly enhanced and stays comparable with the pump pulse length.

The FIR pulses shown are not pure single modes, but contain some modulation. This is probably due to the presence of additional weaker longitudinal cavity modes. The FIR laser cavity mode spacing for longitudinal modes is 37 MHz.

#### 3.3.5. Comparison of D<sub>2</sub>O lasers.

For a better comparison between our laser system and other D<sub>2</sub>O lasers, either developed at CRPP [19,22,38], or elsewhere [27,40], the relevant data has been listed in table 3.3.

Columns 1 to 8 refer to the FIR laser cavity. In column 2 "s" stands for stable, "u" for unstable D<sub>2</sub>O resonator. Column 3 gives the output coupler reflectivity and is followed in the next columns by the laser cavity length, diameter, area, volume and finally the optimum D<sub>2</sub>O gas pressure. The cavity diameter is defined to be the pump beam diameter.

The next eight columns refer to the CO<sub>2</sub> pump beams including the total energy, losses before the FIR laser cavity, energy densities, power and power densities expressed in different units and finally the pump pulse length.

D2O cavity			CO <sub>2</sub> laser							D2O laser															
Ref	Refl	Length	Diam	Area	Vol	Pres	E	Iran	E-den	E-vol	P	P-den	P-sat	Pulse	E	E-den	E-vol	P	P-den	P-sat	Eff	Rel-eff			
Z	cm	cm	cm <sup>2</sup>	cm <sup>2</sup>	dm <sup>3</sup>	Torr	J	Z	J	J	MW	MW	kW	μs	kJ	kJ	kJ	kW	kW	kW	%	%	Z		
---	1	2	3	4	5	6	7	8	9	10	11	12	13	14	15	16	17	18	19	20	21	22	23	24	
	---	---	---	---	---	---	---	---	---	---	---	---	---	---	---	---	---	---	---	---	---	---	---	---	
s	5	400	5.0	28.3	11.3	6.0	60 <sup>1</sup> 82	1.74 <sup>1</sup>	1.45 <sup>1</sup> 57.9 <sup>1</sup>	2.05 <sup>1</sup>	56.9 <sup>1</sup> 0.85	180	6.37	2.65	212	7.49	208	1.83	7.6						
[19]	u	5	400	12.4	120.8	48.3	6.0	320	100	2.65	2.21	266.7	2.21	61.3	1.20	1200	9.94	4.14	1000	8.28	230	3.75	15.6		
[40]	u	20	360	22.6	401.1	144.4	3.0	360	69	0.62	1.15	49.7	0.12	13.8	5.00	2500	6.23	5.77	500	1.25	138	10.06	41.8		
[40]	u	20	360	22.6	401.1	144.4	4.0	530	69	0.91	1.27	73.1	0.18	11.4	5.00	4500	11.22	7.79	900	2.24	140	12.31	51.1		
[40]	u	20	360	22.6	401.1	144.4	4.5	700	69	1.20	1.49	96.6	0.24	11.9	5.00	5000	12.46	7.69	1000	2.49	123	10.35	43.0		
[40]	u	20	360	22.6	401.1	144.4	6.0	250	69	0.43	0.40	862.5	2.15	59.7	0.20	1000	2.49	1.15	5000	12.46	346	5.80	24.1		
[40]	u	20	360	22.6	401.1	144.4	1.0	60	69	0.10	0.57	207.0	0.52	516.0	0.20	250	0.62	1.73	1250	3.12	3116	6.04	25.1		
[27]	s	60	300	7.4	43.0	12.9	3.0	25	92	0.53	1.19	230.0	5.35	594.2	0.10	80	1.86	2.07	800	18.60	2067	3.48	14.5		
[27]	s	30	400	7.4	43.0	17.2	3.0	25	92	0.53	0.89	230.0	5.35	594.2	0.10	120	2.79	2.33	1200	27.90	3100	5.22	21.7		
[38]	u	10	200	11.0	95.0	19.0	5.0	100	82	0.86	1.73	68.3	0.72	28.8	1.20	75	0.79	0.79	63	0.66	26	0.91	3.8		
[38]	u	5	400	11.0	95.0	38.0	3.0	100	82	0.86	1.44	68.3	0.72	79.9	1.20	105	1.10	0.92	88	0.92	102	1.28	5.3		
[38]	u	5	400	9.0	63.6	25.4	2.0	100	82	1.29	3.22	68.3	1.07	268.5	1.20	110	1.73	2.16	92	1.44	360	1.34	5.6		
[22]	0	100	3.9	11.9	1.2	2.5	1.3	100	0.11	0.87	13.0	1.09	174.1	0.10	1.3	0.10	0.42	13	1.05	167	0.96	4.0			
[22]	0	100	3.9	11.9	1.2	2.5	1.3	100	0.11	0.87	2.2	0.18	29.0	0.60	1.0	0.08	0.33	2	0.14	22	0.77	3.2			
[22]	u	11	100	3.9	11.9	1.2	3.0	1.5	100	0.13	0.84	15.0	1.26	139.5	0.10	1.5	0.13	0.42	15	1.26	140	1.00	4.2		
[22]	s	15	100	3.9	11.9	1.2	6.0	1.5	100	0.13	0.42	15.0	1.26	34.9	0.10	1.1	0.09	0.15	11	0.92	26	0.73	3.0		
[22]	s	15	100	3.9	11.9	1.2	4.0	1.5	100	0.13	0.63	1.9	0.16	9.8	0.80	1.4	0.12	0.29	2	0.15	9	0.93	3.9		
[22]	s	61	100	3.9	11.9	1.2	3.0	1.3	100	0.11	0.73	2.2	0.18	20.2	0.60	1.5	0.13	0.42	3	0.21	23	1.15	4.8		
[22]	s	61	100	3.9	11.9	1.2	3.0	1.3	100	0.11	0.73	1.6	0.14	15.1	0.80	1.4	0.12	0.39	2	0.15	16	1.08	4.5		

<sup>1</sup> Corresponds to the energy and power density for one of the two CO<sub>2</sub> laser beams, each pumping one half (200 cm) of the D2O laser cavity.

TABLE 3.3. Comparison of different D2O lasers, references in column 1. In column 2: u = unstable, s = stable resonator. In column 10: 'Iran' is the fraction of the pump beam available in the D2O laser.

The "P-sat" column (15) is the power density expressed in  $\text{kW}\cdot\text{cm}^{-2}\cdot\text{Torr}^{-2}$ . These values are to be compared with the saturation power density obtained from table 3.2, defined as [1]:

$$I_{\text{p-sat}} = U_{\text{sp}}/G_{\text{p}} = 1.5 \text{ [kW}\cdot\text{cm}^{-2}\cdot\text{Torr}^{-2}] \quad (3.12)$$

$$I_{\text{f-sat}} = U_{\text{sf}}/G_{\text{f}} = 40 \text{ [W}\cdot\text{cm}^{-2}\cdot\text{Torr}^{-2}] \quad (3.13)$$

The final eight columns refer to the FIR lasers. As for the pump laser they include energy, energy densities, power and power densities. Column 23 is the FIR to IR energy conversion efficiency and column 24 is the same conversion efficiency but normalized to the Manley-Rowe limit (equation 3.9), the result is often called the quantum efficiency. Again, the "P-sat" column (22) is to be compared with expression (3.13).

The first row in table 3.3 refers to the FIR laser system described in the present work. The values given are typical for pure  $\text{D}_2\text{O}$  without any buffer gas. The best values measured were 240 mJ FIR radiation and have been obtained using 4 Torr  $\text{D}_2\text{O}$  with 12 Torr  $\text{CF}_4$  buffer gas and two 75 J  $\text{CO}_2$  laser pump pulses.

Some general remarks applying to the data in table 3.3 are:

- All pumping is with single mode laser pulses.
- The  $\text{CO}_2$  energies are measured with similar types of detectors whose calibration should agree to within 25%.
- Transport losses in the path of the pump beam have been taken into account.
- All values are obtained with pure  $\text{D}_2\text{O}$  as the active gas, no buffer gas used.
- All FIR laser pulses show multiple modes.



- The FIR energy values are not corrected for absorption due to the final output window of the FIR lasers.
- The FIR energies are measured with different types of detectors. Cross calibration of the "standard FIR detector" used at CRPP (Laser Instruments, thermopile model 17 AN) and at MIT (Lumonics, model 50D), during a visit of Dr. P. Wosko-boinikow, showed that the same FIR energies measured with the MIT detector were 35 per cent higher than those measured with the CRPP detector. Energies reported by [40] may also differ significantly from the other measurements, because of the lack of calibration standards for energy detectors in the FIR wavelength region.

We conclude that for the lasers described in table 3.3:

- The FIR transition, and to an even higher extent the IR transition, are strongly saturated.
- The best conversion efficiencies are obtained with unstable FIR resonators with large pump beam diameters.
- The laser presented in this work shows the best energy conversion for long pulse operation with a stable FIR cavity.

#### 3.4. Conclusions.

- The pump laser is composed of 6 CO<sub>2</sub> TEA modules, configured in an oscillator-amplifier scheme. The hybrid oscillator produces a single longitudinal and transverse mode on the 9R(22) line center. After a double-pass preamplifier, the beam is split into two. Each of the beams is further amplified in 2 TEA modules connected in series. In this way we obtain two linearly polarized pump beams of 60 J each and of an area of 20 cm<sup>2</sup>. The CO<sub>2</sub> laser pulse length is about 1 μs.

- The triggering of the pump laser modules is controlled by a digital timer incorporated into the detection system. It synchronizes the CO<sub>2</sub> pump lasers and the acquisition system with the tokamak discharge.
- The FIR laser is formed by a stable, 4 m long, laser cavity filled with typically 4 Torr of D<sub>2</sub>O and 12 Torr of CF<sub>4</sub> used as a buffer gas. The FIR laser produces typically 180 mJ (maximum 240 mJ) of FIR energy in a 1 μs long laser pulse. The beam is linearly polarized with the E vector in the horizontal plane. The divergence of the output laser beam is matched by a TPX lens to the following optics, which focus the FIR beam into the plasma vessel.
- The measured FIR laser line half-width is 350 MHz at -30 dB. At the frequency of the Raman line a stray light level 26 dB above the level of the average scattered light could be tolerated if the central 320 MHz of the scattered spectrum is ignored.
- The FIR laser described in the present work does not fulfil the power requirement of 1 MW calculated in the previous chapter. Therefore it will not allow a T<sub>i</sub> measurement in a single discharge. The lack of sufficient power must be compensated by averaging over several tokamak discharges in order to achieve a sufficient signal to noise ratio for observation of a scattered signal.

REFERENCES:

- [1] "Pulsed optically pumped far infrared lasers", T.A. DeTemple, "Infrared and mm-waves", Vol. 1, Chap. 3, Academic Press, (1979).
- [2] "Etude théorique des lasers infrarouges lointains pulsés et de leur comportement multimode", M.A. Dupertuis, Thèse 558, Ecole Polytechnique Fédérale de Lausanne, (1985).
- [3] "Lasers", by P.K. Cheo, Vol. 3, ch. 2, edited by A.K. Levine and A.J. Demaria, Marcel Dekker Inc, N.Y., (1971).
- "Principles of lasers", ch. 6, O. Svelto, Heyden, N.Y., (1976).
- "Long wave optics", Vol. 1 and 2, G.W. Chantry, Acad. Press, N.Y., (1984).
- [4] "Computer modelling of gas lasers", K. Smith and R.M. Thomson, Plenum Press, N.Y., (1978).
- [5] "High-pressure pulsed molecular lasers", O.R. Wood II, Proc. IEEE, 62, 355 (1974).
- [6] "Fundamental kinetic processes in the CO<sub>2</sub> laser", by O. Judd, Inst. Phys. Conf. Ser. No. 29, p. 29 (1976).
- "The interaction of pulsed optical radiation with an inverted medium", O. Judd, Inst. Phys. Conf. Ser., No. 29, p. 45 (1976).
- [7] "Gas lasers and their application to interferometry of laboratory plasmas", P.A. Krug, Ph. D. Thesis, University of Sydney, (1982).
- [8] "Broadening coefficient for the 10P(20) CO<sub>2</sub> laser transition", R.L. Abrams, Appl. Phys. Lett. 25, 609, (1974).
- [9] "Various techniques for producing a single longitudinal mode TEA CO<sub>2</sub> laser", S.L. Chin, Optics and Lasers technology, p. 85, April 1980.
- [10] "Mode selection in lasers", P.W. Smith, Proc. IEEE, 60, 422 (1972).

- [11] "A tunable stabilized single mode TEA CO<sub>2</sub> laser", by J.P. Nicholson and K.S. Lipton, Appl. Phys. Lett., 31, 430 (1977).
- [12] "The mechanism of single frequency operation of the hybrid CO<sub>2</sub> laser", A. Gondhalekar, N.R. Heckenberg, E. Holzhauser, IEEE J. Quant. Electr., QE-11, 103 (1975).
- [13] "An investigation into the origin of frequency sweeping in a hybrid TEA CO<sub>2</sub> laser", P.W. Vilets, M.R. Harris, J. Phys D: Appl. Phys., 15, 51 (1982).
- [14] "An introduction to lasers and masers", A.E. Siegmann, McGraw-Hill, N.Y., (1971).
- [15] "Theory of pulse propagation in a laser amplifier", by L.M. Frantz and J.S. Nodvik, J. Appl. Phys, 34, No. 8, 2346 (1963).
- "The case for buying an E-beam CO<sub>2</sub> laser amplifier for the FIR scattering program at CRPP, Lausanne", P.D. Morgan, CRPP internal report, (1979).
  - D.J. James, Lumionics Research limited, private communication, Mai 1979.
- [16] "Feasibility of measuring the plasma ion temperature in JET by Thomson scattering using a FIR laser", M.R. Green, M.R. Morgan, M.R. Siegrist, R.L. Watterson, LRP-168-80 CRPP-EPFL report, (1980).
- [17] "Isolation between amplifiers in a TEA CO<sub>2</sub>-laser using absorbing gases", M.R. Green, P.D. Morgan, M.R. Siegrist, R.L. Watterson, M.A. Dupertuis, I. Kjelberg, J.L. Scartezzini, R. Duperrex, H. Van den Bergh, LRP-152-79 CRPP-EPFL report, (1979).
- [18] "Broadband gas isolator for high power CO<sub>2</sub> lasers", S.J. Czuchlewski, A.V. Nowak, E. Foly, J.F. Figueira, Opt. Ltr. 2, 39 (1978).
- [19] "Buffer gases to increase the efficiency of an optically pumped FIR D<sub>2</sub>O laser", R. Behn, M.A. Dupertuis, I. Kjelberg, P.A. Krug, S.A. Salito, M.R. Siegrist, IEEE J. Quant. Electr., QE-21, 1278 (1985).

- [20] "A 40 joule CO<sub>2</sub> TEA laser module with a uniform-field electrode profile and side-arc preionisation", M.R. Green P.D. Morgan, M.R. Siegrist, LRP-141-78 CRPP-EPFL report, (1978).
- [21] "Laser gain profiling with uniform-field electrodes", by A.M. Robinson, J. Appl. Phys., 47, 608 (1976).
- [22] "A comparative study of D<sub>2</sub>O oscillators emitting at 385  $\mu\text{m}$ ", M.R. Green, I. Kjelberg, R. Behn, P.D. Morgan, M.R. Siegrist, IEEE J. Quant. Elect., QE-19, 222 (1983).
- [23] "Studies of a high performance TE CO<sub>2</sub> laser using additives", K.J. Andrews, R. Bahatnagar, P.E. Dyer, G. Salvetti, Opt. Comm., 26, 228 (1978).
- [24] "Operation of an unstable resonator TE CO<sub>2</sub> laser with large electrode spacing using additives", S. Salvetti, Opt. Comm., 30, 397 (1979).
- [25] "A 66 $\mu\text{m}$  D<sub>2</sub>O laser having an unstable Reststrahlen resonator", M.R. Green, I. Kjelberg, P.D. Morgan, M.R. Siegrist, R.L. Watterson, E. Akhmetov, J. Phys. D: Appl. Phys., 13, 1029 (1978).
- [26] "Microwave spectroscopy", C.H. Townes and A.L. Schawlow, Dover publ., (1975).
- [27] "High-power tunable 385- $\mu\text{m}$  D<sub>2</sub>O vapor laser optically pumped with a single-mode tunable CO<sub>2</sub> laser", P. Woskoboinikow, H.C. Praddaude, W.J. Mulligan, D.R. Cohn, B. Lax, J. Appl. Phys., 50, 1125 (1979).
- [28] "Single-mode optical pumping and superradiant emission in D<sub>2</sub>O and CH<sub>3</sub>F", K.S. Lipton, J.P. Nicholson, Opt. Com., 24, 321 (1978)
- [29] "Assignment of laser lines in optically pumped CH<sub>3</sub>OH", J.O. Henningsen, IEEE J. Quant. Electr., QE-13, 435, (1977).
- [30] R.J. Temkin, IEEE J. Quant. Electr., QE-13, 450, (1977).

- [31] "Heterodyne measurements of infrared absorption frequencies in D<sub>2</sub>O", T.L. Worchesky, K.J. Ritter, J.P. Sattler, W.A. Riessler, *Opt. Let.*, 2, 70 (1978).
- [32] "Optical pumping and tunable laser spectroscopy of the  $\nu_2$  band of D<sub>2</sub>O", F. Keilmann, R.L. Sheffield, J.R.R. Leite, M.S. Feld, A. Jackson, *Appl. Phys. Let.*, 26, 19 (1975).
- [33] "Forward stimulated raman scattering (385 $\mu$ m) in a D<sub>2</sub>O laser", G.F.D. Levy, *Opt. Com.*, 38, 143 (1981).
- [34] "Laser-pumped molecular lasers - Part II: Submillimeter laser experiments", Z. Drozdowicz, R.J. Temkin, B. Lax, *IEEE J. Quant. Electr.*, QE-15, 865 (1979).
- [35] "Parametric study of an optically pumped far infrared oscillator", M.R. Siegrist, M.R. Green, P.D. Morgan, I. Kjelberg, R.L. Watterson, *J. Appl. Phys.*, 51, 3531 (1980).
- [36] "Principles of quantum electronics", F. Marcuse, Academic Press, (1980).
- [37] "Laser Physics", M. Sargent, M.O. Scully and W.E. Lamb, Addison Wesley, (1974).
- [38] "A high power D<sub>2</sub>O laser optimized for microsecond pulse duration", R. Behn, I. Kjelberg, P.D. Morgan, T. Okada, M.R. Siegrist, *J. Appl. Phys.*, 56, 2995 (1983).
- [39] "385  $\mu$ m D<sub>2</sub>O laser linewidth measurements to -60 dB", P. Woskoboinikow, W.J. Mulligan, R. Erickson, *IEEE J. Quant. Electr.*, QE-19, 4 (1983).
- [40] "A high energy D<sub>2</sub>O submillimeter laser for plasma diagnostics", A. Semet et al., *Int. J. IR and mm Waves*, 4, 231 (1983).

## CHAPTER 4 .

### THE FAR INFRARED OPTICS ON TCA.

In this chapter we will discuss all FIR optics used between the D<sub>2</sub>O laser and the detection system. It includes the focusing optics guiding the FIR beam inside the tokamak vacuum vessel and the optics to collect the scattered signal and to adapt the beam size to the required waist for the detection system. We also justify the choice of the beam dump absorbing the laser beam after its passage through the plasma and the viewing dump which reduces the amount of stray radiation sent to the detector. Finally, there is a short description of the vacuum flanges and the quartz windows on the tokamak and the D<sub>2</sub>O laser.

For the design of a transport system involving several mirrors, apertures, and focusing elements one has to be able to compute the beam propagation. In the FIR spectral region, where wavelengths are typically three orders of magnitude larger than those of visible light, beam diffraction effects are important and difficult to avoid. Gaussian beam propagation is applicable as long as the radial Gaussian beam profile can be maintained along the whole beam path [1,2,3]. To keep the cost of the large mirrors required (of the order of 200 mm in diameter) within limits, their diameter will not usually be much larger than the beam diameter, and they will, therefore, always clip a fraction of the beam, introducing diffraction effects [1].

For the following discussion "beam diameter" and "beam waist radius" always refer to the  $e^{-2}$  intensity points. For a Gaussian beam, an aperture of a diameter of three Gaussian radii will transmit 99% of the total intensity and produces negligible diffraction losses.

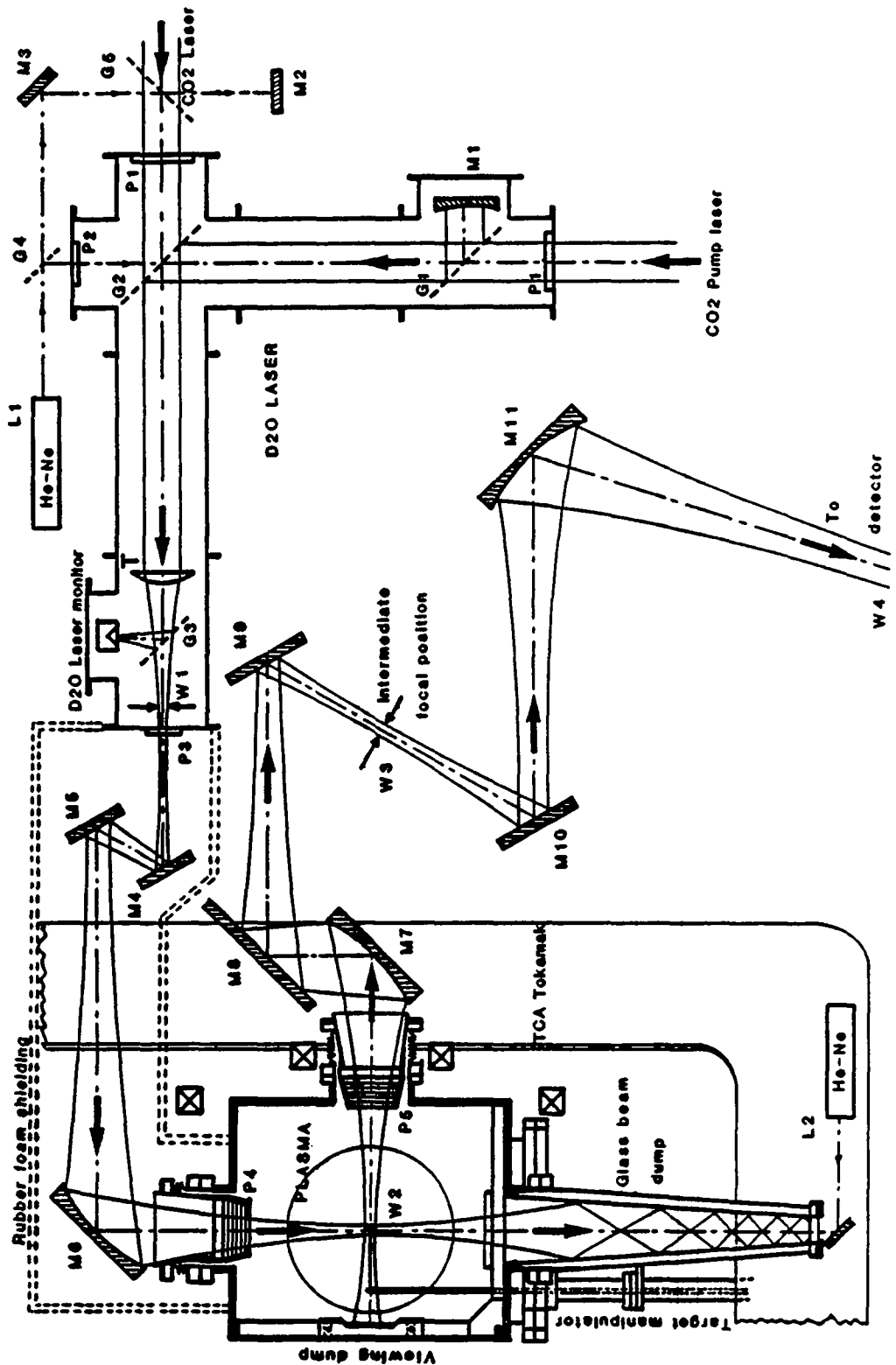


FIGURE 4.1. The FIR optics on TCA, including the D2O laser. The laser cavity length is 4 m, the optical path from the D2O laser to TCA is 2 m and the path length from TCA to the detector is 11 m.



Mirrors: (Al on glass if not otherwise specified)

- M1 spherical, 27 m radius of curvature, 250 mm in diameter.
- M2, M3, M4, M5, M8, M9 and
- M10 all flat steering mirrors.
- M6 90° off-axis elliptical brass mirrors (see figure 4.8).
- M7 as for M6.
- M11 75° off-axis elliptical brass mirror (see figure 4.8).
- T TPX lens (plano-concave) of 750 mm focal length and 70 mm diameter.

Vacuum windows:

- P1 KCl, 120 mm in diameter, for the two CO<sub>2</sub> laser beams.
- P2 quartz for He-Ne alignment laser.
- P3 crystal quartz, etalon cut for maximum transmission at the D<sub>2</sub>O laser Raman frequency (778.58 GHz). 50 mm in diameter, thickness 9.135 mm.
- P4 as for P3, but thickness 14.981 mm, diameter 120 mm. The window is followed by 7 alumina baffles to absorb uncollimated stray light.
- P5 as for P5, but etalon cut for maximum transmission at 779.2 GHz. Thickness 14.992 mm, 120 mm in diameter.

Beam waists: (Gaussian, radius at  $e^{-2}$  of intensity)

- Waist of empty cavity, fundamental mode at T: 34.5 mm.
- W1 waist at focal point after D<sub>2</sub>O laser (see figure 4.3).
- W2 waist in TCA, measured:  $1.25 \pm .1$  mm (see figure 4.5).
- W3 waist of LO at intermediate focus (see figure 4.3).
- W4 waist at optical diplexer (see figure 4.9).
- Burn marks of CO<sub>2</sub> lasers at P1:  $60 \pm 10$  mm in diameter.

Grids and beamsplitters in use:

- G1 10  $\mu$ m tungsten wire grid, with 100  $\mu$ m spacing, clear aperture 150 mm in diameter.
- G2 as for G1, but with 90  $\mu$ m spacing and 125 mm clear aperture.
- G3 Mylar sheet 12  $\mu$ m thick, for D<sub>2</sub>O laser pulse monitoring.
- G4 Mylar pellicle beam splitters for He-Ne laser, removed for normal operation.
- G5 as for G4.

For the purpose of clarity the drawing shows the beam path only in one plane. Half the D<sub>2</sub>O resonator and the beam going to the detector have been turned by 90° around an axis defined by the beams between the ports P1-P3, and the mirrors M10-M11. In reality these two beams go out of the paper.

TABLE 4.1. Components of figure 4.1.

#### 4.1. The constraints for the design of the optical system.

The access on the TCA tokamak for a scattering experiment is limited. Such an experiment needs three large ports allowing the use of optics with an F number up to 3 [4]. On TCA, there is only one set of three ports satisfying this criterion. They permit scattering at angles of  $90 \pm 5^\circ$  at the position of the geometrical center of the vacuum vessel. Fortunately this corresponds within 20 mm to the plasma center. Stable supports for the large optical elements of the FIR beam transport optics are required. These supports must be constructed such that they are not influenced by the pulsed magnetic fields of the tokamak.

The FIR laser has been positioned as close as possible to the TCA tokamak to minimize beam transport losses. For the same reason we use reflecting instead of transmissive optics wherever possible.

All mirrors used for the beam transport (see figure 4.1) are oriented in such a way that the plane defined by the incident and reflected beam is either parallel or perpendicular to the plane of polarization. Only in this case will the linear polarization be conserved through the whole optical system.

Due to the very low scattering cross section, extreme care must be taken to dump the laser beam after the passage through the plasma and to minimize stray light caused by spurious reflections of the incident laser beam. The stainless steel walls of the TCA tokamak vacuum chamber act as good reflectors for the FIR.

#### 4.2. The FIR laser beam profile.

As described in detail in chapter 3, the FIR laser used for the scattering experiment has a stable, 4 m long oscillator cavity (see figure 4.1). For calculations, its beam profile can in a first order approximation be replaced by the profile of the fundamental mode of the empty FIR cavity which has a Gaussian profile with a radial waist of 34.5 mm.

For an optically pumped laser the real beam profile will strongly depend on the shape of the pump beam which, in our case, does not have a Gaussian profile. The radial intensity of the pump beam has not been precisely measured, but qualitatively, based upon examination of burn marks, it appears relatively flat, with a diameter of  $60 \pm 10$  mm (see figure 3-11). A measurement of the  $D_2O$  laser beam profile and beam divergence at the  $D_2O$  laser output coupler has not been performed. However, the FIR laser beam waist at the focal position in the plasma (W2) has been measured (see figure 4.9). From this measurement the beam propagation code presented in §4.3 predicts a radial waist at the output coupler of the laser of 20 mm (see figure 4.2).

#### 4.3. General calculations of the FIR beam size.

Figure 4.1 shows the total beam path including the  $D_2O$  laser. The optical part of the detection system is described in chapter 5, figure 5.4. Wherever possible, the diameter of the optical elements was chosen to be at least three beam waists. The crystal quartz windows on TCA are somewhat smaller than this because of availability.

To take into account diffraction effects we have used a numerical code [1] to give an estimate of the FIR beam size through the system. The numerical code evaluates the Rayleigh Sommerfeld diffraction formula, which mathematically describes the Huygens-Fresnel principle. This equation, written in cylindrical coordinates and assuming axial symmetry gives the radiation field  $U_2$  due to propagation of the beam from a plane where the distribution  $U_1$  is known [1]:

$$U_2(r, z) = \frac{-ik}{z} \exp\left(\frac{ik(r^2 + 2z^2)}{2z}\right) \int_0^R \rho d\rho U_1(\rho, 0) J_0\left(\frac{r\rho k}{z}\right) \exp\left(\frac{ik\rho^2}{2z}\right) \quad (4.1)$$

where

- $U_2$  is the field distribution of interest,
- $r$  is the radial position of  $U_2$ ,

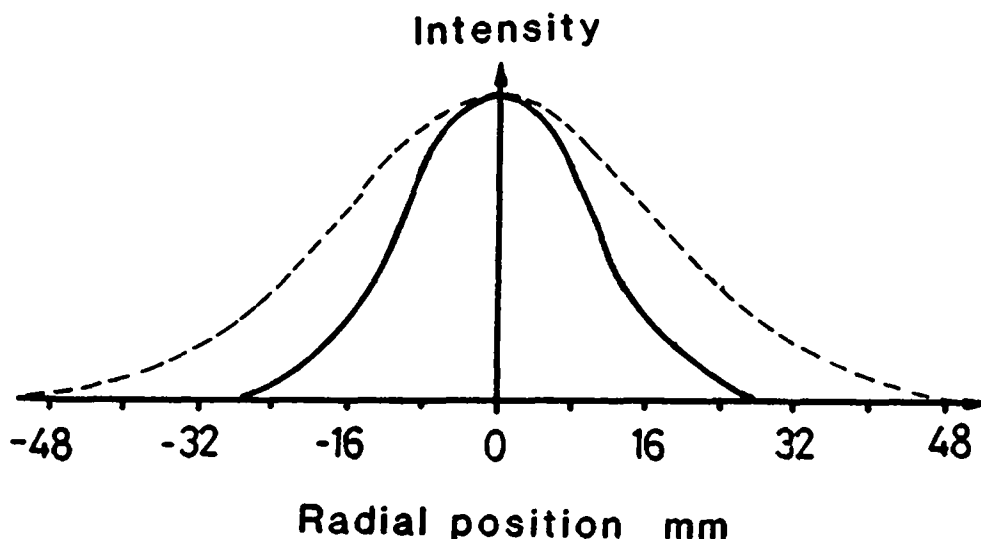


FIGURE 4.2. Calculated beam waist at the output coupler of the D<sub>2</sub>O resonator (position T in figure 4.1). The dashed line is the empty FIR cavity mode of 34.5 mm radial beam waist, and the solid line (radial waist 20 mm) is obtained by propagating the beam profile measured at position W2.

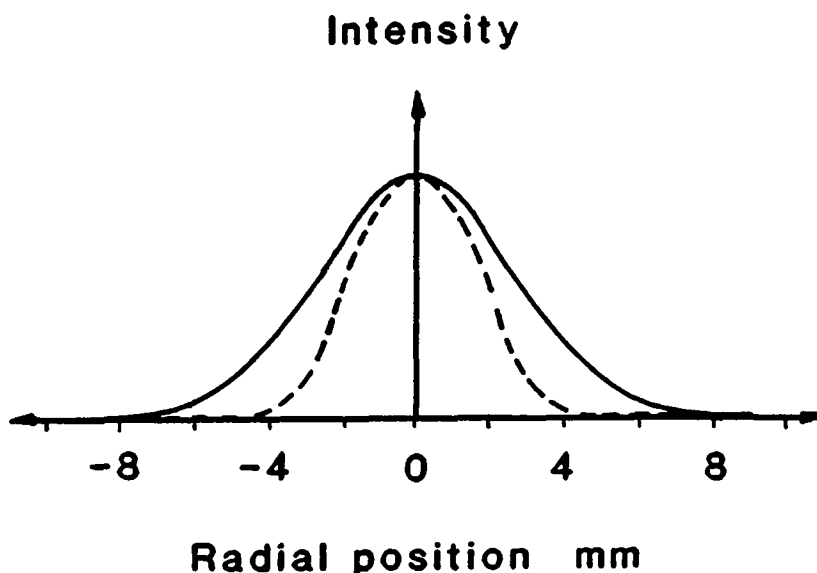


FIGURE 4.3. Calculated beam waists at the intermediate focal position W1. Mirrors M6 and M7 are the same so these waists should also correspond to position W3. The dashed line (radial waist 3.1 mm) is obtained from the propagation of the empty FIR cavity mode and the solid line (radial waist 5.1 mm) is obtained from the propagation of the measured beam profile at position W2.

$z$  is the axial distance from the previous field  $U_1$ ,  
 $k$  is the wave vector,  
 $R$  is the total radial extent of the field  $U_1$ ,  
 $U_1$  is the previous field distribution,  
 $\rho$  is the radial position at the previous field,  
 $J_0$  is the first order Bessel function.

The calculation can only be performed if we know the phase and intensity distribution somewhere in our optical system. We have done two calculations. - Firstly by assuming that the  $D_2O$  laser beam corresponds to a fundamental mode of the empty  $D_2O$  resonator (see §4.2). - Secondly we have used the data obtained by a numerical least square fit to the intensity profile measured at the focal position W2 in the plasma assuming a constant phase (see §4.7). These calculations are illustrated in figures 4.2 to 4.5.

Figure 4.2 shows the profile at the output coupler of the FIR laser (position T). The profile obtained by propagating the measured beam profile of position W2 has a radial waist of one third of the pump beam diameter measured from burn marks.

Figure 4.3 shows the beam waists at the intermediate focus W1. Since the focusing mirror M6 and the collecting mirror M11 are the same these profiles should also be valid for the intermediate focal position W3. A diaphragm is positioned at W1 to act as a spatial filter, see §4.4.

Figure 4.4 shows the beam waist at the focusing mirror M6. The beam profile obtained from propagating the empty cavity mode is clearly clipped by the edge of the mirror M11 (clear aperture 200 mm). The vacuum window on the tokamak will further aperture this beam, see §4.8.

Finally, figure 4.5 shows the beam waists at the focal position in the plasma (W2). The propagated cavity mode is 70% smaller than the measured beam (figure 4.9). The cavity mode is, however, subjected to higher losses which do not appear on these normalized curves.

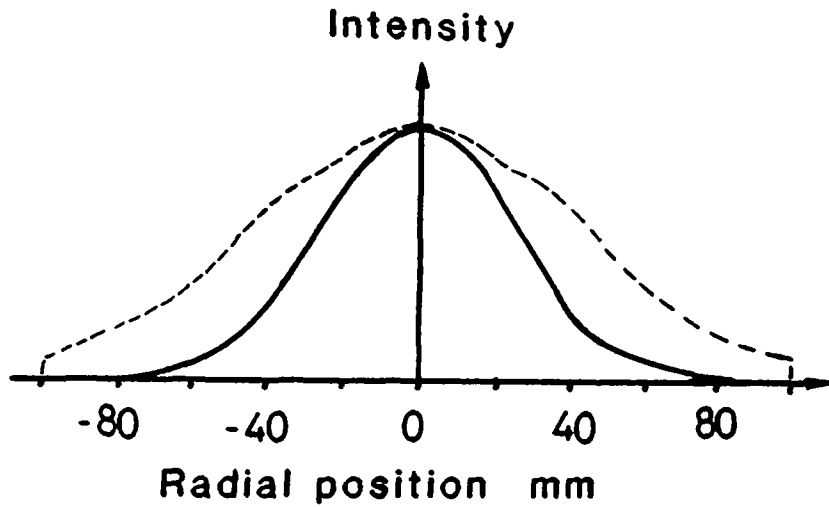


Figure 4.4. Beam size at the position of the mirror M6. The dashed line (beam radius 91.5 mm) is obtained from the propagation of the empty FIR cavity mode and the solid line (beam radius 48.1 mm) is obtained from the propagation of the measured beam profile at position W2.

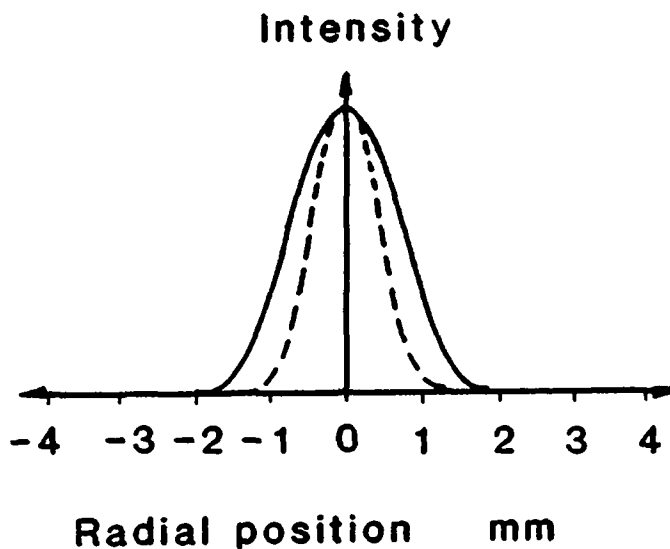


Figure 4.5. Beam waists at the position of the focal spot W2. The dashed line (radial waist 0.95 mm) is obtained from the propagation of the empty FIR cavity mode and the solid line (radial waist 1.35 mm) is the measured beam profile at position W2, see figure 4.9.

#### 4.4. The spatial filter and the laser vacuum window.

The choice of an output window material for the  $D_2O$  laser necessarily involves balancing the high cost, difficulty of supply and high surface reflectance of crystalline materials (quartz, sapphire) [4 to 6] against the high losses and possible fragility of plastics (Teflon, TPX, Mylar) [7,8]. Table 4.2 lists a set of optical constants for various materials measured in the laboratory or taken from the literature [5-16].

We finally chose Z-cut crystal quartz windows. To minimize the surface reflections the thickness of the quartz has been matched to act as etalon with maximum transmission for the  $D_2O$  laser Raman emission (778.58 GHz), and to minimize absorption losses the laser window is kept small and thin by focusing the FIR beam just in front of the window (100 mm). The focal spot is kept in the (relative) vacuum to avoid an air breakdown, which occurs frequently at the power levels of the FIR laser.

Figure 4.6 shows the transmission curve of the  $D_2O$  laser output window (bold line), and the beam profiles calculated from the empty cavity mode of the FIR laser (dashed line) and from the measured waist in the TCA vacuum chamber. The etalon transmission is shown versus the radial position along the window. To calculate the transmission we assume that the beam at a radial position  $r$  has an incident angle given by  $\theta = \tan^{-1}(r/z_m)$  where  $z_m$  is the distance from the waist to the window (see figure 4.7).

With an intermediate focus we also have the possibility of spatial filtering to reduce side-lobes at the focal position W2, which defines the scattering volume. It will further reduce the amount of stray light missing the beam dump, see §4.9. An aperture with external adjustment of diameter, horizontal and vertical position is mounted at the focal spot W1. The diameter of the aperture is generally set to 15 mm which corresponds to three expected beam waists (see figure 4.3).

OPTICAL CONSTANTS AT  $\lambda = 385 \pm 15 \mu\text{m}$ .

<u>Material:</u>	<u>Surface reflectivity</u>	<u>Index of refraction</u>	<u>Absorption <math>\text{cm}^{-1}</math></u>	<u>Measured Refl. normal incidence</u>	<u>Measured Abs. <math>\text{cm}^{-1}</math></u>
Graphite	79%	(17)	--	75±5 %	--
Macor	14%	(2.2)	4	20±5 %	>5
Pyrex glass	7%	(1.7)	>13	--	--
"Window glass" <sup>*</sup>	18%	(2.5)	--	23±5 %	>10
Fused Quartz	(3-14%)	1.4-2.2	2	--	--
Crystal Quartz	(13%)	2.1076°/2.1561 <sup>1</sup>	0.1	(12.70%)°	--
Alumina	(27%)	3.2	0.9	25±3%, 31±5% <sup>2</sup> , 37±5% <sup>3</sup>	~ 1
Polyethylene	(4%)	1.5	1.4	--	--
TPX	(3%)	1.45	--	--	0.2-0.4
Mylar	(7%)	1.7	13	--	~ 17
Plexiglass	(7%)	1.7	5.5	--	--

Values in ( ) are calculated from the relation:  $R = ((n-1)/(n+1))^2$

\* Depends on quality.

° For the ordinary ray.

<sup>1</sup> For the extraordinary ray.

<sup>2</sup> Alumina lightly metallized by sputtering from the TCA plasma.

<sup>3</sup> Alumina highly metallized by sputtering from the TCA plasma.

TABLE 4.1. Optical constants at 385  $\mu\text{m}$  taken from the literature [5 to 16] and values measured at the CRPP.



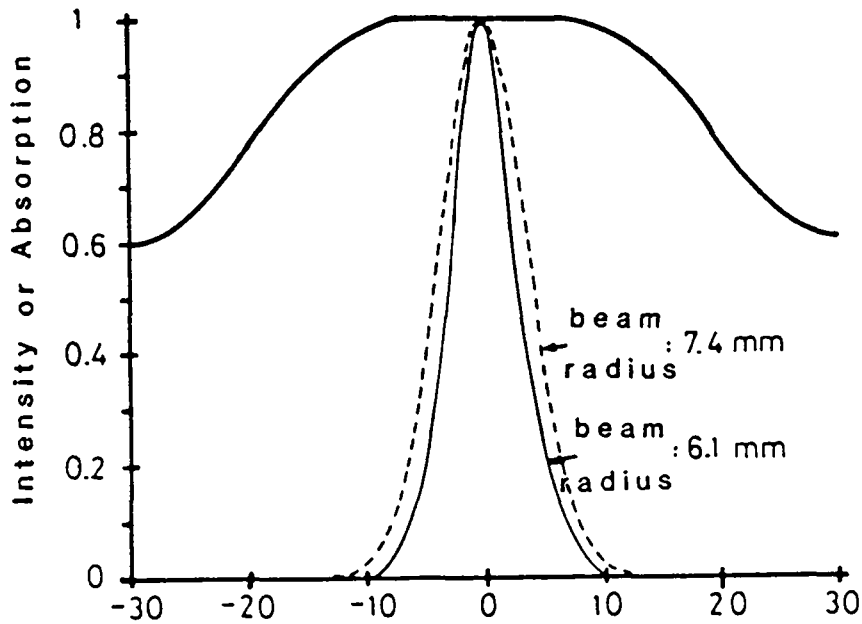


FIGURE 4.6. Transmission of the D<sub>2</sub>O laser window (bold line) with the calculated Gaussian beam radius from the propagation of the measured waist at position W<sub>2</sub> (solid line), and from the empty D<sub>2</sub>O laser cavity mode (dashed line).

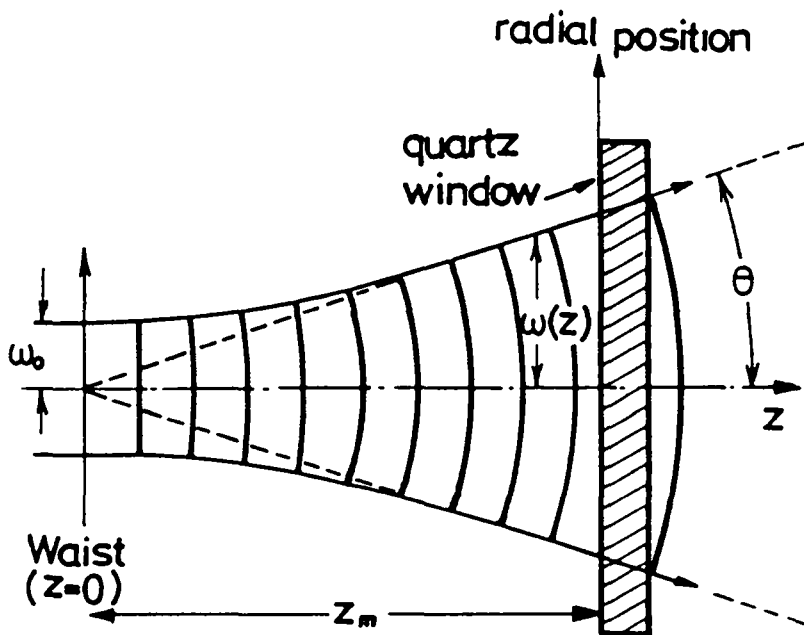


FIGURE 4.7. Sketch of a Gaussian beam propagating through a window. The beam hitting the window at the radial position  $r$  is considered to have an incident angle  $\theta$  given by the ratio  $\tan^{-1}(r/z_m)$ .

#### 4.5. The beam transport to the first focusing mirror.

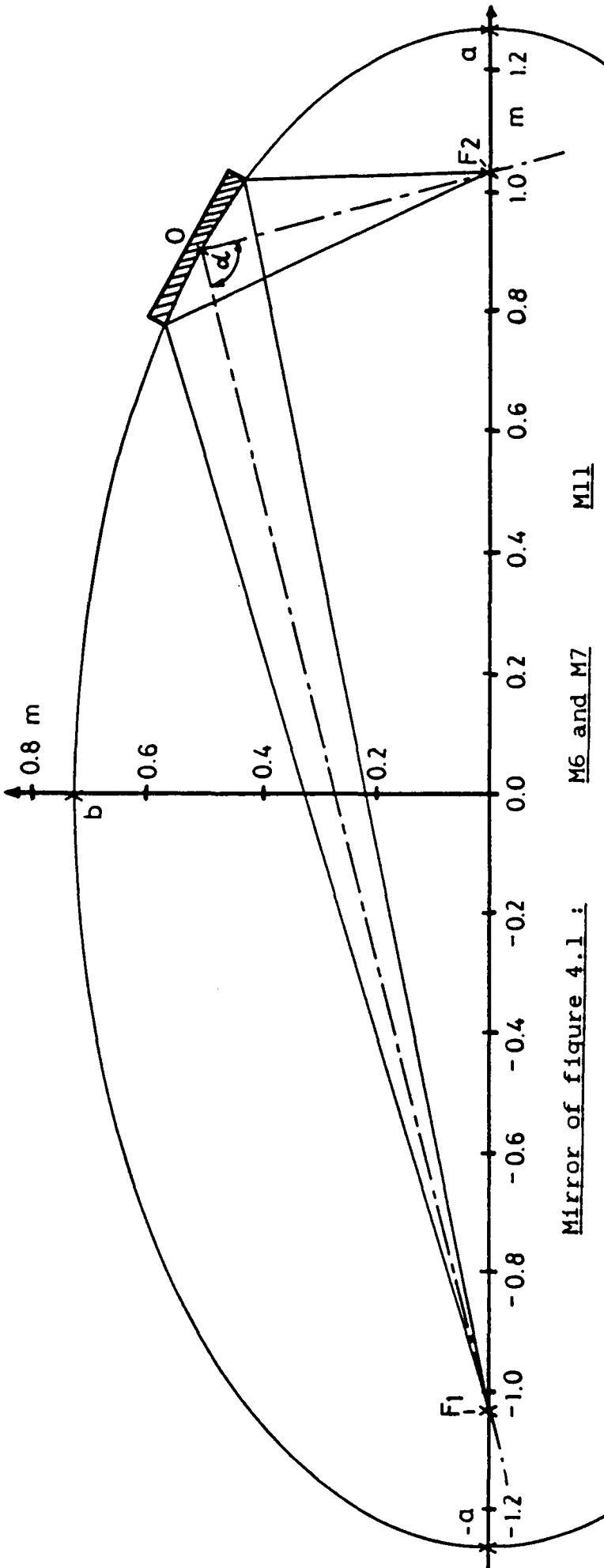
The FIR beam emerging from the laser window P3 is reflected off two flat, aluminium on glass mirrors. The tilt and the distance between the mirrors can be adjusted, providing all three degrees of freedom required to adapt the beam direction and path length to the next focusing element.

We have observed that for the  $D_2O$  transition at 385  $\mu m$ , the absorption in the atmosphere can be neglected for the distances considered here. Stray light scattered from dust particles in the air and on the mirrors gives, however, signals strong enough to saturate the detector situated 10 m away. For this reason the whole passage from the FIR laser to the window on the TCA tokamak is enclosed in 100 mm thick polyether foam (see figure 4.1). This assures more than 60 dB attenuation for this source of parasitic light, hence reduces it to an acceptable level.

#### 4.6. The ellipsoidal mirrors.

Because of the limited available space, we had to use an off-axis imaging mirror. Spherical mirrors were disregarded because they would cause unacceptable aberrations. We have chosen a  $90^\circ$  off-axis elliptical mirror which makes use of the intermediate focus W1 at the output of the FIR laser. We use mirrors with the same optical characteristics for the focusing and collecting optics. This symmetric arrangement assures that the scattering volume defined by the incident beam profile at W2 is matched to the volume observed by the detection system. The requirements of the antenna theorem (see §5.1) are also fulfilled with this arrangement, ensuring optimal performance of the heterodyne detection system.

An ellipsoid has the geometrical property that the sum of the distances from the two focal points is constant for any point on its surface [2]. By varying the beam waist, hence



Mirror of figure 4.1.1 :

	M6 and M7	M11
Focusing distance 1	OF = 2.000 m	7.000 m
Focusing distance 2	OF <sup>1</sup> = 0.530 m	2.000 m
Equivalent focal length	f <sup>2</sup> = 0.419 m	1.560 m
Off-axis angle	alpha = 90.0 °	75.0 °
Image magnification	= 0.265	3.5
Equivalent F number 1	= 8.6	28.5
Equivalent F number 2	= 2.3	8.1
Mirror diameter	= 0.280 m	0.300 m
Mirror thickness	= 0.030 m	0.030 m
Ellipse axis	a = 1.265 m	4.500 m
Ellipse axis	b = 0.728 m	2.968 m
Ellipse focal points	c = 1.034 m	3.382 m

FIGURE 4.8. The off-axis elliptical mirrors.

the beam divergence, of the intermediate focus  $W_1$  we can change the size of the scattering volume. The limiting solid angle is imposed by the tokamak vacuum window diameters (see §4.8). The collected scattered power is proportional to the solid angle which should be kept as large as possible (equation 2.7) [4].

To apply the beam propagation code to the elliptical mirrors, we replace the mirror by an on-axis lens with an equivalent focal length  $f$  given by:

$$1/f = 1/OF_1 + 1/OF_2 \quad (4.2)$$

where  $OF_1$ ,  $OF_2$  are the distances from the elliptical mirror to the respective focal points. All distances are taken positive.

The elliptical mirrors have a focusing distance  $OF_1$  of 530 mm towards the plasma (see figure 4.8) and a focusing distance  $OF_2$  of 2000 mm towards the FIR laser and the detector. Thus the magnification of the elliptical mirrors is 0.265. We can also define an equivalent F number as the ratio of the focusing distance to the effective diameter of the mirror seen from each of the focal points of the ellipse, see figure 4.8. The effective diameter of the mirrors are 280 mm, which is such that the mirrors are not the smallest aperture in the beam path. In a first approximation, the lens positioned at the output coupler of the FIR laser should have a F number corresponding to the equivalent F number 2, which would give a diffraction limited focal spot in the plasma defined by the equivalent F number 1 of the elliptical mirror.

The off-axis mirrors were machined from brass discs with a numerically controlled milling machine. The elliptical shape was approximated by a series of arcs as the computer controlling the milling machine could only perform two dimensional circular interpolations. Three dimensional corrections for the finite size of the milling tool were previously added to the raw data given to the numerical milling machine.

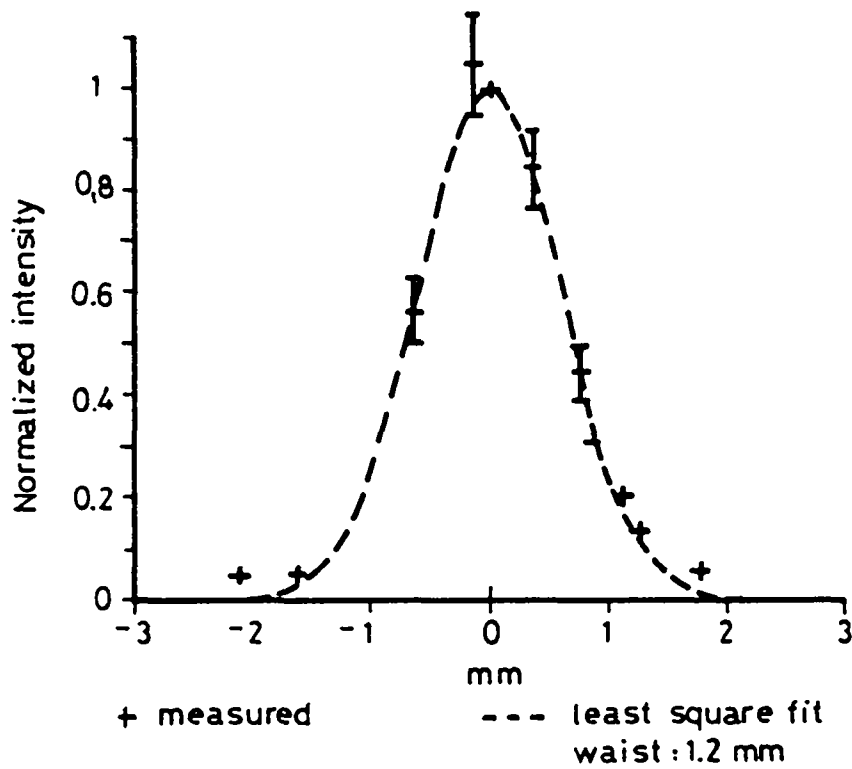


FIGURE 4.9. FIR beam profile at waist W2, measured in the toroidal direction of TCA.

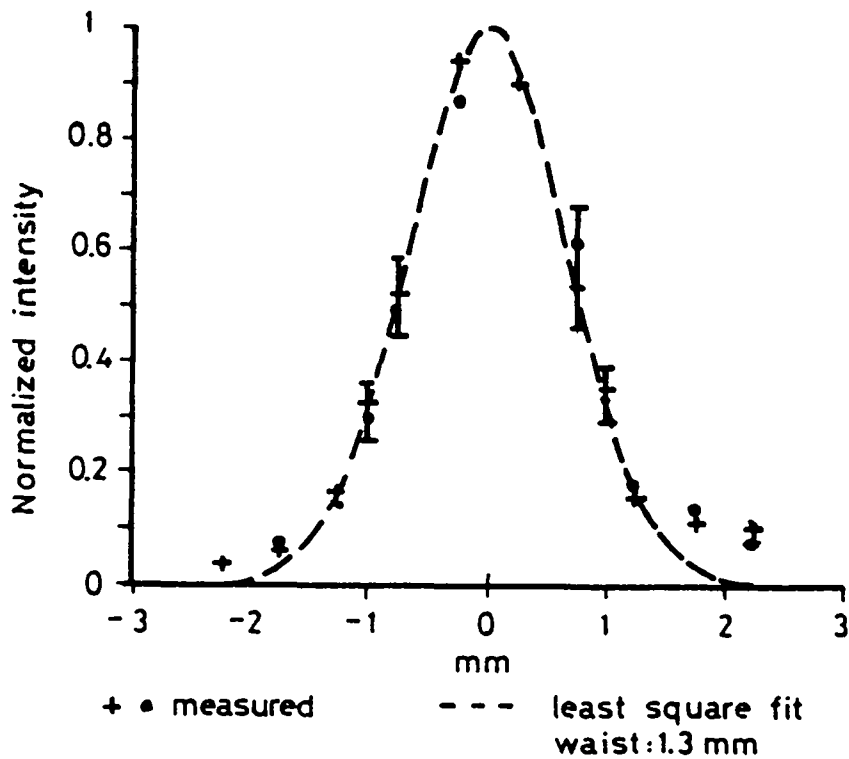


FIGURE 4.10. FIR beam profile at waist W2, measured in the radial direction of TCA.

The reflectance of the clean mirror surface was measured to be above 95% without the need for a gold coating. The surface finish after the milling was better than  $\lambda/40$  at 385  $\mu\text{m}$  which was further improved by polishing the surfaces. The surface finish is not, however, satisfactory for visible light, thus seriously complicating the He-Ne laser alignment procedure.

#### 4.7. Measured FIR beam profile of the scattering volume.

The measurement of the focal spot at the position of the plasma could not be done inside the vacuum vessel. Therefore, the off-axis mirror had to be displaced and the effect of the quartz vacuum window was simulated by an aperture at the correct distance from the mirror.

The profiles were measured by scanning a slit through the focal point in two perpendicular directions. At each position the average of several FIR laser shots was taken. A monitor detector was used to correct the measurements for fluctuations in the laser energy. Care was taken to prevent the formation of air-breakdown on the slit, a phenomenon which can reflect or scatter part of the incident FIR radiation and falsify the measurements. The resulting beam profiles are given in figure 4.9 and 4.10. The dashed curves are the Gaussian beam shapes obtained by a least square fit to the data for normalized intensity above 0.2. The measurement covers a diameter of 3.5 radial waists. No attempts were made to measure possible side lobes outside this distance.

#### 4.8. The TCA tokamak vacuum windows.

Crystal quartz windows were chosen, since they were found to be compatible with the strict requirements of high vacuum on the TCA tokamak.

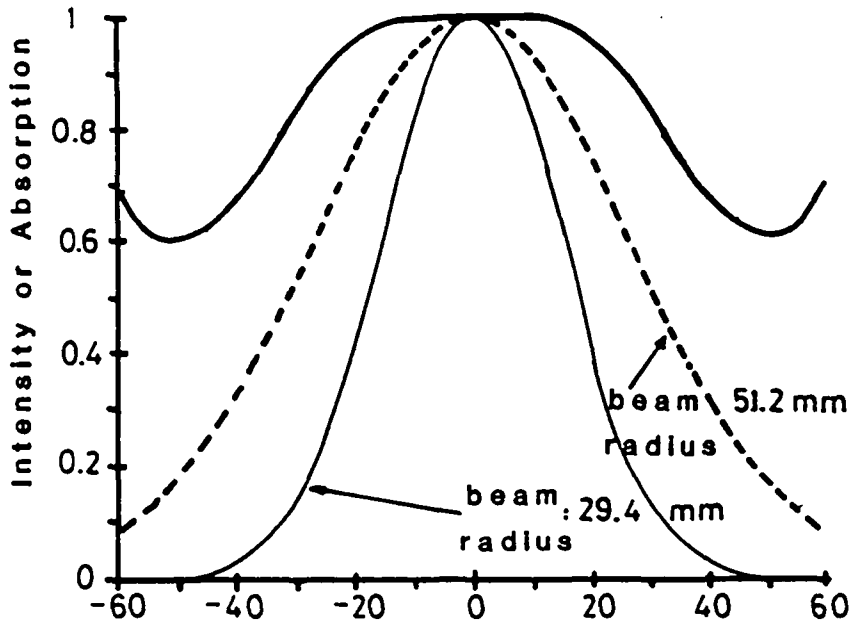


FIGURE 4.11. Transmission of the TCA vacuum window (bold line) obtained as for figure 4.6, with the calculated Gaussian beam radius from the measured waist at the focal position of the tokamak (solid line) and from the empty laser cavity mode (dashed line).

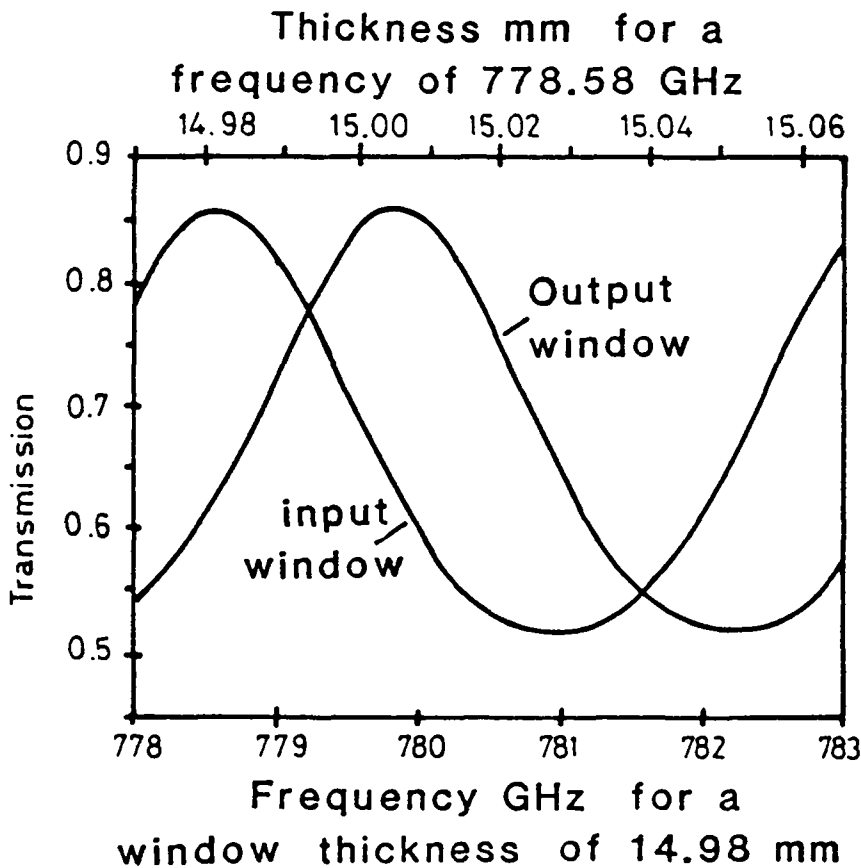


FIGURE 4.12. Transmission of the TCA vacuum windows for normal incidence. Losses from bulk absorption are included. The input window has a thickness of 14.981 mm and a maximum transmission at 778.58 GHz (laser Raman transition) while the output window is optimized for the higher frequency part of the scattered spectrum.

The maximum available window dimension for Z cut crystal quartz was 120 mm in diameter and 15 mm thickness (bought from SPECAC, Great Britain). The thickness was adjusted to minimize elastic deformations, and to act as a maximum transmission etalon for the 385  $\mu\text{m}$  wavelength FIR beam. Figure 4.11 gives the transmission curve for these windows, and figure 4.12 the influence of the etalon on the spectral transmission.

With the aim of obtaining the largest possible solid angle of the focusing beam, the windows were positioned as close as possible to the plasma (120 mm from the plasma edge). The cone which forms part of the window support (see figure 4.13) has been lined with a layer of rubber material to reduce stray light [8]. On the vacuum side, a series of nonporous alumina rings collect most of the diffused stray light. These baffles partially protect the windows from sputtering from the plasma. The alumina rings extend to within 65 mm of the plasma edge (plasma limiter position).

After several months installed in the tokamak, the windows were found to be covered with a deposit sputtered by the plasma. The film was measured to absorb about 20% of the incident FIR energy. Unfortunately, chemical means were not successful in removing the deposit, and the windows needed to be repolished. In the near future, a shutter system will be installed which will protect the windows during the period when the Thomson scattering experiment is not operated.

A sketch of the window support is given in figure 4.13 and a photo of the output window support is given in figure 4.14. The output window support can be tilted by  $\pm 5^\circ$  around a horizontal axis to allow scattering from 25 mm above or below the plasma center. Because of the lack of sufficient scattered power for the feasibility experiment, all measurements were done on axis where the plasma density is the highest.



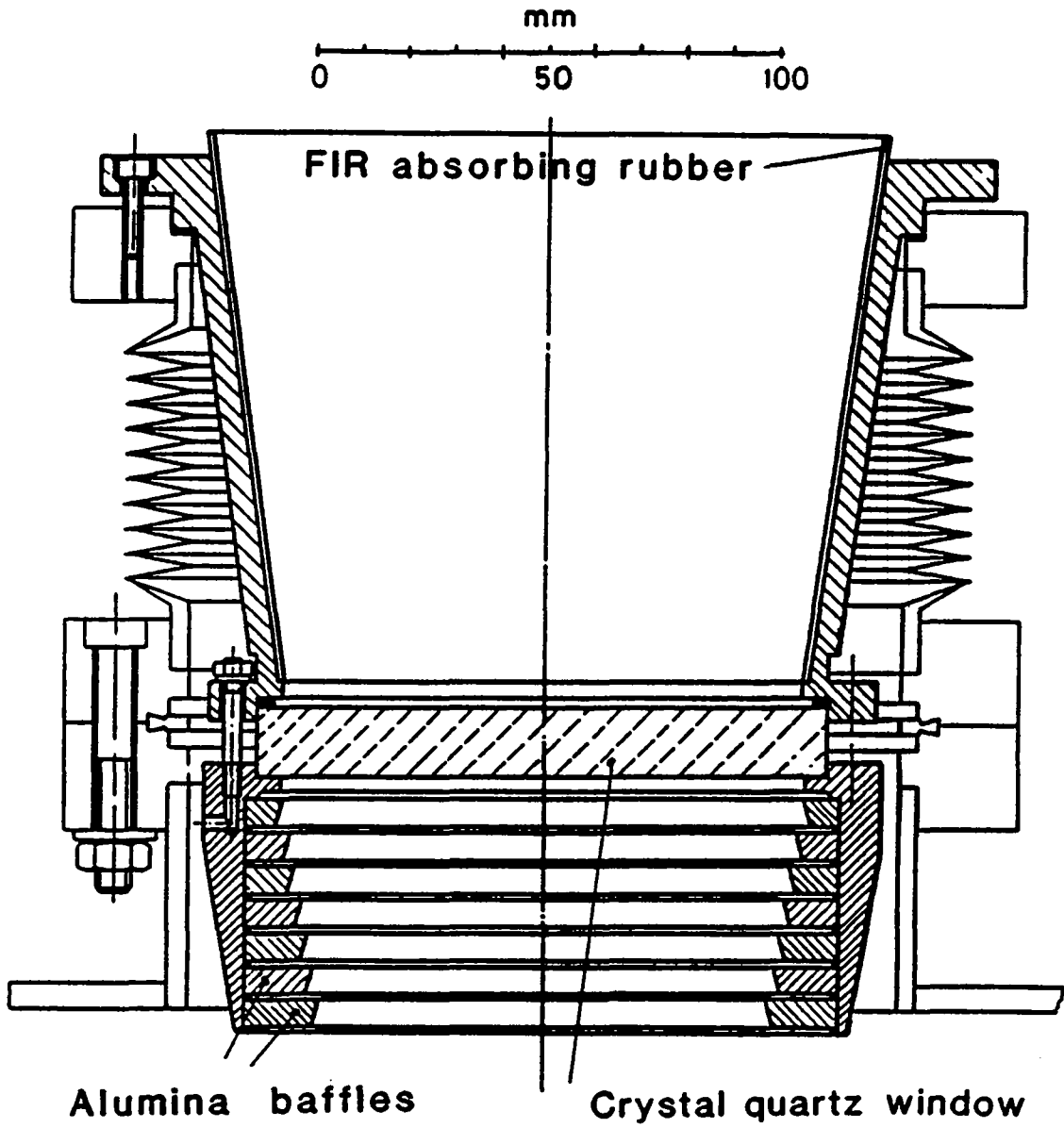


FIGURE 4.13 The quartz window supports on TCA.

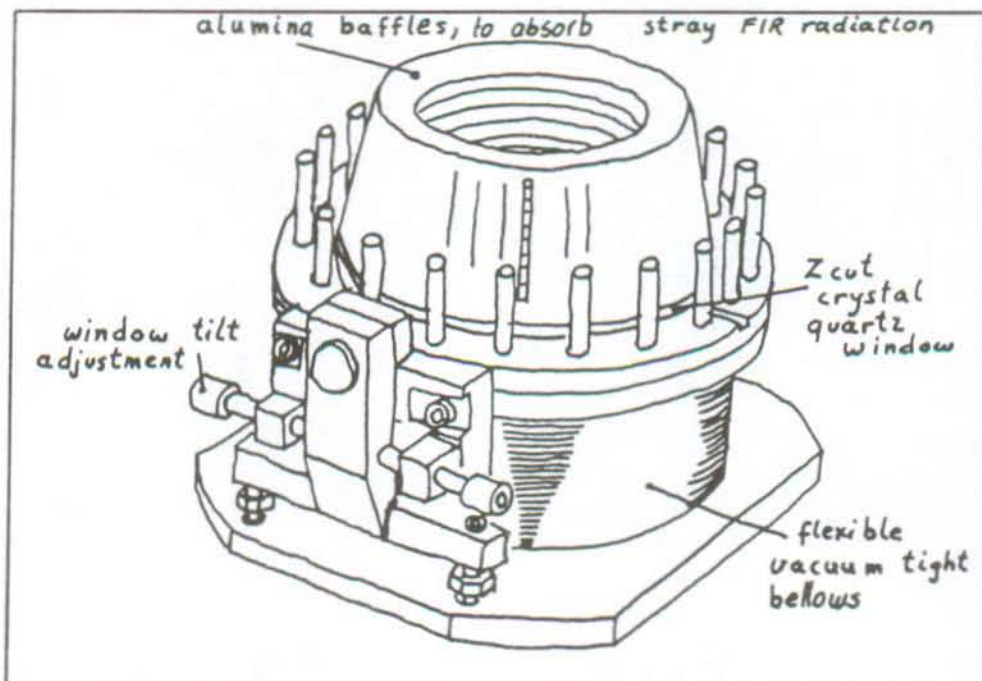
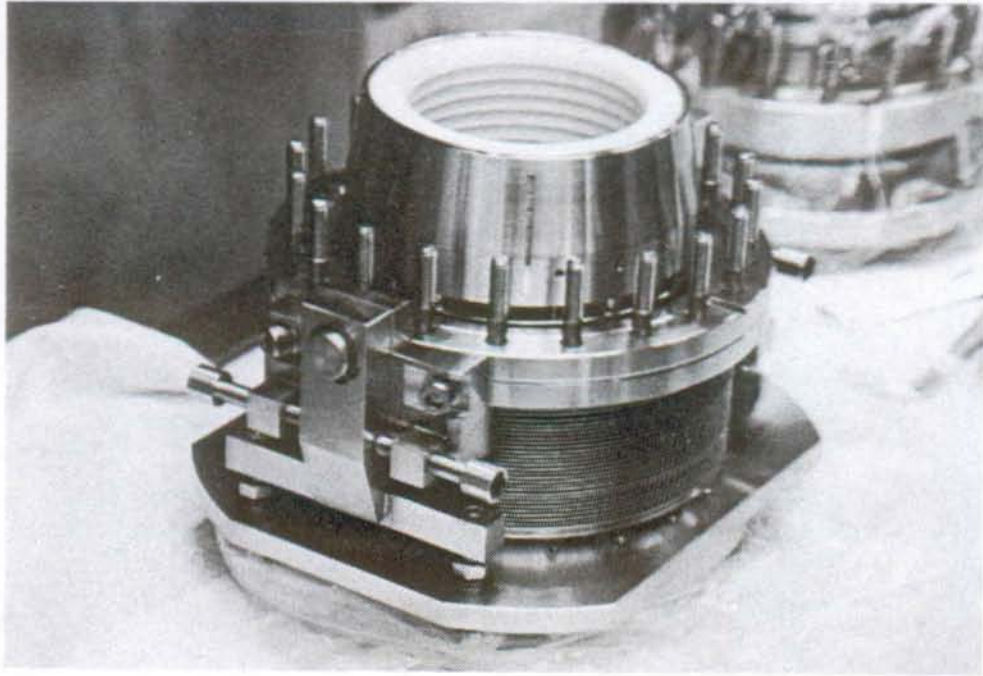


FIGURE 4.14. Photo of the observation window support.

#### 4.9. The beam and viewing dumps.

As stated earlier, the absorption of the unscattered FIR beam leaving the plasma is of great importance due mainly to the efficiency of the scattering process which is less than  $10^{-14}$  (see equation 2.8). On the TCA tokamak we have available a 150 mm diameter vacuum port directly opposite to the FIR beam entry port.

A straight, 1.2 m long Pyrex glass cone [10 to 16] is used to absorb the radiation during multiple reflections. Pyrex glass was chosen because it strongly absorbs FIR radiation and it withstands the thermal cycling of the torus walls. The torus walls are regularly heated to 85° C to enhance the outgassing of the walls and to improve the vacuum on TCA.

The glass cone is extended by a stainless steel annulus to within 40 mm of the plasma limiter edge. The cone opening is 144 mm see figure 4.15. The full cone angle is 5.5°. The average number of reflections made by a ray entering the cone before it exits again can be estimated by the following formula [17]:

$$N = 2 \cdot (90^\circ - \delta) / \alpha \quad (4.3)$$

where  $N$  represents the number of reflections,  $\delta$  the incident beam angle (see figure 4.16) and  $\alpha$  the full cone angle.

This result can also be obtained geometrically as illustrated in figure 4.16 [17,18]. An incident ray (the bold dotted line) has in figure 4.16 an incident angle equal to the full cone angle  $\alpha$ . The ray is reflected at the point  $a$ , and is sent to the opposite side of the cone to point  $b$  which geometrically has the image point  $b'$ . From the point  $b$  the ray is reflected towards  $c$ ,  $d$  and finally exits the cone at point  $e$ . For each reflection the incident angle of the ray increases by the full cone angle  $\alpha$ . Incident rays with 1 to 6 reflections are shown in figure 4.16.

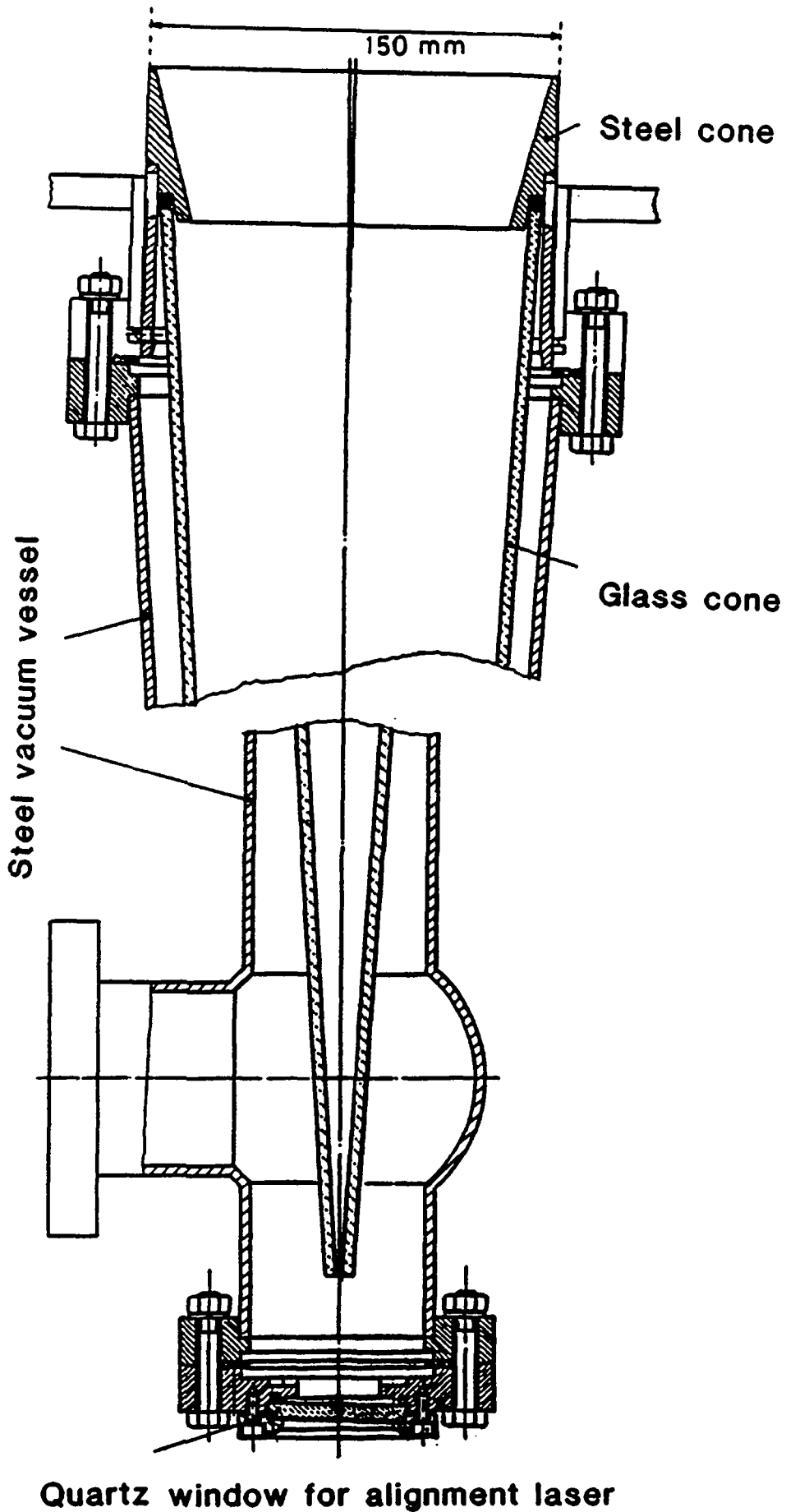


FIGURE 4.15. The 1.2 m long pyrex glass cone beam dump.

In our case, the full cone angle is  $5.5^\circ$ , hence for a  $5^\circ$  incident angle beam, there will be a mean of 30 reflections against the pyrex glass, and even more for a ray of skewed incidence [17,18].

Pyrex glass has an index of refraction of the order of 2 and an absorption greater than  $10 \text{ cm}^{-1}$  at  $385 \mu\text{m}$  wavelength (see table 4.1). The wall thickness of the glass cone is 10 mm, thus absorbing all the radiation which is not reflected at the surface. We can estimate the beam losses by multiplying the surface reflectances at the different incident angles.

The reflectance of an incident ray at angle  $\delta$ , polarized with its electric vector perpendicular to the plane of incidence (worst case) is calculated by the Fresnel equation [19]:

$$R_{\perp} = \left\{ \frac{n \cos(\delta) - \sqrt{1-n^2 \sin^2 \delta}}{n \cos(\delta) + \sqrt{1-n^2 \sin^2 \delta}} \right\}^2 \quad (4.4)$$

where

$R_{\perp}$  is the intensity reflectance,

$\delta$  is the incident beam angle,

$n$  is the relative index of refraction of glass.

This finally gives a total attenuation factor of more than  $10^{-20}$  (-200 dB). From this estimation it is clear that the light which misses the glass cone is the principal source of stray light. Assuming a Gaussian beam emerging from position W2, the fraction of the intensity outside the area covered by the beam dump would be about  $7 \cdot 10^{-9}$  (-82 dB). The beam waist W2 is 1.3 mm and is situated 220 mm from the entrance of the glass cone, see figure 4.19.

The tip of the glass cone is cut so that there is a hole of approximately 2 mm in diameter, see figure 4.15. This hole allows us to send a He-Ne laser beam through the bottom of the dump (see figure 4.1) to simplify the alignment procedure for the scattering experiment.

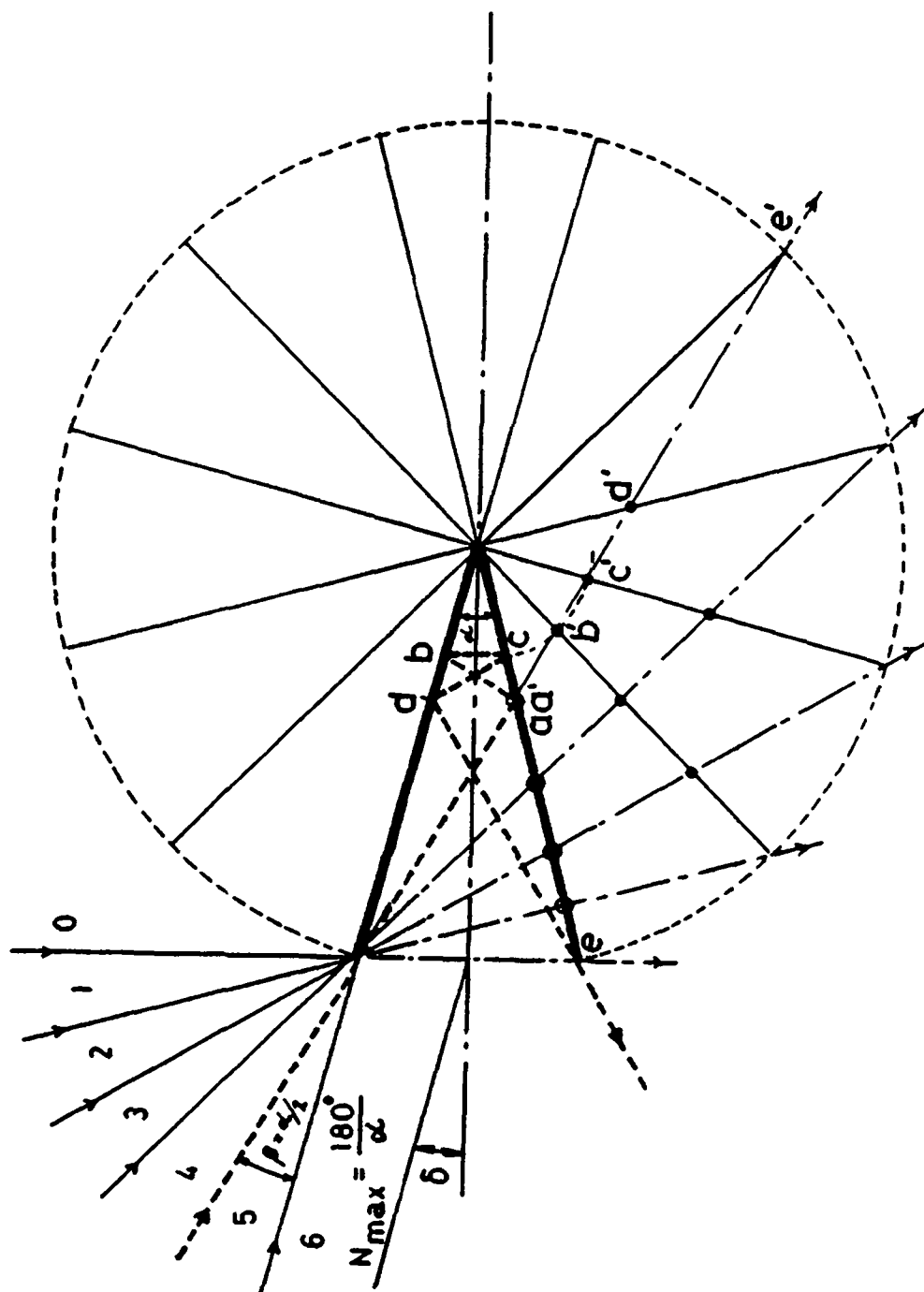


FIGURE 4.16. Ray tracing for a cone absorber. Depending on the incident ray angle, the mean number of reflections from the cone surface will decrease as shown [18].

The pyrex cone is surrounded by a stainless steel tube and is inside the evacuated volume of the TCA vessel. In this way there is no need for an exit window, see figure 4.15.

The choice of material for the viewing dump was more critical than for the beam dump since the plasma edge is situated only 34 mm from the inner vacuum vessel wall. This does not allow a dump thicker than 20 mm. We use Macor glass ceramic with two carbon "limiters" positioned on each side of the dump (see figure 4.17). These limiters are 12 mm further away from the plasma edge than the regular inner plasma limiter.

The Macor viewing dump has a rectangular shape of 100 by 160 mm. In the surface facing the beam there have been cut 31 V-shaped grooves, 10 mm deep and with a 15° vertex angle in order to decrease the effective reflectivity (see figure 4.18). The grooves are oriented perpendicular to the electric vector of the incident radiation for a maximum of absorption [13-16]. We assume that diffuse reflection from the sharp knife edges is negligible as long as the dimension of the edge is much less than the wavelength of the incident radiation.

The Macor ceramic, at 385  $\mu\text{m}$  wavelength, has a measured surface reflectance of 14% and a bulk absorption of  $4 \text{ cm}^{-1}$  (see table 4.1 and [13 to 16]). The net absorption of the dump is estimated to be better than 60 dB.

For a comparison the surface reflectance of carbon at 385  $\mu\text{m}$  wavelength is 80% which, for a dump machined in the same way as the Macor, gives an absorption of about 12 dB [13,14].

The Macor ceramic was milled without lubricants and with a maximum of care to avoid surface contamination. The machined piece was then baked at 400° C in high vacuum for 6 hours before installation in the tokamak vacuum vessel [15,16]. With these precautions, the out-gassing of the Macor has been measured to be negligible compared to a carbon slab of similar size, and therefore is acceptable for the use in the TCA tokamak vacuum [15,16].

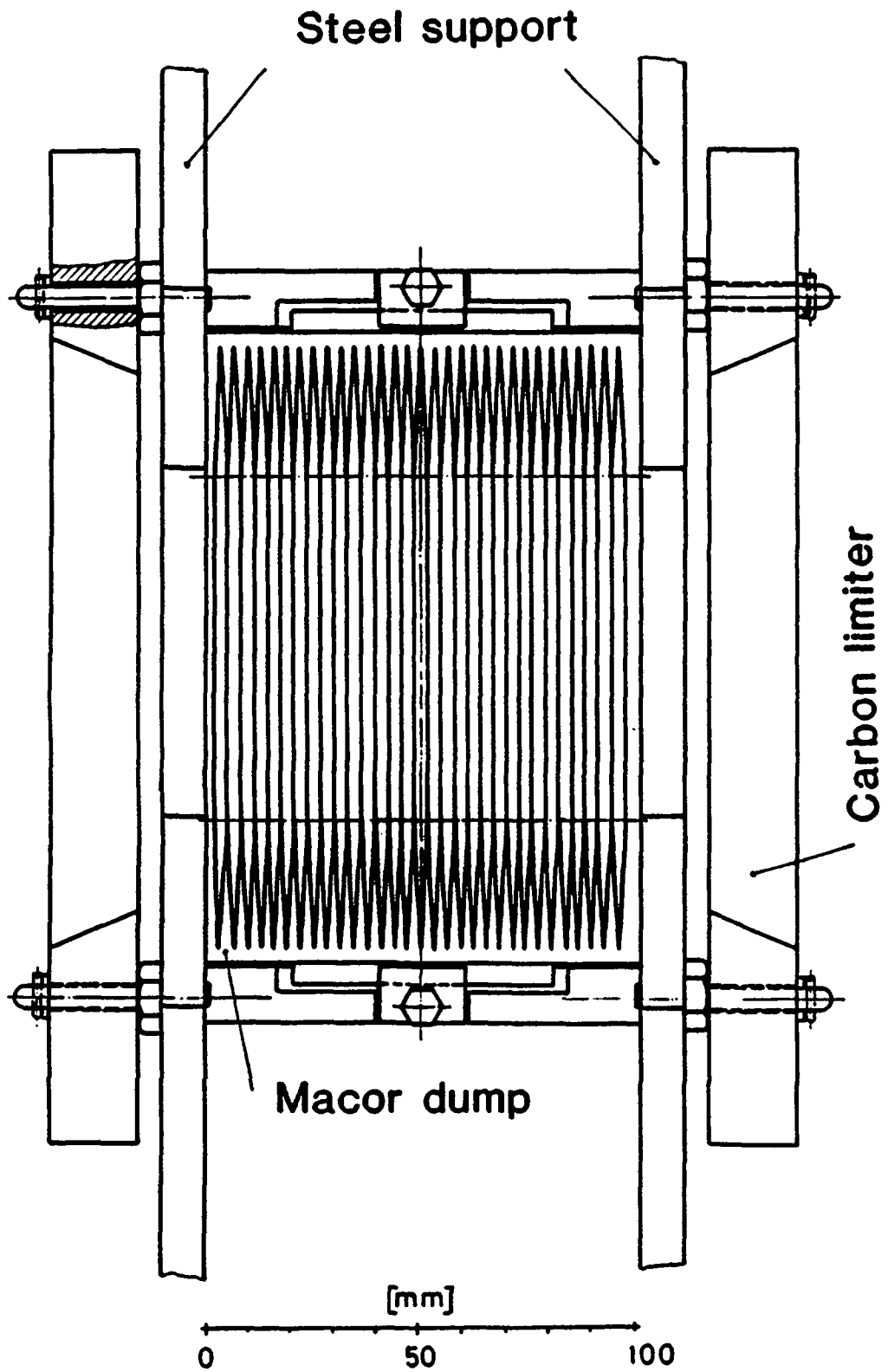


FIGURE 4.17. The viewing dump with its supporting structure and the two carbon limiters.



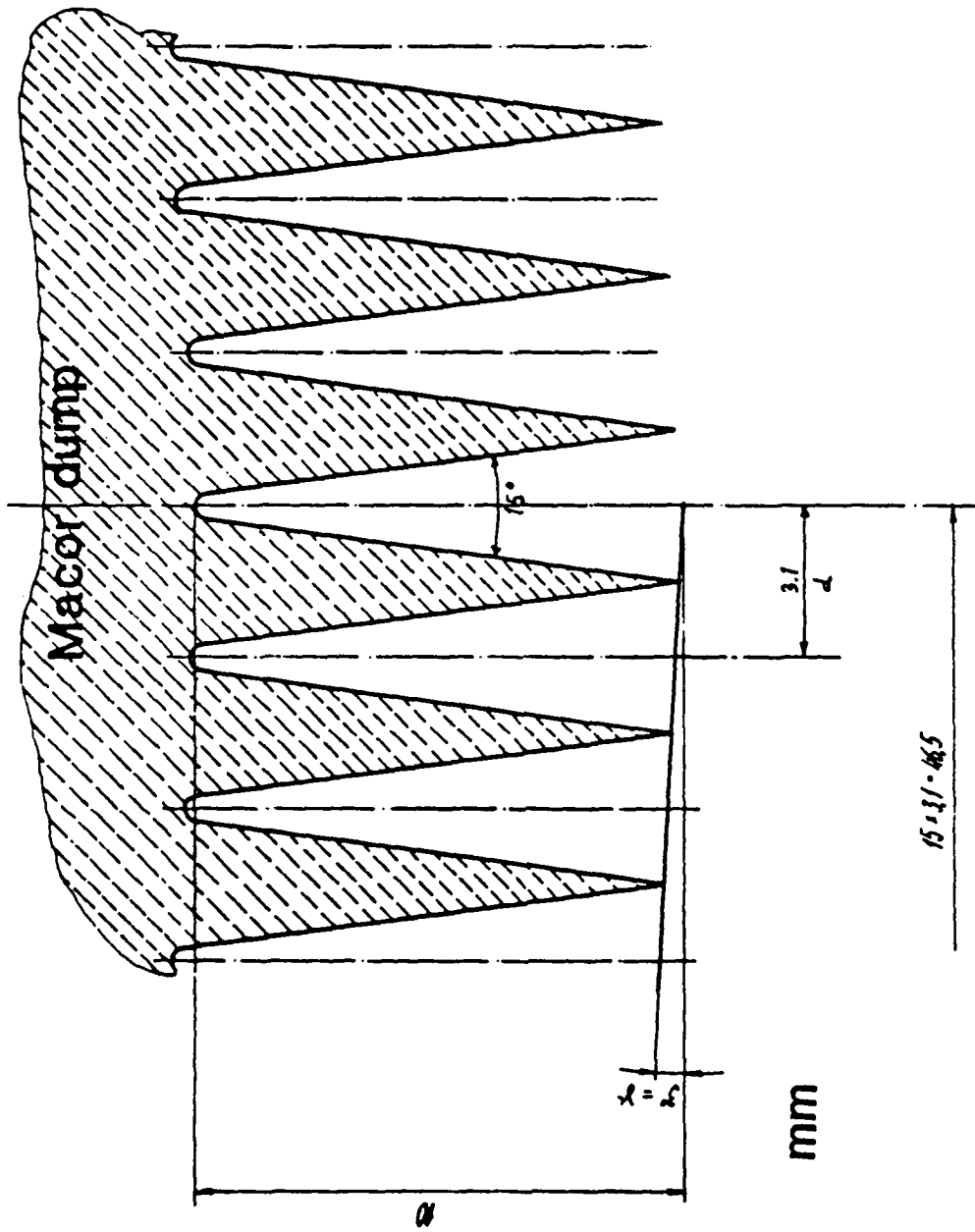


FIGURE 4.18. Detail of cross section of the Macor viewing dump.

During tokamak discharges, the dump quickly gets coated with a thin layer of (presumably) carbon and metals. We have not been able to measure the increase of reflectivity of the dump, but it is replaced at each major opening of the vacuum vessel (roughly each 6 to 8 months).

#### 4.10. The collecting optics.

The scattered radiation collected by the elliptical mirror M7 of figure 4.1 (page 4-2) is sent to the detection system via a set of steering mirrors M8 to M12. The three flat, aluminium on glass steering mirrors M8 to M10, are used to match the axis and focal distances of the elliptical mirror M7 and M11 on the intermediate focal point W3. The optical components on the laser side (M4 to M6) and on the side of observation (M7 to M10) have the same parameters, therefore the dimension of the intermediate images of the scattering volume, and the divergence of the beams are identical. At the focal point W3 has been mounted an aperture set typically to 15 mm diameter to block stray radiation which does not originate from the scattering volume W2.

The off-axis elliptical mirror M11 adapts the image of the scattering volume to the size accepted by the optical diplexer, which forms the front end of the detection system (beam waist W4 of 14 mm). This elliptical mirror has been designed for off-axis imaging at  $75^\circ$  and has a diameter of 0.32 m. The magnification factor is 3.5, seen from the tokamak side (2 and 7 m focal distances, see figure 4.1 and 4.8).

#### 4.11. The removable target.

Whereas for visible wavelengths Rayleigh scattering can be used for alignment purposes, this is not possible in the FIR, a removable mechanical target at the scattering point

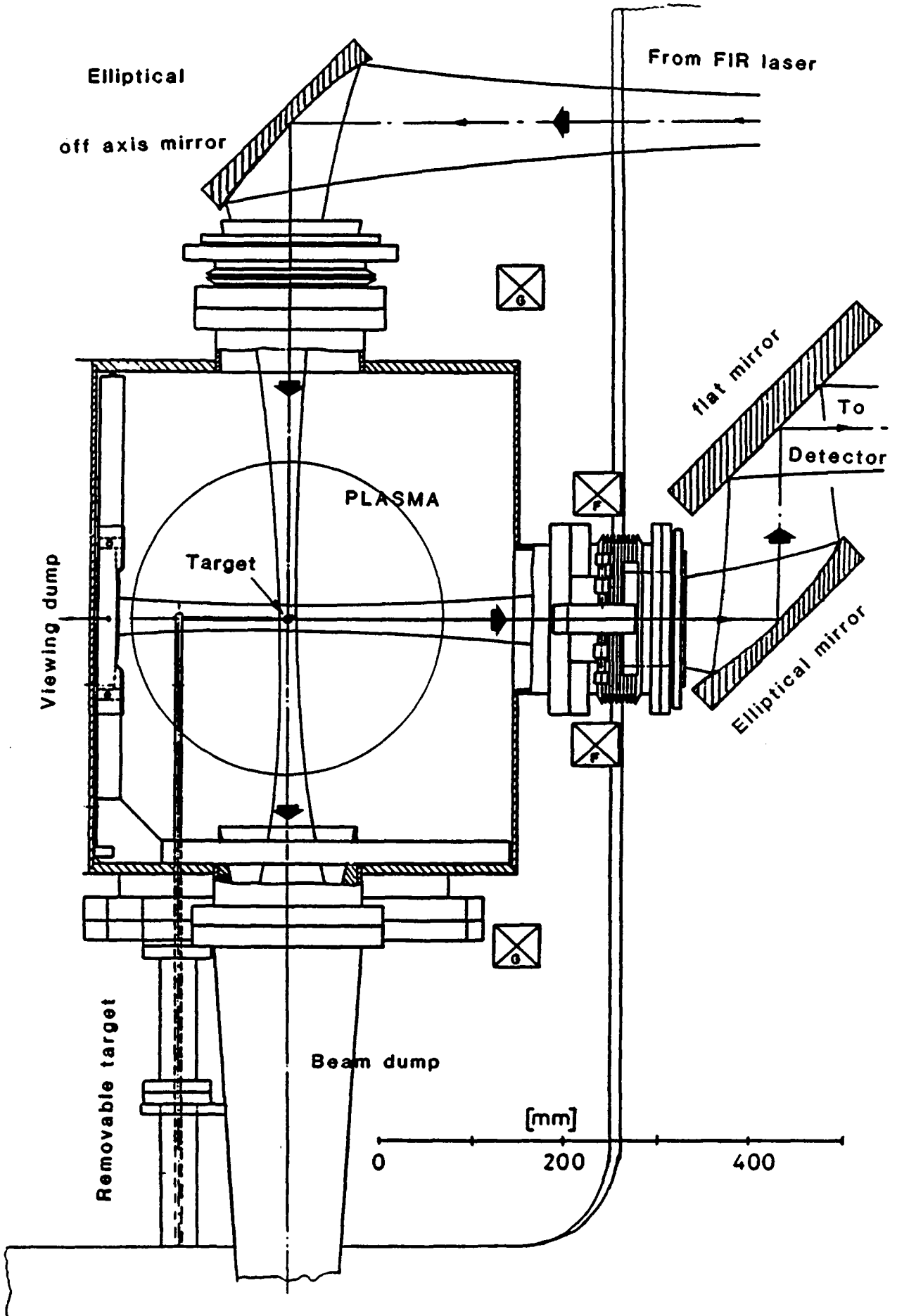


FIGURE 4.19. Cut through the TCA vacuum chamber.

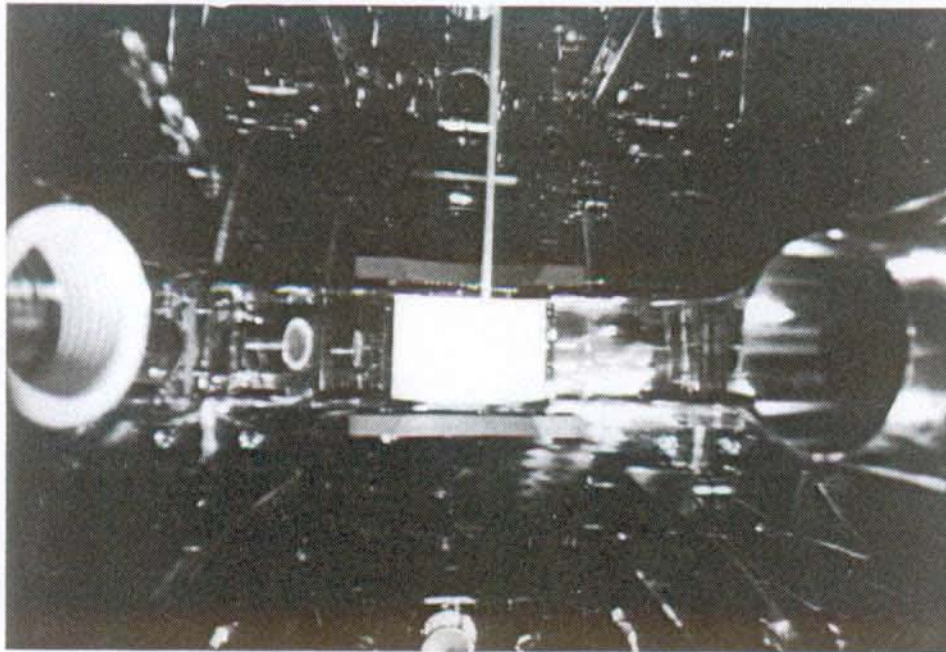
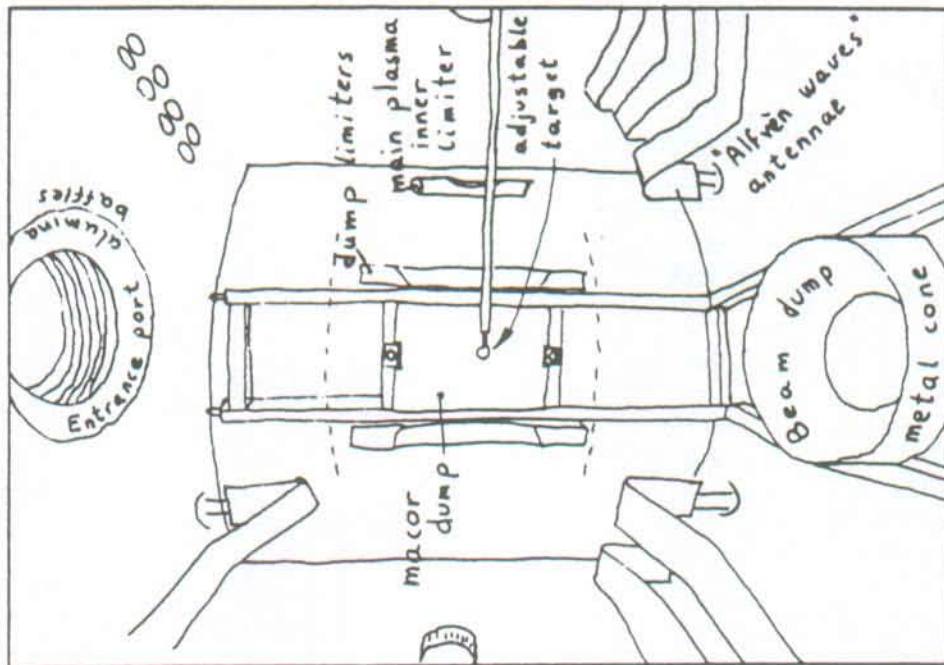


FIGURE 4.20. Photo of the TCA vacuum vessel as seen through the observation window. The target is positioned at the scattering volume.

in the chamber is necessary for the alignment of the optics, see figure 4.19 and 4.20.

We have mounted a double target. Either a metal sphere diffuser of 2 mm in diameter or a 1 cm<sup>2</sup> Macor surface, inclined at 45° with respect to the incident and the scattered beams, can intercept the scattering volume. Both elements are attached to a metallic bar that can be positioned in the vertical plane and can be rotated to intersect the axis defined by the incident laser beam. The manipulator is adjusted from the outside of the vacuum vessel by a magnetic coupling. This method does not require any vacuum feed-through. During tokamak operation the target is retracted and secured at the bottom of the vacuum vessel.

#### 4.12. The alignment procedure.

The alignment procedure of the scattering optics is time consuming but straight-forward. We have noticed that a He-Ne laser beam (L1 in figure 4.1) colinear with the FIR laser axis can be used as a good reference for the FIR beam.

The L-shaped FIR laser has its axis (G5-P3) defined permanently with a He-Ne laser beam. By sending a second He-Ne beam, issued from laser L2, through the beam dump we define the axis of the scattering optics (dump-W2-M6). Then both laser beams have to be made colinear with the flat steering mirrors M4 and M5. The lengths M6-W1 and W1-T are measured and adjusted as required by translating the lens T or mirrors M4 and M5.

A third He-Ne laser (L3 on figure 5.4) defines the axis of the optical diplexer W4 and the mirror M11. This beam is sent backwards to the tokamak. Mirrors M10 to M7 are adjusted so that this beam intercepts the target at W2 in the vacuum vessel. The distances M7-W3 and W3-M11 are measured and adjusted as required by translating mirrors M9 and M10.

The alignment is considered satisfactory when, looking from the position of the detector (W4), we can observe the He-Ne beams from L1 and from L2 scatter off the target.

Because the He-Ne beams are less than 5 mm in diameter, and cover only a small fraction of the surface of the elliptical mirrors, we have used a 200 W incandescent light source positioned at the intermediate focus W3 (also at W1). The light fills the surface of the elliptical mirrors, but does not significantly improve the alignment due to the poor surface quality of the elliptical mirrors for visible light and due to the limited access to observe the target when all mirrors are positioned correctly.

#### 4.13. Measured FIR beam profiles at W3.

The heterodyne detection system is only sensitive to a beam that interferes with the local oscillator laser (LO) beam at the diplexer, and that matches the antenna lobe of the Schottky diode mixer (see §5.1). This allows us to direct the LO beam towards the scattering volume and use it as a measure of the useful part of the observation beam.

The measurements of the beam intensity profile at the intermediate focus W3, as shown in figure 4.21 and 4.22, were obtained by scanning a small detector in two perpendicular axes (a horizontal and a vertical axis) and observing the radiation emitted from the local oscillator laser propagating backwards from the detection system to the tokamak. A least square fit of the measured data to a gaussian beam profile (dashed lines) is also given in the figures. The waist measured at W3 is well matched to the image through M7 of the waist at position W2 which defines the scattering volume, see figure 4.8.

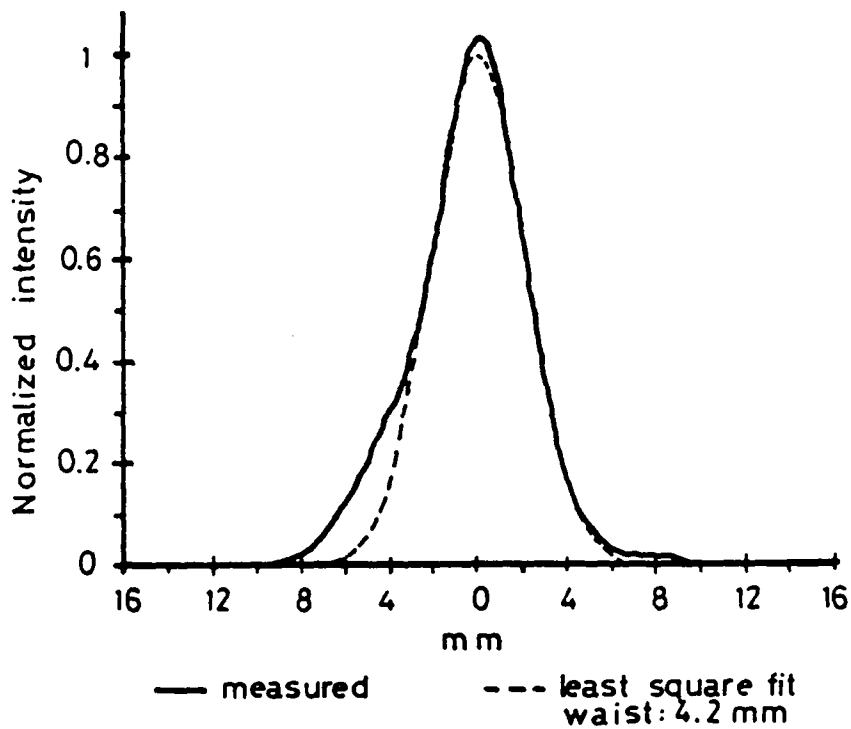


FIGURE 4.21. Horizontal scan of the L0 laser beam profile at the intermediate focal position W3 (see figure 4.1).

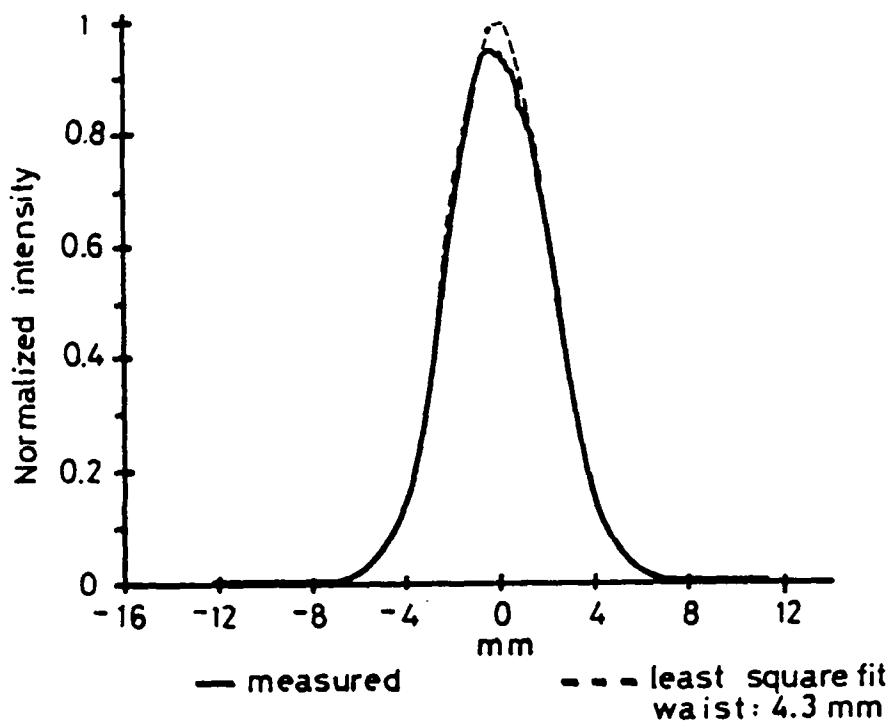


FIGURE 4.22. Vertical scan of the L0 laser beam profile at the intermediate focal position W3 (see figure 4.1).

#### 4.14. Mechanical stability of the FIR optics.

The mechanical stability of the FIR optics is of great importance, mainly because of the small beam waist  $W_2$  in the plasma. A tilt of only 2.5 mrad, or 0.35 mm at the mirror edge, of the mirrors M6 or M7 is sufficient to move the focal spot  $W_2$  in the plasma by one beam waist. This is not acceptable. The measurement of the vibration of these mirrors was found not to be trivial due to the difficult access, illustrated in figures 4.23 and 4.24, and the lack of a stable reference to which a steering mirror could be attached if a He-Ne laser were to be used as a displacement monitor.

It is known that the TCA torus chamber vibrates with an amplitude of approximately one millimeter during a discharge due to the magnetic stresses. We expect that all three mirrors M6, M7 and M8 will move together because of their common attachment (see figure 4.23). The elliptical mirror M6, however, is supported by a 750 mm long lever and could vibrate on its own during a tokamak discharge.

The tubes composing the stainless steel structure supporting mirrors M6 to M8 have been filled with sand to damp any vibrations. They are fixed to the support structure of two of the toroidal coils of the TCA tokamak. As a general precaution, all supports of mirrors as well as the  $D_2O$  laser vessel itself are made out of non magnetic material like stainless steel or plastic and glass fiber. Special care has been taken to avoid the creation of eddy currents from closed electric conducting loops.

It has been considered to increase the scattering volume in order to reduce the sensitivity to possible vibrations. This would, however, reduce the amount of scattered light observed by the detection system, which is not reasonable for the feasibility experiment on TCA because of the limited available FIR power.



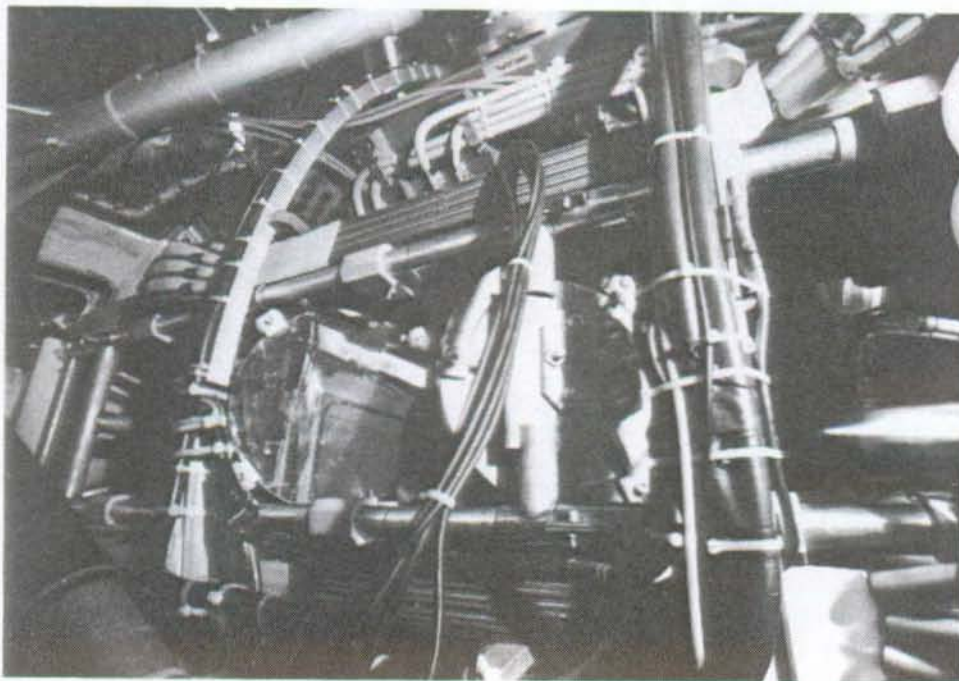
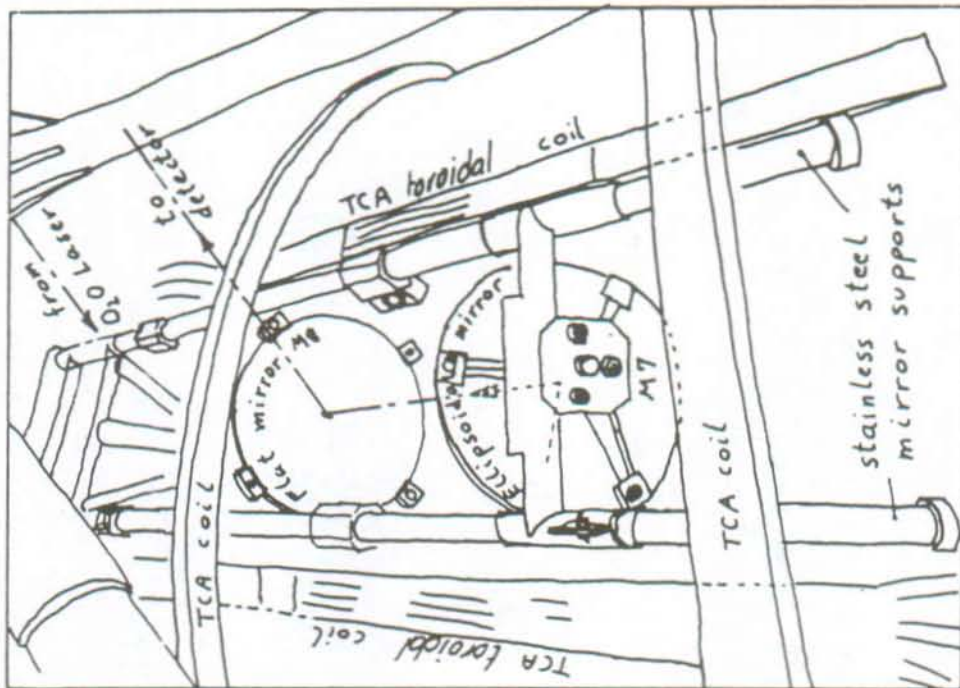


Figure 4.23. View of mirrors M7 and M8 and their support structure on TCA.

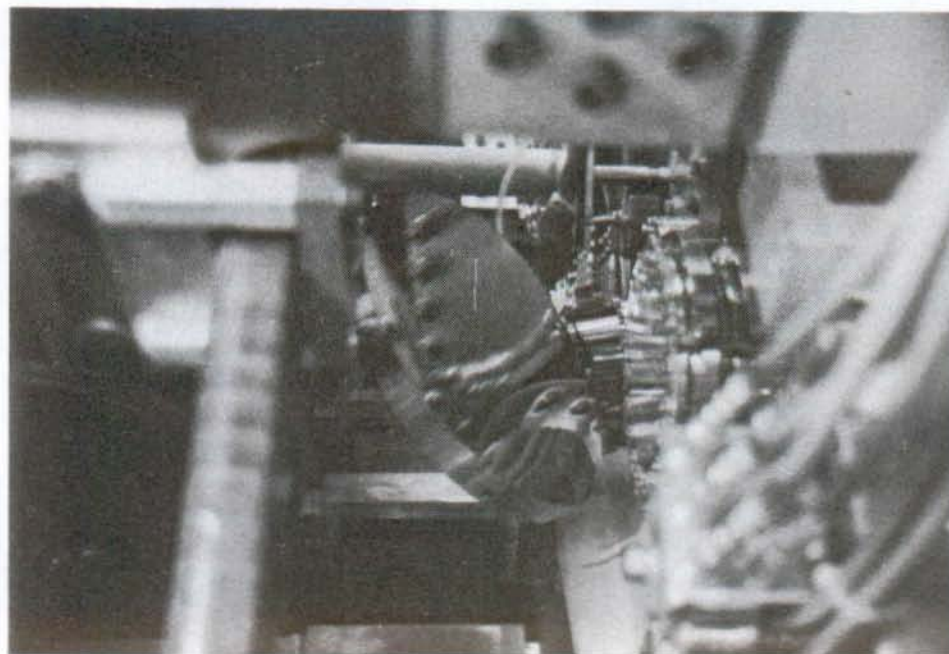
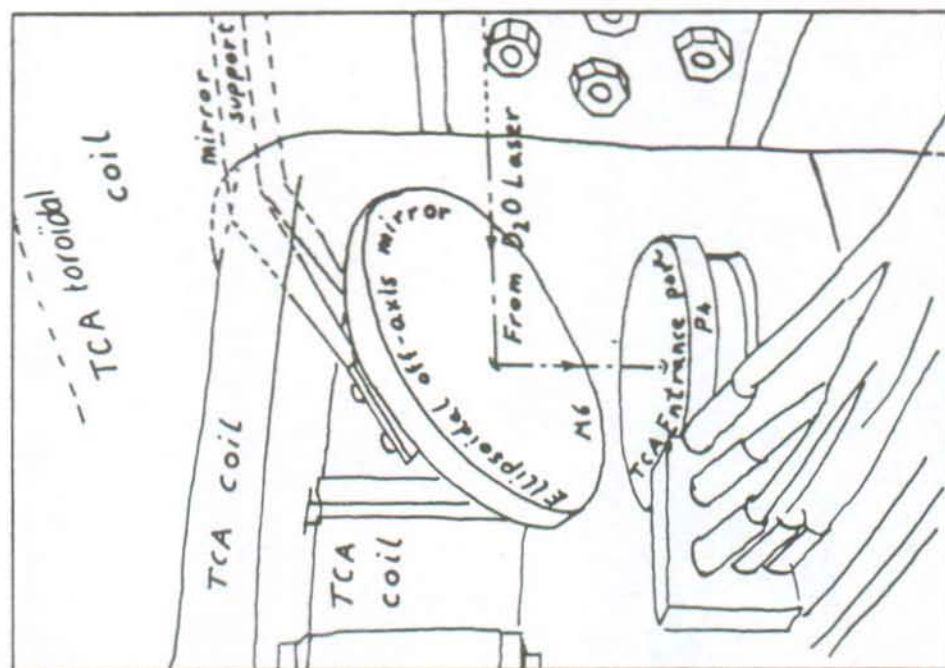


Figure 4.24. View of the elliptical mirror M6 and the input window support on TCA.

#### 4.15. Conclusions.

To minimize beam transport losses the  $D_2O$  laser has been positioned close to the TCA tokamak. For the same reason reflecting optics are used wherever possible. Two off-axis elliptical mirrors focus the incident FIR beam and collect the scattered signal. Z-cut crystal quartz, 120 mm in diameter, is used as vacuum window on the tokamak. The quartz windows are cut as etalons for the FIR wavelength to optimize their transmission.

The stability of the optical elements is of major importance. A tilt of only 2.5 mrad of one of the elliptical mirrors is sufficient to move the focal spot in the plasma by one beam waist. This would introduce a high shot to shot fluctuation to the scattered signal seen by the detection system. A stable mechanical structure, supporting both elliptical mirrors on the tokamak, has been designed to minimize the sensitivity to mechanical distortions.

To minimize the level of stray light, a 1.2 m long pyrex cone is used to dump the main FIR laser beam after its passage through the plasma.

A Macor glass ceramic viewing dump is positioned behind the scattering volume. To improve the dump efficiency narrow V-shaped grooves have been milled in the Macor.

The focal spot in the plasma has a measured gaussian beam waist of 1.3 mm, which matches the area seen by the detection system.



**REFERENCES:**

- [1] "Transportation of Far-IR beams for use in plasma diagnostics", M.R. Siegrist, I. Kjelberg, R. Behn, Appl. Opt., 22, 1318 (1983).
- [2] "Microwave optics", S. Cornbleet, Acad. Press, ISBN: 0-189650-1, (1976).
- [3] "Infrared and millimeter waves, Vol. 6 Systems and components", Chap. 5, by P.F. Goldsmith, Acad. Press, ISBN: 0-12-147706-1, (1982).
- [4] "A study of the feasibility of measuring the plasma ion temperature in JET by Thomson scattering using far infrared laser", M.R. Green, P.D. Morgan, M.R. Siegrist, R.L. Watterson, CRPP report, LRP-168-80, (1980).
- [5] "Measurement of the optical constants of crystal quartz in the far infrared with the asymmetric fourier transform method", E.E. Russel, E.E. Bel, J. Opt. Soc, 57, 341, (1967).
- [6] "Precise mm-wave measurements of complex refractive index, complex dielectric permittivity and loss tangent of GaAs, Si, SiO<sub>2</sub>, Al<sub>2</sub>O<sub>3</sub>, BeO, Macor, and glass", M.N. Afsar, K.J. Button, IEEE-MIT-31, 217, (1983).
- [7] "Optical constants of Far Infrared materials. 2: Crystalline solids", E.V. Loewenstein, D.R. Smith, R.L. Morgan, Appl. Opt., 12, 398, (1973).
- [8] "Material suitable for making filters beyond 300  $\mu\text{m}$ ", B. Melchiorri, V. Natale, B. Fiscella, P. Lombardini, Infr. Phys., 16, 253, (1976).
- [9] "Optical constants of Far Infrared materials. 3: Plastics", D.R. Smith, E.W. Loewenstein, Appl. Opt., 14, 1335, (1975).
- [10] "The optical constants of pure fused quartz in the Far-Infrared", T.J. Parker, J.E. Ford, Infr. Phys., 18, 215, (1978).
- [11] "The far-infrared absorption of different types of fused silica", I.H. Hutchinson, Infr. Phys., 22, 117, (1982).

- [12] "The optical constants of ordinary glass from 0.29 to 4000  $\text{cm}^{-1}$ ", J.R. Birch, R.J. Cook, A.F. Harding, R.G. Jones, G.D. Price, J. Phys. D, Appl. Phys., 8, 1353, (1975).
- [13] "Submillimeter-wave dumps for fusion plasma diagnostics", P. Woskoboinikow, R. Erickson, W.J. Mulligan, PFC-JA-83-11 MIT report, (1983).
- [14] "Design and performance of compact submillimeter beam dumps", K. Kato, I.H. Hutchinson, PFC-RR-84-11 MIT report, (1984).
- [15] "Final report on the scientific and engineering design of an soft X-ray diode array diagnostic system for JET", H.U. Fahrback, H. Goss, E. Harmeyer, G. Schram, Max-Planck Institute, IPP-JET-report 6-1-209, (1982).
- [16] "Investigation of various probe sheath materials in the Texas Tech tokamak, P.D. Coleman, B.D. Blackwell, M. Kristiansen, M.O. Hagler, IEEE Tr. Pl. Sc., IEEE-PS-9, 123, (1981).
- [17] "Cone channel condenser optics", D.E. Williamson, J. Opt. Soc., 42, 712, (1952).
- [18] "Ray traces through hollow metal light-pipe elements", E.V. Loewenstein, D.L. Newell, J. Opt. Soc., 59, 407, (1969).
- [19] "Classical electrodynamics", J.D. Jackson, Chap. 7, John Wiley, ISBN: 0-471-42132-X, (1975).

## CHAPTER 5.

### THE HETERODYNE DETECTION SYSTEM.

As discussed in §2.6 [1,2,3], we have chosen a heterodyne receiver using a Schottky diode mixer with a noise equivalent power (NEP) of at least  $10^{-18}$  W/Hz at the frequency of 778.58 GHz. Heterodyne detection consists of coherently mixing the signal to be detected with a narrow bandwidth local oscillator signal, thus converting the signal spectrum to a more accessible intermediate frequency (IF). Since our signal is pulsed and wideband, the analysis of the IF spectrum is best achieved with a multichannel filter bank. The filter bank divides the IF signal into a set of narrow spectral channels, each leading to an integrator. The following description considers the state of the detection system as used for the first attempts to observe scattered light from the TCA tokamak. The description includes the IF amplifier-filter bank and the CAMAC data acquisition system.

#### 5.1. Introduction to heterodyne detection.

Figure 5.1 shows a block diagram of a heterodyne receiver. It consists of: (1) an optical diplexer combining the scattered and the local oscillator signals, (2) a mixer producing the IF signal and (3) the IF amplifier, filters, square law detectors and integrators necessary to record the spectrum of the signal.

The current delivered by a mixer ( $i_1$ ) in a heterodyne receiver is usually proportional to the product of the incident electromagnetic power and the detection efficiency integrated over the detection area [4]. For visible wavelengths the detection area is well defined, because the radiation is

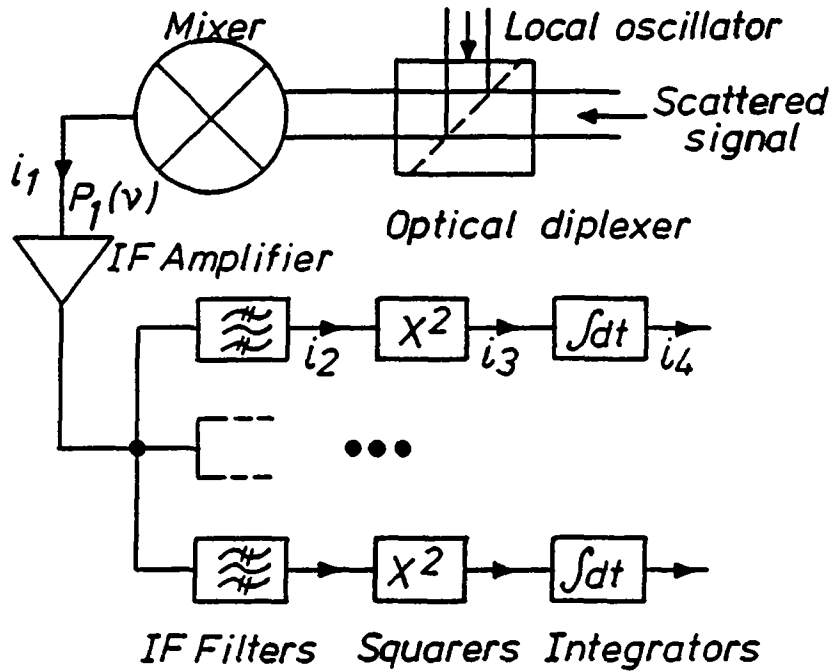


FIGURE 5.1. Block diagram of a heterodyne receiver system.

coupled optically to the mixer, that is the signal is imaged directly on the finite surface of the mixer. In the FIR and microwave wavelength region antenna-coupling is mostly used. The physical size of antenna-coupled mixers, such as the Schottky diode, is small compared with the incident wavelength, thus a detection area can not be defined. The current responsivity of the antenna-coupled mixer is obtained by integrating over the solid angle defining the antenna pattern of the mixer [4,5,6].

For both schemes of radiation coupling to the mixer, only the incident signal mode coinciding with the local oscillator field contributes coherently to the detected current [3 to 6], thus the heterodyne receiver is only sensitive to a single radiation mode<sup>1</sup>. This leads to the antenna theorem of hete-

---

<sup>1</sup> A single radiation mode is defined by T.G. Blaney [3] as: "linearly polarized radiation propagating such that its etendue  $A\Delta\Omega \approx \lambda^2$  is preserved", where A is the beam area and  $\Delta\Omega$  the solid angle defining the spread of the beam.



detection stating that the incident beam etendue should be smaller than  $\lambda^2$  [3,4,5,7]:

$$A\Delta\Omega \leq \lambda^2 \quad (5.1)$$

For antenna-coupled devices the incident beam is generally focused to a diffraction limited spot. Within the area of the first Airy lobe the antenna theorem is always verified. It has been shown that for heterodyne detection the optimum coupling of a Gaussian local oscillator (LO) beam of waist  $w$  to an Airy field signal beam of F-number  $F$  is [8]:

$$w/F \approx 0.7 \lambda \quad (5.2)$$

The useful etendue of the beam emerging from the scattering volume in our experiment is the etendue that fulfills the antenna theorem through the observation optics. A measure of this antenna beam can be obtained as described in §4.13, since the field distribution defining the antenna beam of an optical mixing receiver is simply the field distribution of the LO beam propagated backward through the observation optics [4,6].

If  $E_s$  represents the signal field incident on the mixer, and  $E_{10}$  the field of a linearly polarized local oscillator then we have [4,6]:

$$i_1(t) = C \iint_A d^2x |E_s(\mathbf{x},t) + E_{10}(\mathbf{x},t)|^2 \quad (5.3)$$

where  $C$  is a conversion constant and  $A$  any cross section for which the antenna theorem is respected for both the signal and LO fields incident onto the mixer.

By expanding the integrand, assuming the monochromatic local oscillator field is much stronger than the signal field, we end up with two DC terms due to signal power ( $P_s \propto E_s \cdot E_s^*$ ) and LO-power ( $P_{10} \propto E_{10} \cdot E_{10}^*$ ), and an interference term at the IF frequency  $\nu_{if} = |\nu_s - \nu_{10}|$  [4,5,6].

The current due to this interference term is [6]:

$$i_{if}(t) = C \iiint_A d^2x |E_s(\mathbf{x}, t) \cdot E_{10}^*(\mathbf{x}, t) + c.c.|^2 \quad (5.4)$$

$$\propto 2\sqrt{P_s P_{10}} \cos(2\pi\nu_{if}t)$$

Since the local oscillator power is large in comparison to the signal power, we have  $P_{10} \gg P_{if} \gg P_s$  where  $P_{if}$  is the power due to the current  $i_{if}$ .

The DC terms mentioned previously will not pass through the IF amplifiers, but they will contribute to the generation of noise in the mixer, whose bandwidth extends to the IF frequency range. For Schottky diode mixers this is mainly shot noise (see equation B.35 in appendix B) produced by the current circulating in the diode. The total noise power  $P_n$  entering the first IF amplifier has then a contribution from shot noise due to the radiation incident on the mixer which is mainly due to the LO field, hence the power  $P_{10}$ , and an intrinsic noise power from the mixer and the IF amplifier  $P_{cn}$  which is independent of the optical signals. Since only  $P_{if}$  contains a term related to the signal, the signal to noise ratio after the mixer is proportional to:

$$S/N \propto \frac{P_{if}}{P_n} \propto \frac{P_s \cdot P_{10}}{P_{10} + P_{cn}} \quad (5.5)$$

To improve this signal to noise ratio, apart from increasing  $P_s$ , one would have to increase  $P_{10}$  so that its noise contribution represents the dominant noise source. This is referred to as the shot noise limit.

Shot noise limited heterodyne detection is generally achieved at visible and near infrared wavelengths, but in the FIR, where  $kT \gg h\nu$  noise due to thermal emission from the surroundings contributes strongly to  $P_{cn}$ , and other parameters, like the conversion loss of the Schottky diode mixer, are also strongly influenced by the LO power. This is discussed in more details in §5.9

The filter-squarer-integrator combination which forms the spectrum analyser in figure 5.1 will influence the final signal to noise ratio observed after the integrators [4,5,7]. The noise and signal just after the mixer are wideband, compared to the IF filters, and can be assumed to follow Gaussian statistics. The IF filters will extract a portion of the full bandwidth, while the squarer will transform the noise statistics to a  $\chi^2$  distribution [4,5,7]. It can be shown that the average current  $i_3$  after the square law detector is proportional to the power  $P_1$  at the mixer, which is the sum of the signal and noise power when an optical signal is incident on the mixer, and which is just the noise power in absence of an optical signal. Accordingly, the useful signal at this stage is [5,7]:

$$\langle i_3 \rangle_{s+n} - \langle i_3 \rangle_n \propto P_1(s+n) - P_1(n) = (P_s + P_n) - P_n \quad (5.6)$$

A measure of the noise in the current  $i_3$  is the root mean square fluctuation of the mean [5,7]:

$$\langle (\Delta i_3)^2 \rangle^{1/2} = (\langle i_3^2 \rangle - \langle i_3 \rangle^2)^{1/2} \quad (5.7)$$

The signal to noise ratio is given by the ratio of available signal power to the total contribution of fluctuations, which is for the current  $i_3$  :

$$(S/N)_3 = \frac{\langle i_3 \rangle_{s+n} - \langle i_3 \rangle_n}{\langle (\Delta i_3)^2 \rangle^{1/2}} = \frac{P_s}{P_s + P_n} = \frac{s}{1 + s} \quad (5.8)$$

where  $s = P_s/P_n$  is the signal to noise ratio after the mixer.

The effect of the integrator is to reduce the fluctuations of the current by averaging, hence improve the signal to noise ratio. It can be shown that the final signal to noise ratio (or post integration signal to noise ratio) is related to the pre integration signal to noise ratio by [5,7]:

$$(S/N)_4 = (S/N)_3 (1 + B\tau)^{1/2} \quad (5.9)$$

where  $B$  is the bandwidth of the signal before the integrator and  $\tau$  is the integration time.

Before the final integrator the available signal to noise ratio (in presence of an optical signal on the mixer) is always below one (equation 5.8). From the moment that  $s \geq 1$ , an increase of the signal power can only contribute by a factor 2, while an increase in integration time  $\tau$  (laser pulse length) can significantly improve the final signal to noise ratio. Assuming that  $P_s$  and  $\tau$  can be chosen for a given laser pulse energy, there is no point in increasing  $P_s$  far beyond  $P_s = P_n$ . Once this level is reached, the signal to noise ratio can be increased more efficiently by increasing  $\tau$  [1,5,6].

The output current  $i_4$  as a function of time is illustrated in figure 5.2 [5].

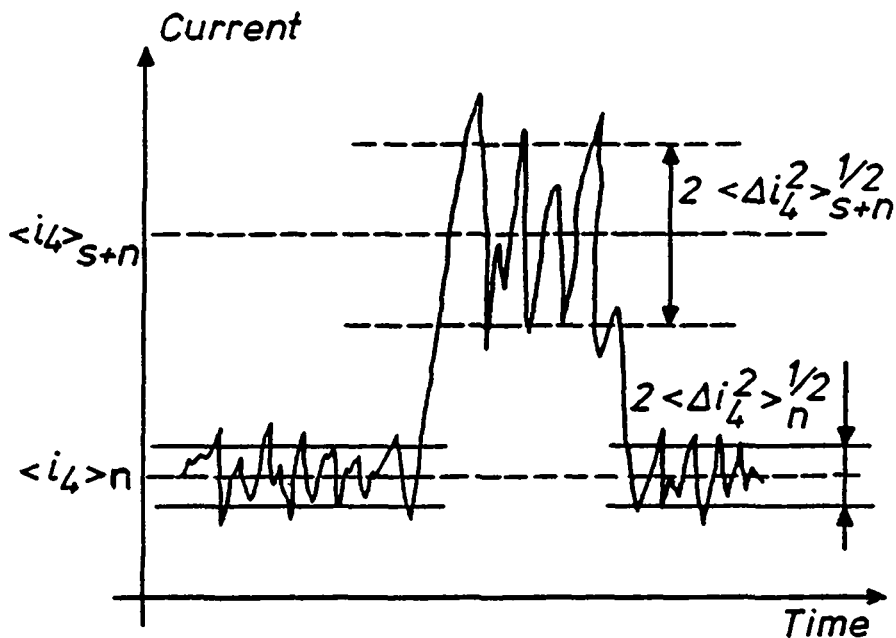


FIGURE 5.2. A schematic output current from the integrator, with and without a signal [5].

Concerning Schottky diode mixers two parameters must be introduced. They are the Schottky diode mixer conversion loss  $L_c$  and the noise equivalent power (NEP)<sup>1</sup>.

The conversion loss is defined as the ratio of the mean signal power (time averaged) incident on the optical diplexer to the available power at the IF frequency after the mixer:

$$L_c = \frac{P_s}{P_{if}} = \frac{P_s}{Z \bar{I}_{if}^2(t)} \quad (5.10)$$

where  $Z$  is the IF impedance of the mixer and  $\bar{I}_{if}$  the mean IF current. Equation 5.10 shows that the conversion loss is strongly dependent on the local oscillator power and on the Schottky diode and IF amplifier characteristics through the impedance  $Z$ .

The NEP is defined as the power per bandwidth, incident on the mixer to give a detectable signal at the level of the first IF amplifier equivalent to the signal generated by noise sources in the detection system (in other words the equivalent signal power to achieve a signal to noise ratio  $s = 1$ ). Contributions to the total noise power come from shot noise and from noise generated in the IF amplifiers.

In the FIR when  $\kappa T \gg h\nu$  the NEP is often replaced by the effective noise temperature which represents the effective temperature of a thermal noise source. They are related by (see also appendix B, equation B.4 and B.13):

$$NEP_{SSB} = \kappa T_s = \kappa (T_m + L_c T_a) \quad [W/Hz] \quad (5.11)$$

where  $T_s$  is the total system temperature which corresponds to the mixer temperature  $T_m$  plus the IF amplifier temperature  $T_a$  corrected by the mixer conversion loss  $L_c$ .

---

<sup>1</sup> In a heterodyne detection system signals from frequency bands on both sides of the local oscillator will contribute to the IF signal unless special measures are taken. When quoting an NEP it needs to be specified whether single (SSB) or double (DSB) sideband conditions are considered. The NEP used in this text implies a double sideband if not specifically stated. The NEP of a single sideband receiver is twice that of the double sideband receiver !

THE FIR HETERODYNE RECEIVER

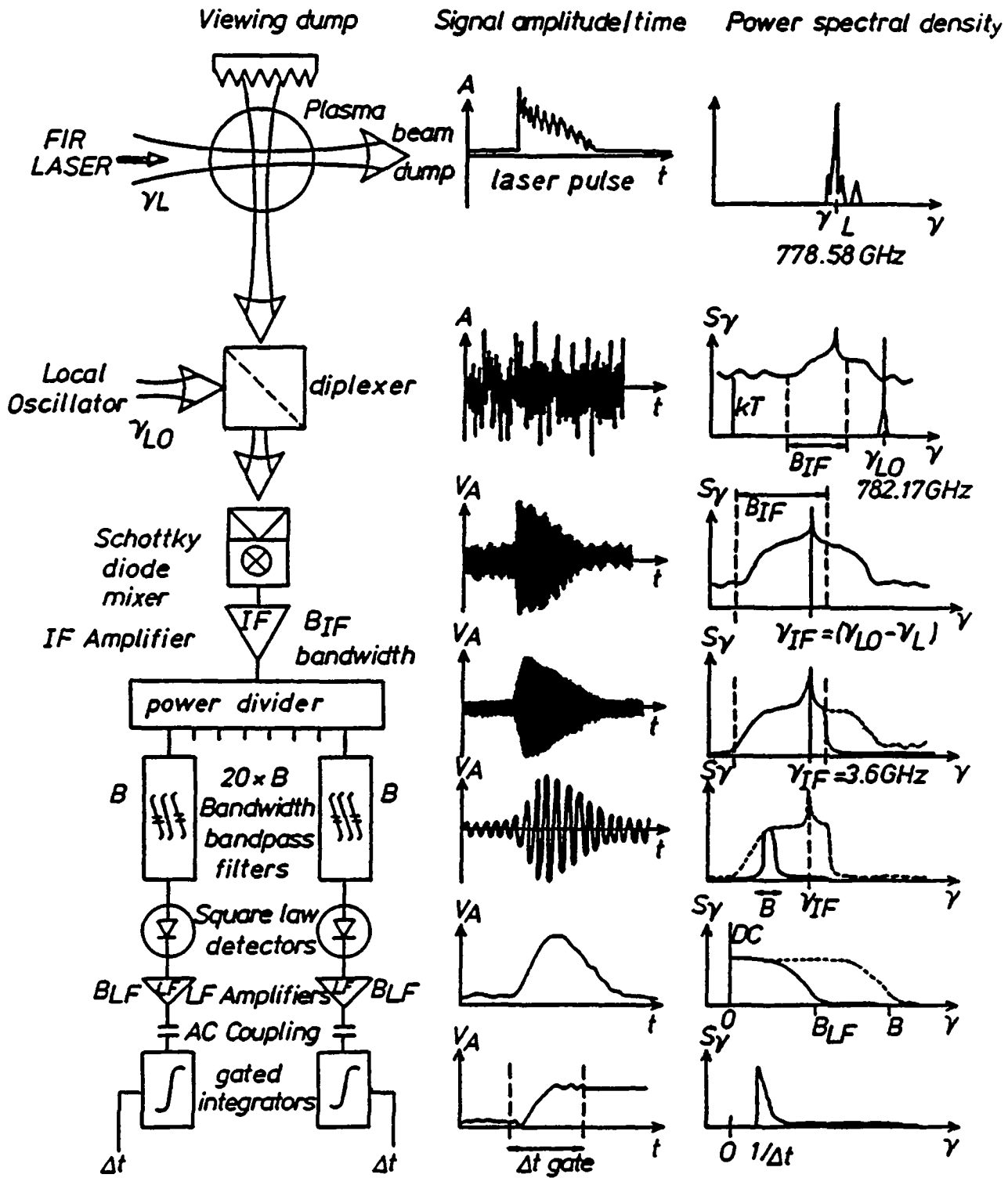


FIGURE 5.3. The principle of a heterodyne detection system [9].

### 5.2. The elements of the heterodyne detection system.

The total detection system installed on TCA is outlined in figures 5.3 [9] for details of the optical part see figure 5.4, and 5.5 which shows a photo of the Schottky diode mixer mount and the last parabolic mirror. The heterodyne receiver is composed of:

- A quasi-CW, optically pumped FIR laser used as the local oscillator.
- A Mach-Zehnder type diplexer to combine the scattered signal with the LO laser beam.
- A Schottky barrier diode mixer to convert the incident power to an IF signal.
- Microwave (S band) low noise amplifiers and filters to analyze the spectrum of the IF signal.
- A data acquisition system composed of:
  - A CAMAC controlled multichannel gated integrating ADC which integrates and digitizes the signal at the output of the receiver channels.
  - A CAMAC controlled timer for synchronization of the acquisition system with the laser pulses.
  - A microprocessor based CAMAC controller to establish communication between the acquisition units and the local PDP-11 computer.

Figure 5.3 shows not only the basic elements of the heterodyne detection system, but also typical signals (time and spectral power behavior) at different points through the detection system. The final value obtained by the integrator of each channel is digitized before being sent to the local computer (PDP-11) for storage and analysis.

### 5.3. The local oscillator.

The three essential parameters of the LO are its frequency, spectral purity and power.

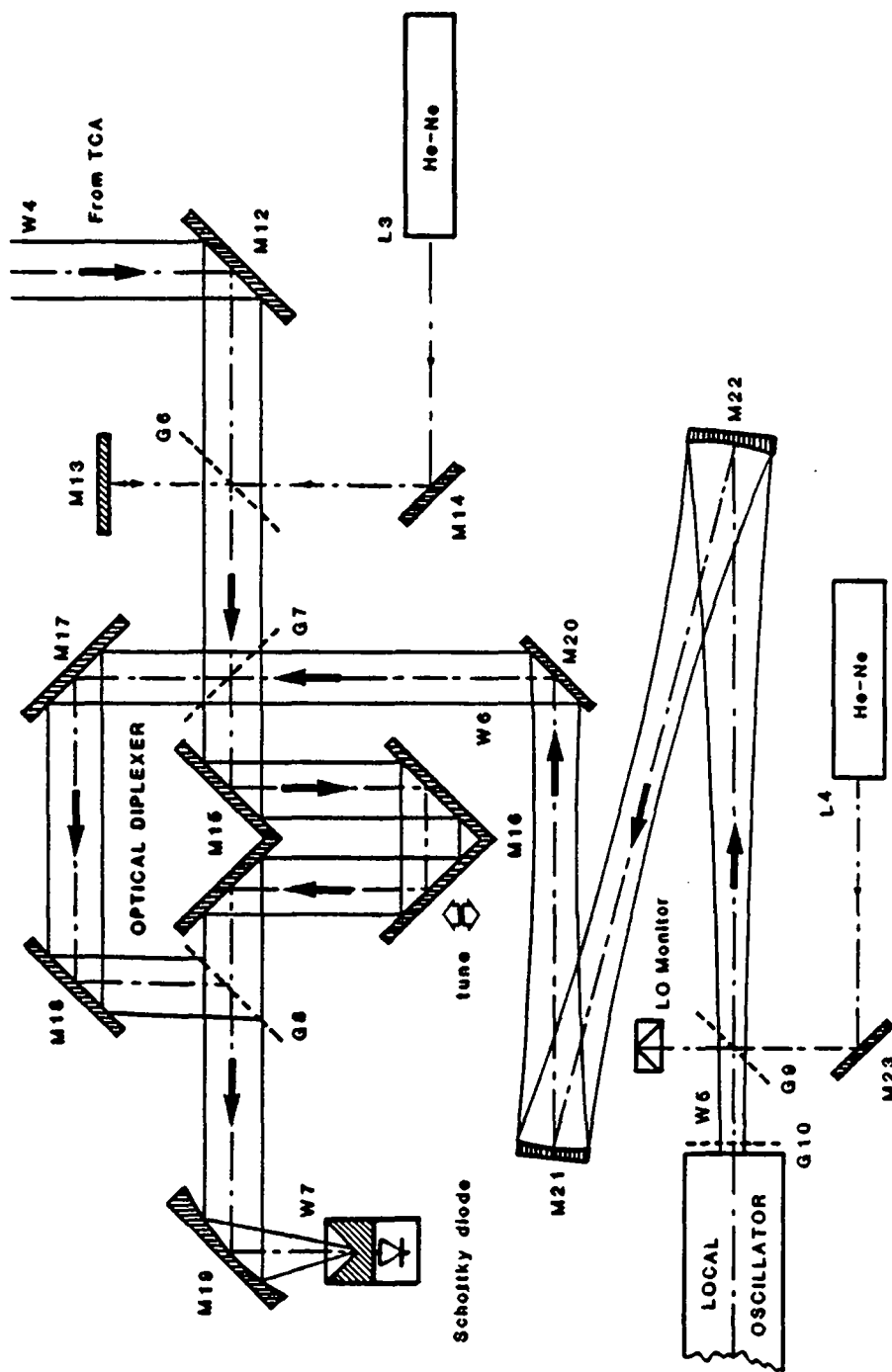


FIGURE 5.4. The optics of the detection system, including the Mach-Zehnder optical diplexer and the local oscillator, see also figure 5.5 and 5.6.



The mirrors: (Al on glass if not otherwise specified)

- M12 Translatable flat steering mirror to collect the beam coming from the off-axis elliptical mirror M11 of figure 4.1.
- M13 Steering mirror for He-Ne alignment laser beam.
- M14 As for M12.
- M15 Flat Al roof-top mirror.
- M16 As M15 but mounted on a translation stage to adapt the diplexer path length, typically set to 540 and 590 mm.
- M17 Flat steering mirror forming the fixed length arm of the interferometer.
- M18 As for M17.
- M19 Parabolic, 90° off-axis mirror of 110 mm focal length, matching the waist of the beam from the diplexer to the antenna pattern of the Schottky diode mixer. It is a gold coated epoxy mirror.
- M20 Flat steering mirror.
- M21 Spherical 1 m radius of curvature mirror. It forms a telescope with mirror M22.
- M22 As for M21, but with a 0.6 m radius of curvature.

Beam waists: (Gaussian, radius at  $e^{-2}$  of intensity)

- W4 Waist at entrance of optical diplexer, designed for a beam of 14 mm waist.
- W5 Waist of local oscillator, measured: 8.3 mm.
- W6 Waist of LO at diplexer, measured:  $14 \pm 4$  mm, see figure 5.7 and 5.8.
- W7 Waist on Schottky diode mixer. Focused to a diffraction limited spot with a divergence matched to the mixer antenna lobe. The antenna lobe has a full cone angle of 15° at 3 dB intensity.

Grids or beam-splitters:

- G6 Retractable He-Ne pellicle beam-splitter.
- G7 Copper wire mesh, clear aperture 55 mm, 50% transmitting at 778.58 GHz.
- G8 As for G7, forms the optical diplexer with mirrors M15 to M18 and grid G7.
- G9 Fixed He-Ne beam splitter. A few per cent of the LO beam power is sent to the LO monitor detector.
- G10 LO laser output coupler. Capacitive gold mesh (100 lines per inch) deposited on a crystal quartz substrate.

Table 5.1. Elements composing the detection system shown in figure 5.4.

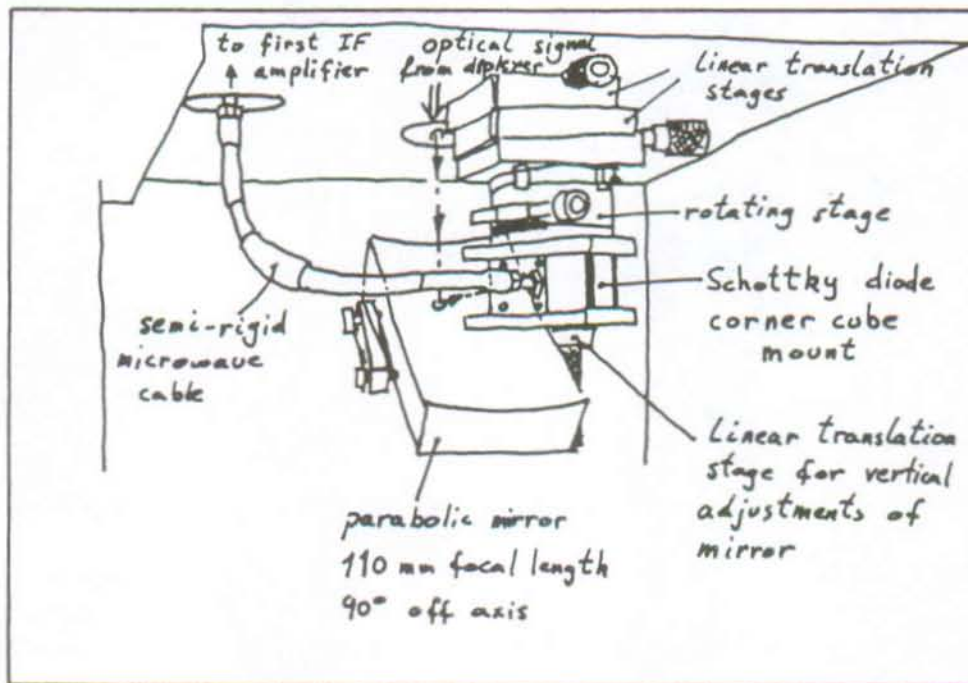
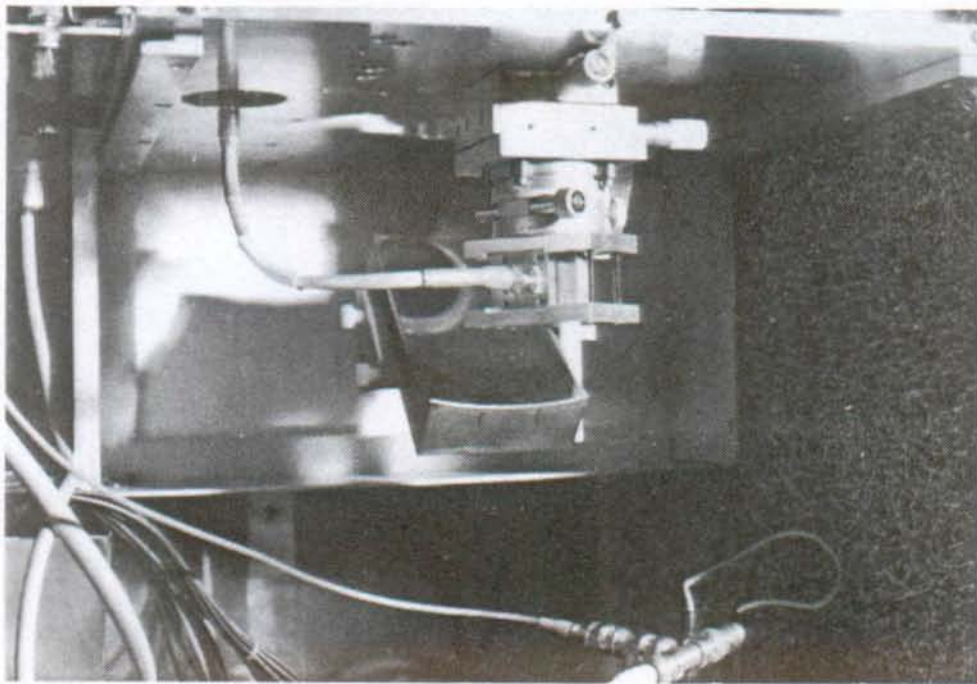


FIGURE 5.5. The Schottky diode mixer and the parabolic mirror.

The LO emission frequency defines the IF centre frequency and therefore the type of microwave equipment needed for further signal processing. The spectral purity of the LO signal is important because only for a narrow band LO does the IF spectrum reflect the spectral distribution of the scattered radiation. The LO power contributes to signal amplification in a heterodyne detection scheme (see equation 5.4). For optimum operation of the Schottky diode mixer a minimum LO power of 3 to 10 mW is required [1,10 to 14].

We have chosen an optically pumped FIR laser as local oscillator. The emission of such a laser can be kept stable in frequency with a linewidth of some megahertz when operated at pressures below one Torr. The exact laser frequency and total power depends on the choice of molecule and lasing transition.

The choice of LO frequency involves a compromise between keeping the IF low enough to be able to exploit easily available, low noise components, and minimization of the relative bandwidth  $\Delta\nu_{\text{signal}}/\nu_{\text{if}}$ . To keep the IF below 10 GHz, we restrict the LO frequency to  $778.58 \pm 10$  GHz. Since the scattered signal halfwidth  $\Delta\nu_{\text{signal}} \approx 1.5$  GHz, and the relative bandwidth should be kept below 0.5 for current microwave equipment we have finally:

$$3 \text{ GHz} \leq \nu_{\text{if}} \leq 10 \text{ GHz} \quad (5.12)$$

From the literature we have found only three gases that satisfy these conditions, and which provide several milliwatts of FIR power [15,16]. They are: DCOOD,  $\text{CH}_2\text{F}_2$  and  $\text{CD}_3\text{Cl}$ .

We have chosen to use  $\text{CD}_3\text{Cl}$ , which emits at 782.166 GHz (383.05  $\mu\text{m}$  wavelength) when pumped by the 9R(34) line of the  $\text{CO}_2$  laser. Mixing this LO emission with the Raman line of the  $\text{D}_2\text{O}$  laser results in a IF frequency of 3.6 GHz.

The DCOOD molecule, which was used as LO at MIT [17], emits at a wavelength of 381  $\mu\text{m}$  (IF of 9 GHz). It was disregarded because of problems of availability of very low noise

5. DETECTION SYSTEM

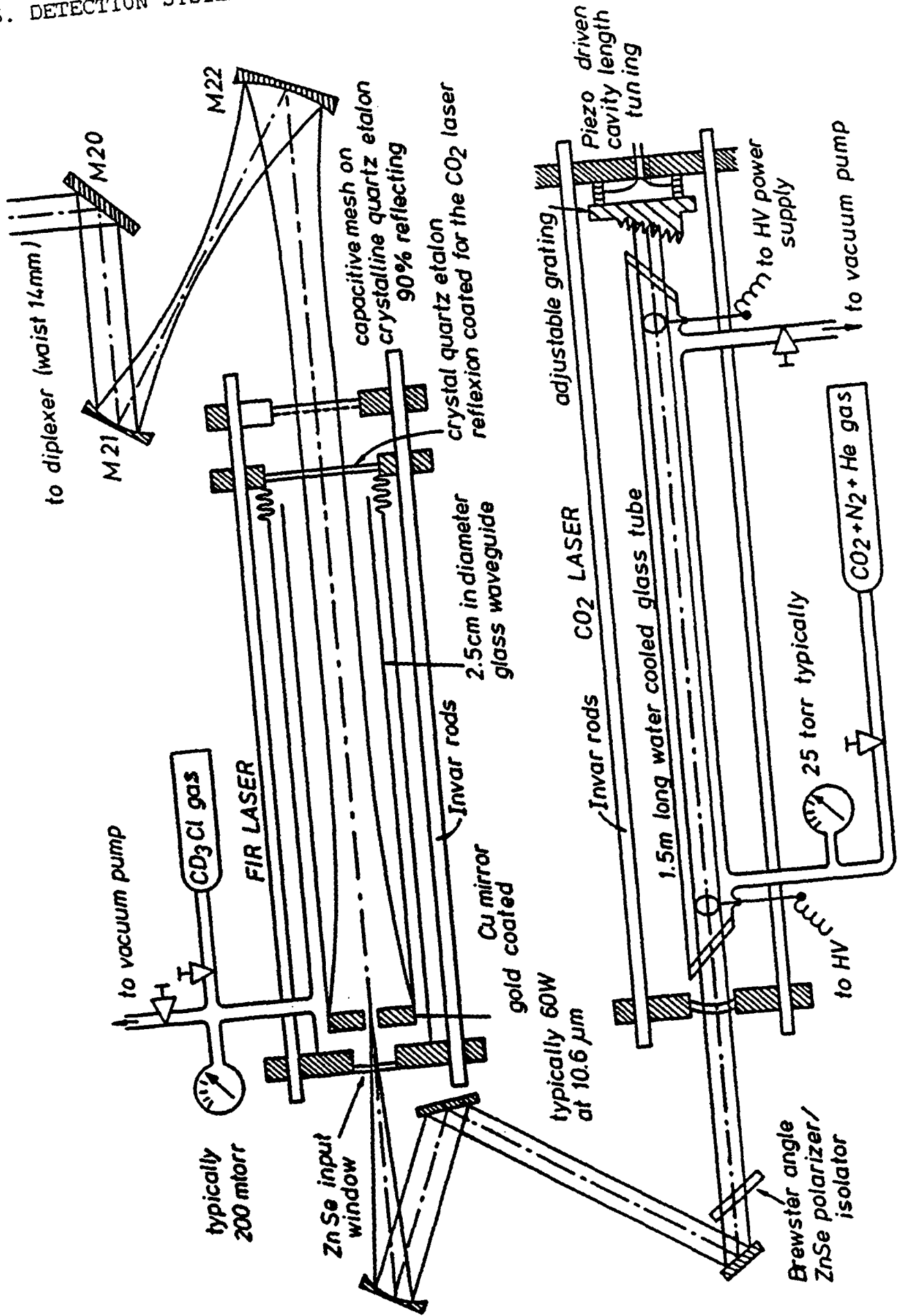


FIGURE 5.6. The local oscillator lasers.

amplifiers in the X-band. This would not have been such a problem today.

The  $\text{CH}_2\text{F}_2$  molecule, emitting at 783.5 GHz (IF of 4.9 GHz) was not chosen because it emits simultaneously on three cascade lines, which would require special means for the line selection and monitoring. However, it could be used with the present detection system to allow the study of the outer part of the spectrum of a  $\text{H}^+$  plasma. This part of the spectra cannot be observed with the  $\text{CD}_3\text{Cl}$  as LO because of limitations in the pass band of the IF filter set.

The optically pumped FIR laser is a commercial system supplied by Edinburgh Instruments (model PL4), consisting of a CW  $\text{CO}_2$  laser and a dielectric waveguide type FIR resonator (see figure 5.6).

The  $\text{CO}_2$  laser delivers up to 60 W of linearly polarized IR radiation. The active gas mix used is 75% He, 18%  $\text{N}_2$  and 7%  $\text{CO}_2$ , at a typical working pressure of 25 Torr. The laser cavity is formed by a 1.5 m long invar stabilized structure supporting a blazed grating to select the emission line and a ZnSe output coupler. For fine tuning of the cavity length the output coupler is mounted on a piezo-electric translation stage. Cavity length tuning allows the emission frequency of the  $\text{CO}_2$  laser to be adjusted to the absorption line of the  $\text{CD}_3\text{Cl}$  molecule. For optimum coupling into the FIR laser cavity the  $\text{CO}_2$  laser has to be operated on a low order transverse mode.

The optically pumped FIR laser is composed of a 1.5 m long, 25 mm diameter, glass waveguide tube. The focused pump beam is coupled into the FIR laser resonator via a hole in the flat end mirror. As output coupler we use a capacitive mesh, (100 lines per inch) of 90% reflectivity, deposited on the surface of a flat Z-cut crystal quartz substrate. The quartz window is cut as an etalon with maximum transmission for the FIR laser wavelength. In addition a dielectric coating with high reflectance at the  $\text{CO}_2$  laser wavelength has been deposited on the substrate.

At a typical working pressure of 250 to 300 mTorr the FIR laser output is 1.5 mW in CW operation and 7 mW in chopped mode. The 5 ms long pulse produced in chopped mode can be considered to be CW compared with the 1  $\mu$ s long  $D_2O$  laser pulse. Only in performing a calibration of the detection system does the chopped nature of the LO cause complications (see §5.8). For stable operation and to minimize thermal drifts the LO laser is run in chopped mode with a repetition rate of typically 10 Hz. The synchronization with the  $D_2O$  laser pulse is controlled by the CAMAC timer see §5.12.

The beam profiles at the entrance of the optical diplexer have been measured by scanning a small detector in two perpendicular directions. The measurements are shown in figures 5.7 and 5.8. The difference between the horizontal and vertical scans comes from astigmatism in the off-axis telescope, which uses spherical mirrors (M21 and M22) to match the LO beam profile ( $W_5$  in figure 5.4) to the required diplexer beam waist  $W_6$ . The dashed lines represent a gaussian least squares fit to the measured data with a normalized intensity of more than 0.25. The bumps in the measured values at the maximum intensity are due to feed-back of radiation from the detector into the local oscillator laser.

#### 5.4. The optical diplexer.

The simplest way of superposing the signal beam (scattered radiation) and the LO beam is to use a semi-transparent beam splitter. However, in this case part of the signal and LO power will be lost. Assuming a symmetric beam splitter with equal reflectance and transmittance only half the signal and LO power will be available at the mixer.

In theory a diplexer formed from an interferometer (e.g. Michelson, Mach-Zehnder or Fabry-Perot) can be made 100% efficient for two beams of different frequencies with the penalty of a finite bandwidth of the instrumental transmission function. When calculating the diplexer's efficiency for the large spectral extent of the scattered signal the instrumental transmission function must be considered.

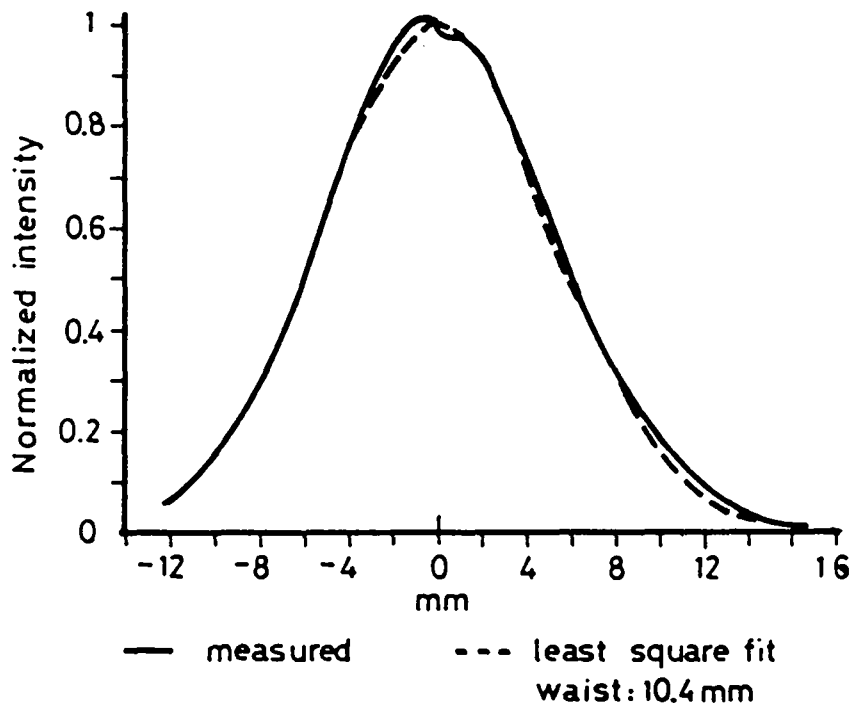


FIGURE 5.7. Horizontal scan of the L0 laser beam profile at the diplexer, position W6 in figure 5.4.

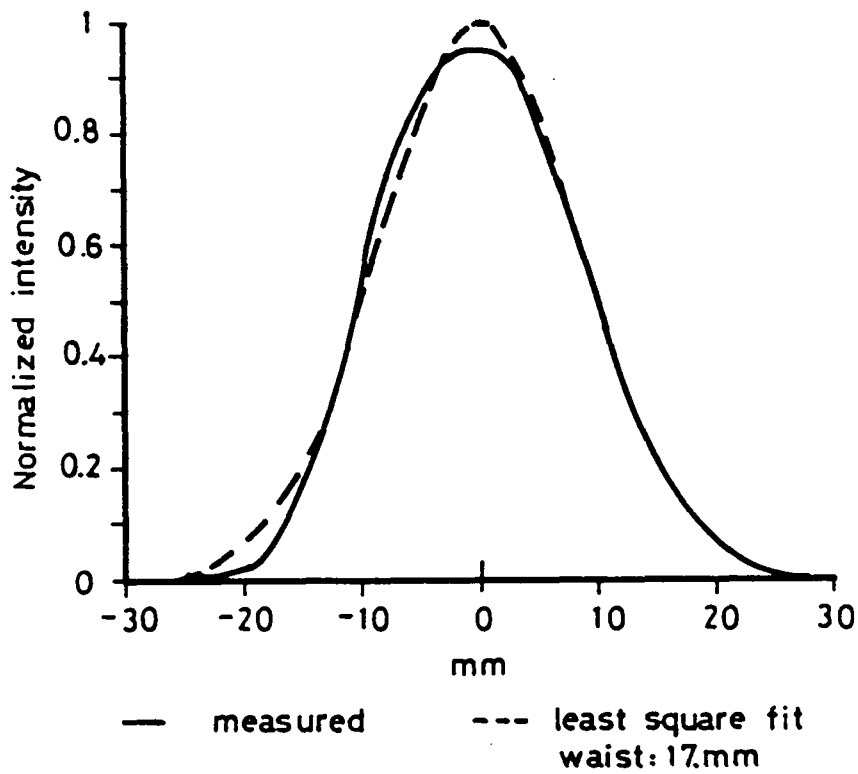


FIGURE 5.8. Vertical scan of the L0 laser beam profile at the diplexer, position W6 in figure 5.4.

The diplexer used in our experiment has the configuration of a Mach-Zehnder type interferometer, as shown in figure 5.4. The optical elements have a diameter of 50 mm which is well adapted to accept a beam with a waist of 14 mm. The transmission function of this diplexer can be derived when the simplified configuration shown in figure 5.9 is considered. The metal mesh beam-splitters are assumed to be lossless and will introduce a constant dephasing of  $90^\circ$  between the reflected and transmitted beams. The path difference for the two arms of the interferometer is given by  $\Delta\ell$ .

For a monochromatic wave of wavelength  $\lambda_s$  and frequency  $\nu_s$  incident on port 1 (the signal port) it can be shown that the amplitude at port 3 (ignoring arbitrary phase terms) is related to the signal amplitude  $A_s$  by [18,19,20]:

$$A_{13} = A_s (t_1 t_2 - r_1 r_2 \exp(-2\pi i \Delta\ell / \lambda_s)) \quad (5.13)$$

By analogy we obtain for a wave of wavelength  $\lambda_{10}$  and frequency  $\nu_{10}$  incident on port 2 (the LO port) [18,19,20]:

$$A_{23} = A_{10} (r_1 t_2 + t_1 r_2 \exp(-2\pi i \Delta\ell / \lambda_{10})) \quad (5.14)$$

where  $A_{10}$  is the amplitude of the incident LO field.

Now two cases are of special interest [20]:

a) One wants to maximize both  $A_{13}$  at the wavelength  $\lambda_s$  and  $A_{23}$  at wavelength  $\lambda_{10}$  (see figure 5.10). This implies that [18.19.20]:

$$\Delta\ell = (N + \frac{1}{2})\lambda_s \quad \text{and} \quad \Delta\ell = M\lambda_{10} \quad (5.15)$$

where  $N$  and  $M$  are integers. This combines to give:

$$\Delta\ell = (2K+1)\lambda_{if}/2 \quad (5.16)$$

where  $K = |M - N|$  is an integer,  $\lambda_{if} = c/\nu_{if}$  and  $\nu_{if} = |\nu_s - \nu_{10}|$ .



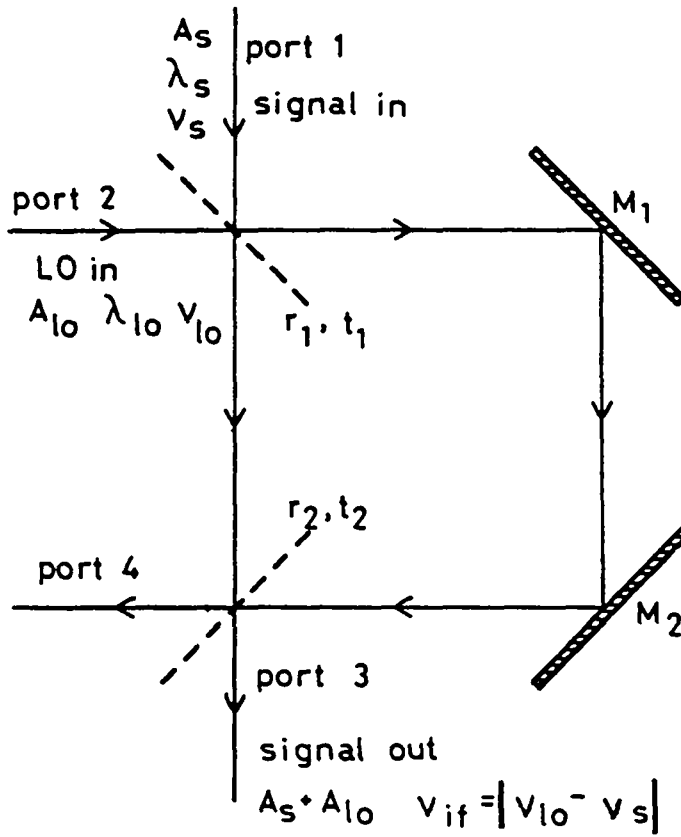


FIGURE 5.9. A simple Mach-Zehnder type interferometer. The reflection and transmission of the grids are given by  $r$  and  $t$  respectively.

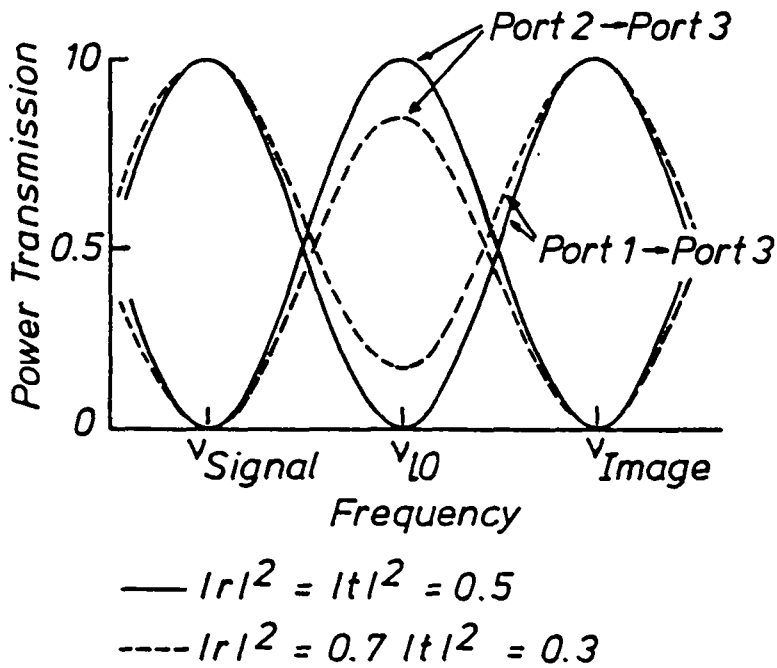


FIGURE 5.10. The diplexer transmission function for case a) with  $K=0$ .

It appears that in this case the transmission is also maximum for the signal image frequency.

It should also be noted that if the two beamsplitters were not balanced ( $r \neq t$ ), then part of the L0 signal would exit through port 4. If, however, port 4 was chosen as the output port and the path length difference was optimized, then the signal would not be fully transmitted to port 4; part of the signal power would be lost through port 3.

b) One wants a maximum transmission of the signal but a maximum rejection at the image frequency, thus [20]:

$$\Delta l = (2K+1) \lambda_{IF}/4 \quad (5.17)$$

In this case, for an identical value of  $K$ , the instrumental function bandwidth is twice as large as for the case a), but the transmission of the L0 signal is only one half for the case  $K=0$ , the rest of the L0 power is lost through port 4, if it is not used to monitor the L0.

An IF frequency of 3.6 GHz corresponds to a path length difference of 41.6 mm for the diplexer arms for case a). The frequency bandwidth of interest (see figure 5.22) is centered around 3 GHz, which corresponds to a path length difference of 50 mm for the case a) with  $K=0$ . The diplexer arm lengths were adjusted to 160 and 210 mm. With the diplexer adjusted this way the signal at the  $D_2O$  Raman emission frequency (channel #18) is tapered by 10% by the instrumental function of the diplexer, while the spectral channel at the extreme of the pass band (channel #1) is tapered by 16%. The total transmission of the L0 path of this diplexer has been measured to be better than 80%, we assume a similar transmission for the signal path in addition to the tapering due to the instrumental function.

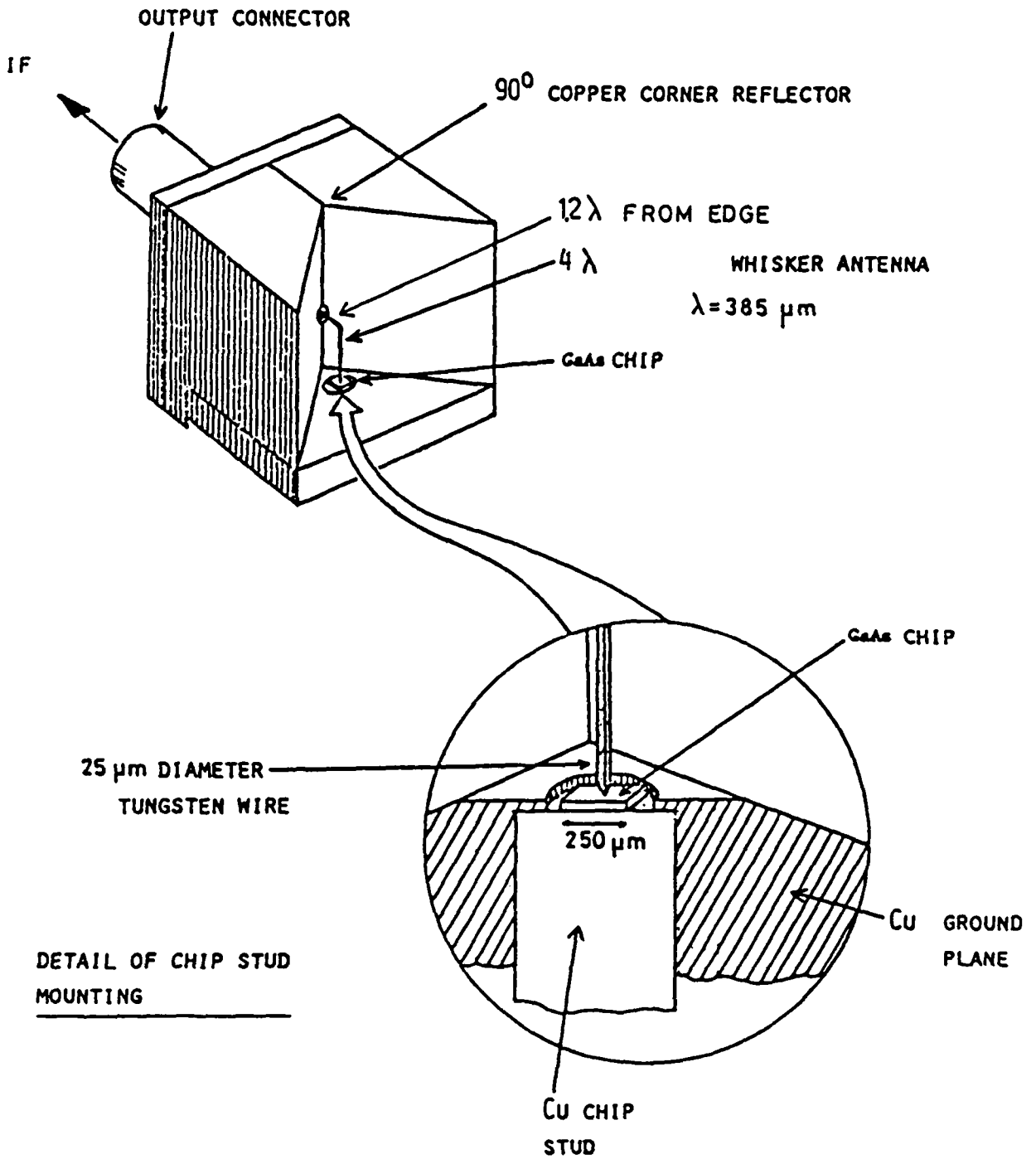


FIGURE 5.11. The Schottky barrier diode mixer mount [21].

### 5.5. The Schottky barrier diode mixer.

The Ga-As Schottky diode is mounted in a corner cube reflector as shown in figure 5.11 [10-12,20,21]. A 25  $\mu\text{m}$  in diameter phosphor-bronze whisker, is bent to form a  $4 - 1.2 \lambda$  antenna. Calculations and measurements [22-24] have shown that the antenna pattern forms a single lobe of 12 dB maximum gain, compared to a free standing antenna. The antenna lobe is oriented at an angle of  $25^\circ$  with respect to the  $4\lambda$  wire and has a full-width angle of  $15^\circ$  at -3dB [22,23].

The gaussian FIR beam of 14 mm waist emerging from the diplexer must be matched to the dimensions of the mixer antenna pattern. This is achieved by a parabolic mirror (M19 figure 5.4) of 110 mm focal length.

The position of the whisker in the corner cube mount is rather critical [13], and can only be adjusted before the contacting of the diode. An adjustable corner reflector would be advantageous although difficult to build because of the small dimensions.

The diode chips and the corner cube mount were supplied by Farran Research Associates, Cork Ireland [21]. Each chip contains several hundred diode elements of 1  $\mu\text{m}$  diameter (see figure 5.14), a section of a chip is shown in figure 5.12. The Schottky barrier is formed between the Au-Pt metal layer and the N-epilayer, the whisker is only serving as a microwave antenna and does not contribute to the contact apart from a slight increase of the stray capacitance of the diode.

#### 5.5.1. Contacting the Schottky diode.

The whiskers are electrolytically etched in a solution of 5% NaOH with a voltage typically of 1.2 V AC to get a tip of approximately 0.5  $\mu\text{m}$  in diameter.

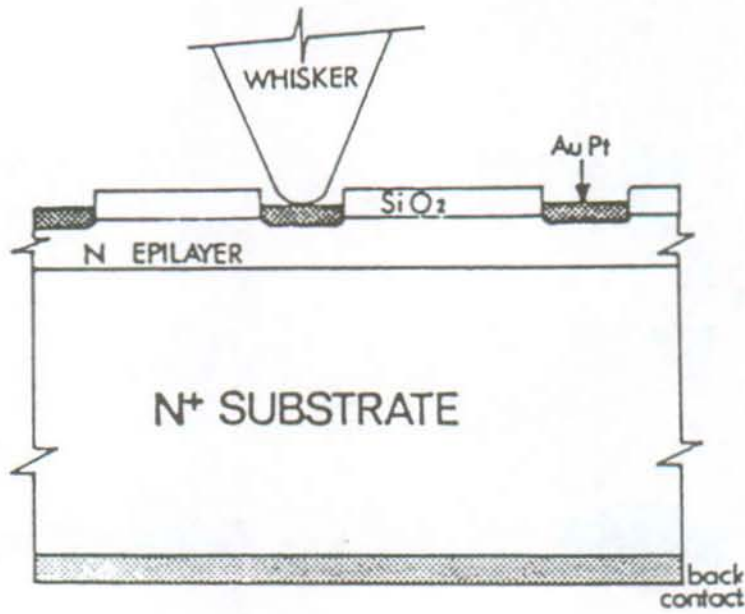


FIGURE 5.12. Cross section of a Schottky diode chip [10].

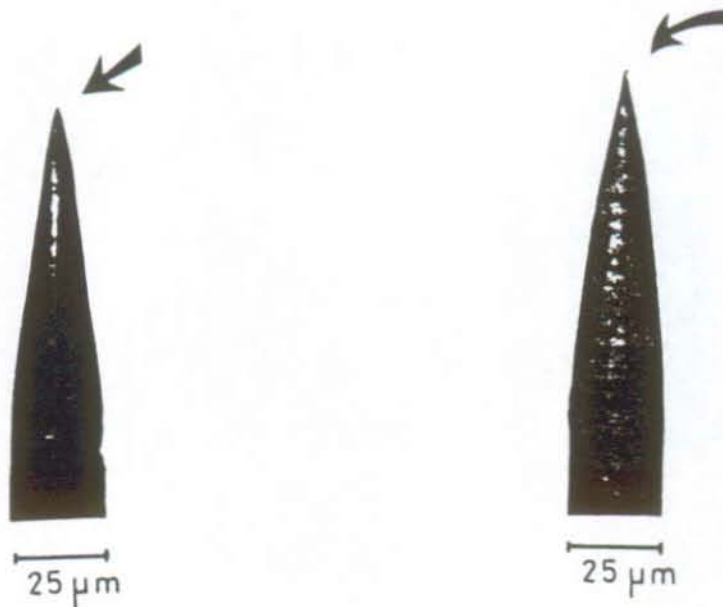


FIGURE 5.13. The whisker tip as seen through a high power optical microscope. The one on the left has an acceptable shape, while the right whisker tip has been bent during contacting.

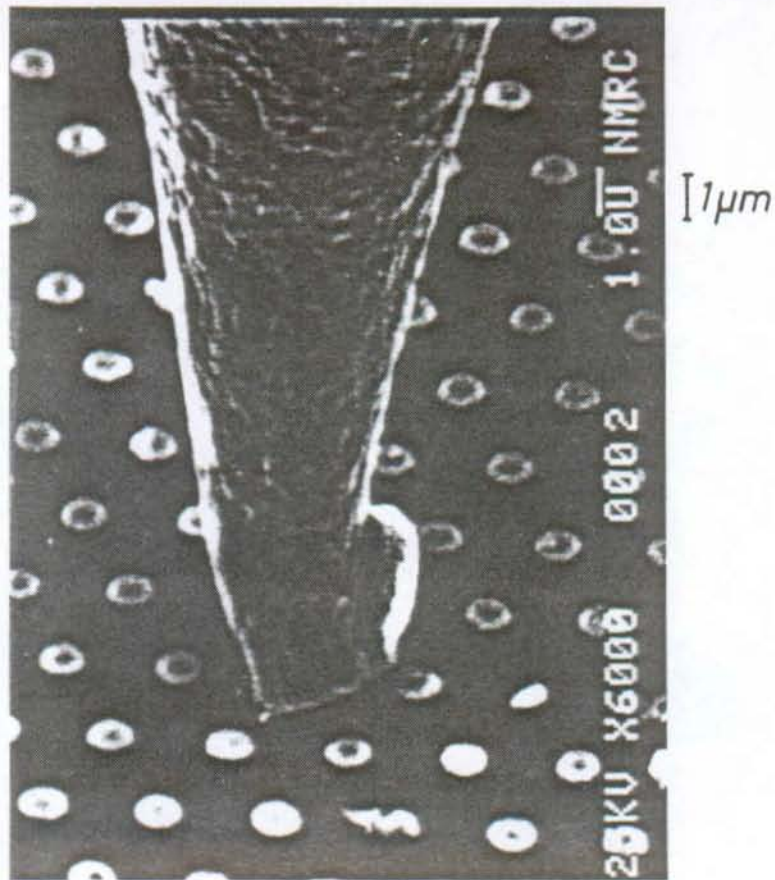


FIGURE 5.14a. Enlargement of a bad Schottky diode contact.

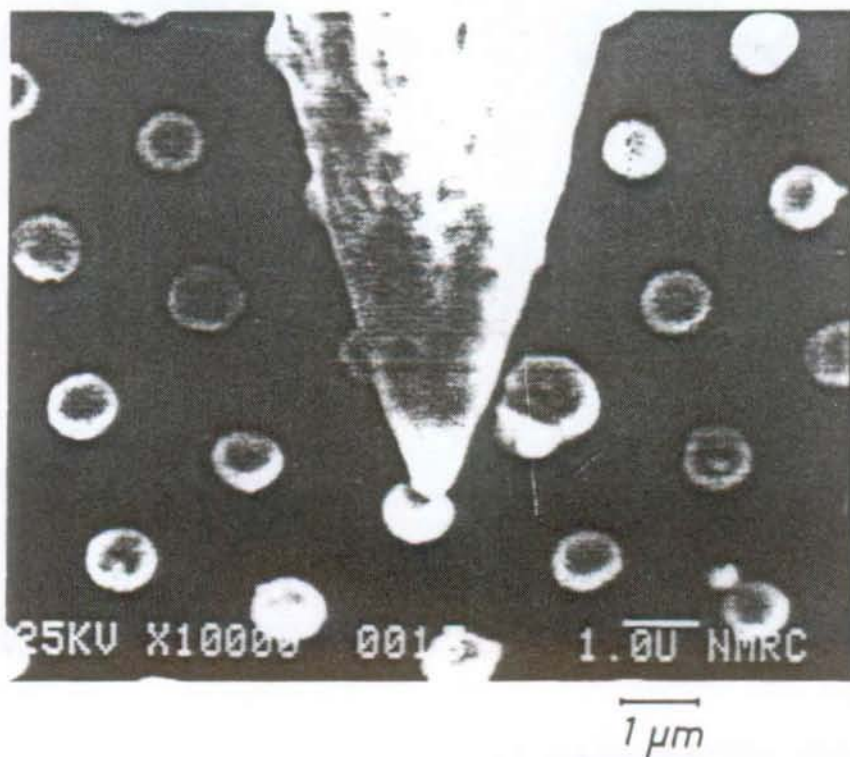


FIGURE 5.14b. Enlargement of a good Schottky diode contact.

Figure 5.13 shows two whisker tips as seen in an optical microscope (magnification 500x). The left whisker has been etched to obtain the desired sharp point, the tip of the whisker on the right has been damaged during contacting. It is preferable to reetch the whisker before each contacting procedure to obtain optimum performance of the mixer.

Figures 5.14a and b show scanning electron microscope photographs of the whisker and the chip surface (courtesy Farran Research). The individual diodes show up as small dots (1  $\mu\text{m}$  in diameter). Figure 5.14a shows a badly contacted diode with the whisker tip bent due to excess contact pressure on the chip surface after a mechanical shock to the corner cube.

The current-voltage dependence of a Schottky barrier diode is given by the following relation [11,12,21]:

$$I = I_s \exp(q(V - IR_s) / (\eta kT)) \quad (5.18)$$

where  $I$  is the current through the junction,  $I_s$  is the saturation current,  $V$  the measured voltage across the junction,  $R_s$  the series resistance,  $\eta$  the quality factor,  $q$  the electron charge,  $k$  the Boltzmann constant and  $T$  the junction temperature. The quality factor is a measure of how close the real diode matches the theoretical exponential I-V curve. For a good diode contact  $\eta$  is close to one, but always  $\eta \geq 1$ .

Figure 5.15 shows the equivalent electric circuit of a Schottky barrier diode. The signal is generated by the non linear capacitance and resistance  $C(V)$  and  $R(V)$ . For optimum operation in the FIR the series resistance  $R_s$  and parasitic capacitance  $C_p$  must be kept small. The diodes we use have typically 12-18  $\Omega$  series resistance, 2-4 fF junction capacitance and a quality factor of 1.1-1.3. The equivalent RC cutoff frequency of these diodes is higher than 10 THz and is mainly limited by the stray capacitance of the whisker contact and the series resistance of the barrier.

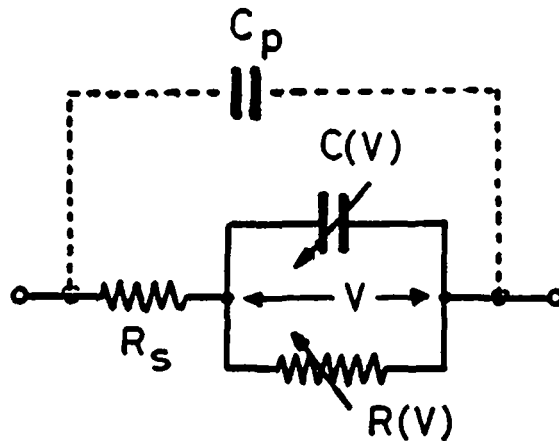


FIGURE 5.15. The equivalent electric circuit of a Schottky barrier diode. Typical values for normal operation are:  $R_s = 12 \Omega$ ,  $C_p + C(V) = 2.5 \text{ fF}$ ,  $R(V) \sim 100 \Omega$ .

In general  $R_s$  and  $\eta$  are determined by measuring the voltage across the diode for 4 currents (1, 10, 1000, 10000  $\mu\text{A}$ ). From these data points the parameters can be evaluated using expressions derived from equation 5.18 [11]:

$$\eta \approx q(V_1 - V_{10}) / (\kappa T \ln(10)) \quad (5.19)$$

$$R_s \approx 100 \left( (V_{10000} - V_{1000}) - (V_{10} - V_1) \right) [\Omega] \quad (5.20)$$

From our experience, the values obtained with these formulas underestimate the theoretical values by up to 50%. It is to be noted that for a current flow of 10 mA, the current density in the 1  $\mu\text{m}$  diameter diode is of the order of  $1.3 \cdot 10^6 \text{ A/cm}^2$ , which is often fatal for the diode junction.

For routine measurements of the I-V characteristics of Schottky diodes we have developed an instrument which samples the I-V curve at typically 250 points, stores the data in digital form and transfers it to a PDP-11 for further analysis.



*I-V Trace of Schottky Diode*

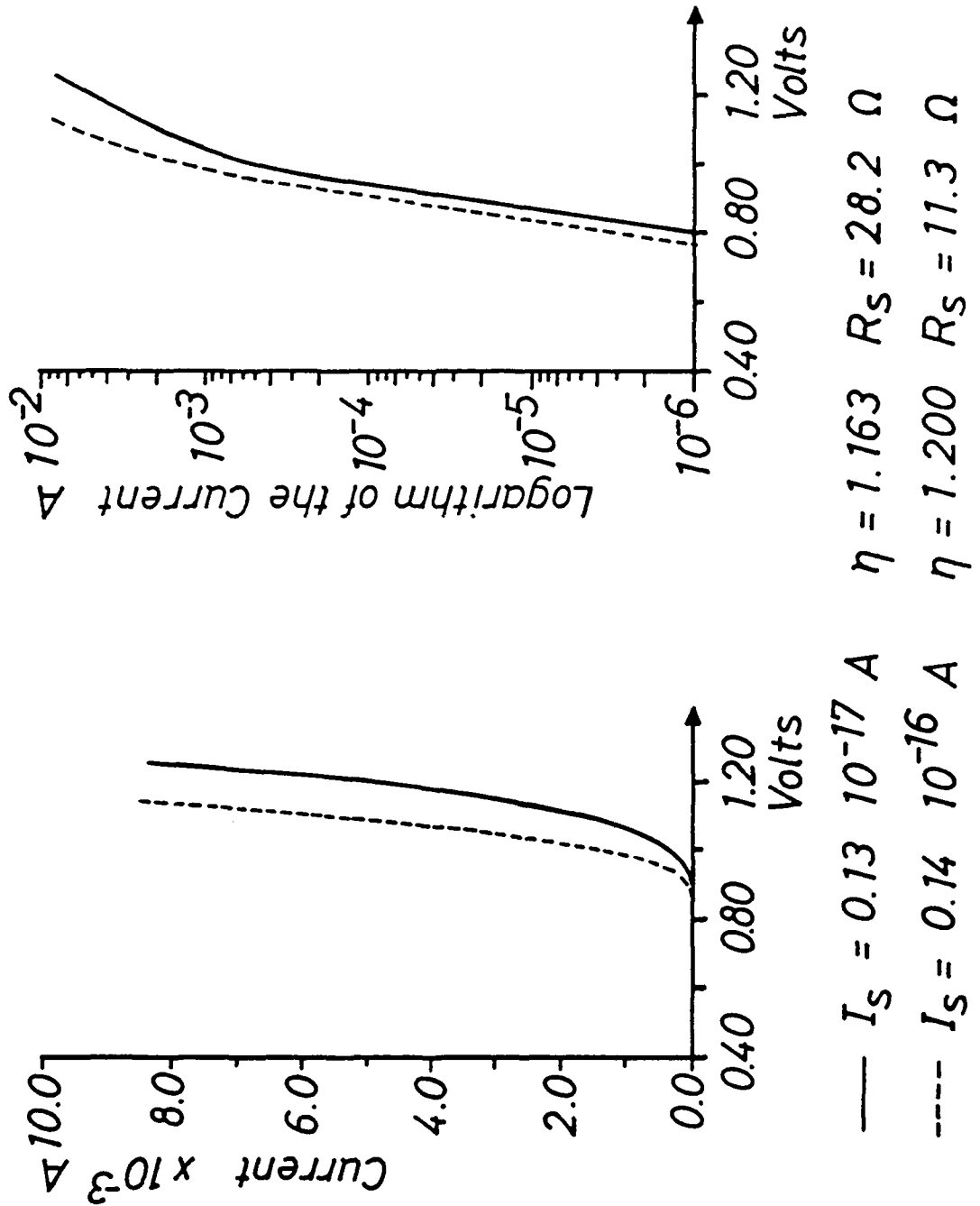


FIGURE 5.16. Measured I-V curves of Ga-As Schottky diodes.

The microprocessor controlled instrument applies to the diode a series of voltage pulses generated by a 12 bit DAC of less than 1 ms duration and with increasing amplitude. At the same time the voltage drop across a calibrated series resistance is measured by a 12 bit ADC to obtain the current flowing through the diode. In a measurement with short pulses the risk of damaging the diode at high current is decreased. The analysis taking into account a complete I-V curve is more precise in the determination of the parameters  $R_s$  and  $\eta$  which are obtained from a numerical fitting procedure to equation 5.13.

Figure 5.16 shows the I-V (current-voltage) curve of two diode contacts, a good and a rather poor contact, with  $R_s > 16 \mu\Omega$ , measured by the instrument described above. The effect of the series resistance  $R_s$  on the I-V curve is evident on the upper part of the curve ( $I > 1 \text{ mA}$ ) which is drawn with a logarithmic scale.

#### 5.5.2. Operating the Schottky diode.

The Schottky diode is operated with a constant bias current of 200 to 600  $\mu\text{A}$  to reach a point on the I-V curve with optimum mixer performance. The bias current is provided by a battery powered current supply to ensure electric isolation and to minimize ground loop problems.

Special care has been taken to keep the bias current of the diode constant even when a pulsed local oscillator is used. For the circuit shown in figure 5.17. the change in current during the LO pulse is less than 0.5% as shown in figure 5.18, and we measure a voltage modulation of 150 to 200 mV during the LO pulse, see figure 5.19.

The voltage modulation, which is proportional to the LO power incident on the mixer, is used to optimize the adjustments of the diplexer and the alignment of the diode.

SCHOTTKY DIODE STABILIZED CURRENT SOURCE

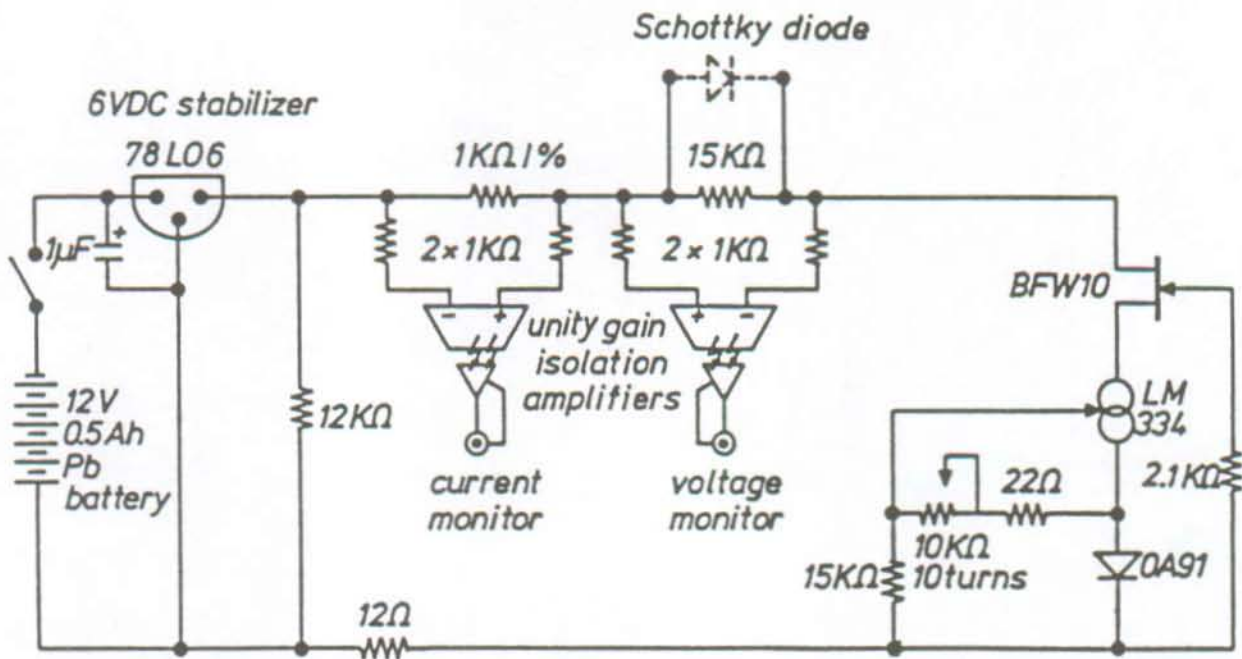


FIGURE 5.17. The battery powered constant bias current supply.

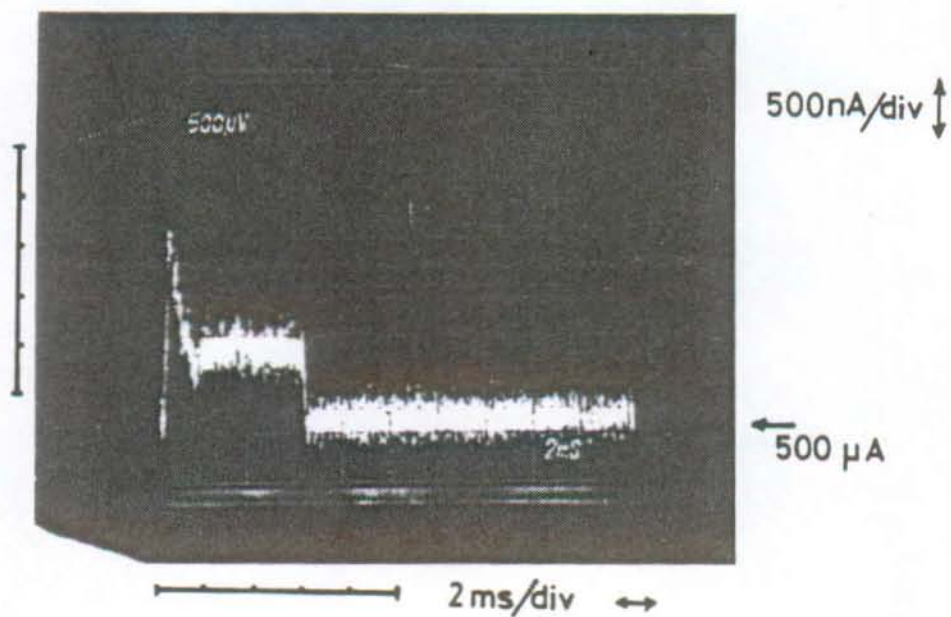


FIGURE 5.18. The current change in the Schottky diode during the LO laser pulse.

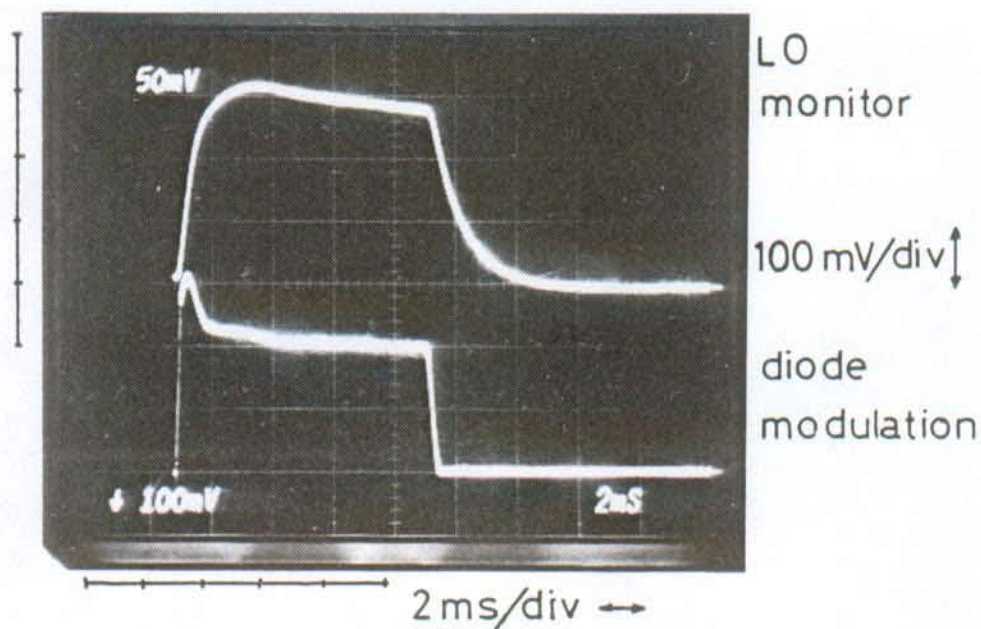


FIGURE 5.19. The voltage drop across the Schottky diode during the LO laser pulse (lower trace). The upper trace is the signal from the LO pulse monitor.

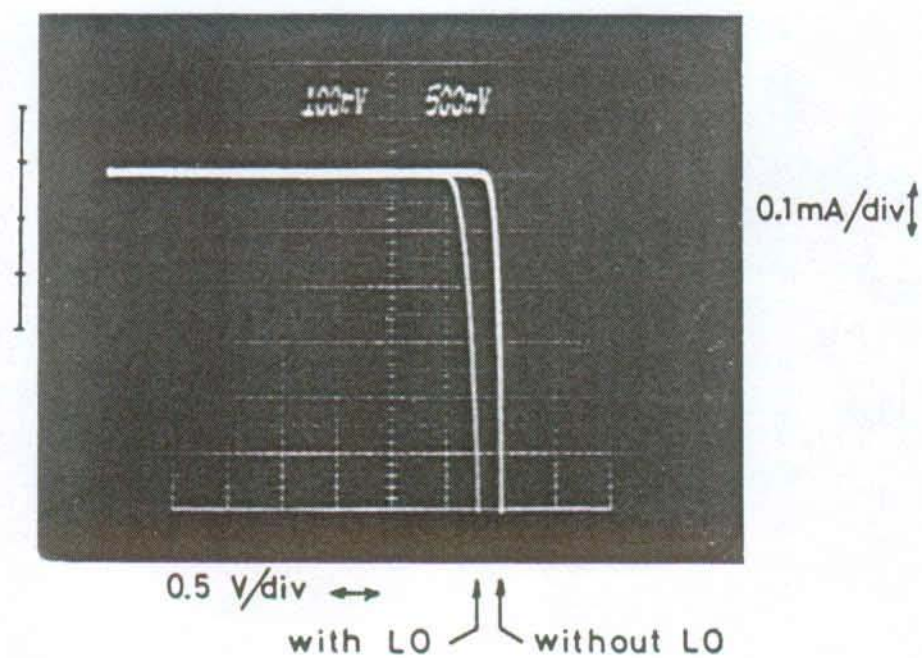


FIGURE 5.20. The effect of the LO on the Schottky diode I-V curve.

The effect of the optical power incident on the mixer, which is mainly the power of the LO laser, is given in figure 5.20. This figure shows the diode I-V curve measured with and without the LO power on the mixer diode. With a constant bias current applied to the diode the voltage modulation of figure 5.19 represents a displacement on figure 5.20 along a horizontal line at the level of the imposed bias current. Figure 5.18 shows the displacement from the horizontal position of this line during the LO pulse.

The sensitivity of a Schottky diode can be specified by the amplitude of this voltage modulation for a given incident LO power. The comparison of modulation values quoted in the literature for different Schottky diode mixers is only possible if the bias supply circuit is really insensitive to the changes in the diode I-V characteristics due to the incident LO power. This is, however, not always the case.

#### 5.6. IF amplifiers, filters and square law detectors.

At the output of the Schottky diode mixer the signal to noise ratio is of the order of one. Low noise amplification, filtering and integration must be used to be able to distinguish the signal from the noise. Figure 5.21 shows the IF circuit used for the heterodyne receiver.

Throughout the system low noise Ga-As amplifiers with a pass band from 2 to 4 GHz (the S-band) were used (Miteq model AMF-3B-2040). The design of the IF section is based on a heterodyne receiver built by Farran Research [21].

With respect to the noise temperature of the mixer, the first amplifier in the chain (A1) is the most important one (see appendix B equation B.21). We use a broadband, low noise amplifier with 35 dB gain and a noise figure of 2.3 dB. The input noise level is approximately -80 dBm. A second amplifier with a 2.5 dB noise figure and similar gain is connected in series. Because of the high gain of these two first ampli-

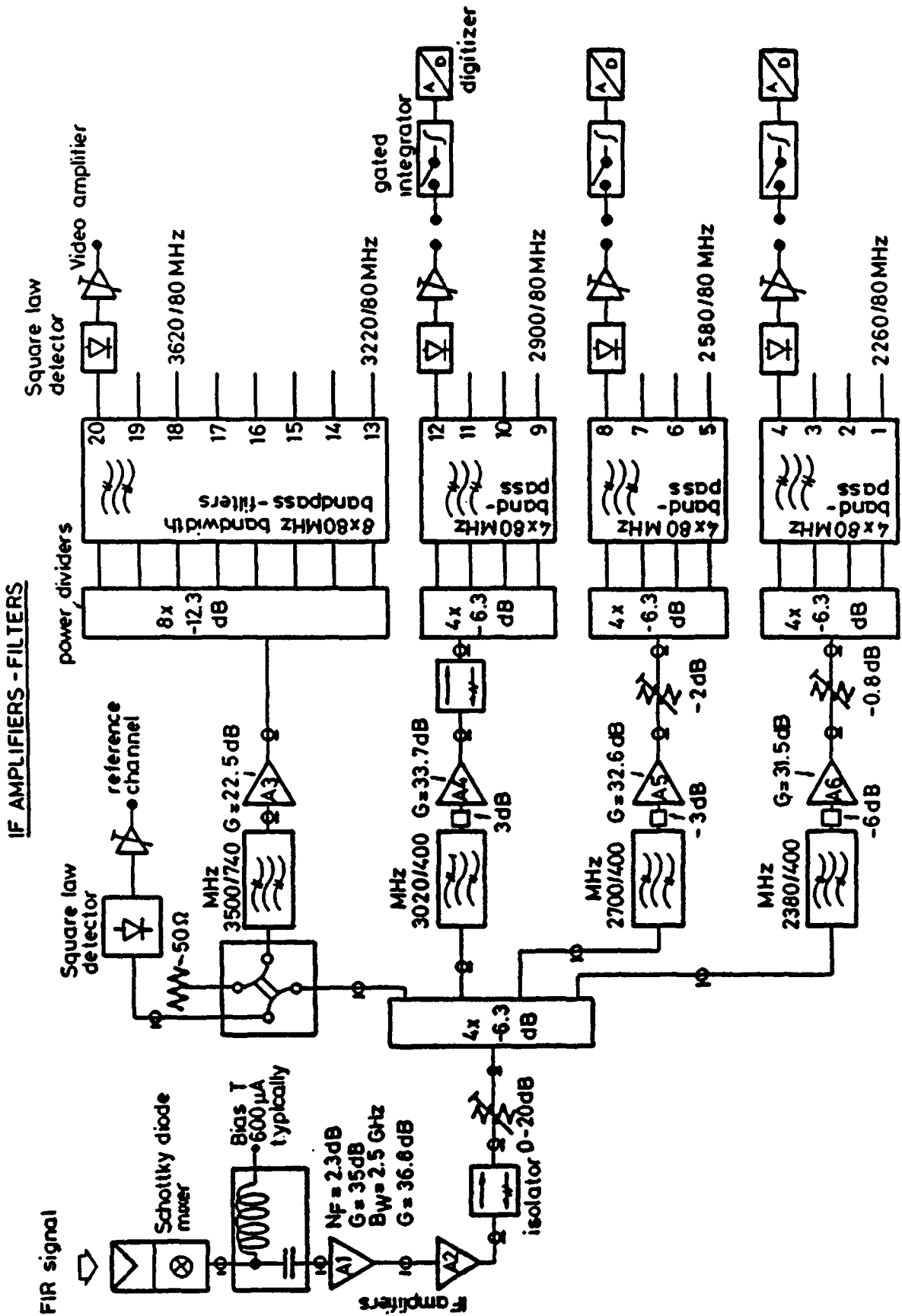


FIGURE 5.21. The IF amplifiers - filters section.

fiers the contributions of the later stages do not affect the overall receiver NEP. The two amplifiers have not shown any tendency to self oscillate. The output noise signal level after this second amplifier is about -10 dBm.

For decoupling of the following stages a microwave isolator separates the IF amplifier A2 and the filter bank. A -0.3 to -20 dB, continuously adjustable attenuator allows us to adjust the signal level to stay within the dynamic range of the following amplifiers.

The signal is divided into four branches by a first power divider. In three of these branches the signals are pre-filtered (A-C: 400 MHz bandwidth) then amplified and separated again into four 80 MHz bandwidth channels by a set of pass-band filters (channels #1 to #12). The signal in the fourth full-band branch is either sent to a square law detector and used as a monitor signal (channel "ref."), or sent to another amplifier (A3, filter D) and a set of 80 MHz bandpass filters to resolve the frequency region just around the FIR laser Raman line (channels #13 to #20). These channels are used essentially for recording and adjusting of the FIR laser by observing the stray light. The pass-bands of the filters, relative to the spectral distribution of the scattered light is shown in figure 5.22.

All filters used are coaxial 8 or 10 stage microwave filters from K&L, Maryland, model B120. They have typically 1 to 5 dB insertion losses. Since the band pass filters reflect the spectral components outside their pass band some interference between parallel channels is to be expected. At the input of the 80 MHz filters we have observed distortions of  $\pm 1$  dB due to interference with reflected signals. These distortions are of the same magnitude as the gain variations over the spectral width of the IF amplifiers and can be tolerated.

We use the general purpose Hewlett-Packard model 33330B coaxial square law detectors to detect the IF signal in each of the 20 IF channels. These detectors cover the 0.01 to 18

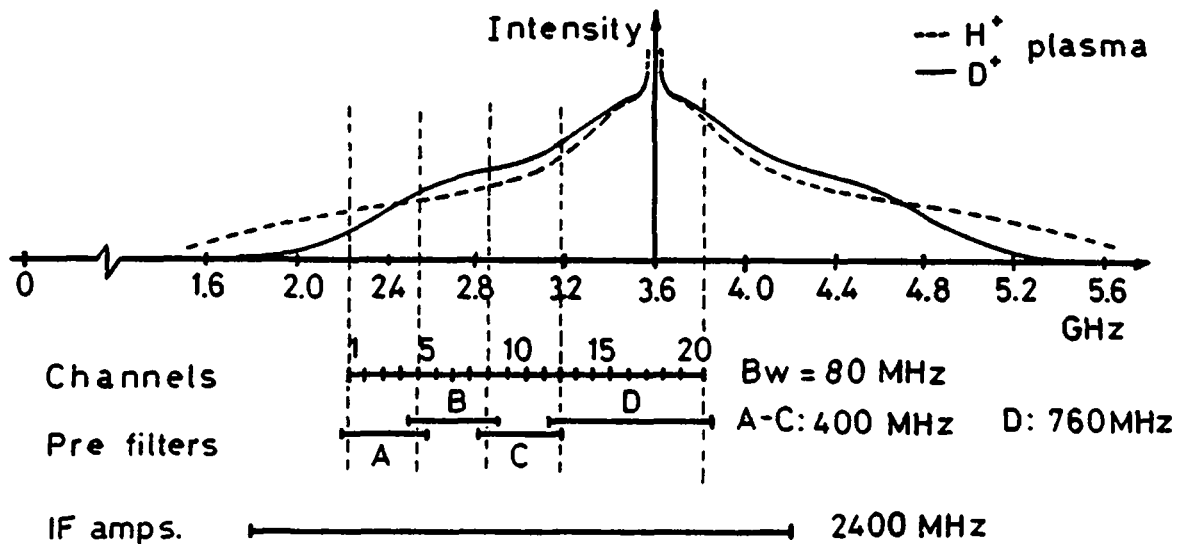


FIGURE 5.22. The frequency distribution of the IF filters for typical hydrogen and deuterium plasmas on TCA.

GHz frequency band and have the advantage of a certified frequency response within  $\pm 0.3$  dB for all devices. The responsivity is typically 10 mV for -10 dBm power with a 475  $\Omega$  load. The power limit for square law response is about -5 dBm.

The 20 adjacent 80 MHz channels cover the 2.22 to 3.8 GHz region. The available integrator-digitizer bank has 12 channels, so that the filters actually in use are selected depending on the expected frequency width of the scattered signal.

#### 5.6.1 Measurement of the IF amplifier noise figure.

The overall NEP of the receiver system depends to a large extent on the noise level generated in the IF amplifiers (see equation 5.11). The equivalent noise temperature can be estimated using the specified parameters of the individual components. An experimental confirmation is, however, necessary. It is common practice to determine the equivalent noise temperature by comparing the output signals for different calibrated power levels. A well defined, broad band power level is obtained from a thermal source at a specified temperature. In our case we use a 50  $\Omega$  load at room temperature  $T_h$  and at



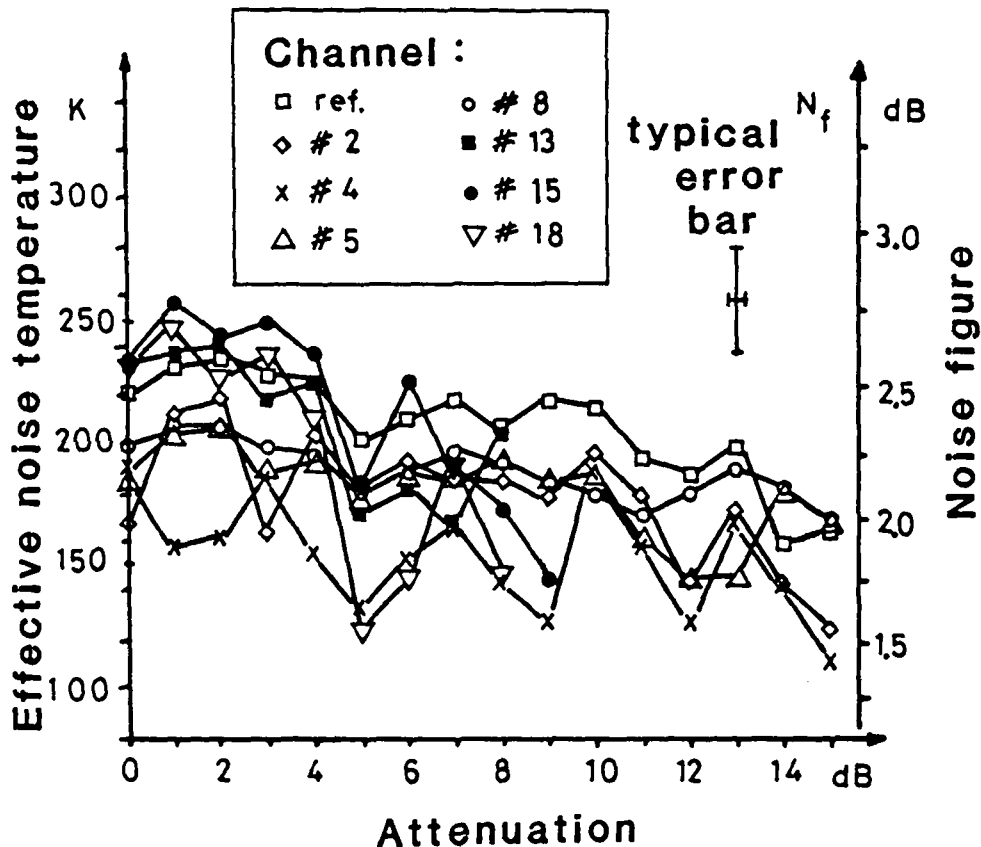


FIGURE 5.23. The IF amplifier noise temperature for a set of channels. Typical errors are  $\pm 10\%$ .

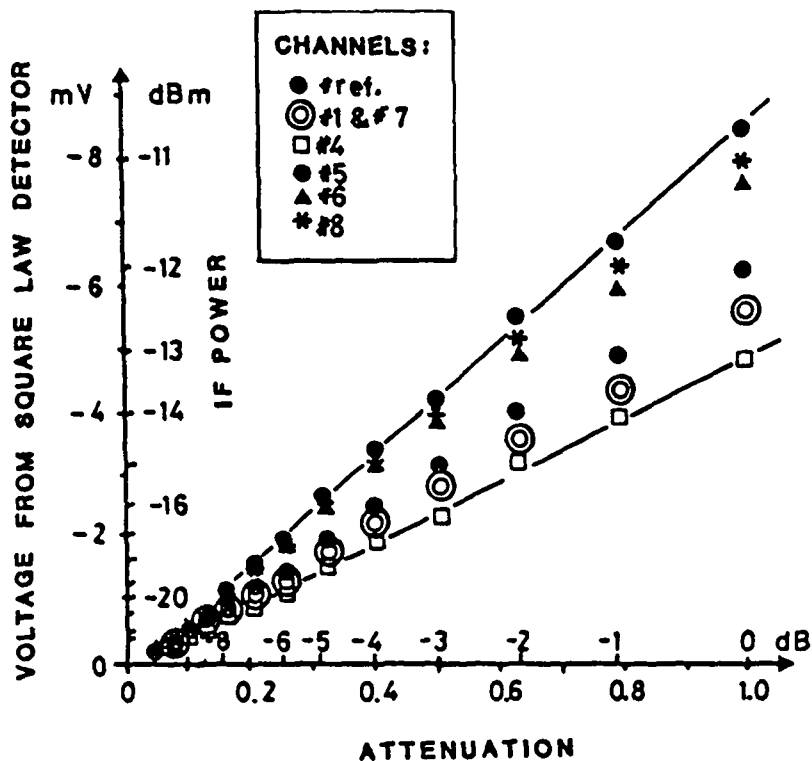


FIGURE 5.24. The IF amplifier linearity for some of the 80 MHz channels. The different slopes come from the dispersion in the gain of the IF amplifiers and intrinsic losses in the components. A  $50 \Omega$  thermal load was used instead of the Schottky diode.

liquid Nitrogen temperature  $T_c$  respectively. We can deduce the amplifier noise temperature  $T_a$ , and the noise figure  $N_f$  using the following equations (see also appendix B):

$$Y = V_h/V_c \quad (5.21)$$

$$T_a = (T_h - YT_c)/(Y-1) \quad [K] \quad (5.22)$$

$$N_f = 10 \log((T_a+T_0)/T_0) \quad [dB] \quad (5.23)$$

where

- $T_0 = 290$  K, is the standard effective noise temperature.
- $T_a$  is the amplifier effective noise temperature.
- $T_c$  is the effective noise temperature of the cold source.
- $T_h$  is the effective noise temperature of the hot source.
- $V_c$  is the output voltage after the square law detector when measuring the radiation from the cold source.
- $V_h$  is the output voltage when observing the hot source.
- $Y$  is the quality factor (see appendix B).

The noise figure for a set of channels and for different adjustable attenuator settings (attenuator positioned after the second IF amplifier of figure 5.21) is shown in figure 5.23. We measure with the method just described a mean value of 210 K (2.37 dB) which corresponds to the noise figure of 2.3 dB of the first IF amplifier. Values as low as 150 K are measured indicating that the noise figure of the amplifiers are below 2.3 dB within certain parts of the amplifier bandwidth. The fluctuations are explained as changes in the standing wave ratio (SWR) in the adjustable attenuator. The overall tendency to measure a lower noise figure for lower power levels (higher attenuation) is not fully understood.

The linearity of some of the 80 MHz channels for output voltages up to 8 mV (IF power of -12 dBm) are shown in figure 5.24. This is well below the saturation power of the IF amplifiers, which have typically the 1 dB compression point at +14 dBm. Figure 5.24 is obtained using the output voltages of the square law detectors when replacing the mixer by a 50  $\Omega$  thermal load at room temperature.

The dispersion of the gain in the different channels is due to variations of up to  $\pm 2$  dB of the gain over the full bandwidth of the IF amplifiers, interferences of the parallel channels also contribute to up to  $\pm 1$  dB.

### 5.7. Impedance matching of the Schottky diode to the IF amplifier.

Optimum power transfer between two microwave components is achieved when their respective impedances are complex conjugated [9] (see equations B-43 and on). Typical microwave equipment has an impedance of  $50 \Omega$ , with a negligible imaginary part. The impedance of a Schottky diode mixer, however, is strongly dependent on the bias current and on the incident optical power. The effect of the power loss between the Schottky diode mixer and the IF amplifier section is to an increase of the conversion loss, hence an increase of the system NEP (see equation 5.11).

Measurements of the electric properties of the Schottky diode were done on a network analyser system (Hewlett Packard models HP 8510-A, 8514-A and 8350-B) at the "Laboratoire de Traitements des Signaux", of the "Département d'Electricité" at the EPFL. Figure 5.25 shows the voltage standing wave ratio (VSWR) as a function of frequency for the first IF amplifier (VSWR of 0.5 to 2.3 dB) and for the Schottky diode with a  $200 \mu\text{A}$  bias current. The diode exhibits VSWR values of 6 to 8.5 dB within the frequency range of interest. The influence of the LO signal, on the VSWR, has not been measured because neither the network analyser, nor the LO laser were portable.

The reflection coefficients of the Schottky diode mixer have been measured for different bias currents and in the presence of incident LO power. These measurements are given in table 5.2. They show that the presence of LO power increases the reflection coefficient, and thus reduces the effective power transfer from the mixer to the IF amplifier.

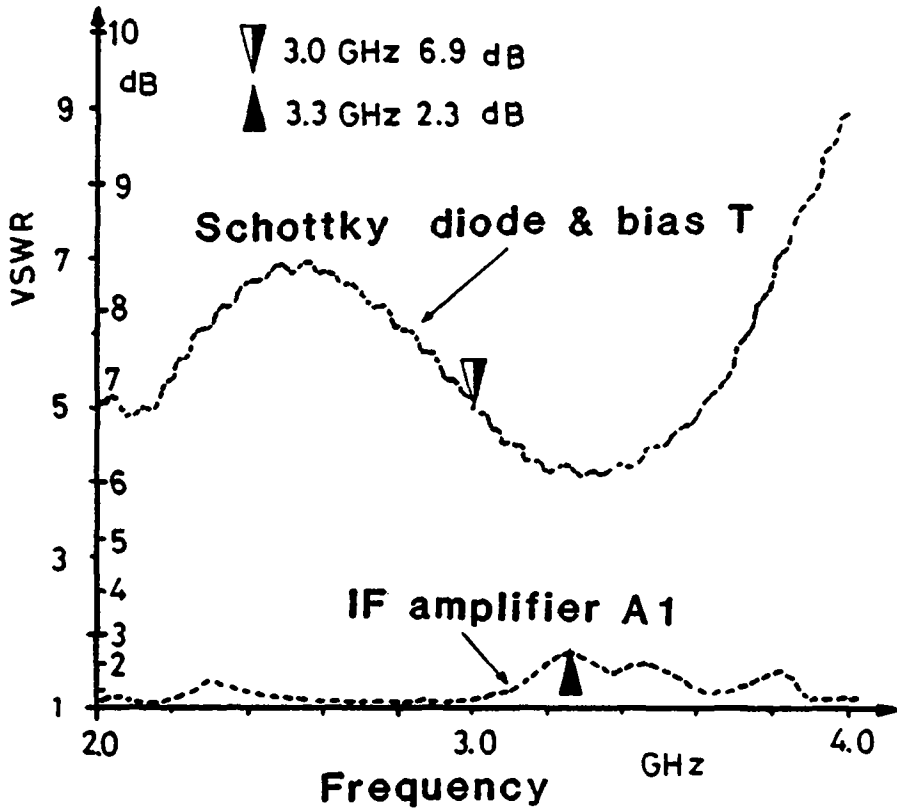


FIGURE 5.25. VSWR of the IF amplifier and the biased Schottky diode.

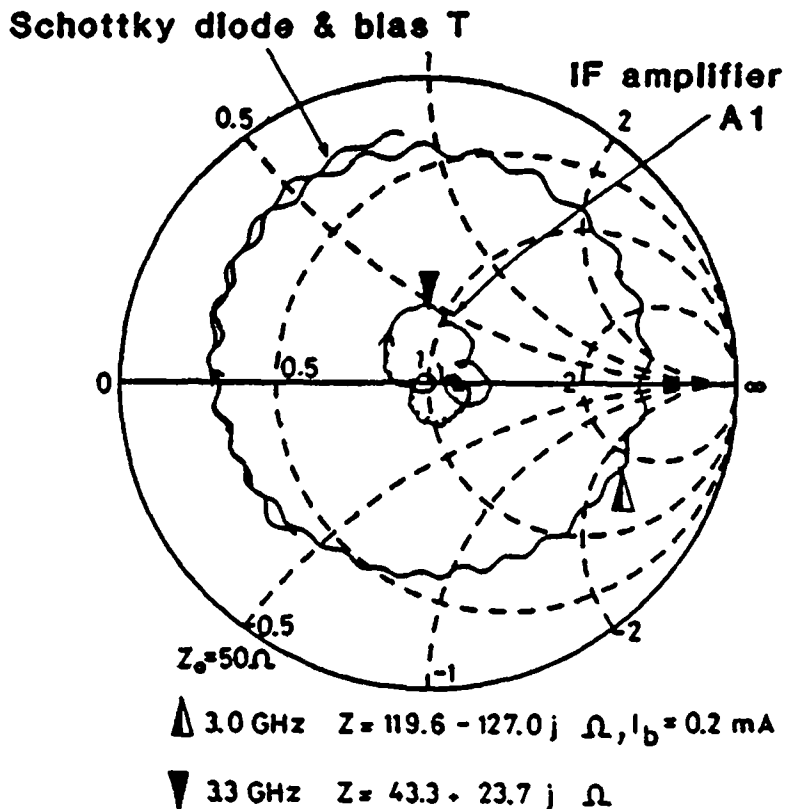


FIGURE 5.26. Smith chart of the IF amplifier and Schottky diode. Frequency scan from 2 to 4 GHz.

<u>Bias current</u>	<u>Without LO</u>	<u>With LO</u>
$\mu\text{A}$	dB	dB
200	-5.0	-3.0
300	-6.5	-3.5
400	-8.0	-4.0

TABLE 5.2. Reflection coefficient of Schottky diode mixer for different bias currents and with or without LO power incident on the mixer. Typical variation over the spectral range 2.2 to 3.8 GHz is  $\pm 1$  dB.

Figure 5.26 shows the Smith chart <sup>1</sup> (map of the complex impedance) of the first IF amplifier (A1) and the Schottky diode mixer with a 200  $\mu\text{A}$  bias applied. The frequency scan covers 2 to 4 GHz. Both amplifier and diode show an inductive behaviour, since the signal is rotating clockwise with the frequency.

An impedance matching L-C transformer, inserted between the diode mixer and the first IF amplifier, cannot be effective over the full 2.2 to 3.6 GHz bandwidth of interest. A matching circuit for a bandpass of 600 to 800 MHz (from 2.2 to 3 GHz) is however conceivable, but it must have an insertion loss below 4 dB to be of any interest. Such a device must be custom made, and a supplier has not been found.

### 5.8. Measurement of the total detection system NEP.

The basic concept of a measurement to determine the noise equivalent power or the noise temperature of the complete receiver is the same as for the measurement of the IF amplifier noise temperature. It relies on thermal radiation sources, which can be considered as absolute power standards. In this case, the cold source is a sheet of Eccosorb floating in liquid nitrogen, and the hot source a sheet of Eccosorb at room temperature. A rotating chopper wheel alternately exposes the receiver input to either of the two sources.

---

<sup>1</sup> The formulas relating the values of figures 5.25, 5.26 and table 5.2 are given in the appendix B, equation B.43.

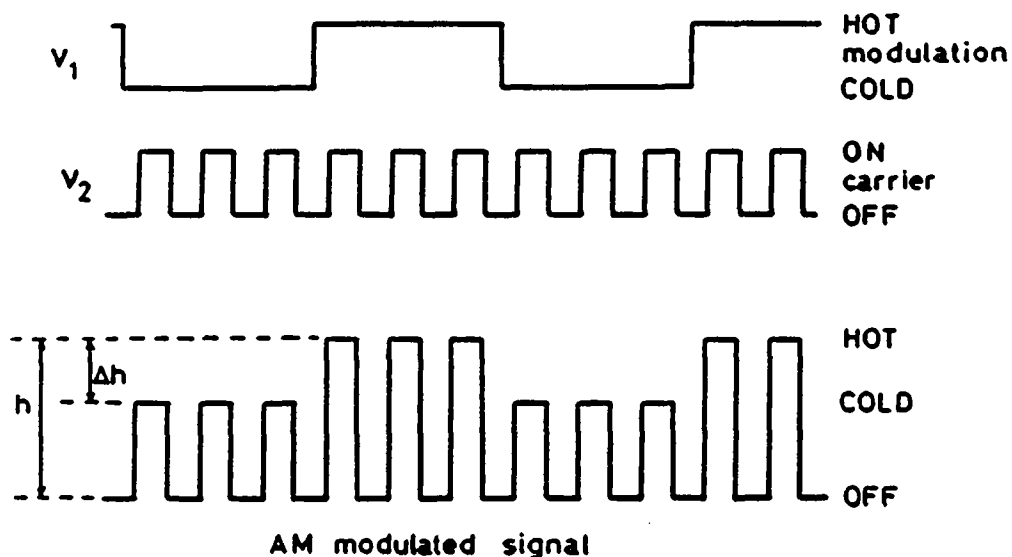


FIGURE 5.27. The AM modulation used for the system NEP calibration. Upper trace: the hot and cold sources, middle trace: the LO pulses giving the AM carrier frequency, and the lower trace: the AM pulse train sent to the lock-in amplifier. The modulation amplitude  $\Delta h/h$  is typically less than 0.5%.

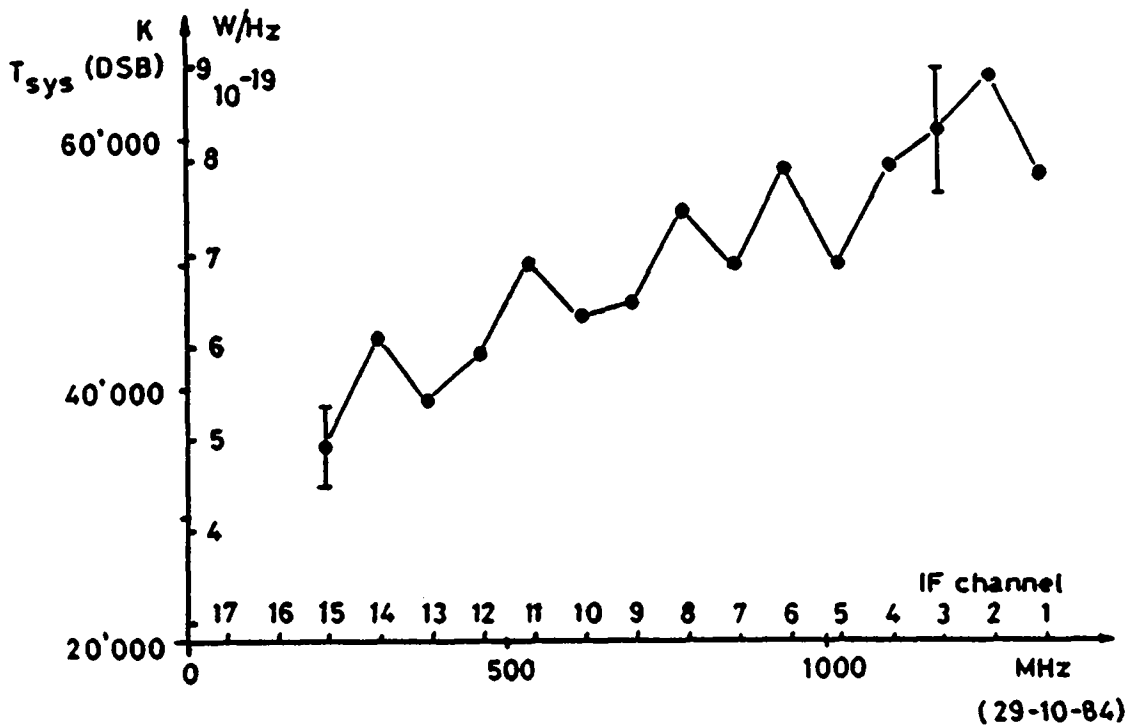


FIGURE 5.28. The measured double sideband NEP for different IF channels.

The equations 5.21 to 5.23 can be applied directly by replacing the amplifier temperature  $T_a$  by the system temperature  $T_{sys}$ . The typical 0.5% modulation of the output voltage of the square law detectors is extracted from noise with a lock-in amplifier.

As discussed earlier, the only way to provide sufficient power for the heterodyne detection is to use the LO laser in chopped mode. If the LO laser is adjusted for 50% duty cycle pulses at a frequency  $\nu_2$  and the hot and cold sources are alternated at a frequency  $\nu_1$  with  $\nu_2 \gg \nu_1$  then the resulting pulse train represents an amplitude modulated signal at the carrier frequency of the LO laser pulse frequency  $\nu_2$ , as illustrated in figure 5.27. This modulated signal is detected by a lock-in amplifier used as a kind of AM receiver by synchronizing the lock-in on one of the sidebands of frequency  $\nu = |\nu_2 - \nu_1|$ . This AM reception scheme has been calibrated for square pulses as shown in figure 5.27, the efficiency is  $20 \pm 5\%$ . The losses are due to the observation of one sideband (50% loss) and to the lock-in that measures the RMS value of the detected signal.

Since our diplexer has no side band rejection filters we measure directly the DSB (double side band) effective noise temperature, which is half of the SSB noise temperature (see appendix B). Our best measurement gives a DSB system temperature of  $35000^\circ$  Kelvin as shown in figure 5.28, with typical values around  $60000^\circ$  Kelvin ( $8 \cdot 10^{-19}$  W/Hz DSB). The NEP measurements do not include the losses in the optical system between the receiver and the tokamak. A correction factor of 3 to 6 dB will have to be taken into account.

The NEP of the receiver depends also on the local oscillator power through the conversion loss  $L_c(P_{l0})$ . The NEP may be further decreased if higher power from the  $CD_3Cl$  laser was available. During the scattering experiment the LO laser is operated in chopped mode with a 5% duty cycle, which results in a higher power than for the calibration measurement. Therefore the calibrated NEP values can be considered as an upper limit.

The measured NEP values of our system are up to one order of magnitude higher than the best values quoted in the literature [10-14,25,26]. The large bandwidth of 2 GHz of our receiver and the impedance mismatch can explain part of this difference.

### 5.9 Estimate of the conversion loss.

To further investigate this high NEP value, one has to sort out the contributions of the different elements of the heterodyne detection system. Let us assume a thermal source of power  $P_s$  is applied to the signal port of the diplexer. It will result in an electrical IF signal  $P_{IF}$  entering the first IF amplifier. The power conversion of this process implies a total conversion loss  $L$ , which includes optical losses  $L_o$  due to the diplexer, the mixing efficiency with the LO beam and the matching to the antenna pattern of the Schottky diode mixer. It also includes the intrinsic mixer diode loss of the optical to electrical conversion, and finally the loss due to the impedance mismatch of the mixer diode to the IF amplifier.

The two latter causes (defined by  $L_c$ ) are functions of the LO power  $P_{lo}$  and the Schottky diode bias current  $I_b$ :

$$L(P_{lo}, I_b) = L_o L_c(P_{lo}, I_b) = P_{\text{optical-signal}} / P_{if} \quad (5.24)$$

The NEP measurement consists of comparing this IF signal power to the intrinsic noise power generated by different elements of the detection system. These contributions are noise from the IF amplifier section and noise from the Schottky diode mixer. The latter comes from two independent noise sources, which are [10-12,26]:

- Thermal noise from the Schottky mixer diode internal resistance,
- Shot noise due to the current in the diode junction, produced by the bias current and the rectified current of the LO laser power.



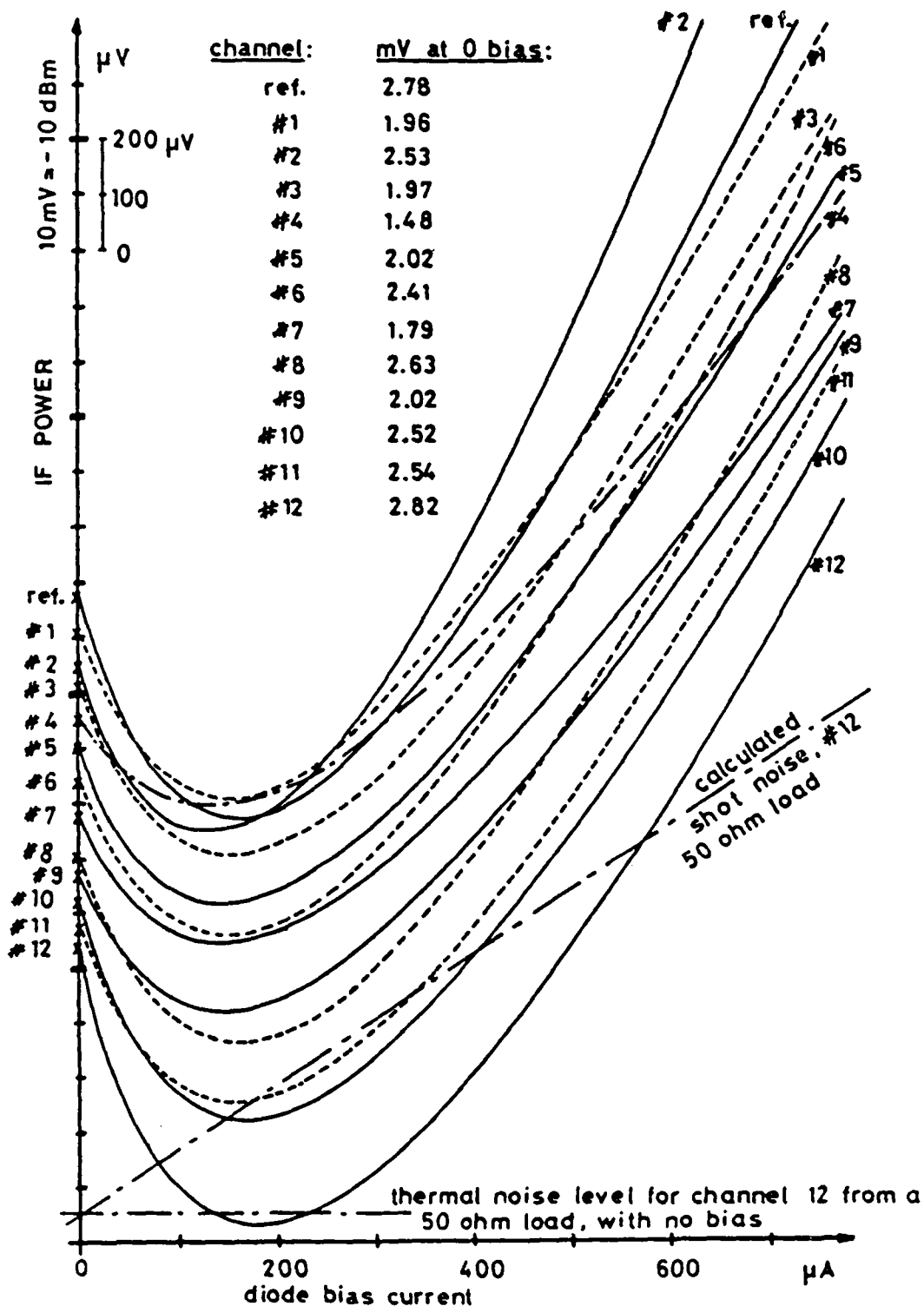


FIGURE 5.29. Measured noise power variation due to the Schottky diode bias current. For clarity the curves are displaced vertically by an arbitrary amount. The initial values (zero bias) are listed above. The noise power from a  $50\ \Omega$  load, replacing the Schottky diode mixer, produces a power level that corresponds to within 5% to the minimum value of each curve. The measurement is obtained by recording the variation of output voltage from the square law detectors versus the Schottky diode bias current.

The current flowing through the diode junction causes also excess noise in the semiconductor material [26,10-12]. A more detailed description of the noise sources of the diode mixer goes beyond the aim of this presentation, but would be needed to fully explain the values presented in figure 5.29, which represents the total IF noise power varying with the mixer diode bias current. Even by considering variations of the mixer diode impedance with the bias current, we cannot explain the decrease of noise power for bias currents below 200  $\mu$ A as shown in figure 5.29. The measured thermal and calculated shot noise powers from a 50 Ohm load replacing the Schottky diode mixer are given for channel 12.

By using standard microwave terminology we can express the total system NEP by its equivalent noise temperature referred to the system input port (the diplexer signal port) by:

$$T_{\text{sys}} = (L_o - 1) T_d + L_o T_m + L_o L_c (P_{\text{if}}, I_b) T_a \quad (5.25)$$

where

- $T_{\text{sys}}$  is the total system effective noise temperature,
- $T_d$  is the diplexer temperature, set to 290 Kelvin,
- $T_m$  is the Schottky diode mixer temperature,
- $T_a$  is the IF amplifier effective noise temperature,
- $L_o$  is the optical loss up to the mixer diode,
- $L_c$  is the mixer loss (including impedance matching).

Of the optical losses, only the diplexer transmission of 80% is known. The resulting mixer temperature and conversion loss can be estimated by inserting known attenuators between the Schottky diode and the first amplifier (see appendix B, equation B.36). We have measured conversion losses of 17 to 20 dB. Assuming that our Schottky diode mixer has an effective noise temperature of 5000 K, which is comparable with values quoted in the literature, then equation 5.25 and the result from figure 5.28 leads to an optical loss  $L_o$  of at least 3 dB.

With these high losses there is room for improvements, both on the coupling of the optical radiation onto the diode whisker, and on the power transfer to the first IF amplifier.

#### 5.10. The video amplifiers.

The signal levels from the square law detectors of the 20 IF channels are of the order of 0.5 to 10 mV on a 475  $\Omega$  load. A set of video amplifiers adapt these signal levels to the dynamic range of the integrators.

The Hewlett-Packard square law detectors used should not be biased. This means that care must be taken to avoid that the input current offset of the subsequent video amplifier changes the operation point and therefore the square law characteristic of these detectors.

Two stages of video amplifiers were used in front of the integrators-digitizers: (1) a fixed gain amplifier including a 50  $\Omega$  line driver situated close to the square law detector, and (2) a variable gain amplifier with a switch-in attenuator of -20 dB. Both stages have similar bandwidths.

The circuit diagram of the first video amplifier is shown in figure 5.30. It provides a gain of typically 33 dB and a bandwidth from DC to 15 MHz. The cut-off frequency varies somewhat from one unit to the other. The input offset current is less than 5 pA so that perturbations of the square law detectors are not to be expected. These amplifiers have, however, an output offset voltage of  $\pm 20$  mV with a temperature dependence of 2 mV/ $^{\circ}$ C. DC coupling to the following amplifier and the integrator is therefore not acceptable. These amplifiers can neither be used for the calibration measurement because of this DC offset and their high temperature dependence. Since the DC component is not important for the analysis of the signals during the scattering experiment a high pass filter with a cut-off frequency of 30 kHz was used. The final bandwidth of 30 kHz to 15 MHz was found to be adequate for a scattering experiment with laser pulses of 0.5 to 1.5  $\mu$ s duration.

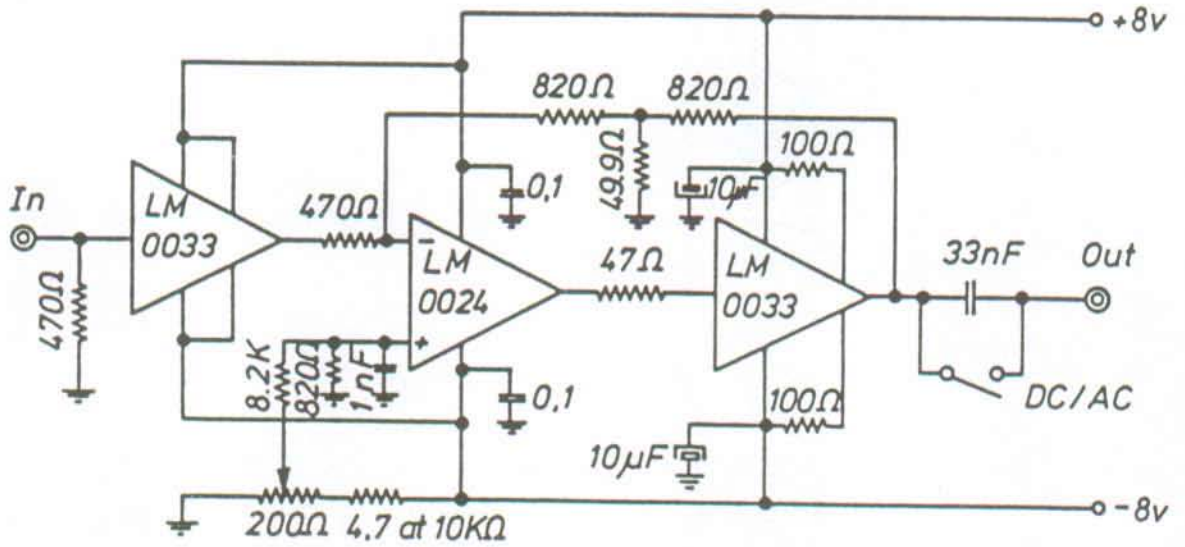


FIGURE 5.30. The first 33 dB fixed gain video amplifier. The typical input current offset is less than 5 pA.

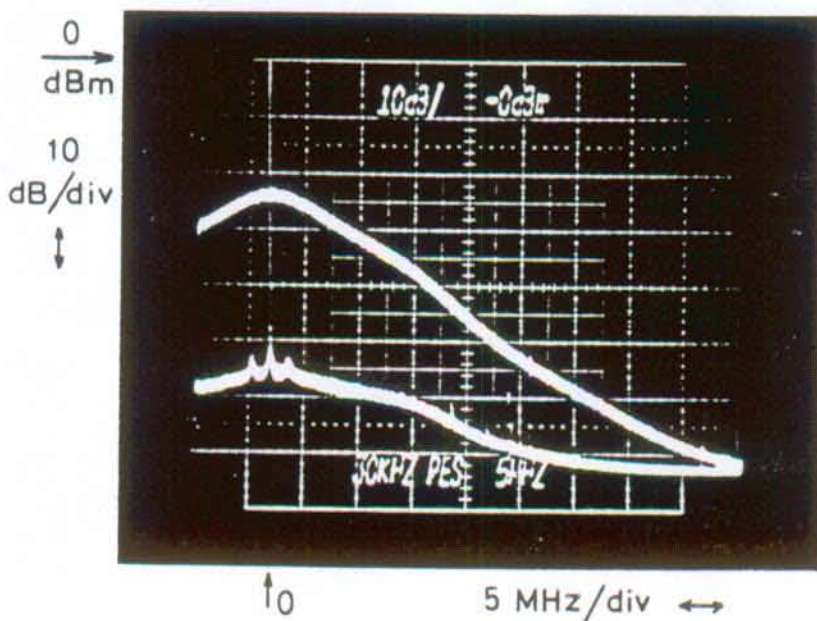


FIGURE 5.31. The noise power spectrum of the video amplifiers (lower trace) and of the total IF system (upper trace).

The second set of video amplifiers have an adjustable gain of -30 to +30 dB, and were built into a CAMAC module. During the measurement of the scattered signals, these amplifiers were also used with an AC coupling to avoid 50 Hz pick-up.

Figure 5.31 represents the noise power spectrum with and without IF amplifier noise applied to the square law detection diodes. The IF noise contribution came from a 50  $\Omega$  load installed in place of the Schottky diode mixer. It is clear from figure 5.31 that the noise due to the video amplifiers can be neglected compared to the IF amplifier noise source.

#### 5.11. The CAMAC integrators - digitizers.

As has been shown in §5.1 the signal to noise ratio at the receiver output is improved by an integration over the duration of the D<sub>2</sub>O laser pulse. The signal to noise ratio after integration is given by (see equation 5.9):

$$s = \frac{P_s}{P_s + B \cdot NEP} \sqrt{1+B\tau} \quad (5.26)$$

where  $P_s$  is the scattered power within the IF bandwidth,  $B$  is the final channel bandwidth (80 MHz) and  $\tau$  the integration time (typically 1  $\mu$ s). For these conditions the improvement due to the integration (the square root value) is about 9.

The stored data element, one per channel and per acquisition, represents the time integrated signal of a particular spectral channel. The gate pulse during which the integrator is activated has to be synchronized precisely, and its duration matched, to the D<sub>2</sub>O laser pulse. This also discriminates against signals from electric pick-up, appearing a few hundred nanoseconds before the laser pulse, due to noise from the spark-gaps of the CO<sub>2</sub> laser.

We use the CAMAC, LeCroy model 2250L, gated current integrator, which is a 12 channel, 9 bit, fast ADC using a charge to time conversion technique. It needs only 11  $\mu\text{s}$  to perform a conversion, and has a 32-deep FIFO (first in, first out) memory buffer per channel. This allows us to obtain information on the background noise level by taking typically 9 pre- and 9 post-samples covering 150  $\mu\text{s}$  before and after the laser pulse. The mean background noise level is determined by averaging over these data elements.

The integrator accepts negative-going signals onto a 50  $\Omega$  impedance. The sensitivity is 12.8 V $\cdot$ ns or a charge of 0.48 pC per count. Gate durations from 10 ns to 3  $\mu\text{s}$  can be accepted, although the resolution decreases somewhat for gate durations above 200 ns due to thermal drift. For a 1.2  $\mu\text{s}$  gate the temperature coefficient is 5 counts per  $^{\circ}\text{C}$ . It is to be noted that for 1  $\mu\text{s}$  long gates a constant input voltage of -12 mV will saturate the integrator, hence the importance of minimizing parasitic signals.

To avoid blocking the integrator by a small positive going pulse, a current is injected to create a pedestal of some counts. The value of this pedestal is linearly related to the gate duration up to 3  $\mu\text{s}$ . The typical pedestal value is set to  $150 \pm 50$  counts.

As a demonstration of the linearity of the integrator figure 5.32 represents the ADC counts versus the product of input voltage times the gate duration for channel 12. The measurements of the other channels differ by less than 5%. The origin, or zero count, of figure 5.32, corresponds to the level of the pedestal. These measurements were obtained by applying to the integrator constant input voltages from +100 mV to -1 V and gate durations between 10 ns to 3  $\mu\text{s}$ , keeping within the limit of 12.8 V $\cdot$ ns. We notice that the slopes for positive and negative counts with respect to the pedestal value are slightly different. The expected scattered signal should, however, only give positive counts.

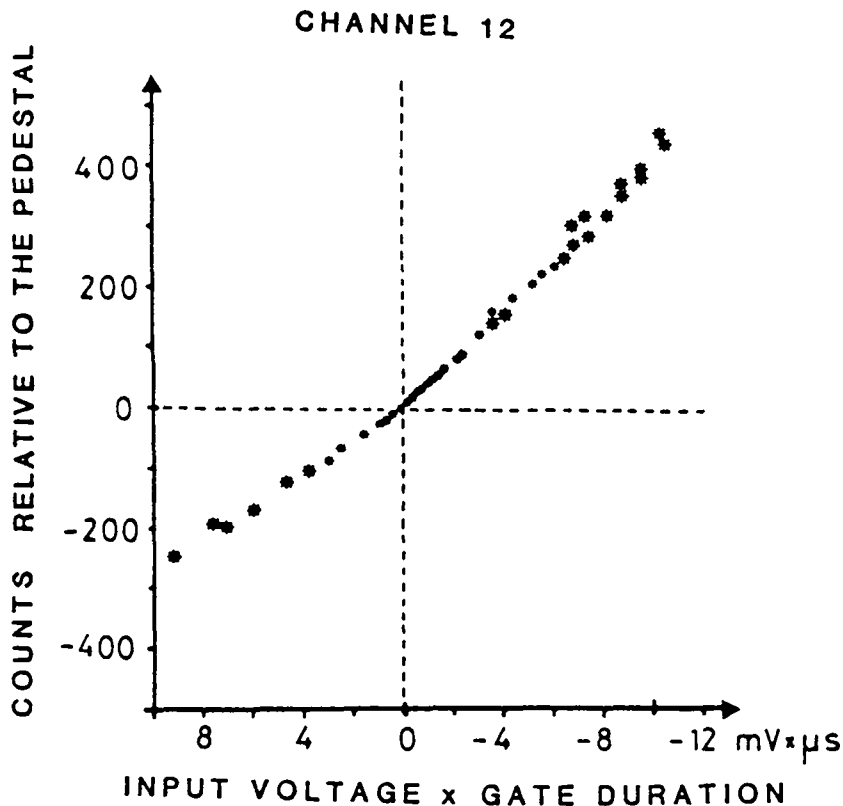


FIGURE 5.32. Linearity of channel 12 of the LeCroy model 2250-L integrator-digitizer. The curve is a superposition of several measurements for gate durations between 10 ns and 3  $\mu$ s, and input voltages from +100 mV to -1 V. The ADC counts are normalized to the pedestal value.

#### 5.12. The CAMAC timer and trigger system.

We have built a CAMAC timer unit to control the lasers and to synchronize the acquisition gates. It is a 10 channel programmable timer using a 20 MHz clock frequency. It provides TTL signals for triggering of the 6 different laser modules (see §3.2.6) and gate signals for the gated integrator digitizer unit.

The schematic diagram of this CAMAC unit is given in figure 5.33. It responds to standard CAMAC functions like "write data", "execute" (trigger) and has a full interrupt ("Look-At-Me" or LAM) support. The trigger and inhibit signals from the TCA tokamak timing unit are relayed via fiber optics to this timer, which is close to the detection system.

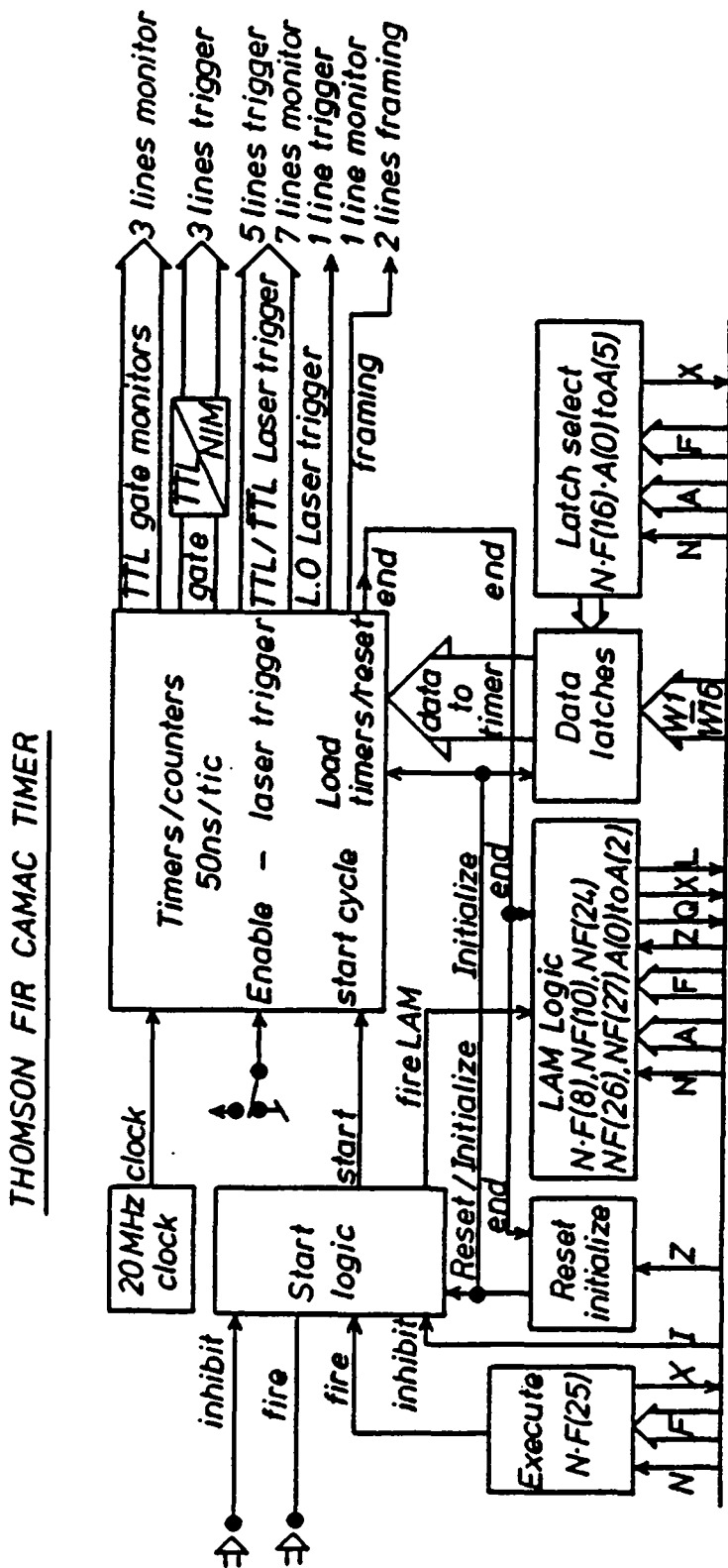


FIGURE 5.33. Functionality diagram of the CAMAC timer unit.



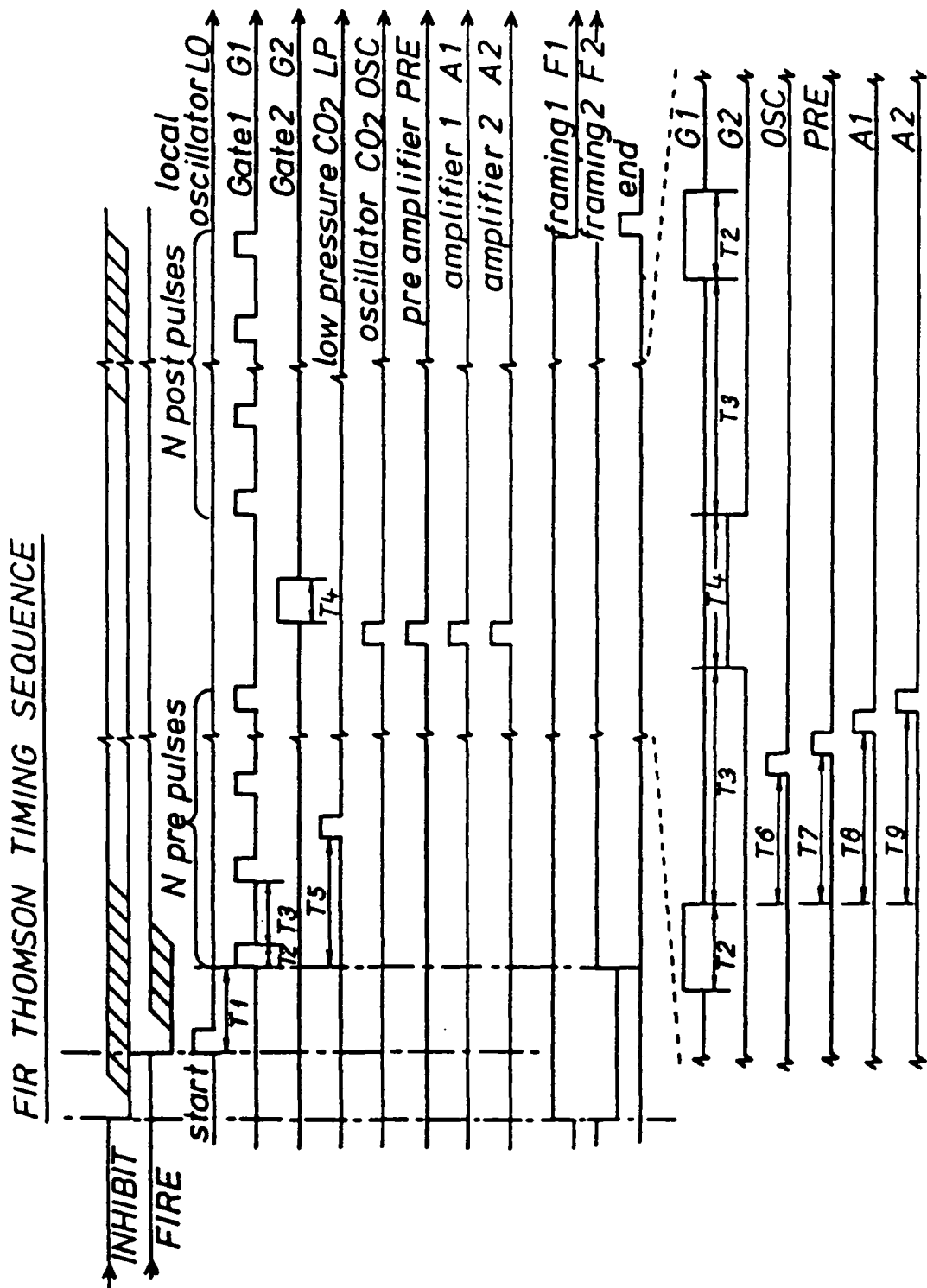


FIGURE 5.34. Typical timing sequence of the experiment.

The sequence of trigger pulses is given in figure 5.34. The first pulse to be generated is the trigger for the local oscillator laser. The power of the LO pulse reaches a flat top about 3 ms after the triggering of the laser. This is followed by typically 9 pre-pulses gating the integrator for acquisition of the background noise level. The last pre-pulse starts the countdown for the trigger pulses of the CO<sub>2</sub> laser modules (see §3.2.6). The signal gate pulse is then produced, followed by 9 post-pulses for the integrator, for background noise level monitoring.

### 5.13. The CAMAC controller and the data transfer.

The mini CAMAC crate (11 slots) situated in the same enclosure as the detection system is controlled by a MACAMAC model 1521A CAMAC controller from Borer, Switzerland. It is a INTEL 8080 microprocessor based unit with 4 kbytes of EPROM and 2 kbytes of RAM storage. The controller is intended to be connected to a computer via a RS-232, 20 mA current loop, with a transfer rate of 110 bauds.

The MACAMAC operating system was fully rewritten with the following basic ideas:

- The RS-232 port should allow 9600 baud full duplex communication with or without echo.
- The controller should be able to be run as a stand-alone system when connected to a terminal.
- A minimum of program debugging facilities should be provided (breakpoints, memory listing etc).
- All low level CAMAC functions should be provided for debugging and testing of the CAMAC units.
- There should be sufficient free memory space to include specific data treatment and communication programs for binary data transfer with the PDP-11 instead of the terminal.

A typical acquisition sequence is as follows: The controller, after a first initialization of the system and timer values, continuously triggers the LO laser at 10 to 20 Hz to keep it in a steady working condition. The TCA tokamak and the CO<sub>2</sub> laser power supplies are charged and the tokamak discharge is initiated. About 50 ms before the predefined trigger point of the FIR Thomson scattering experiment, an inhibit signal is sent from the TCA tokamak control system to the CAMAC timer unit. This signal resets the timer and inhibits the internal trigger signal generated by the MACAMAC controller for pulsing the LO laser. The timer sets the LAM line, which is sensed, recognized and reset by the MACAMAC controller. The trigger signal is sent to the CAMAC timer unit and the timing sequence shown in figure 5.34 is initiated. The lasers are triggered and the different acquisition gate pulses are sent to the integrator.

At the end of this sequence, the timer sets the LAM line again. The controller then copies the data from the timer and the integrator into its dedicated memory. The data are translated and held, ready to be sent upon request on the RS-232 line. The data are transferred either formatted to a terminal, or in binary blocks of 128+1 bytes, the "TCA standard" for computer data transfers. The repetitive triggering of the LO laser is turned on again, and the whole acquisition sequence can be repeated.

#### 5.14. Possible improvements of the detection system.

Several possible improvements to the detection system can be suggested. A decrease in the conversion losses, together with improved coupling of the optical radiation onto the mixer would bring substantially better performance. Neither of these improvements would be easy to implement. Some changes in the concept of the IF section or the data acquisition could also be envisaged.

A better corner cube design with more degrees of freedom for the alignment of the reflectors with respect to the

whisker would improve the optical coupling efficiency of the mixer. Addition of extra reflectors to a corner cube has shown to give an extra gain of 2 dB [24].

Integration of the mixer diode, the bias T and the first IF amplifier stage into one common block would allow to improve the impedance matching of these devices, and thus would lower the mixer conversion loss (about 3 dB). Currently, several laboratories interested in radio-astronomy are developing such devices, but mainly for bandwidths below 1 GHz [27].

The system noise temperature can be reduced by changing the IF amplifiers to lower the noise temperature of the first unit since its contribution to the total system noise temperature is multiplied by the high mixer conversion loss. With current microwave technology the amplifier noise figure could be lowered by 30% without going to cryogenically cooled systems. A new IF amplifier with a 1.5 dB noise figure has been installed recently. Cooling the IF amplifier to liquid nitrogen temperatures would lower the amplifier noise temperature to below 100 K, an improvement of more than a 50%. It would, however, add some technical problems for its implementation.

Cooling the mixer and the first IF amplifier is possible and would also lower the mixer noise temperature by up to a factor 2 [10-12], but thermal cycling of the diode is often fatal to the diode contact, and it would require an additional window in the optical path and a high pass filter to block room temperature noise sources.

We have indications that a slight improvement of the mixer conversion efficiency could be obtained by increasing the LO laser power. A LO power level above 10 mW would be preferred. It is, however, not clear if a factor 2 could be gained [13]. A stable CW operation of the LO would also facilitate the calibration and the operation of the detection system. A change of the laser medium would imply a new IF frequency and probably a complete change of the following IF section (the case if DCOOD is used).

To improve the data treatment one could replace the analog integrator by a high speed digitizer providing time resolved pulses for each of the filter channels. This would imply 12 digitizers with 30 MHz sampling rate and 8-bit resolution. The scattered data must then be correlated with the digitized FIR laser pulse before performing a numerical integration. This has the advantage that it would be easy to monitor and correct for background plasma and electrical induced noise and to correct for jitter of the FIR laser pulse. Off line data treatment also ensures a better use of the data, by the fact that the different treatments can be executed on the same given set of raw data. This is especially interesting when we consider cost and effort needed to produce a set of scattering data with the actual system. The total cost of 12 digitizers would be 50000 francs.

The current IF design, performing the spectral analysis of the scattered signal through a multichannel filter bank, is not optimal because the full IF bandwidth is amplified but only a fraction passes each filter. This implies a very high total gain (105 dB in our case) which can lead to self oscillations in the IF section. There are other ways to multiplex the scattered signal spectrum with a better efficiency. Recently, coaxial microwave equipment for satellite communications has been built with multiplexers such that the full signal power is redistributed over all channels. A 24 channel multiplexer with 40 MHz bandwidth per channel in the 2.2 to 3.2 GHz region is presented in reference [28]. The overall losses are only 4 dB (including 3 dB from a two way power splitter) instead of the 35 dB we have with our system. This would have required only 2 IF amplifiers instead of the 6 in use now. The improvement of the system NEP, however, would not be significant.

Digitizing the IF signal in real time during the 1  $\mu$ s pulse could also be envisaged. The spectra would then be obtained by the Fourier transform of the time signal, and no filter bank would be required. Current technology does not provide a fast enough digitizer with sufficient memory to store the full pulse length. Still, it remains a promising technique for the future.

### 5.15. Conclusions.

The heterodyne detection system of the FIR Thomson scattering experiment consists of a Mach-Zehnder type optical diplexer which combines onto a Schottky diode mixer the local oscillator signal, emitted from an optically pumped FIR laser at 782.2 GHz, with the scattered signal centered at 778.6 GHz.

To achieve sufficient FIR power the LO laser is operated in chopped mode with 5 ms long pulses, which appear continuous compared to the microsecond long scattered signal. A special technique to calibrate the system in chopped mode has been successfully developed.

The IF signal at 3.6 GHz is amplified and filtered by a S-band filter bank into 20 channels of 80 MHz bandwidth each. The signals from 12 of these channels are passed to a gated analog integrator and are digitized before being sent to a PDP-11 computer for data storage and treatment.

The synchronisation of the acquisition gates and the triggering of the lasers is controlled by a CAMAC programmable timer situated alongside the detection system.

Typical measured system noise temperatures of the complete detection system is 60000 Kelvin ( $8 \cdot 10^{-19}$  W/Hz) double side-band. The mixer conversion loss has been measured to be 17 to 20 dB, and the optical losses are about 3 dB assuming a mixer noise temperature of 5000 K, all values are for a 1.6 GHz signal bandwidth.

System noise temperatures of one order of magnitude less are commonly reported [10-14,25,26] for similar frequencies but narrower bandwidths (100 MHz). This indicates that substantial improvements of the sensitivity of the heterodyne detection system are possible. In particular, it is feasible to reduce the conversion loss by improving the optical coupling efficiency of the mixer, and by reducing the impedance mismatch between the Schottky diode and the first IF amplifier.

REFERENCES:

- [1] "A study of the feasibility of measuring the plasma ion temperature in JET by Thomson scattering using a far-infrared laser", M.R. Green, P.D. Morgan, M.R. Siegrist, R.L. Watterson, LRP-168-80 CRFP-EPFL report (1980).
- [2] "Radiation detection at submillimetre wavelengths", T.G. Blaney, J. Phys. E: Sci. Instrum., 11, 856, (1978).
- [3] "Detection techniques at short millimeter and submillimetre wavelengths: An overview", T.G. Blaney, Infrared and millimeter waves, Vol. 3, Chap. 1, Academic Press, (1980).
- [4] "Infrared detectors for low background astronomy: incoherent and coherent devices from one micrometer to one millimeter", P.L. Richards, L.T. Greenberg, Infrared and millimeter waves, Vol. 6, Chap. 3, Academic Press, (1982).
- [5] "Signal to noise requirements for interpreting submillimetre laser scattering experiments in a tokamak plasma", L.E. Sharp, A.D. Sanderson, D.E. Evans, Plasma Phys., 23, 357, (1981).
- [6] "An analysis of optical mixing in plasma scattering experiments", E. Holzhauser, J.H. Massig, Plasma Phys., 20, 867, (1978).
- [7] "Progress in optics", Vol. 8, Ch. III, "Light beating spectroscopy", H. Z. Cummins and H.L. Swinney, North Holland, (1970).
- "Optical homodyne detection", E. Kakeman, C.J. Olivier, E.R. Pike, Advances in physics, 24, 349, (1975).
- [8] "Heterodyne detection: phase front alignment, beam spot size, and detector uniformity", S.C. Cohen, Appl. Opt., 14, 1953, (1975).
- [9] "Microwave remote sensing", F.T. Ulaby, R.K. Moore, A.K. Fung, Vol. 1, Chap. 6, Addison Wesley, (1981).
- [10] "Low noise Schottky barrier diode mixers for wavelengths <1 mm", G.T. Wrixon, W.M. Kelly, Infr. Phys., 18, 413, (1978).

- [11] "Optimization of Schottky-barrier diodes for low-noise, low-conversion loss operation at near millimeter wavelengths", W.M. Kelly, G.T. Wrixon, *Infrared and millimeter waves*, Vol. 3, Chap. 2, Academic Press, (1980).
- [12] "Metal-semiconductor junctions as frequency converters", M.V. Schneider, *Infrared and millimeter waves*, Vol. 6, Chap. 4, (1982).
- [13] "Investigation of different Schottky barrier diodes in a submillimeter heterodyne receiver", E.J. Durwen, H.P. Röser, G.V. Schultz, R. Wattenbach, 7th. Int. Conf. IR and MM waves, Marseille, February 1983.
- [14] "Optimization of the performance of a 693 GHz heterodyne receiver", H.P. Röser, E.J. Durwen, G.V. Schultz, R. Wattenbach, 7th. Int. Conf. IR and MM waves, Marseille, February 1983.
- [15] "Handbook of laser science and technology", Vol. 2, editor: M.J. Weber, CRC Press, (1982).
- [16] "Optically pumped millimeter lasers", G.Duxbury et al., *J. Phys. B*, 11, No. 5, (1978).
- [17] "Measured sub-millimeter synchrotron background in Alcator A - Implications for D<sub>2</sub>O laser Thomson scattering", P. Woskoboynikow, H.C. Praddaude, I.S. Falconer, W.J. Mulligan, *Nucl. Fusion*, 21, 1028, (1981).
- [18] "A directional filter diplexer using optical techniques for millimeter to submillimeter wavelengths", N.R. Erickson, *IEEE-MTT*, 25, 865, (1977).
- [19] "Quasi-optical diplexer for millimeter wavelengths", J.M. Payne, M.R. Wordeman, *Rev. Sci. Instrum.*, 49, 1741, (1978).
- [20] "Quasi-optical techniques at millimeter and submillimeter wavelengths", P.F. Goldsmith, *Infrared and millimeter waves*, Vol. 6, Chap. 5, Academic Press, (1982).
- [21] "6 channel superheterodyne receiver at 780 GHz", Farran Research Ass. Cork, Ireland, (1980).



- [22] "Far-IR heterodyne radiometric measurement with quasi-optical Schottky diode mixers", H.R. Fetterman, P.E. Tannenwald, B.J. Clifton, C.D. Parker, W.D. Fitzgerald, N.R. Erickson, Appl. Phys. Lett., 33, 151, (1978).
- [23] "Antenna characteristics of whisker diodes used as sub-millimeter receivers", H. Kräutle, E. Sauter, G.V. Schultz, Infr. Phys., 17, 477, (1977).
- [24] "An improved quasi-optical Schottky-diode detector", K. Herrmann, 10. Int. Conf. IR and MM Waves, Florida, December 1985.
- [25] "Characteristics of metal-semiconductor junctions for mm-wave detectors", H. Zirath, E. Kollberg, M.V. Schneider, A.Y. Cho, A. Jelenski, 7. Int. Conf. IR and MM Waves, Marseille, February 1983.
- [26] "Interfacial stress and excess noise in Schottky barrier mixer diodes", G.K. Sherrill, R.J. Mattauch, T.W. Crowe, IEEE-MTT, 34, 342, (1986).
- [27] Private communication, H.P. Röser, Max Planck Institute für Radioastronomie, Bonn, FRG. (1985).
- [28] "Coaxial multiplexers aid in EW signal sorting", H.L. Schumacher, Microwave System News, 13, 105, (1983).



## CHAPTER 6 .

### THE OBSERVED SCATTERED SIGNAL.

Several series of measurements for different plasma parameters have been carried out. Three of the series showing scattering from thermal density fluctuations are described in this chapter. We also justify in this chapter the choice of the spectral channels and the plasma parameters, discuss the calibration and measurement procedures and present some scattered spectra. From these results we are able to derive the overall sensitivity of the heterodyne detection system and the required increase of laser power for a  $T_i$  measurement.

#### 6.1. Choice of the spectral channels.

As shown in figure 5.22, the resolution of the scattered spectrum is given by 20 adjacent channels of 80 MHz bandwidth each. This filter bank covers roughly half the scattered signal spectral width. However, knowing that our FIR laser is weak, and that the final post-integration signal to noise ratio is proportional to the bandwidth of the final spectral channels (equation 5.9 and 5.26), we decided to measure the signal after the set of pre-filters (A,B,C in figure 5.22, see also figure 5.21), keeping the 80 MHz channels only for the central part of the scattered spectrum (channels #13 to #20). This leads to an increase of the final signal to noise ratio for the channels A, B and C of:

$$\frac{S/N_{400}}{S/N_{80}} = \sqrt{400/80} \approx 2.2. \quad (6.1)$$

This increase in signal to noise ratio has to be paid for by a loss in spectral resolution, which is now limited to 5 channels, three of 400 MHz (A,B,C) and two of 80 MHz bandwidth (#13 and #14). The high level of stray light at the  $D_2O$  laser

Raman line center prevents us from extracting the scattered signal with sufficient precision in the 6 central channels (#15 to #20 of figure 5.21), see §6.3.

### 6.2. Tokamak parameters.

From the conclusions of chapter 1 we note that the optimum plasma parameters to produce a maximum of scattered signal are high electron and ion temperatures and the highest possible plasma density at the plasma center. A deuterium plasma is preferred, since it produces a narrower and somewhat intenser scattered signal. To avoid problems from electric pick-up, the measurements were done without RF-heating of the plasma, the 400 kW RF generator being situated only some meters away from our detection system.

Favorable tokamak operation conditions were obtained at the end of the plasma discharge, typically 100 ms after the beginning of the discharge. The typical TCA plasma parameters during the measurement of the scattered radiation are listed in table 6.1, page 6-13; see also appendix A.

### 6.3. Measurement procedure.

The different contributions to the signal entering the gated integrators are shown schematically in figure 6.1. The gate pulse, which is typically 850 ns to 1  $\mu$ s long, demarcates the useful portion of the signal as shown in figure 6.2. Normally the first 50 to 100 ns and the last few hundred nanoseconds of the laser pulse during which the laser power is low are outside the gate. The electric noise burst appearing about 1  $\mu$ s before the FIR laser pulse, due to pick-up from the spark-gaps of the CO<sub>2</sub> laser modules, is of no consequence since it decays before the gate is activated. This is only the case, however, if the video amplifiers used in front of the gated integrator have a sufficiently large bandwidth (see §5.10). A fast response time is required to prevent the pick-up merging with the weak scattered signal.

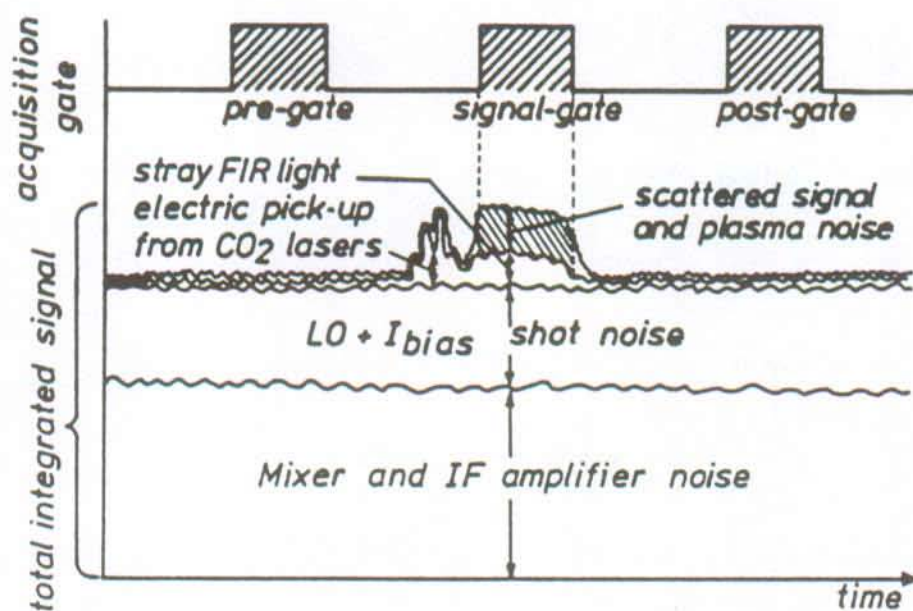


FIGURE 6.1. Noise and scattered light contributions to the observed signal. For clarity, in this example the signal to noise ratio is much higher than in the real scattering experiment.

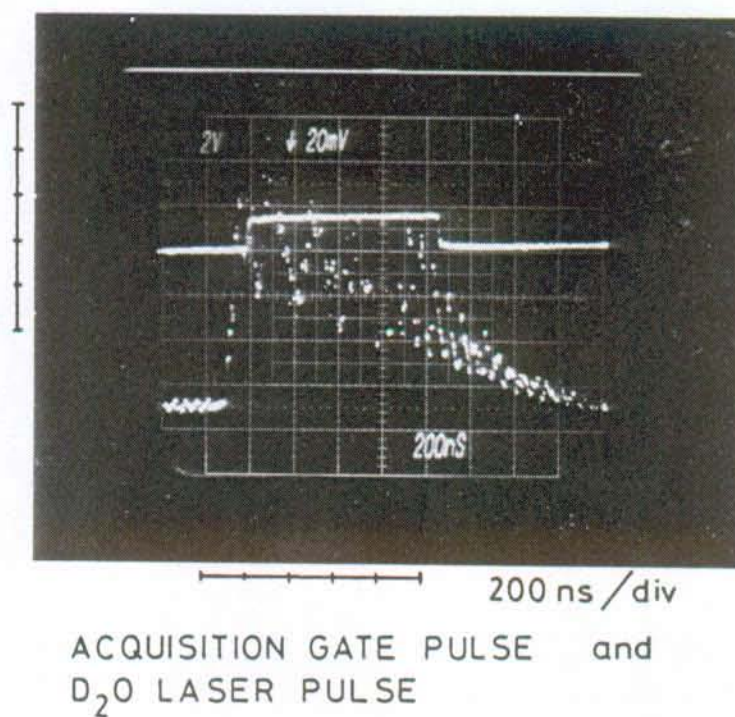


FIGURE 6.2. The acquisition gate (upper trace) superimposed on a FIR laser pulse (lower trace).

As described in §5.12, the integrator is gated to acquire a series of 9 measurements before and 9 after the actual laser pulse with a delay of 13  $\mu$ s between adjacent gate pulses. The average values of these 18 acquisitions represent the total background noise level. These average values are then subtracted from the measured scattered signals. The differences represent the net contribution due to scattered signal and stray light from the FIR laser for each channel. To compensate for the variations of the FIR laser pulse energy from shot to shot, the measurements are normalized to the time integrated signal of the D<sub>2</sub>O laser pulse monitor.

To separate the contribution of the scattered signal from that of the stray light this measurement procedure is repeated alternately with and without a plasma discharge. The difference between the mean values obtained from the two latter cases represents then the net scattered signal. By averaging in this way over typically 10 consecutive plasma discharges we obtain an increase in the signal to noise ratio of  $\sqrt{10}$ .

We have not observed any statistically significant change in the FIR laser performance correlated with the plasma discharges. An important perturbation of this measurement is a change in the FIR laser line width from shot to shot. The D<sub>2</sub>O laser pulse is not single mode, which can be observed from the pulse shape of figure 6.2, but when pumped with a single mode CO<sub>2</sub> laser it produces a rather stable line width as given in figure 3.25. We observe that a multimode pump laser results in strong stray light signals in all channels #13 to #20. The FIR and CO<sub>2</sub> laser pulse shape is monitored for each shot and cases with strong mode beating are discarded.

It is clear that in the central channels, where the amount of stray laser light is more than an order of magnitude greater than the expected scattered signal (see figure 3.25), the limited precision of the integrator, which is effectively

7 bits or 20 dB, will not allow a precise measurement. This concerns channels #15 to #20, and to some extent channels #13 and #14.

#### 6.4. Relative calibrations of the spectral channels.

The relative calibration of the spectral channels excluding the integrator-digitizer is done in the following way:

Firstly, the sensitivity of the heterodyne receiver is obtained from the NEP measurement (see §5.8). The relative sensitivities of the spectral channels are given by the measured voltage modulation amplitudes at the output of the respective square law detectors. This voltage modulation results from periodically chopping between the blackbody radiation of hot and cold sources incident on the receiver input. The thermal sources are assumed to have flat spectral emission over the bandwidth of the receiver. The spectral filtering by the optical diplexer (see §5.4) is automatically included by this calibration procedure. The other optical elements guiding the scattered signal from the tokamak to the heterodyne receiver are assumed not to alter the spectral shape of the scattered signal.

Secondly, the gains of the video amplifiers are determined separately, since they cannot be included in the previous measurement: the 10 Hz voltage modulation due to the optical signal from the two thermal sources does not pass the limited band-pass of the video amplifiers. Their gains are simply measured by injecting a 5 MHz sinusoidal signal in place of the usual signal from the square law detectors.

The sensitivities of the 12 channels of the integrator-digitizer are balanced to within 5% (see §5.11) and their contribution to the relative calibration of the receiver can be ignored.

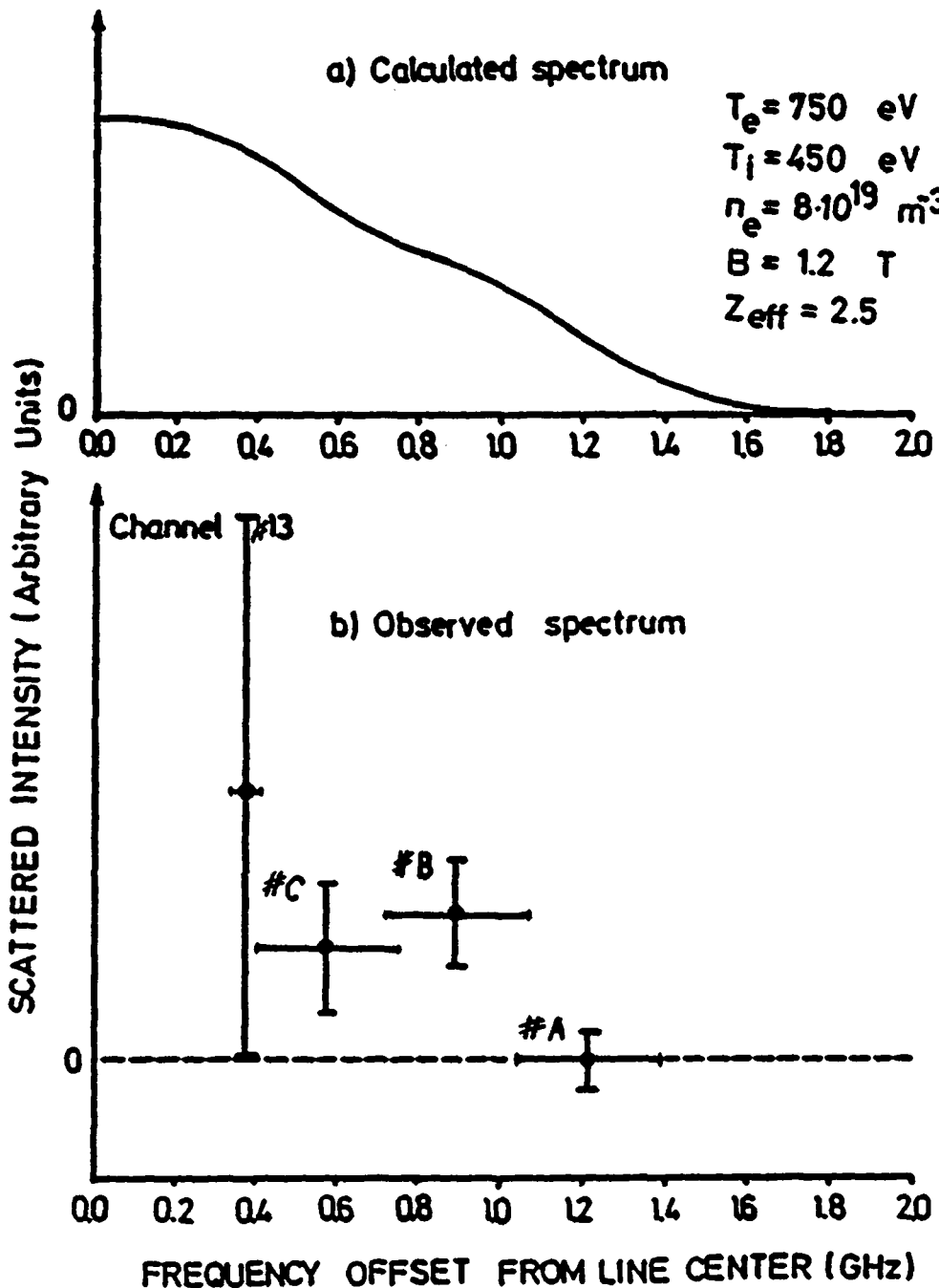


FIGURE 6.3. Observed scattered spectral data from a deuterium plasma [1]. The data represent the mean values of 10 plasma shots. The vertical error bars are the standard error of the mean, and the horizontal bars the widths of the spectral channels. The calculated scattered spectrum for corresponding plasma conditions is given above. The detector NEP was about  $1.5 \cdot 10^{-18}$  W/Hz.



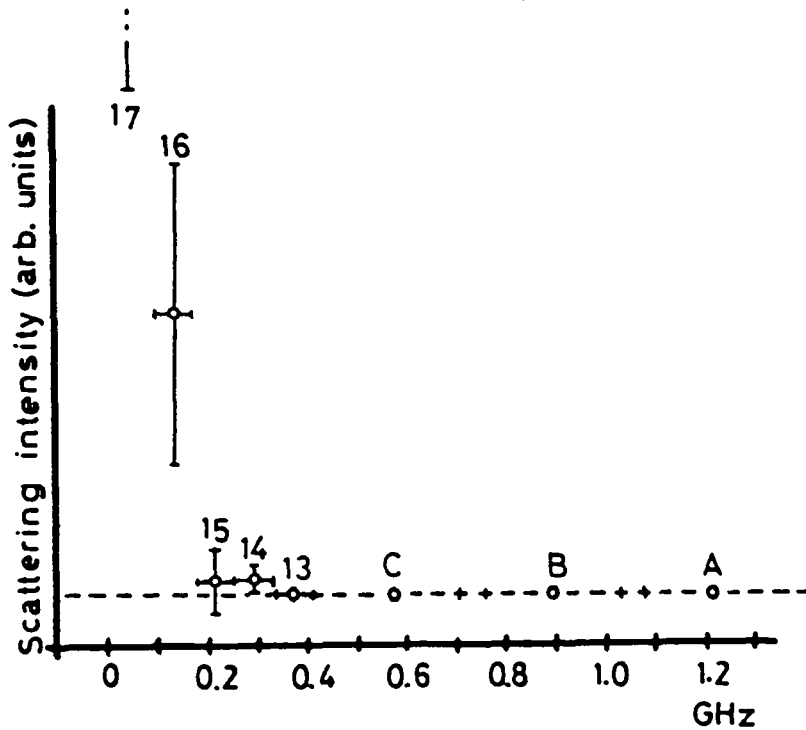


FIGURE 6.4. Observed spectrum as for figure 6.3 but with the data from channels #14 to #17 added. The vertical scale has been increased by about two orders of magnitude.

### 6.5. Measured spectra.

The first measured spectrum is given in figure 6.3, the upper trace being the calculated spectrum for the typical TCA deuterium plasma parameters during those measurements [1].

The data represent the mean value of 10 plasma shots obtained as described in §6.3 by alternating acquisitions with and without a plasma at a rate of one measurement each 3 min, thus 6 min between the tokamak shots. The horizontal bars represent the spectral channel widths, and the vertical error bars are the standard error  $s_e$  of the mean  $\bar{x}$  from  $n$  samples, defined by [2]:

$$s_e^2 = \frac{\sum (x - \bar{x})^2}{n(n-1)} \quad \text{where} \quad \bar{x} = \frac{\sum x}{n} \quad (6.2)$$

The data from channels #14 to #17 have been added in figure 6.4. The vertical scale had to be increased by about two orders of magnitude to include these channels. All data

have been corrected for relative sensitivity of the heterodyne receiver and normalized against the FIR laser energy.

The typical FIR laser pulse energy for these first measurements was 100 mJ. The gate duration of the integrator was 850 ns, which was comparable with the full width at half maximum of the laser pulse (see figure 6.2). The detection system had a typical  $NEP_{DSB}$  of  $1.5 \cdot 10^{-18}$  W/Hz. These values do not take into account beam transport losses and losses from the quartz vacuum windows on the tokamak.

Results from another series of measurements are shown in figures 6.5 to 6.7 [3]. They again represent the average difference between 10 shots with a plasma and 10 without. For these measurements the NEP of the heterodyne receiver had been improved to about  $8 \cdot 10^{-19}$  W/Hz double side band (see figure 5.28). The FIR laser provided an average power of 150 mJ for a pulse duration / integration time of 850 ns. Figure 6.5 shows the results from a deuterium plasma, normalized to the FIR laser energy, but not corrected for the relative sensitivity of the receiver channels. The latter is included in figure 6.6. The true signal level of channel #17 is an order of magnitude above that of channel #16. The results for the  $D^+$  plasma of figure 6.7 show the same data but the central channels up to 240 MHz are omitted. The calculated spectra for corresponding plasma conditions are given above the measured data. Figure 6.7 also shows the results obtained for a hydrogen plasma and the corresponding calculated spectrum.

#### 6.5.1. Discussion.

Comparing the laser power and the receiver NEP that were achieved during these experiments with the requirements derived in chapter 2, it is clear that the performance is not sufficient for an ion temperature measurement. We observe, however, from figure 6.3 and 6.7, systematically, and for all channels except for channel A of the deuterium plasma, a net signal correlated with the presence of the plasma that we can only explain by scattering from thermal fluctuations.

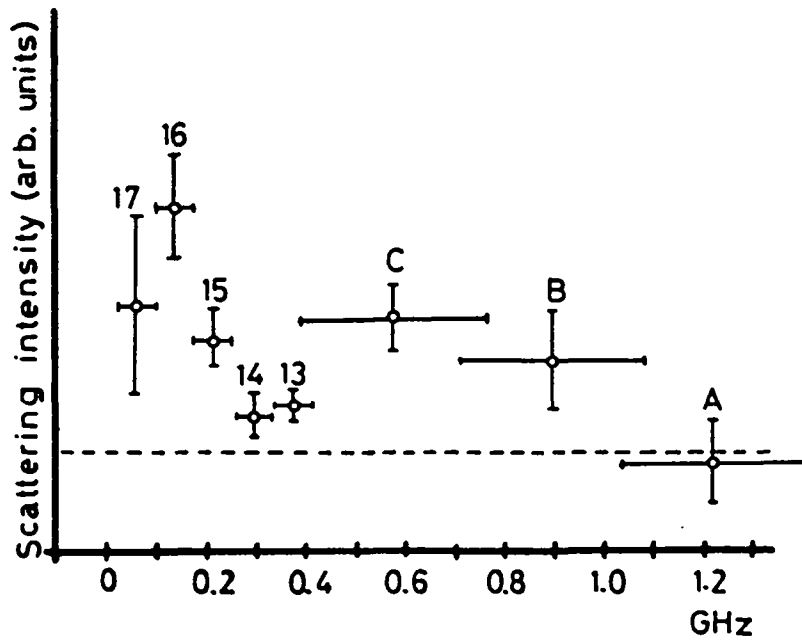


FIGURE 6.5. Spectral distribution of scattered signal from a deuterium plasma. The data have been corrected for the FIR laser power fluctuations, but not for the sensitivity of the receiver channels.

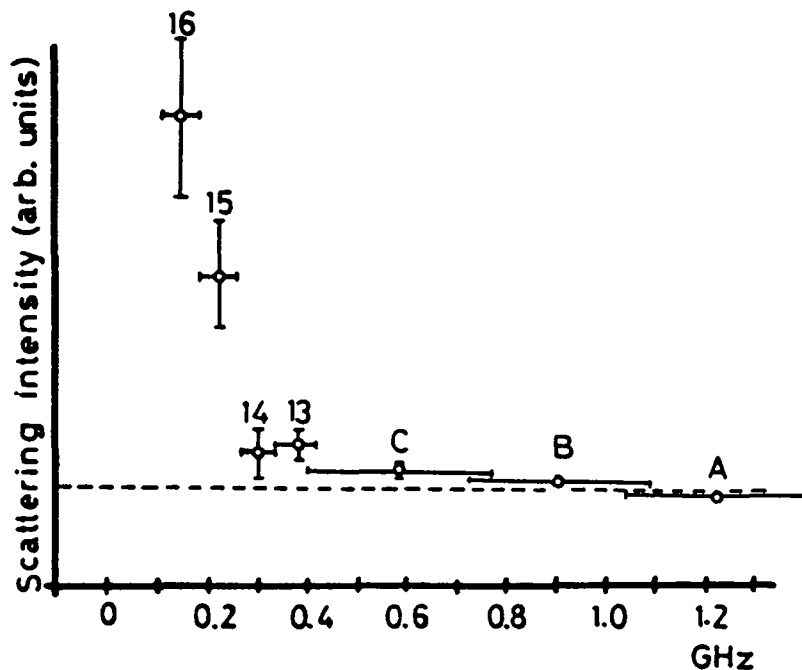


FIGURE 6.6. Signal due to scattering from a deuterium plasma, as for figure 6.5, but corrected for the relative sensitivity of the receiver channels.

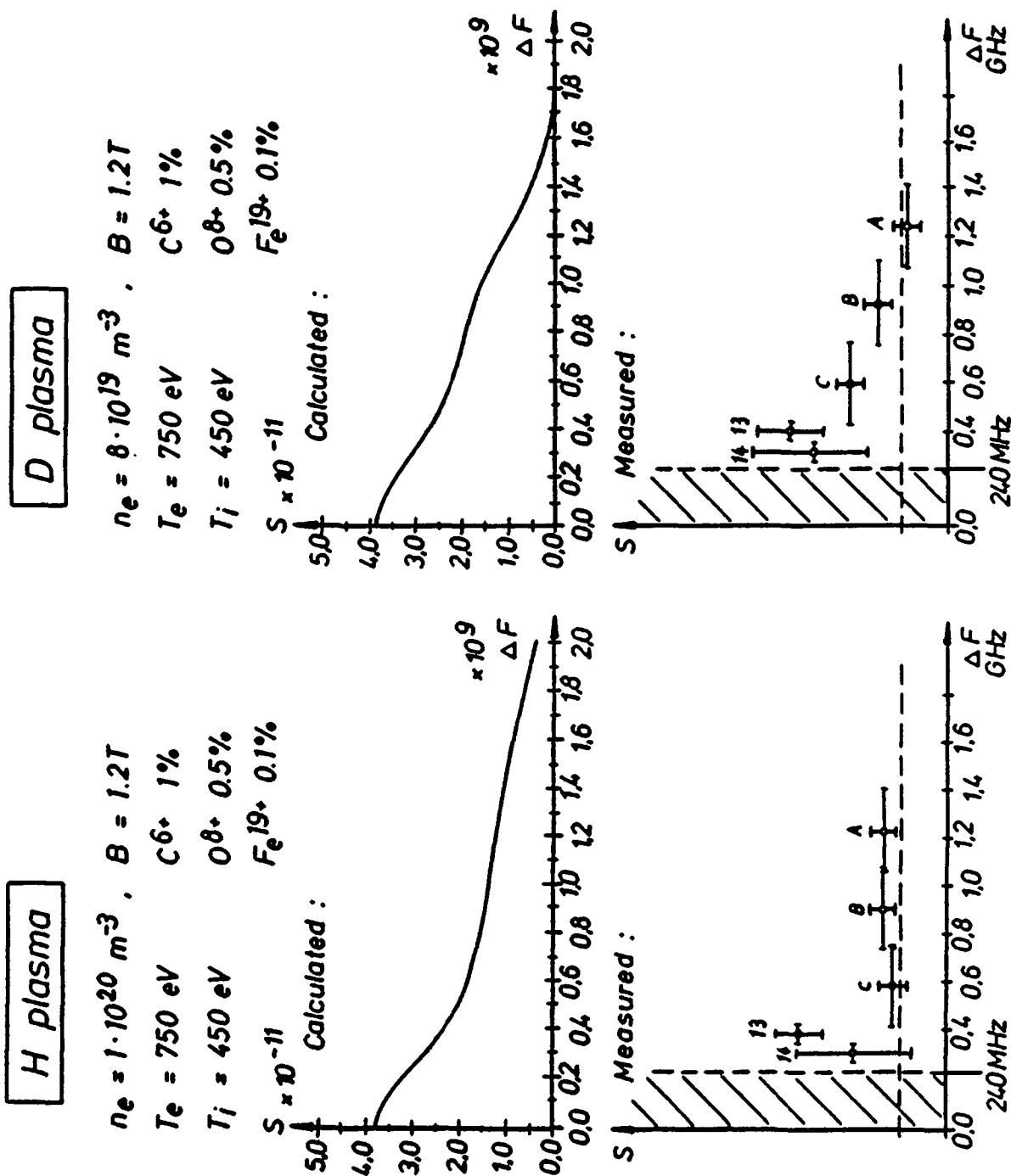


FIGURE 6.7. Observed scattered spectra, with the corresponding calculated spectra [3]. The left-hand data set was obtained from scattering off a hydrogen plasma by averaging over 12 plasma shots, while the data presented on the right were obtained for a deuterium plasma, averaged over 10 plasma shots. The detector NEP was about  $8 \cdot 10^{-19} \text{ W/Hz}$ .

For both measurements of deuterium plasma (figures 6.3 and 6.7), when ignoring the first 240 MHz of the spectrum, the measured and calculated spectra are qualitatively similar. For a hydrogen plasma the spectral shape is somewhat different from the shape of the measured spectrum obtained for the  $D^+$  plasma (figure 6.7), and shows a flatter and broader profile in qualitative agreement with the calculated spectrum.

If we include the measurements of channels #14 to #17 we observe scattered signal that decreases with frequency in a similar way to the  $D_2O$  laser emission spectrum presented in figure 3.25. Because the stray light contribution has been subtracted from the data in figure 6.4 and 6.6, the existence of a laser like feature in the scattered spectrum must be connected with the presence of the plasma. We will proceed to examine three explanations of this phenomena.

As mentioned in §1.7.6, scattering from plasma impurities increases the central part of the spectrum. This is, however, already included in the calculated spectra of figures 6.3 and 6.7 using the impurity concentration obtained from other diagnostics (mainly from UV spectroscopy) on TCA. Impurities could not increase the scattering form factor by more than a factor 4 for typical TCA conditions.

The effect of the magnetic field, which also influences the central part of the scattered spectrum ( see §1.7.8 ), strongly depends on the angle between the scattering  $k$  vector and the magnetic field direction. With the large solid angle of our collecting optics (see §2.7.1 and §4.6) we observe a range of  $k$  vectors with angles varying from  $85^\circ$  to  $95^\circ$  with respect to the magnetic field direction. Nevertheless it can not explain such an enhancement of the central spectral region.

A possible explanation of the presence of a signal with a spectral shape comparable to the laser line profile would be scattering off plasma microturbulence (see §1.7.5). Since the measured spectrum is a convolution of the laser line profile

and the scattered signal spectrum the expected narrow spectral feature of scattering from microturbulence would be spread over a width corresponding to the FIR laser line width.

A set of measurements done without a plasma but with the magnetic fields of the tokamak, as well as measurements with plasma densities below  $10^{19} \text{ m}^{-3}$ , have not shown statistically significant signals similar to those of figure 6.3 and 6.7.

#### 6.5.2. Comparison with results from MIT.

Our results of figure 6.3 and 6.7 are comparable with the results obtained from coherent Thomson scattering on Alcator C at MIT [4]. From their 32 spectral channels of 80 MHz bandwidth covering both sides of the scattered spectrum, they observe a net scattered signal when averaging and subtracting several measurements with and without a plasma [4]. The 10 central channels covering  $\pm 400$  MHz around the IF frequency were not used because of the high level of stray light. The signal to noise ratio was also not sufficient to attempt a measurement of the ion temperature.

The principal parameters of both experiments are given in table 6.1. The main problems at MIT were stray light due to a very limited access to the torus and plasma background noise from emission at harmonics of the ECE frequency, due to the high magnetic fields on Alcator C. The small (25 mm) diameter windows available acted as diffracting apertures, limiting the focusing optics to F numbers above 15. The beam dumps were made of graphite, with a measured absorption of only 20 dB [4].

#### 6.6. Estimate of the global system NEP.

The data of figure 6.5 has been used to estimate the overall NEP of the heterodyne receiver, including all optical losses. For each spectral channel the ratio  $r$  of the stan-

	<u>TCA</u>	<u>ALCATOR C</u>	
Electron temperature	: 800	1200	[eV]
Ion temperature	: 450	1000	[eV]
Density on axis	: $5 \cdot 10^{19}$	$1.4-3 \cdot 10^{20}$	[ $\text{cm}^{-3}$ ]
Magnetic field	: 1.2	8	[T]
Scattering angle	: 90°	20°	
F number of focusing optics:	F/6	F/15	
FIR laser energy ( $\text{D}_2\text{O}$ )	: 150	200	[mJ]
FIR pulse duration	: 0.8-1	1	[ $\mu\text{s}$ ]
Local oscillator gas	: $\text{CD}_3\text{Cl}$	$\text{DCOOD}$	
Local oscillator power	: 7	30	[mW]
IF frequency	: 3.6	9.4	[GHz]
NEP (double side band)	: $8 \cdot 10^{-19}$	$3 \cdot 10^{-19}$	[W/Hz]
Spectral resolution	: $3 \times 400 + 6 \times 80$	$32 \times 80$	[MHz]
Fraction of spectrum covered	: half	full	

TABLE 6.1. Comparison of the collective Thomson scattering experiment on TCA and Alcator C [4].

=====

Filter number #	Center frequency [MHz]	Channel width [MHz]	Ratio r	Calculated NEP $\times 10^{-18}$ [W/Hz]
17	80	80	0.61	16.8
16	160	80	0.21	4.89
15	240	80	0.25	5.73
14	320	80	0.64	15.2
13	400	80	0.31	6.26
C	600	400	0.27	9.34
B	920	400	0.57	13.7

TABLE 6.2. Calculated NEP of the heterodyne receiver including all optical losses. Average value:  $10^{-17}$  W/Hz. The ratios r of the standard error to the mean value are taken from the measured data of figure 6.5.

standard error to the mean value is calculated. Assuming that the standard errors are mainly due to noise in the receiver and that the plasma parameters are constant over all measurements, then the ratio  $r$  is related to the receiver signal to noise ratio, hence to the NEP. By using the numerical code described in §2.7.2 and specifying (1) all plasma parameters (see figure 6.7), (2) a FIR laser power of 100 kW, (3) an integration gate length of 850 ns, (4) the averaging over 10 shots and (5) this ratio  $r$ , we obtain the NEP values given in table 6.2.

The average value of the NEP from table 6.2 is  $10^{-17}$  W/Hz, which is 12 times greater than the NEP of the receiver measured just in front of the optical diplexer (see figure 5.28). This difference can be explained by the optical beam transport losses of the incident FIR laser beam and the collected scattered signal beam. This value is the best estimate of the overall optical losses in our experiment.

#### 6.7. Requirements for a single shot Ti measurement.

Using this calculated NEP of  $10^{-17}$  W/Hz, we can see from figure 2.5 that a single shot ion temperature measurement with 30% precision would require a FIR laser power of 1.4 MW. A measurement with an expected precision of 15% could be achieved with a NEP of half this value. Currently a FIR laser capable of emitting about 2 J of FIR power with pulse lengths of 1  $\mu$ s and above [5] (see also appendix D) is being installed on TCA. The detection system is also constantly being improved such that an ion temperature measurement on TCA by coherent Thomson scattering should be possible within some months. The main problem remains the amount of stray light. An optical notch filter to absorb the radiation around the D<sub>2</sub>O Raman laser frequency, as used at MIT, could be required. We are searching for a suitable gas that shows an absorption band at the correct frequency. The N<sub>2</sub>O gas used at MIT requires off-tuning of the CO<sub>2</sub> pump laser to match the FIR Raman emission



to the gas absorption line, thus complicating the pump laser. Attempts to operate our e-beam CO<sub>2</sub> laser system [5] with an intracavity etalon in the oscillator to achieve tunability showed that optical feedback precluded operation beyond output energies of 100 J [6].

### 6.8. Conclusions.

The spectral shape of the scattered radiation was recorded using 3 central channels of 80 MHz and 3 outer channels of 400 MHz bandwidth. The 400 MHz channels were used in preference to the 80 MHz channels to improve the final signal to noise ratio. Only one half of the symmetric scattered spectrum is covered by these channels.

We observed a net signal explained by scattering off thermal density fluctuations in the plasma when averaging over typically 10 plasma discharges. The signal to noise ratio does not, however, allow us to extract an ion temperature from these measurements.

Qualitatively the shapes of the observed and calculated spectra agree with each other, and show a flatter profile for scattering off a hydrogen plasma than off a deuterium plasma.

From the observed data we have calculated a global NEP of the system of  $10^{-17}$  W/Hz double side band. The difference between this value and the NEP measured for the detection system indicates 10 dB total optical losses in the beam transport system.

With a NEP of  $10^{-17}$  W/Hz, a 1.4 MW FIR laser is required to achieve a single plasma discharge ion temperature measurement with 30% precision. A laser capable of delivering 2 J in 1  $\mu$ s is currently being installed on TCA. If the stray light can be kept at its present level a  $T_i$  measurement should be possible on TCA within some months.

REFERENCES:

- [1] "Preliminary results from a FIR Thomson scattering diagnostic on TCA, I. Kjelberg, R. Behn, M.A. Dupertuis, P.A. Krug, P.D. Morgan, A. Salito, M.R. Siegrist, International conference on Plasma Physics, Lausanne, June 1984,
- [2] "Applied statistics", L. Sachs, Springer Verlag, (1984).
- [3] "Observation of collective Thomson scattering of D<sub>2</sub>O laser radiation from a tokamak plasma", R. Behn, I. Kjelberg, P.A. Krug, A. Salito, M.R. Siegrist, 10th International Conference on Infrared and Millimeter Waves, Miami, USA, December 1985.
- [4] "385 micron D<sub>2</sub>O laser Thomson scattering plasma diagnostic", P. Woskoboinikow, D.R. Cohn, R.J. Temkin, B. Lax, T.G. Sollner, H.R. Fetterman, P.E. Tannenwald, H.C. Praddaude, W.J. Mulligan, F.J. Tambini, R. Erickson, J. Machuzak, 7th Int. Conf. Infr. MM Waves, paper V10-5, Marseille, (1983).
- "385 micron D<sub>2</sub>O laser collective Thomson scattering ion temperature diagnostic", P. Woskoboinikow, W.J. Mulligan, J. Machuzak, D.R. Cohn, R.J. Temkin, T.C.L.G. Sollner, B. Lax, 11th. EPS Conf. Contr. Fusion Plasma Phys., Aachen, paper E21, (1983).
- [5] "Buffer gases to increase the efficiency of an optically pumped far infrared D<sub>2</sub>O laser", R. Behn, M.A. Dupertuis, I. Kjelberg, P.A. Krug, S.A. Salito, M.R. Siegrist, IEEE J. Quant. Elect., Vol. QE-21, pp. 1278-1285, (1985).
- "Measurement of FIR D<sub>2</sub>O laser radiation collectively scattered by thermal fluctuations in a tokamak plasma", R. Behn, M.A. Dupertuis, I. Kjelberg, P.A. Krug, S.A. Salito, M.R. Siegrist, Conference on the Trends in Quantum Electronics, Bucharest, Romania, September 1985.
- [6] "Frequency tuning of high energy, long pulse CO<sub>2</sub> laser", P.A. Krug, S.A. Salito, M.R. Siegrist, 11th. Int. Conf. on IR and mm waves, Pisa, Italy, (1986).

## CHAPTER 7.

### CONCLUSION.

From numerical simulations we have established that for a measurement of the ion temperature of a tokamak plasma by coherent Thomson scattering of far infrared radiation about 1 MW of incident laser power for a minimum pulse duration of 1  $\mu$ s is required. The precision of the  $T_i$  measurement could be better than 20% if the plasma density and electron temperature were each known to within 10%.

To demonstrate the experimental feasibility of this measurement technique we have developed a high power far infrared laser and a sensitive heterodyne receiver to observe scattering from thermal electron density fluctuations in the plasma of the TCA tokamak.

The optically pumped  $D_2O$  laser produces an average power of 150 kW for a pulse length of typically 1  $\mu$ s duration at the far infrared wavelength of 385  $\mu$ m. The spectral half width of the laser Raman emission is 320 MHz at -30 dB.

The heterodyne receiver uses a Schottky diode mixer and a local oscillator formed by a chopped  $CD_3Cl$  far infrared laser. A Mach-Zehnder type optical diplexer is used to combine the scattered and the local oscillator beams before they are focused on the mixer. The spectral analysis is performed at the IF frequency of 3.6 GHz, and the mixer conversion losses are estimated to be 17 to 20 dB for 7 mW LO laser power. The heterodyne receiver has a noise equivalent power of  $8 \cdot 10^{-19}$  W/Hz.

The experiment on the TCA tokamak was carried out at a scattering angle of  $90^\circ$  ( $\alpha=1.5$ ) with the scattering volume at

the plasma center. Two elliptical off-axis mirrors focus an F/6 diffraction limited incident laser beam and collect the radiation. The laser beam, after passing through the plasma, is absorbed in a dump formed by a 1.2 m long Pyrex glass cone. A Macor glass ceramic viewing dump is used to reduce the amount of stray light entering the collection optics.

For plasma parameters of  $n_e = 5$  to  $8 \cdot 10^{19} \text{ m}^{-3}$ ,  $T_e = 800$  eV,  $T_i = 400$  eV, a net scattered signal is observed when averaging over typically 10 plasma discharges. The shape of the measured spectra changes when scattering either from a hydrogen or from a deuterium plasma, in qualitative agreement with the calculated spectra. The broadband part of the observed spectra (320 to 1360 MHz from line center) is interpreted as scattering from thermal fluctuations in the plasma, while the intenser narrowband signal ( $<320$  MHz) observed around the laser line center could be caused by scattering from microturbulence.

A question arose  
as to whether we were covering the field  
that it was intended we should fill  
with this manual.

- Richard R. DONNELLEY.

Proceedings United Typothetae of America (1897)



## APPENDIX: A.

### THE TCA TOKAMAK AT LAUSANNE.

The collective Thomson scattering experiment has been carried out on the TCA tokamak ("Tokamak pour Chauffage Alfvén") at Lausanne. The main objective of this tokamak is to investigate plasma heating by dissipation of Alfvén waves. The tokamak has been in operation since 1980.

TCA is a circular air-cored tokamak with the following parameters:

Major plasma radius:	$R_0$	=	0.615	[m]
Minor plasma radius:	$a$	=	0.18	[m]
Toroidal magnetic field on axis:	$B_T$	≤	1.52	[T]

The vacuum vessel is constructed in stainless steel, with two gaps. Typical plasma parameters are:

Plasma current:	$I_p$	≤	170	[kA]
Q factor:	$q_a$	≥	2.2	
Line average electron density:	$\bar{n}_e$	≤	$10^{20}$	[m <sup>-3</sup> ]
Impurities on axis (with carbon limiters):	$Z_{eff}$	≤	2.5	
The current plateau is maintained up to:	$\tau$	≤	0.180	[s]

Operation diagram limits are:

$$\begin{aligned} I/e N: & \geq 8.2 \cdot 10^7 \text{ s}^{-1} \\ \bar{n}_{e19} R_0 / B_\phi: & < 4.4 \end{aligned}$$

The vacuum vessel is conditioned by several hours of standard Taylor discharge cleaning each night.

The RF heating parameters are:

$$\begin{aligned} \text{Frequency:} & \quad 2 - 5 \quad \text{[MHz]} \\ \omega/\omega_{ci}: & \quad 0.1 - 0.3 \\ \text{Power:} & \quad \leq 400 \quad \text{[kW]} \end{aligned}$$

The RF power is coupled into the plasma by four groups of six pairs of antennae, situated 90° apart around the torus.

#### A.1. Typical plasma parameters for the scattering experiment.

The measurements of the Thomson scattering experiment were carried out with hydrogen and deuterium plasmas with the following standard conditions:

$$\begin{aligned} \text{Electron temperature:} & \quad T_e = 750 - 800 \quad \text{[eV]} \\ \text{Ion temperature:} & \quad T_i = 400 - 450 \quad \text{[eV]} \\ \text{Mean density on axis:} & \quad n_e = 5 - 9 \cdot 10^{19} \quad \text{[m}^{-3}\text{]} \\ \text{Toroidal field:} & \quad B_T = 1.2 \quad \text{[T]} \\ \text{Effective charge:} & \quad Z_{\text{eff}} = 2.3 - 2.5 \\ \text{Occurrence of the FIR laser pulse} \\ \text{after the beginning of the plasma:} & \quad 100 \quad \text{[ms]} \end{aligned}$$



REFERENCES:

- [1] "The TCA Tokamak project report 1979", A.D. Cheetham et al., CRPP-EPFL report LRP 162-80 (1980).
- [2] "Target plasma conditions in TCA", A. de Chambrier et al., CRPP-EPFL report LRP 241-84 (1984).
- [3] "The TCA Tokamak", by the TCA team, CRPP-EPFL internal report (1985).



## APPENDIX: B.

### MICROWAVE DEFINITIONS AND FORMULAS.

The decibel dB is the ratio of two powers expressed in a logarithmic base. If  $P_0$  and  $P_1$  are two power values their ratio expressed in dB is:

$$R = 10 \log_{10}(P_0/P_1) \quad (\text{B.1})$$

The decibel-milliwatt dBm is a measure of power expressed by the ratio of the power  $P_0$  to a reference value of  $P_1 = 1 \text{ mW}$ .

$$P = 10 \text{ LOG}_{10}(P_0/1 \text{ [mW]}) \quad (\text{B.2})$$

The Boltzmann constant  $\kappa$  is used in the microwave region, where  $\kappa T \gg h\nu$ , as a constant to relate the temperature of a blackbody source to its spectral power density.

$$\kappa = 1.38 \cdot 10^{-23} \quad [\text{J/K}] \quad (\text{B.3})$$

$$\Delta P = \kappa T \quad [\text{W/Hz}] \quad (\text{B.4})$$

At room temperature the power can be expressed by:

$$\Delta P = -174 \text{ dBm/Hz for } T = T_0 = 290 \text{ K} \quad (\text{B.5})$$

The noise bandwidth  $B$  is an equivalent rectangular pass band that passes the same amount of noise power as the actual system being considered. The area under the equivalent rectangular gain versus frequency curve is equal to the area under the actual gain vs. frequency curve. For a multistage system, the noise bandwidth is nearly equal to the 3 dB bandwidth.

The gain of an amplifier is generally referred to the insertion gain  $G$ . This is the gain that is measured by inserting the device between the generator and the load.  $G$  depends on the impedance of both the source and the load.

The noise added  $N_a$  is the component of the output noise power that arises from sources within the network (amplifier) under test.

$$N_a = \kappa T B G \quad (B.6)$$

The noise factor  $F$  is the degradation in signal to noise ratio as a signal passes through the device under test when the noise temperature of the input source is  $T_0 = 290$  Kelvin. The noise output power is often considered to have two components: added noise from the device ( $N_a$ ), and amplified input noise.

$$F = (S/N_{\text{input}})/(S/N_{\text{output}}) \quad \text{for } T_s = T_0 \quad (B.7)$$

$$F = ((T_h/T_0 - 1) - Y(T_c/T_0 - 1))/(Y - 1) \quad (B.8)$$

$$F = (T + T_0)/T_0 \quad (B.9)$$

$$F = (N_a + \kappa T_0 B G)/(\kappa T_0 B G) \quad (B.10)$$

where

- $T_h$  is the temperature of a hot source.
- $T_c$  is the temperature of a cold source.

The noise figure  $N_f$  is the noise factor expressed in decibels.

$$N_f = 10 \log_{10}(F) \quad (B.11)$$

The excess noise ratio ENR of a noise generator expresses the effective noise temperature in dB.

$$ENR = 10 \log_{10} ((T-T_0)/T_0) \tag{B.12}$$

The effective input noise temperature  $T$  is the temperature of a fictitious resistor which produces the same output noise power as the real device when connected to the input of a noise free device.

$$T = N_a / (\kappa BG) \tag{B.13}$$

$$T = T_0 (F-1) \tag{B.14}$$

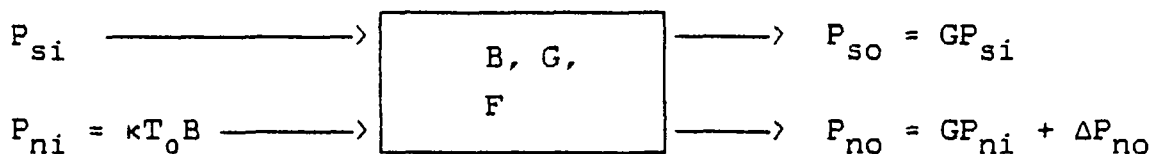
$$T = (T_h - YT_c) / (Y-1) \tag{B.15}$$

$$T = P_{oh} \Delta T / \Delta P_o - T_h = V_h \Delta T / \Delta V - T_h \tag{B.16}$$

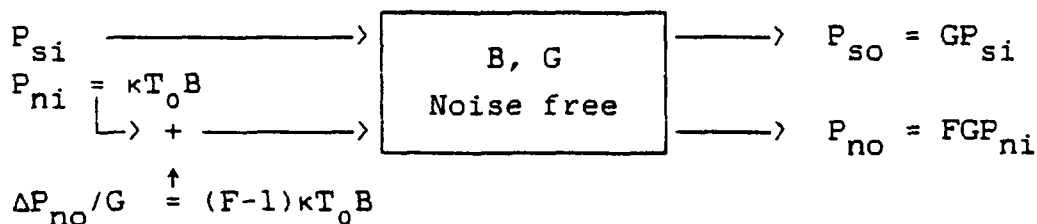
where

- $\Delta T$  is the temperature difference of both sources.
- $P_{oh}$  is the power at the output of the system originating from the hot source.
- $\Delta P_o$  is the power difference at the output of the system due to the two sources.
- $V_h$  is the voltage measured after the square law detector, when observing the hot source ( $V_h \propto P_{oh}$ ).
- $\Delta V$  is the voltage proportional to  $\Delta P_o$ .

If  $i$  designates input,  $o$  output,  $s$  signal and  $n$  noise, then:



is equivalent to: (B.17)



The quality factor  $Y$  is the ratio of the noise power output of the device under test when the noise source is ON, to the power output when the noise source is OFF.

$$Y = N_2 / N_1 \quad (\text{B.18})$$

$$Y = (N_a + \kappa T_h BG) / (N_a + \kappa T_c BG) \quad (\text{B.19})$$

$$Y = (T + T_h) / (T + T_c) \quad (\text{B.20})$$

When several networks are connected in cascade the cascade effect is the relationship of the noise characteristics ( $F$  or  $T$  and  $G$ ) of each individual network to the noise characteristics of the overall or combined network. If  $F$  and  $G$  are expressed in numerical ratios and not dB, then:

$$G = G_1 G_2 G_3 \dots \quad (\text{B.21})$$

$$F = F_1 + (F_2 - 1) / G_1 + (F_3 - 1) / G_2 + \dots \quad (\text{B.22})$$

$$T = T_1 + T_2 / G_1 + T_3 / G_2 + \dots \quad (\text{B.23})$$

As an example, an amplifier system formed by two amplifiers of 20 dB gain and effective input noise temperatures of 200 Kelvin and 800 Kelvin respectively, would have a total effective input noise temperature of:

$$T = 200 + 800 / 100 = 208 \text{ K} \quad (\text{B.24})$$

The second stage contributes only 4% to the total noise temperature. This illustrates the importance of the quality of the first amplifier stage.

The noise characteristics of an attenuator, an example. Let us consider an noisy attenuator of loss factor  $L$  ( $L$  is defined as the inverse of the linear gain  $G$ ) with a matched thermal load at the input and the output.

From the conservation of energy it follows that the power delivered from the attenuator to the output load is equal to the thermal power coming back from the load. If the ambient temperature is defined by  $T_1$ , then the power from a load is equal to  $\kappa T_1 B$ , where  $B$  is the bandwidth. The power coming from the attenuator is the power of the input load divided by the attenuation factor plus the inherent noise power of the attenuator defined as  $\Delta P_a$ . Thus:

$$\kappa T_1 B = P_o = \kappa T_1 B/L + \Delta P_a \quad (\text{B.25})$$

or:

$$\Delta P_a = (1 - 1/L)\kappa T_1 B \quad (\text{B.26})$$

The effective input noise temperature and the noise figure become then:

$$T = (L-1)T_1 \quad (\text{B.27})$$

$$F = 1 + (L-1)T_1/T_0 \quad (\text{B.28})$$

The importance of the losses in the earlier stages of an amplifier system can be easily demonstrated by analogy with the cascade effect. Let us take the example of a receiver with an effective input temperature of 50 Kelvin followed by a 0.5 dB attenuator at  $T_1 = T_0$ . The total effective input temperature would then be the input temperature of the attenuator plus the receiver temperature times the loss factor.

$$T_{\text{tot}} = (L-1)T_0 + LT_r \quad (\text{B.29})$$

$$= (1.123-1) \cdot 290 + 1.123 \cdot 50 = 92 \text{ K} \quad (\text{B.30})$$

The final effective input temperature is 92 Kelvin. The 0.5 dB loss has doubled the effective input noise temperature.

The **single-sideband SSB** of a heterodyne receiver refers to only one of the two main frequency bands that get converted to an IF. Confusion often arises when the double sideband DSB noise figure measurement of a mixer is to be interpreted for a SSB application. The cause of the confusion is that the definition of noise figure states that the numerator should include noise from all frequency transformations of the system, including the image frequency, but the denominator should only include the principal frequency transformation of the system.

For systems that respond equally to the upper and lower sidebands (assuming gain and bandwidth are the same for both bands), but where the intended frequency translation is to be for only one sideband, the denominator noise power in the definition should be half the total measured output power engendered by the input.

For **Double-sideband DSB** noise figure measurements, since the noise source contains noise at all frequencies, all frequency transformations are included in both the numerator and the denominator. Thus, if the final application of the network being measured has the desired signals in only one sideband but responds to noise in both sidebands, the denominator of the DSB measurement is too large and the measured noise figure is too small - usually a factor of about two (3 dB).

$$T_{SSB} = T_{DSB}(1 + L_s/L_i) \quad (B.31)$$

where  $L_s$  is the conversion loss for the signal sideband and  $L_i$  the conversion loss for the image sideband, usually  $L_s = L_i$ .

The **thermal noise** is defined as the fluctuating voltage across a resistance due to random motion of free charge caused by thermal agitation. The probability distribution of the voltage is gaussian with the mean square voltage given by:



$$\langle e_n^2 \rangle = 4\kappa T \int_{\nu_1}^{\nu_2} R(\nu)p(\nu)d\nu \quad (\text{B.32})$$

for

$$p(\nu) = h\nu / (\kappa T (\text{EXP}(h\nu / (\kappa T)) - 1)) \quad (\text{B.33})$$

where

- T is the absolute temperature in Kelvin.
- R is the resistance in Ohms.
- $\nu$  is the frequency in Hertz.
- $\nu_1$  and  $\nu_2$  are the frequency band considered.
- h is Plank's constant ( $6.62 \cdot 10^{-34}$  J·s).

It is to be noted that for frequencies below 100 GHz and for  $T = 290$  K,  $p(\nu)$  is greater than 0.992, so it can be replaced by unity and the average voltage can be expressed by:

$$\langle e_n^2 \rangle = 4\kappa TRB \quad (\text{B.34})$$

The shot noise is noise caused by the quantized and random nature of current flow. Carriers are emitted, injected or otherwise cross boundaries in random manner - giving rise to noise. Shot noise arises from a large number of small events, and exhibits a gaussian probability distribution. The power spectral density is proportional to the current flowing and is often flat with frequency up to frequencies that are the reciprocal of the transit time.

$$\langle i_n^2 \rangle = 2eIB \quad (\text{B.35})$$

where

- e is the electron charge ( $1.6 \cdot 10^{-19}$  C).
- I is the current in A.

It is important to know the mixer temperature and the conversion loss of a heterodyne detection system. The first element of the system is the optical diplexer of unknown loss  $L_d$  and physical temperature  $T_p$ . The diplexer assures the proper superposition of the signal and the local oscillator. This is followed by the mixer of effective temperature  $T_m$  and conversion loss  $L_c$ , both unknown. The mixer is connected to the IF amplifier system, of effective temperature  $T$ , via a cable with loss  $L_i$  and physical temperature  $T_p$ .  $T$  can be measured by comparing the response to two noise sources (50 Ohm terminations at different physical temperatures), using the same method as described here.

The method is based on the detection of the noise signals from two blackbody sources of physical temperature  $T_h$  and  $T_c$ , for the hot, respectively cold source. The corresponding electrical signals appear as the voltages  $V_h$  and  $V_c$  at the output of the square law detectors of the IF amplifier system. By adding extra losses to  $L_i$ , it is possible to obtain sufficient independent equations to estimate  $T_m$  and  $L_c$ .

The other variables are:

$$\Delta T = T_h - T_c \quad (\text{B.36})$$

$$\Delta V(L_i) = V_h(L_i) - V_c(L_i) \quad (\text{B.37})$$

The equations for the effective input noise temperature of the system  $T_s$  can be expressed as:

$$\begin{aligned} T_s &= \Delta T V_h(L_i) / \Delta V(L_i) - T_h \\ &= (L_d - 1) T_p + L_d [T_m + L_c ((L_i - 1) T_p + L_i T)] \end{aligned} \quad (\text{B.38})$$

$$\text{or} \quad (\text{B.39})$$

$$T_p - T_h = L_d (T_p + T_m) + L_d L_c [(L_i - 1) T_p + L_i T] - \Delta T V_h(L_i) / \Delta V(L_i)$$

This is also true for  $L_i=1$ , thus:

$$\begin{aligned} L_d(T_p+T_m) + L_d L_c [(L_i-1)T_p + L_i T] - \Delta T V_h(L_i) / \Delta V(L_i) \\ = L_d(T_p+T_m) + L_d L_c T - \Delta T V_h / \Delta V \end{aligned} \quad (B.40)$$

or

$$L_d L_c = \frac{\Delta T}{(L_i-1) \cdot (T_p+T)} \left( \frac{V_h(L_i)}{\Delta V(L_i)} - \frac{V_h}{\Delta V} \right) \quad (B.41)$$

the first formula becomes then:

$$L_d(T_p+T_m) = \Delta T V_h / \Delta V - L_d L_c T + T_p - T_h \quad (B.42)$$

In most cases this measurement is done with a "hot" source at room temperature so that  $T_p = T_h$ .

$L_d$  can be estimated by using the FIR transmission of the diplexer assuming that the sources are well aligned onto the input port. The other losses like atmospheric absorption and reflection losses on the mirrors are negligible at  $\lambda=385 \pm 2$   $\mu\text{m}$  wavelength.

The reflection coefficient  $\rho$  of a transmission line of length  $\lambda$  and for a given frequency is defined as:

$$\rho = B e^{\gamma \lambda} / A e^{-\gamma \lambda} = |\rho| e^{j\theta} = (Z_L - Z_0) / (Z_L + Z_0) \quad (B.43)$$

Where  $A e^{-\gamma \lambda}$  represents the emitted wave,  $B e^{\gamma \lambda}$  the reflected wave,  $Z_L$  the load impedance (complex) and  $Z_0$  the source impedance (generally 50 Ohms). The reflection coefficient is generally complex with a phase angle  $\theta$ .

Three cases are of special interest. They are the open circuit line with an infinite load impedance which results in a reflection coefficient of +1, the short-circuit line with zero load impedance and a reflection coefficient of -1, and the perfectly adapted line with complex conjugated load and source impedance and a zero reflection coefficient value.

The reflection coefficient can be expressed from the VSWR as follows:

$$|\rho| = (1-s)/(1+s) \quad (\text{B.44})$$

The power reflection coefficient is simply defined as the square of the reflection coefficient, hence:

$$P_{\rho} = \rho\rho^* = |\rho|^2 \quad (\text{B.45})$$

The voltage standing wave ratio VSWR, is defined as the ratio of the maximum and minimum amplitude variation (voltage) of the standing wave present in a transmission line:

$$s = |V_{\max}|/|V_{\min}| = (1+|\rho|)/(1-|\rho|) \quad (\text{B.46})$$

The VSWR is always greater than one and can also be expressed in terms of the source and load impedances as:

$$s = \max(Z_L, Z_0)/\min(Z_L, Z_0) \quad (\text{B.47})$$

The Smith Chart (see figure B.1) is a partial map of the complex plane representing the complex impedance of a microwave device. The chart also allows a direct measurement of the reflection coefficient, the phase angle and the VSWR value [4]. Curves on the Smith chart show generally the changes of the impedance versus frequency. Three types of circles are represented on a Smith Chart, they are: (1) the constant resistance circles, (2) the constant reactance circles, and (3) the constant VSWR circles, the latter are often omitted to avoid overcrowding the chart.

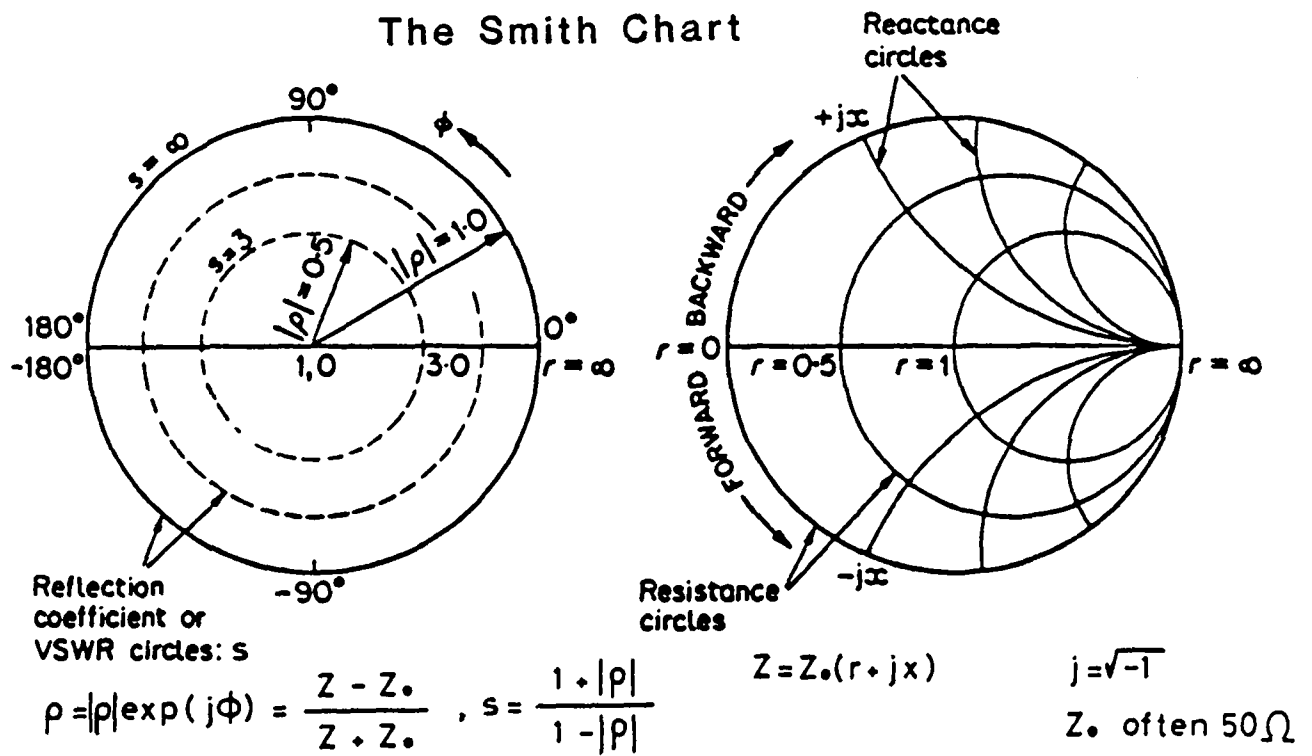


FIGURE B.1. The Smith Chart [4].

REFERENCES:

- [1] "Fundamentals of RF and Microwave Noise Figure Measurement", Application note 57-1, Hewlett-Packard, July 1983.
- [2] "Fundamentals of RF and Microwave Power Measurements", Application note 64-1, Hewlett-Packard, August 1977.
- [3] "Microwave Remote Sensing, Active and Passive", Vol. 1, "Fundamentals and Radiometry", by F. Ulaby, R. Moore and A. Fung, Addison Wesley, 1981.
- [4] "Noise", F.R. Connor, Edward Arnold (Publishers), London, 1982.
- [5] "Wave transmission", F.R. Connor, Edward Arnold (Publishers), London, 1972.

APPENDIX: C.

A COMPARATIVE STUDY OF D<sub>2</sub>O OSCILLATORS  
EMITTING AT 385  $\mu$ m.

M.R. Green, I. Kjelberg, R. Behn, P.D. Morgan,  
R. Siegrist.

IEEE-Journal of Quantum Electronics,  
QE-19, pp. 222-232, (1983).





# A Comparative Study of D<sub>2</sub>O Oscillators Emitting at 385 $\mu\text{m}$

M. R. GREEN, IVAR KJELBERG, R. BEHN, P. D. MORGAN, AND MARK R. SIEGRIST

**Abstract**—The generation of single-mode pulses of far-infrared (FIR) radiation of duration up to 700 ns at 385  $\mu\text{m}$  has been achieved using a confocal unstable resonator with D<sub>2</sub>O as an active medium. Future volumetric scaling to the power levels necessary for measuring ion temperature in tokamak plasmas by Thomson scattering appears encouraging. A comparison between the performance of the unstable resonator and two hemispherical resonators is reported.

Manuscript received April 26, 1982. This work was supported by the Ecole Polytechnique Fédérale de Lausanne, the Swiss National Science Foundation, and Euratom.

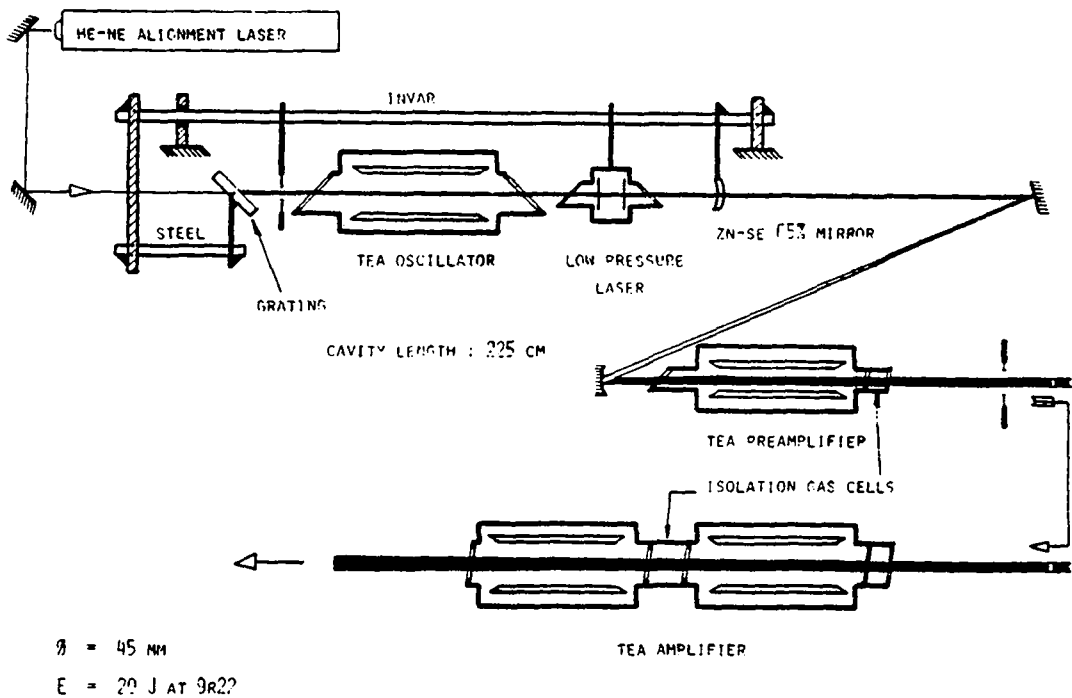
M. R. Green was with the Centre de Recherches en Physique des Plasmas, Association Euratom-Confédération Suisse, Ecole Polytechnique Fédérale de Lausanne, Lausanne, Switzerland. He is now deceased.

I. Kjelberg, R. Behn, P. D. Morgan, and M. R. Siegrist are with the Centre de Recherches en Physique des Plasmas, Association Euratom-Confédération Suisse, Ecole Polytechnique Fédérale de Lausanne, Lausanne, Switzerland.

## INTRODUCTION

THE determination of plasma ion temperature in tokamaks by collective Thomson scattering at FIR wavelengths will require lasers with the following characteristics: wavelength  $\sim 100\text{--}400\ \mu\text{m}$ , power  $\geq 1\ \text{MW}$ , pulse duration  $\geq 1\ \mu\text{s}$ , and linewidth  $\leq 50\ \text{MHz}$  [1].

It is generally recognized that unless new powerful FIR lines are found, the optically pumped D<sub>2</sub>O laser at  $\lambda = 385\ \mu\text{m}$  is presently the most promising candidate. To achieve the required power levels a powerful CO<sub>2</sub> pump laser chain is necessary and the D<sub>2</sub>O laser has to be scaled to large volumes. The linewidth requirement can only be met by single-mode operation. The unstable resonator is of great interest, as it can be used to extract energy from a large excited volume while preserving good mode control.

Fig. 1. CO<sub>2</sub> laser system for optical pumping.

Long pulse operation is important for signal statistical reasons in the detection process of the scattered radiation.

In this paper we compare the performance of an unstable resonator with that of two hemispherical resonators. We report the production of single-mode pulses of duration up to 700 ns FWHM at 385  $\mu\text{m}$ .

#### APPARATUS

##### The CO<sub>2</sub> Laser

The CO<sub>2</sub> laser system used to optically pump the D<sub>2</sub>O has been described in detail elsewhere [2]-[4] and is shown schematically in Fig. 1. It comprises a hybrid oscillator and an amplifier chain. The half-symmetric resonator is tuned by means of a plane diffraction grating and the cavity length, 225 cm, is stabilized against temperature changes by opposed invar and stainless-steel rods [5]. Two gain sections are employed, a TEA section of dimensions 50 × 5 × 5 cm and a low-pressure pulsed section working at a pressure of 10 torr.

The oscillator output, ~130 mJ in a beam of diameter 0.7 cm, has only one longitudinal and one transverse mode. This is amplified by a single pass through three TEA sections, each twice as long as the oscillator section, but otherwise the same. Two gas cells, each of length 20 cm, are used to prevent the occurrence of parasitic oscillations in the 10  $\mu\text{m}$  bands. In each cell equal concentrations of SF<sub>6</sub> and C<sub>4</sub>F<sub>8</sub> are used at pressures of about 10 torr. The transmission spectrum of this gas mixture is given in Fig. 2.

The maximum output measured on the 9R(22) line was ~20 J in a beam of diameter 4.5 cm. The output was plane polarized to better than 95 percent with the *E* vector horizontal. Pulse durations within the range 100 -700 ns could be chosen by varying the delay between the firing of the oscillator and the amplifier stages, in this way amplifying the gain-switched

spike only, or progressively more and more of the tail of the oscillator pulse. Fig. 3. shows typical oscilloscope traces of the pump pulse. The two traces show single-mode outputs of different pulse lengths. The bandwidth of the recording system was 400 MHz.

##### The FIR Oscillator

The unstable resonator is particularly attractive for use at FIR wavelengths as it provides a large uniformly-filled mode volume, excellent transverse-mode control, and variable output coupling with all reflecting optics [6].

Fig. 4 shows the unstable confocal FIR resonator. The CO<sub>2</sub> laser radiation is coupled into the cavity through a free-standing wire grid inclined at 45°, the wires running in the vertical direction. The construction of the grid, wires of thickness 10  $\mu\text{m}$  and periodicity 25  $\mu\text{m}$ , results in a measured reflectivity of better than 95 percent at 385  $\mu\text{m}$  for an incident beam plane polarized parallel to the direction of the wires. However, the transmission of the grid for the CO<sub>2</sub> laser pump beam was only 20 percent. Taking other losses into account, this resulted in a mean energy density of 0.12 J/cm<sup>2</sup> being dumped into the FIR laser cavity over an area of diameter 4.5 cm. A glass tube is used as a beam guide to collect a maximum of the diffracted or scattered CO<sub>2</sub> pump radiation which has passed through the grid. The folded FIR laser cavity is defined by a concave mirror (radius of curvature 300 cm) and as an output coupler, a convex mirror (radius of curvature 100 cm).

The characteristics of FIR emission from a stable cavity could be studied by replacing the convex output coupler with a plane mesh or Mylar film. At 385  $\mu\text{m}$ , the transmission of the mesh (200 lines per in) has been measured to be 39 ± 5 percent while that of the 0.2 mm thick Mylar film was found to be 85 ± 5 percent. In calculating the reflectivity of these elements it is assumed that absorption is negligible.

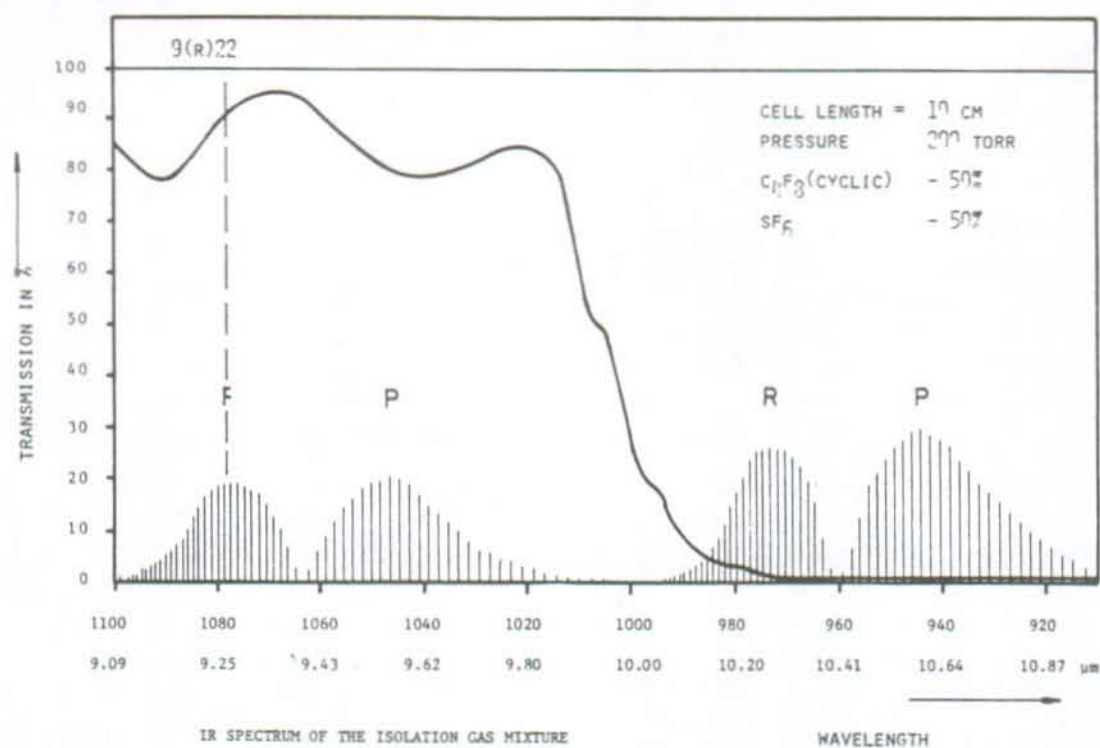


Fig. 2. IR Spectrum of the isolation gas mixture.

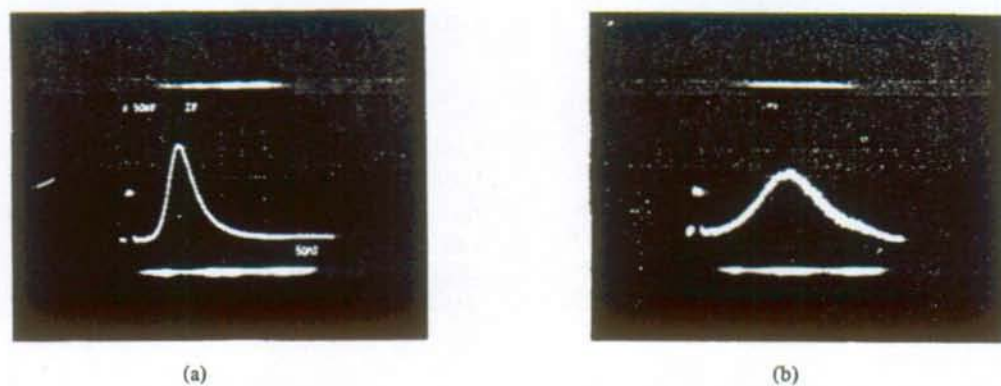


Fig. 3. Typical oscilloscope traces of the pump pulse. (a) 50 ns/div. (b) 200 ns/div.

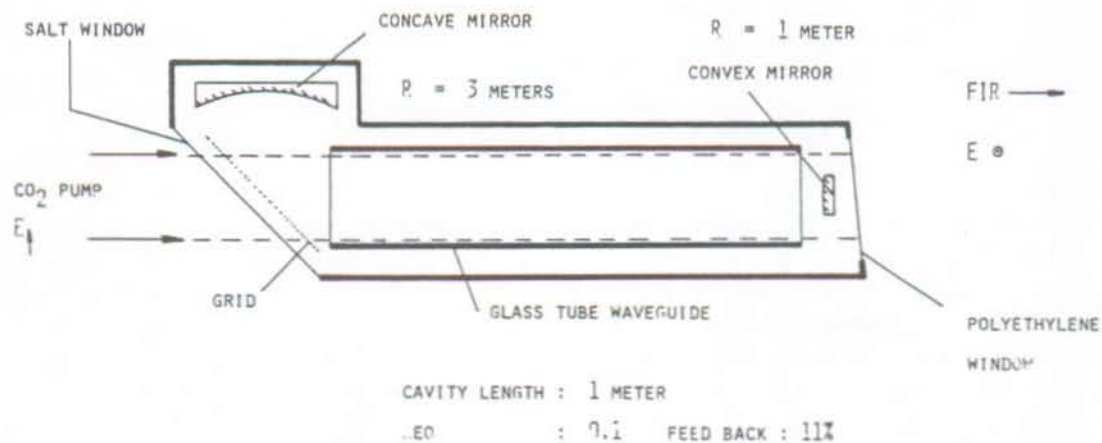


Fig. 4. The folded, unstable, confocal FIR resonator.

For all cavity configurations the length of the FIR laser resonator was 100 cm, its thermal stability being assured by using invar steel rods. Superradiant emission could also be studied by the removal of the output coupler altogether.

## RESULTS

### Energy Measurements

Using a 0.25 m Jarrell-Ash spectrometer, employing a grating ruled at 1.6 grooves/mm, the various emission lines of D<sub>2</sub>O when pumped by the 9R(22) CO<sub>2</sub> laser line could be identified. With reference to the partial energy level diagram for D<sub>2</sub>O, Fig. 5, the energy ratio between the 385  $\mu\text{m}$  line and the cascade line at 359  $\mu\text{m}$  was measured to be 10:1, for the case of the unstable resonator. No other lines were observed. The polarization of the FIR laser output was found to be better than 90:1, in a direction perpendicular to the polarization of the CO<sub>2</sub> laser beam.

In Fig. 6 the FIR energy output is plotted as a function of the D<sub>2</sub>O vapor pressure, for different cavity configurations and pump pulse lengths. The FIR energies were measured using a pyroelectric detector (Laser Precision RjP 736 RF) with an extended spectral response. Careful cross-checking with other energy detectors enables the uncertainty in the absolute energy values to be quoted as not exceeding  $\pm 25$  percent while the uncertainty in the relative measurements is better than  $\pm 15$  percent.

The mean pump energy density deposited in the FIR laser cavity was 0.12 J/cm<sup>2</sup> at most, in a single-mode pulse of duration between 100 and 700 ns FWHM. The cavity configurations were either a confocal unstable resonator [Fig. 6(a)], with 11 percent feedback, or a hemispherical resonator with 15 or 61 percent feedback (Mylar film, Fig. 6(b), and mesh, Fig. 6(d), respectively). Also shown, in Fig. 6(c), is the case without feedback (superradiant emission). For all resonator configurations, maximum energy outputs were recorded at vapor pressures between 2.5 and 5.5 torr.

In Fig. 7 the variation of FIR laser output with the pump energy is plotted for the unstable resonator. From this plot it is possible to obtain the conversion efficiency, which we define as the FIR laser energy produced per J of CO<sub>2</sub> laser energy. For the 385  $\mu\text{m}$  line, a conversion ratio of 1.2 mJ/J was measured. This agrees well with the values obtained at 66  $\mu\text{m}$  from an unstable resonator using D<sub>2</sub>O [4], if the energy is scaled according to the Manley-Rowe relation. No saturation behavior is observed in the relationship between FIR laser energy and pump energy.

### Temporal Profiles

Figs. 8-11 are a series of time-resolved pulses of the FIR laser emission and the pump output. The oscilloscope traces representing the CO<sub>2</sub> pump pulses are on the left of each figure while the corresponding FIR pulses are on the right. The square pulse at the beginning of each trace is a digital marker which provides a common time reference for both oscilloscopes. A Rofin photon drag detector was used for the CO<sub>2</sub> laser pulses

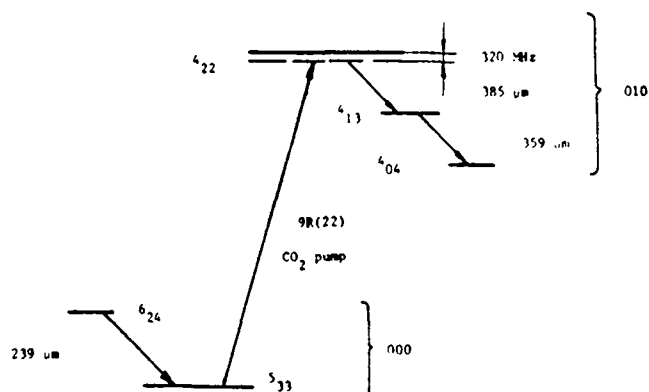


Fig. 5. Partial energy level diagram of the D<sub>2</sub>O molecule (spacings of levels not to scale).

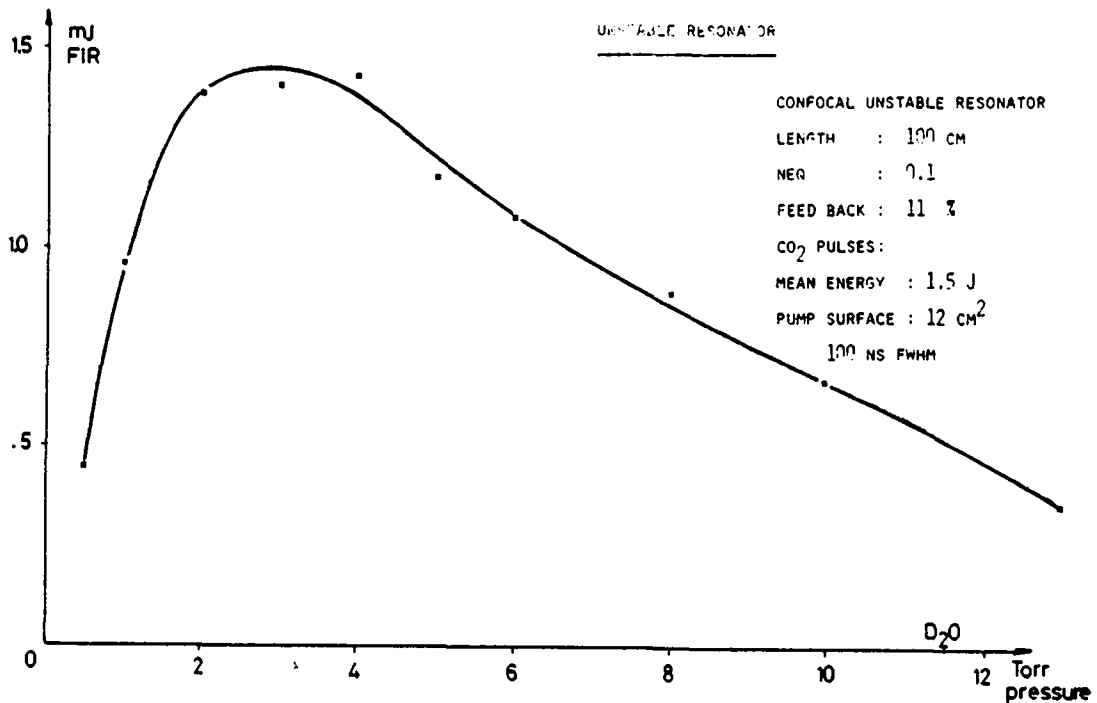
while a Molecron P5-01 pyroelectric detector was used for the FIR pulses. Both devices had rise times of less than 1 ns and both were used with oscilloscopes of bandwidth 400 MHz at a sensitivity of 10 mV/cm. Under some conditions it was necessary to use a preamplifier (gain 26 dB, bandpass 0.1-1300 MHz) with one or other of the detectors to achieve adequate sensitivity. The temporal profile of all FIR pulses was obtained after the FIR laser output had been passed through the grating spectrometer. Consequently, only the contribution due to the 385  $\mu\text{m}$  transition was recorded.

The oscilloscope traces of FIR radiation shown in Figs. 8 and 9 were obtained using the hemispherical resonator with a mesh output coupler and a D<sub>2</sub>O vapor pressure of 10 torr. In Fig. 8, for the case of a single-mode pump pulse of duration 100 ns, the presence of several longitudinal modes in the FIR laser cavity can be inferred from the beating in the FIR emission. The time separation of 6.7 ns between the peaks corresponds to the cavity roundtrip time  $c/2L$ , for the meter-long FIR resonator. This is particularly evident in the trace obtained at a sweep speed of 20 ns/cm.

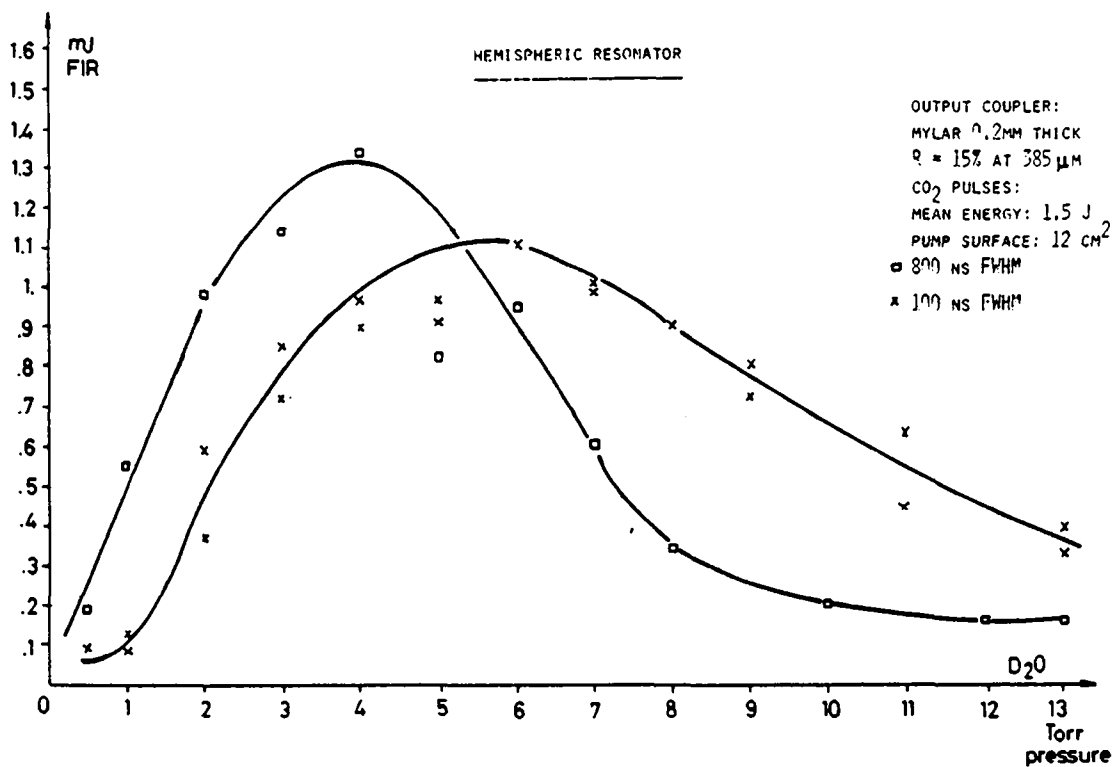
However, for a single-mode pump pulse of duration  $\sim 700$  ns the FIR laser emission exhibits no beating and indicates the presence of only one longitudinal mode in the cavity (upper half of Fig. 9). When pumping with a CO<sub>2</sub> laser pulse, of duration  $\sim 700$  ns, which exhibits mode beating with a separation of  $\sim 15$  ns between peaks, corresponding to the cavity roundtrip time in the 225 cm long CO<sub>2</sub> resonator, the FIR emission also exhibits the same modulation. However, there is no structure which indicates the beating of FIR laser modes (lower half of Fig. 9), which shows only part of a pulse.

For pressures of less than 5 torr, the output of the FIR stable resonator always exhibits modulation irrespective of the pump pulse duration. When using a single-mode pump pulse, the FIR emission displays beating due to several longitudinal modes in the FIR laser cavity. For pumping using a multimode pulse, the FIR output exhibits structure identifiable with both cavities.

In Figs. 10 and 11 we present pulse shapes obtained using the unstable FIR resonator. The traces in Fig. 10 were obtained using a pump pulse of duration  $\sim 100$  ns and a D<sub>2</sub>O vapor pressure of 5 torr. When the pump pulse is single mode, the result-



(a)



(b)

Fig. 6. The FIR output energy as function of D<sub>2</sub>O vapor pressure for different cavity configurations and pump pulse lengths.

ing FIR pulse also exhibits only one mode (upper half of Fig. 10). However, when the pump pulse shows amplitude modulation due to the presence of two longitudinal cavity modes, Fig. 10 lower traces, the FIR pulse is also modulated at the

same frequency. In Fig. 11 the output from the FIR laser when using a pump pulse of duration  $\sim 700$  ns is shown. The upper traces show a single-mode pulse for both the pump and FIR laser, while the lower traces show multimode operation

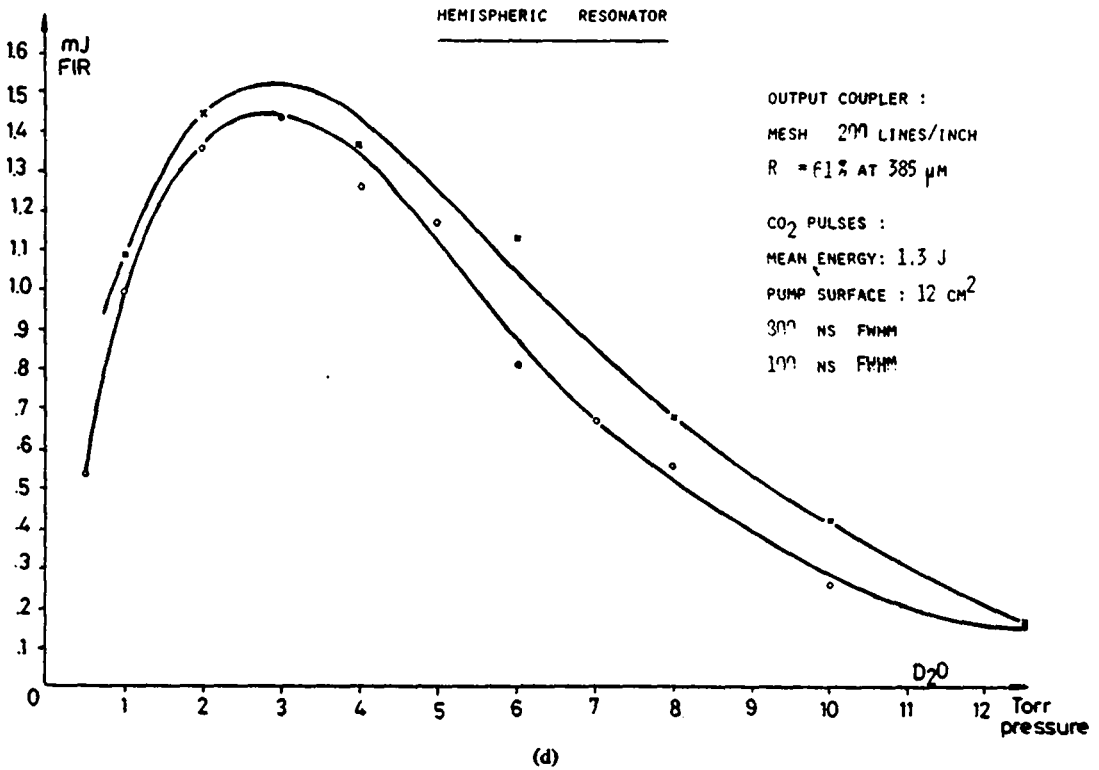
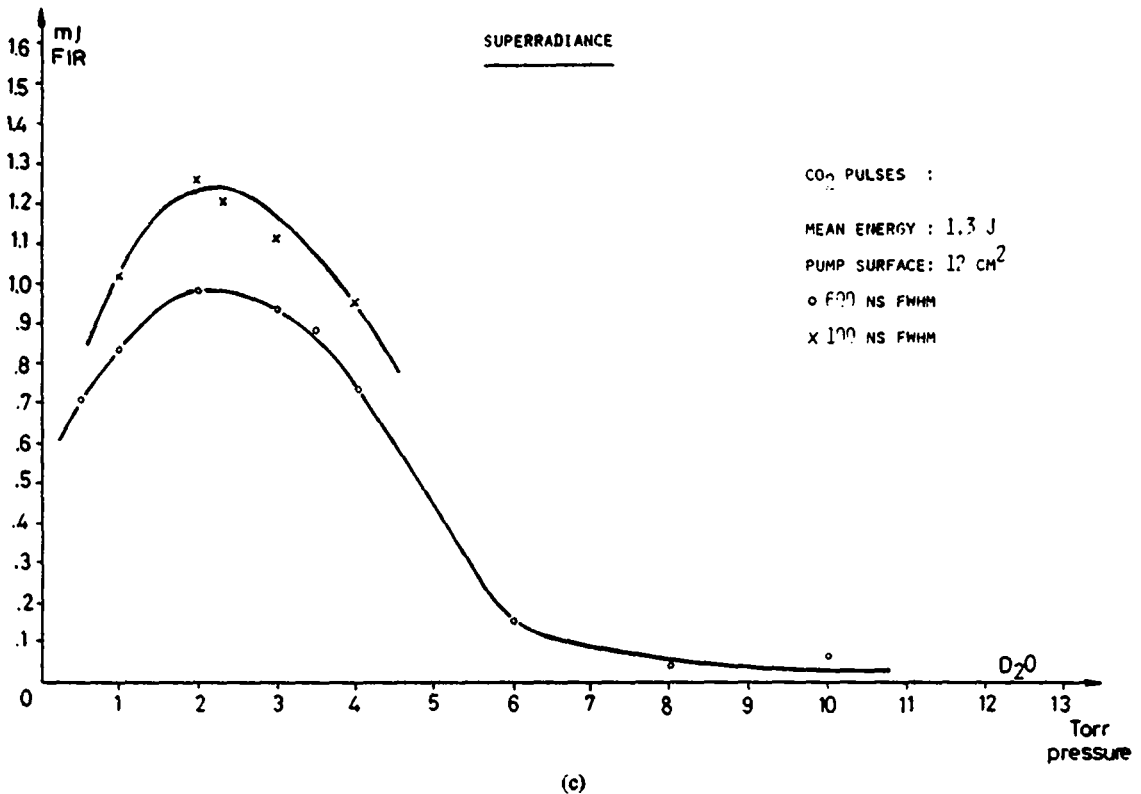


Fig. 6. (Continued.)

for both lasers. Within the pressure range 1-12 torr the performance of the FIR laser was found to be insensitive to pressure, with respect to the pulse shape.

Temporal profiles were also obtained in the case of superradiant emission. It was found that the output exhibited strong irregular fluctuations in amplitude irrespective of the

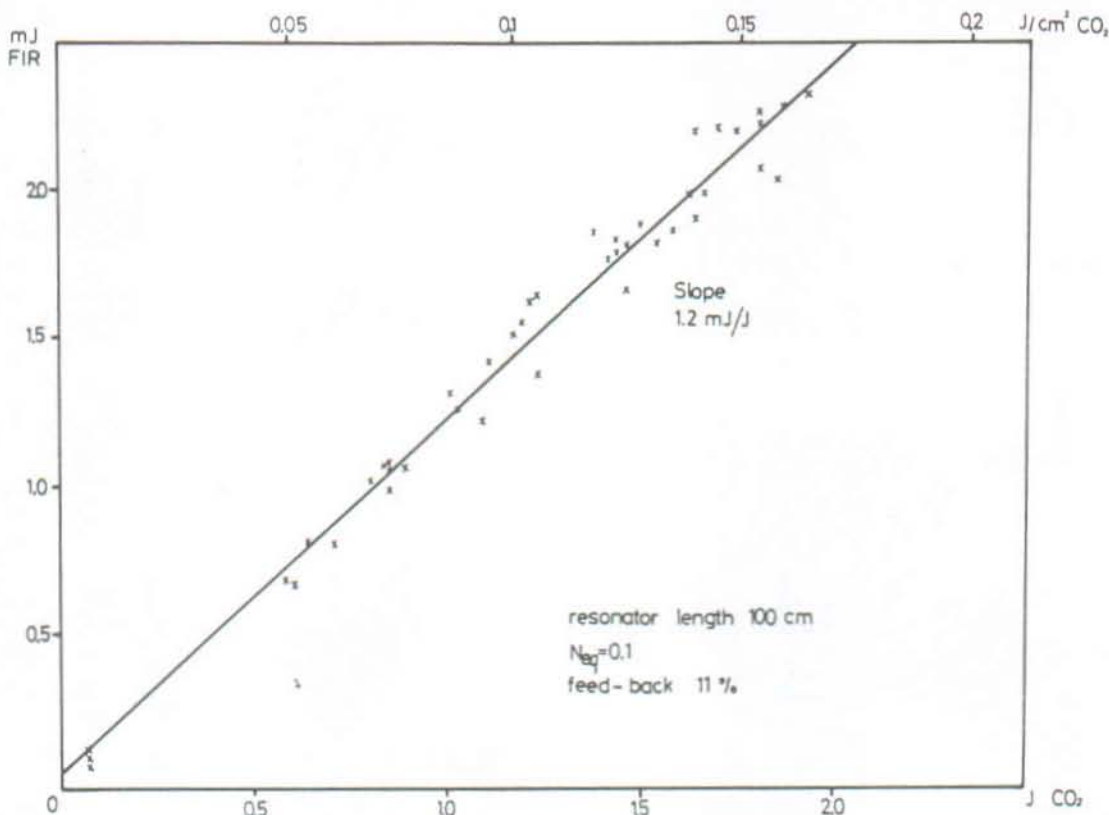


Fig. 7. The FIR output energy versus pump energy for the confocal unstable resonator.

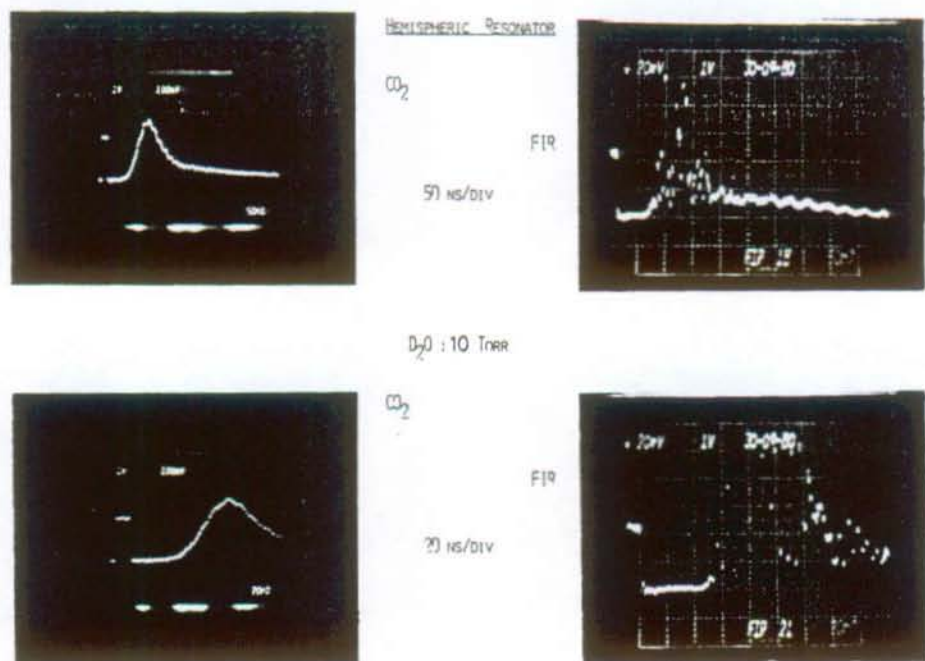


Fig. 8. Time resolved pulses.

pulse duration of the pump or the vapor pressure employed. No structure was observed in these fluctuations which could be associated with modes in either of the lasers.

#### DISCUSSION

From the energy measurements, it is apparent that all of the FIR cavity configurations give approximately the same output for a given pump energy. Furthermore, within the range of

pump intensities explored ( $170 \text{ kW/cm}^2$  to  $1.2 \text{ MW/cm}^2$ ) there is no significant variation in energy output with pump pulse duration, for constant pump energy. The best efficiency  $\epsilon$  obtained is about 4.7 percent of the theoretical maximum for a stimulated Raman process, i.e., it is assumed that each photon of  $CO_2$  laser energy can produce one photon of FIR radiation. The efficiency may then be calculated since  $\epsilon = E_{FIR} \times \lambda_{FIR} / (E_{CO_2} \times \lambda_{CO_2})$ .

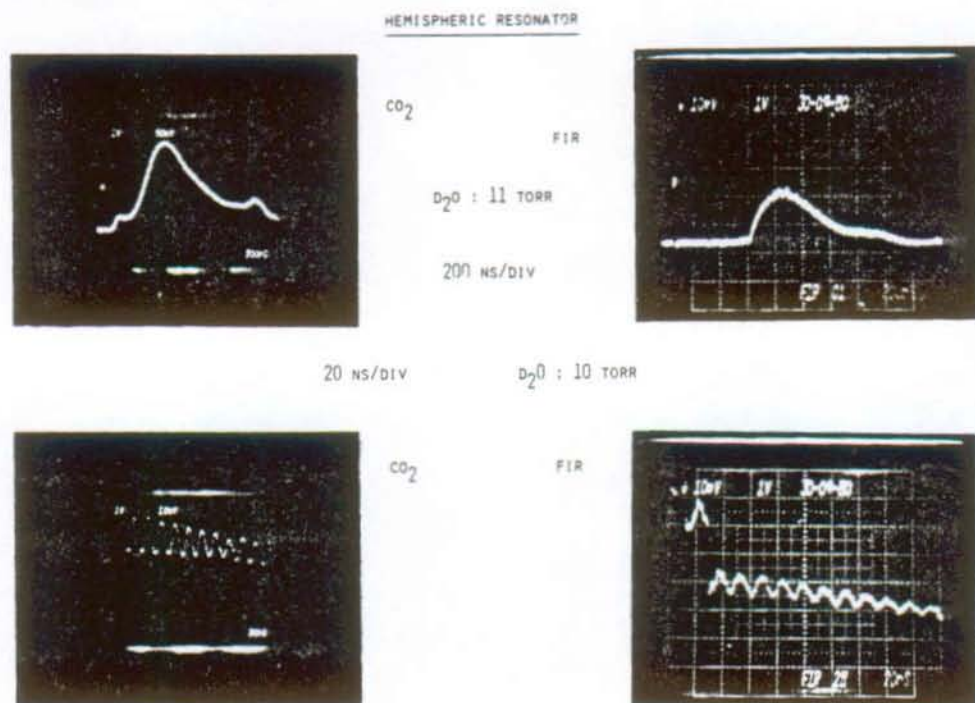


Fig. 9. Time resolved pulses.

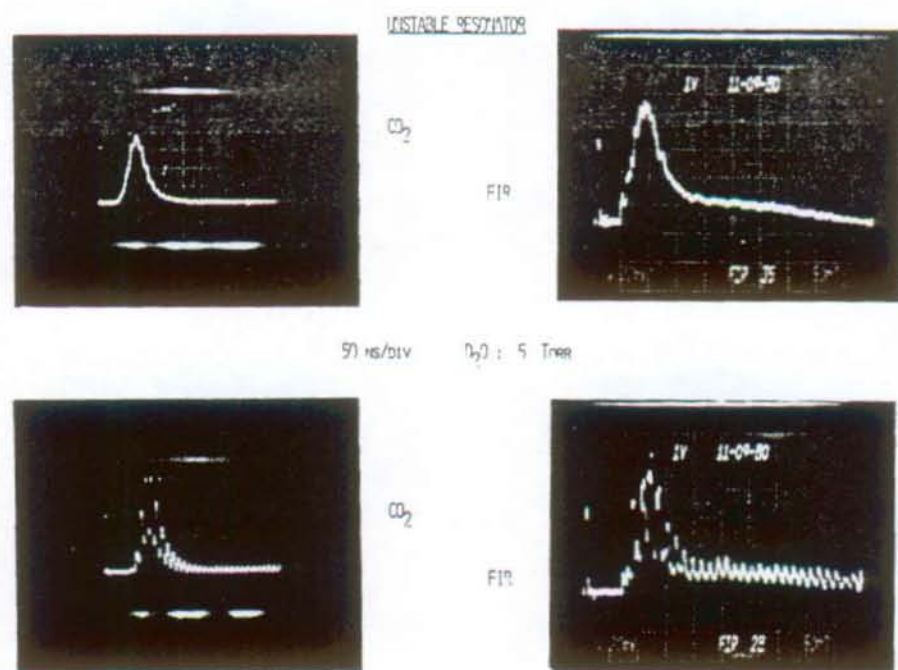


Fig. 10. Time resolved pulses.

The maximum output achieved,  $\sim 2.3$  mJ, was produced using 2 J of useful pump energy in a volume of 1.6 l at a pressure of 3 torr. Thus, the volume extraction is  $0.47$  mJ/l · torr and the energy produced is  $\sim 1.1$  mJ/J of CO<sub>2</sub> laser energy. These figures compare with  $0.80$  mJ/l · torr and  $2.2$  mJ/J from the Princeton group [7] and  $0.95$  mJ/l · torr and  $2.0$  mJ/J from the M.I.T. group [8], respectively. For all three experiments, the pumping energy density was  $\sim 0.4$  J/l · torr. However, in the work currently being reported the cavity length used was 1 m compared with 4 m in the other two experiments. Hence, absorption of the CO<sub>2</sub> laser radiation would be increased for

the latter, resulting in an improved conversion efficiency and volume extraction.

The implication of these values is that to scale up to FIR laser energies of  $\sim 1$  J, CO<sub>2</sub> pump lasers will be required capable of delivering energies in the range of  $\sim 450$ – $900$  J. Furthermore, from the volume extraction, it is seen that a volume of between  $\sim 200$  and  $700$  l will be required, for pressures of a few torr, to scale up to the required energy. However, the maximum energy that can in principle be extracted from a number  $n_m$  of molecules in the case of laser emission by a stimulated Raman process is  $0.5 n_m hc/\lambda$ . It has been assumed



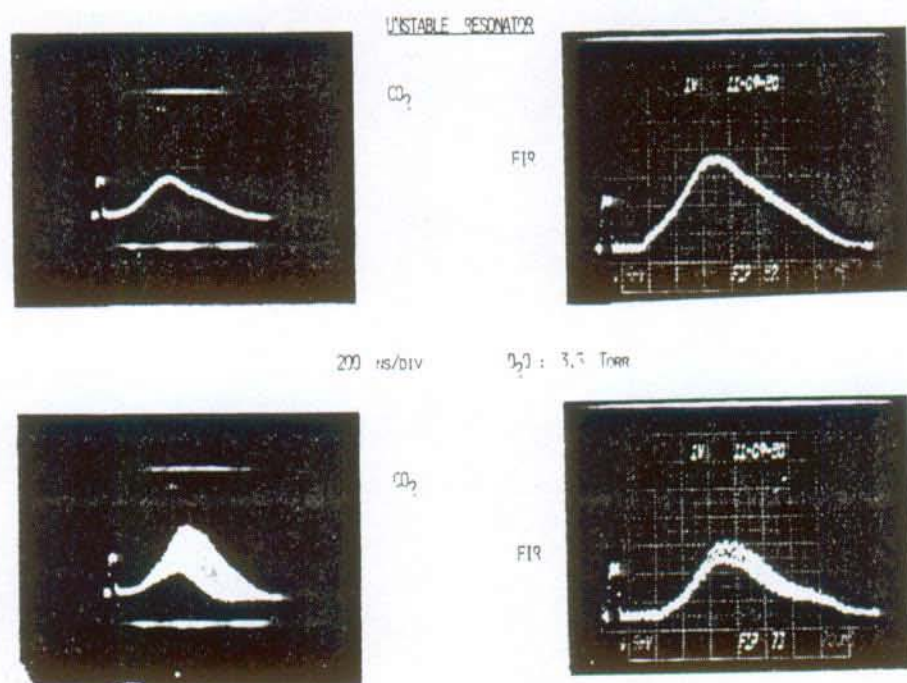


Fig. 11. Time resolved pulses.

that none of the molecules excited to the  $\nu_2 = 1$  vibrational level relax back into the  $\nu_2 = 0$  ground level during the duration of the pumping pulse. Consequently, for  $\lambda = 385 \mu\text{m}$  the maximum volume extraction is  $\sim 17 \text{ mJ/l} \cdot \text{torr}$ , which is considerably higher than any of the values quoted and which indicates some room for improvement. Also, in the event of the pumping pulse being much longer than the time for vibrational equilibration of the  $\nu_2 = 0$  level, an even greater volume extraction could be expected. Consequently, it is reasonable to anticipate that energies of  $\sim 1 \text{ J}$  could be extracted from volumes of the order  $100 \text{ l}$  for pump pulses of duration  $\sim 1 \mu\text{s}$ .

It is interesting to note the change in the temporal behavior of the FIR emission from the stable resonator, with both pulse duration and working pressure. At high pressure (10 torr) and for long pulse duration (700 ns) single-mode output is obtained when the pumping pulse is itself single mode. However, for short pump pulse duration (100 ns) or at low pressure (1.5 torr, for example) the output of the hemispherical resonator is always multimode, always exhibiting modulation indicative of several longitudinal FIR cavity modes beating, irrespective of the form of the pump pulse. These changes in the form of the FIR emission may be explained by saturation effects.

According to DeTemple [9] for the  $385 \mu\text{m}$  line of  $\text{D}_2\text{O}$  the saturation intensity  $I_{sp}$  for the pump transition is  $\sim 7.1 \text{ kW} \cdot \text{cm}^{-2} \cdot \text{torr}^{-2}$ . Consequently, at 10 torr pressure  $I_{sp} \sim 710 \text{ kW} \cdot \text{cm}^{-2}$ , and at 1.5 torr pressure  $I_{sp} \sim 16 \text{ kW} \cdot \text{cm}^{-2}$ . In comparison, the pump intensity is  $\sim 1.2 \text{ MW} \cdot \text{cm}^{-2}$  and  $\sim 170 \text{ kW} \cdot \text{cm}^{-2}$ , for 100 and 700 ns pulses, respectively. Likewise, the saturation intensity  $I_{sf}$  for the FIR lasing transition is given [9] as  $\sim 18 \text{ W} \cdot \text{cm}^{-2} \cdot \text{torr}^{-2}$ . Hence, at a pressure of 10 torr  $I_{sf} \sim 1.8 \text{ kW} \cdot \text{cm}^{-2}$ , while at a pressure of 1.5 torr the

value is  $\sim 40 \text{ W} \cdot \text{cm}^{-2}$ . At 10 torr pressure the intensity of FIR emission is  $\sim 410 \text{ W/cm}^2$  and  $\sim 40 \text{ W/cm}^2$ , for pump pulses of duration 100 and 700 ns, respectively, while at a pressure of 1.5 torr the corresponding intensities are  $\sim 1.3 \text{ kW/cm}^2$  and  $\sim 170 \text{ W/cm}^2$ .

For pump intensities which are in excess of the saturation intensity  $I_{sp}$  the gain profile is modified due to the ac or dynamic Stark effect [10]. With increasing pump intensity, and for low levels of FIR emission, the profile splits into two components which move further apart in frequency as the intensity increases—Rabi splitting. In addition, as the intensity of FIR emission increases above the saturation intensity  $I_{sf}$  the frequency band over which emission occurs becomes progressively broader. This effect is termed power broadening. At sufficiently high intensities the effect of power broadening is to fill in the trough in the emission due to Rabi splitting. This qualitative description is strictly only true for resonance pumping, i.e., when the frequency of the pump radiation coincides exactly with the line center of the absorption transition. For off-resonance pumping, the Rabi splitting and power broadening develop asymmetrically—the degree of asymmetry varying with the frequency offset [10].

The work of Temkin [10] has been followed in obtaining the emission profiles particular to the conditions under which the results reported herein were obtained. Turning to the results obtained using the stable resonator, the 1 m long cavity has a longitudinal mode spacing of 150 MHz. At a pressure of 10 torr, and in the absence of pump saturation, the width of the pressure-broadened gain profile would be  $\sim 400 \text{ MHz FWHM}$  (broadening  $\sim 40 \text{ MHz/torr}$ ). Consequently, a mode which coincided with the profile maximum would experience a gain

which was ~50 percent greater than that for adjacent modes and would dominate, i.e., single-mode output would be expected. This is indeed what is observed for pump pulses of duration ~700 ns, even though the gain difference mentioned is reduced to ~31 percent because of a small role played by the ac Stark effect. However, for pulses of duration ~100 ns, the ac Stark effect would result in a gain profile which is broader by a factor of 2.7 than in the simple pressure-broadened case—the pump intensity not being sufficient to produce distinct splitting into two components. In this case, the maximum difference in relative gain between adjacent modes would be only ~8 percent. No single mode would dominate and multimode FIR emission could be expected, as is observed experimentally. In neither of the cases considered is the intensity of the FIR emission sufficient to lead to power broadening.

At a pressure of 1.5 torr, however, the situation is quite different. For both short and long pump pulses the pump and FIR transitions are well saturated. Consequently, both Rabi splitting and power broadening play a role. Typically, for the ranges of intensities encountered in the present work, the width of the FIR emission profile can be up to about 20 times greater than the width of the gain profile due to pressure broadening. Consequently, there is not a sufficiently great difference in gain between adjacent FIR cavity modes to ensure single-mode operation, and the FIR emission is always multimode irrespective of whether or not the pump pulse is multimode.

Strangely, for a single-mode pump pulse, within the ranges explored, the FIR output from the unstable resonator is always single mode, irrespective of the pressure of the active medium or the duration of the pump pulse. However, the feedback of the output coupler of the unstable resonator is much lower than in the case of the stable resonator, 11 percent compared with 61 percent. A likely explanation of the persistent single-mode operation is that, in spite of Rabi splitting and power broadening at lower pressures, the cavity losses are so high that only the longitudinal mode closest to gain maximum is well above the threshold for oscillation.

#### CONCLUSIONS

We have demonstrated the generation of FIR laser pulses of duration up to 700 ns FWHM at 385  $\mu\text{m}$ . Single longitudinal and transverse mode control were achieved using a confocal unstable resonator with D<sub>2</sub>O as the active medium and optically pumped using a CO<sub>2</sub> laser. The results are an encouragement to scaling up the system volumetrically and to extending the pulse duration in an attempt to achieve the MW power level and  $\mu\text{s}$  pulse length necessary to perform a scattering measurement of ion temperature in a tokamak plasma.

For a given cavity length and volume, as much energy can be extracted from D<sub>2</sub>O using an unstable resonator as using stable resonators. However, much larger beam diameters can be accommodated with unstable resonators than with stable ones while preserving a single transverse mode. Also, provided that the equivalent Fresnel number [11] is correctly chosen for the unstable resonator, good longitudinal mode control can be achieved. In the case of the stable resonator, either the

cavity length must be limited so that the intermode spacing is greater than the gain width of the lasing transition or extra elements must be incorporated into the cavity to achieve mode selection. The latter approach can lead to substantial losses.

#### ACKNOWLEDGMENT

The authors acknowledge fruitful discussions with T. Okada of Kyushu University, Japan.

#### REFERENCES

- [1] M. R. Green, P. D. Morgan, M. R. Siegrist, and R. L. Watterson, "A study of the feasibility of measuring the plasma ion temperature in JET by Thomson scattering using an FIR laser," CRPP/EPF-Lausanne, Rep. LRP 168/80.
- [2] M. R. Green, P. D. Morgan, and M. R. Siegrist, "A 40 J CO<sub>2</sub> TEA laser module with a uniform-field electrode profile and side-arc preionisation," CRPP/EPF-Lausanne, Rep. LRP 141/78.
- [3] M. R. Green *et al.*, "Isolation between amplifiers in a TEA CO<sub>2</sub> laser using absorption gases," *J. Phys. D. Appl. Phys.*, vol. 13, pp. 1399-1404, 1980.
- [4] M. R. Green *et al.*, "A 66  $\mu\text{m}$  D<sub>2</sub>O laser having an unstable Reststrahlen resonator," *J. Phys. D. Appl. Phys.*, vol. 13, pp. 1029-1042, 1980.
- [5] J. P. Nicholson and K. S. Lipton, "A tunable stabilized single-mode TEA CO<sub>2</sub> laser," *Appl. Phys. Lett.*, vol. 31, pp. 430-432, 1977.
- [6] A. E. Siegmann, "Unstable optical resonators," *Appl. Opt.*, vol. 13, no. 2, pp. 353-367, 1974.
- [7] L. C. Johnson and A. Semet, "High energy FIR laser for Thomson scattering in TFTR," in *Proc. 5th Int. Conf. on Infrared and Millimeter Waves*, Würzburg, Germany, Oct. 1980, pp. 272-273.
- [8] P. Woskoboinikow, H. C. Praddaude, W. J. Mulligan, and D. R. Cohn, "Efficient, high-power D<sub>2</sub>O laser oscillator at 385  $\mu\text{m}$ ," in *Tech. Dig. 4th Int. Conf. on Infrared and Millimeter Waves and Their Applications*, Miami, FL, Dec. 1979, p. 237.
- [9] T. A. DeTemple, "Pulsed optically pumped far infrared lasers," in *Infrared and Millimeter Waves*, K. A. Button, Ed. 1979, vol. 1, pp. 129-184.
- [10] R. L. Panock and R. J. Temkin, "Interaction of two laser fields with a three-level molecular system," *IEEE J. Quantum Electron.*, vol. QE-13, pp. 425-434, June 1977.
- [11] P. F. Kellen and M. Smith, "Operating point choice in unstable confocal resonators," *Opt. Eng.*, vol. 18, no. 2, pp. 157-160, 1979.

M. R. Green, photograph and biography not available at the time of publication.



Ivar Kjelberg was born in Baerum, Norway, on January 13, 1955. He received the "Diplôme d'ingénieur physicien" at the Ecole Polytechnique Fédérale, Lausanne, Switzerland, in 1979.

In 1978 he spent three months as a student at CERN, Geneva, working on the ISOLDE project and is currently studying for the Ph.D. degree at the Centre de Recherches en Physique des Plasmas, Lausanne, Switzerland. His major field of research is the development and use of far-infrared lasers for an ion temperature measurement by collective Thomson scattering on the Lausanne TCA tokamak.



R. Behn received the degree in physics from the University of Stuttgart, Stuttgart, West Germany, in 1975, specializing in plasma physics and optical methods in plasma diagnostics, and the Ph.D. degree in electrical engineering in 1980.

In 1980 he joined the Centre de Recherches en Physique des Plasmas, Lausanne, Switzerland, where he is presently involved in the development of far-infrared lasers and their application to plasma diagnostics.

Dr. Behn is a member of the European Physical Society.



Mark R. Siegrist received the diploma in physics from the University of Berne, Berne, Switzerland, in 1969 and the Ph.D. degree from the Australian National University, Canberra, Australia, in 1974.

In 1976 he joined the Centre de Recherches en Physique des Plasmas, Lausanne, Switzerland, where he became involved in the development of far-infrared lasers for plasma diagnostics. He is currently leader of a project to determine the ion temperature in the TCA

tokamak from collectively scattered far-infrared radiation.

Dr. Siegrist is a member of the European Physical Society and the Optical Society of America.

P. D. Morgan, photograph and biography not available at the time of publication.



APPENDIX: D.

BUFFER GASES TO INCREASE THE EFFICIENCY OF  
AN OPTICALLY PUMPED FAR INFRARED D<sub>2</sub>O LASER.

R. Behn, M.A. Dupertuis, I. Kjelberg, P.A. Krug,  
S.A. Salito, and M.R. Siegrist.

IEEE-Journal of Quantum Electronics,  
QE-21, pp. 1278-1285, (1985).



# Buffer Gases to Increase the Efficiency of an Optically Pumped Far Infrared D<sub>2</sub>O Laser

R. BEHN, MARC-ANDRÉ DUPERTUIS, IVAR KJELBERG, PETER A. KRUG,  
S. A. SALITO, AND MARK R. SIEGRIST

**Abstract**—The effects of buffer gas additives on the performance of an optically pumped D<sub>2</sub>O laser operating at 385 μm have been investigated both experimentally and by numerical simulation. Three gases, sulphur hexafluoride, carbon tetrafluoride, and *n*-hexane, were found to produce an increase of up to 40 percent in the pumping efficiency, as well as significant lengthening of the far infrared pulse. Under optimum conditions, 2.6 J in a 1 μs long pulse have been obtained.

The buffer gases are shown to eliminate the vibrational deexcitation bottleneck, which in pure D<sub>2</sub>O leads to an accumulation of population in the upper vibrational level and, hence, a reduction in the efficiency of absorption of the pump beam.

Comparison of the observed buffer gas effects with the predictions of a numerical simulation code based on a rate equation model gives information about the constants for vibrational and rotational relaxation rates due to D<sub>2</sub>O–D<sub>2</sub>O and D<sub>2</sub>O–buffer gas collisions.

## I. INTRODUCTION

THE development of a high-power far infrared (FIR) D<sub>2</sub>O laser is mainly motivated by its application to plasma diagnostics. In order to measure the ion temperature of a tokamak plasma by collective Thomson scattering of FIR radiation, we require a laser source that is capable of producing 1 MW in a pulse of at least 1 μs duration. The optically pumped D<sub>2</sub>O laser emitting on the 385 μm line has been chosen because it delivers sufficiently powerful output at a wavelength where sensitive detectors are available.

Although the megawatt power level has already been reached for shorter pulses (about 150 ns) [1], high power operation is more difficult to obtain for pulse lengths exceeding 0.5 μs. The mechanism preventing efficient long pulse operation is a bottleneck in the vibrational deexcitation which hinders recycling of D<sub>2</sub>O molecules to the ground state. The depletion of ground state population reduces pump beam absorption and, thus, leads to a decrease in efficiency of the FIR laser.

Pump saturation can be avoided if the pump beam power density can be reduced by increasing the cross section of the active volume of the D<sub>2</sub>O laser. However, the high cost

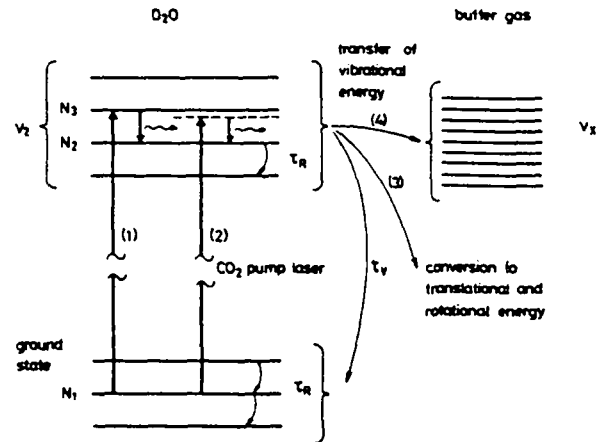


Fig. 1. Schematic diagram of D<sub>2</sub>O energy levels. Pump process (1) leads to a laser and (2) to a stimulated Raman transition at 385 μm. Relaxation of the vibrational excitation can occur either via conversion to translational and rotational energy (3) or via transfer of energy to a buffer gas molecule with a vibrational level close to that of D<sub>2</sub>O (4).

and technical problems of manufacturing large optical components will set a limit to this approach.

An alternative method to prevent ground state depletion is the addition of buffer gases to remove the vibrational bottleneck by collisional energy transfer.

In this paper, the requirements for selection of suitable buffer gases are discussed, and an experimental and numerical study of the influence of these additives on the performance of the 385 μm optically pumped D<sub>2</sub>O laser is presented.

## II. THEORY

The optically pumped D<sub>2</sub>O laser has been investigated extensively both in theory [2] and experiment [3], [4]. In particular, it has been shown that the far infrared emission at 385 μm is due to a stimulated Raman process, during which the D<sub>2</sub>O molecules are excited to the *v*<sub>2</sub> vibrational state by the 9R(22) line of the CO<sub>2</sub> laser. Fig. 1 shows a simplified diagram of the energy levels involved. Apart from the optical transitions, the description of the dynamics of optical pumping has to include molecular relaxation processes. Within the rotational sublevels of each vibrational state, the equilibrium population is reestablished on a very fast time scale (typically 8 ns · torr), whereas the relaxation of the vibrational levels is slower by several orders of magnitude. The energy of the molecules excited

Manuscript received November 19, 1984.

R. Behn, I. Kjelberg, P. A. Krug, S. A. Salito, and M. R. Siegrist are with the Centre de Recherches en Physique des Plasmas, Ecole Polytechnique Fédérale de Lausanne, 1007 Lausanne, Switzerland.

M.-A. Dupertuis was with the Centre de Recherches en Physique des Plasmas, Ecole Polytechnique Fédérale de Lausanne, 1007 Lausanne, Switzerland. He is now with the Research Institute for Theoretical Physics, Helsinki, Finland.

to the  $\nu_2$  vibrational state has to be transferred by molecular collisions to translational and rotational degrees of freedom. For the  $\nu_2$  vibrational level of  $D_2O$ , a relaxation time constant of  $1 \mu s \cdot \text{torr}$  has been measured [5]. For typical operating pressures of the  $D_2O$  laser of several torr, the relaxation time will be almost as long as the pump pulse duration. The relatively low vibrational relaxation rate causes an accumulation of population in the  $\nu_2$  vibrational state and simultaneously a depletion of the ground state. This bottleneck effect leads to a decrease in absorption of the pump radiation and, as a consequence, to a decrease of the FIR laser gain.

It has been predicted that pump saturation may cause serious problems when attempting to achieve FIR laser pulses of  $1 \mu s$  or longer [2]. During an earlier study [4] a decrease in the energy conversion efficiency of the  $D_2O$  laser was indeed observed when the pulse length was increased from 500 ns to  $1.2 \mu s$ . The influence of the bottleneck effect on the pulse shape of an optically pumped FIR laser has been investigated by Dangoisse *et al.* [6]. The limitations on laser efficiency due to a bottleneck effect are already well known from studies of the  $CO_2$  laser [7], [8].

As an efficient solution to the problem, buffer gas additives have been used to obtain energy redistribution via intermolecular collisions. In the case of the  $CO_2$  laser, for instance, He atoms play an important role in depopulating the lower laser level. Buffer gases have also been used successfully with CW FIR lasers [9], [10]. Whereas in CW operation, improvements can be achieved if the rate of collisional deexcitation exceeds the rate of energy transfer by diffusion to the laser tube walls, in pulsed operation energy transfer has to be established on a much faster time scale. Since relaxation is dominated by collision processes, shorter relaxation times can, of course, be obtained by increasing the gas pressure. However, at higher  $D_2O$  pressures, the effect of collisional broadening of the rotational levels becomes dominant and causes the FIR gain to decrease. Therefore, we seek buffer gas additives which selectively enhance the vibrational deexcitation but do not affect the lifetime of the  $D_2O$  rotational levels within the operating pressure range.

It is well known that the cross section for vibrational deexcitation can be increased by several orders of magnitude when near-resonant energy exchange is possible [11]. An efficient buffer gas molecule therefore should have vibrational levels in close proximity to the  $\nu_2$  band of  $D_2O$ . Collisional broadening, on the other hand, is considerably larger for molecules interacting via long range dipole-dipole forces [12]. In order to avoid this detrimental effect, buffer gas molecules without a permanent dipole moment are preferable.

Taking these points into account, we have selected buffer gas candidates according to the following guidelines:

- 1) vibrational energy levels allowing resonant energy transfer from the  $\nu_2$  level of  $D_2O$  at  $1079 \text{ cm}^{-1}$
- 2) negligible absorption of the pump radiation at  $9.3 \mu m$
- 3) negligible absorption of FIR at  $385 \mu m$

- 4) minimum collisional broadening of the  $D_2O$  rotational levels.

Resonant energy transfer only requires coincidence of the levels to within  $E = kT = 200 \text{ cm}^{-1}$ , so a conflict between requirements 1) and 2) can be avoided. Furthermore, molecules may be considered for which the particular vibrational transition is not infrared active. If we choose molecules which have no permanent dipole moment and therefore have no far infrared active rotational transitions, criteria 3) and 4) can be satisfied simultaneously.

### III. NUMERICAL SIMULATION

A numerical simulation code [13] has been used to study the influence of a buffer gas additive on FIR output energy, pump absorption, and FIR laser pulse shape. The generation of FIR radiation is described by a Raman process in a three-level system. Both the coupling of the individual rotational levels and the vibrational relaxation into the ground state are taken into account. The corresponding time constants for  $D_2O$  are  $\tau_{R,d}$  and  $\tau_{V,d}$ . Using a simplified model, additional relaxation rates, proportional to  $1/\tau_{V,b}$  and  $1/\tau_{R,b}$ , are introduced to describe the vibrational deexcitation and the rotational line broadening of  $D_2O$  due to the interaction with the buffer gas molecules. For a mixture of  $D_2O$  and buffer gas at partial pressure  $p_d$  and  $p_b$ , respectively, we obtain an effective relaxation time constant  $\tau_{i,\text{eff}}$  by adding the rates associated with  $D_2O$ - $D_2O$  and  $D_2O$ -buffer gas collisions:

$$\tau_{i,\text{eff}} = \frac{p_d + p_b}{p_d/\tau_{i,d} + p_b/\tau_{i,b}} \quad (1)$$

where

- index  $i = V$  for vibrational relaxation  
 index  $i = R$  for rotational relaxation.

During the pump pulse duration of about  $1 \mu s$ , the probability of multiple collisions between  $D_2O$  and buffer gas molecules is low. Therefore, all buffer gas molecules are assumed to be in the vibrational ground state, and the time constants for equilibration of vibrational energy within the buffer gas molecule do not have to be taken into account.

Results from the numerical simulation code for a set of parameters describing our  $D_2O$  laser (active length  $L = 4 \text{ m}$ ; output coupling  $T = 0.95$ ; pump energy  $E_p = 320 \text{ J}$ ; pulse length  $\sim 1 \mu s$  FWHM) are presented in Fig. 2. Vibrational and rotational relaxation time constants of  $\tau_{V,d} = 1.5 \mu s \cdot \text{torr}$  and  $\tau_{R,d} = 8 \text{ ns} \cdot \text{torr}$ , consistent with published data [5], have been used. The three curves show the variation of FIR output energy as a function of  $D_2O$  pressure for different pumped volume cross sections  $A$ , at fixed pump energy. The laser system used during the experiments had a cross section of  $A = 0.014 \text{ m}^2$ . The calculations predict that the optimum operating pressure shifts to higher values and the energy conversion efficiency decreases when the pump energy density is increased, indicating that pump saturation is important.



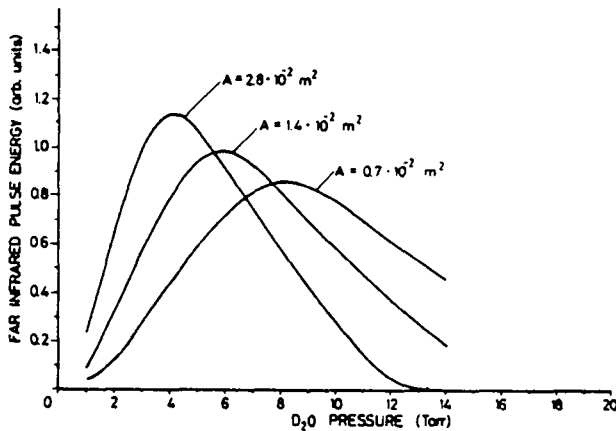


Fig. 2. Results from the numerical simulation code showing FIR output energy as a function of  $D_2O$  pressure for the active volume cross sections (a)  $A = 0.028 \text{ m}^2$ , (b)  $A = 0.014 \text{ m}^2$ , and (c)  $A = 0.007 \text{ m}^2$ . The time constants used in the calculations are  $\tau_{v,d} = 1.5 \mu\text{s} \cdot \text{torr}$  and  $\tau_{r,d} = 8 \text{ ns} \cdot \text{torr}$ .

For the intermediate case in Fig. 2 ( $A = 0.014 \text{ m}^2$ ), the effect of a buffer gas additive on the FIR output energy has been investigated.

The influence of each of the two parameters  $\tau_{v,b}$  and  $\tau_{r,b}$  characterizing the buffer gas has been studied separately. The parameters describing the  $D_2O$  laser are identical to those of Fig. 2 for the case with  $A = 0.014 \text{ m}^2$ . The results of the calculations are presented in Fig. 3(a) and (b), which shows the variation of FIR pulse energy when the total pressure is increased by adding buffer gas to a starting pressure of 4.0 torr of  $D_2O$ . The curve describing operation in pure  $D_2O$  is included for comparison (solid line). In Fig. 3(a),  $\tau_{r,b}$  has been chosen to be the same as  $\tau_{r,d}$ , the corresponding parameter for  $D_2O$ - $D_2O$  collisions. The results of Fig. 3(b) are obtained for  $\tau_{r,b} = 5 \cdot \tau_{r,d}$ , thus assuming a weaker broadening of the  $D_2O$  rotational level by interaction with the buffer gas molecules. For both sets of curves  $\tau_{v,b}$  was varied from  $0.5 \mu\text{s} \cdot \text{torr}$  to  $2.0 \mu\text{s} \cdot \text{torr}$ , covering the range of values smaller and larger by a factor of 2 than the corresponding parameter for  $D_2O$ - $D_2O$  collisions.

Comparing Fig. 3(a) and (b), it can be seen that  $\tau_{r,b}$  determines the behavior at high partial pressures of buffer gas, whereas  $\tau_{v,b}$  is most important at low partial pressures. In particular, for the case of  $\tau_{r,b} = \tau_{r,d}$ , an increase in FIR energy can only be obtained if  $\tau_{v,b} < \tau_{v,d}$ . When, however,  $\tau_{r,b} > \tau_{r,d}$ , as in Fig. 3(b), higher partial pressures of the buffer gas can be used and even molecules with  $\tau_{v,b} \geq \tau_{v,d}$  allow us to obtain higher pulse energies than with pure  $D_2O$ .

From the results of the numerical simulation, it is concluded that for an efficient buffer gas, criteria 1) and 4) are equally important. For vibrational and rotational time constants which are of the same order of magnitude as those quoted for  $D_2O$ - $D_2O$  collisions, a noticeable increase in the efficiency of a high-power  $D_2O$  laser can be expected.

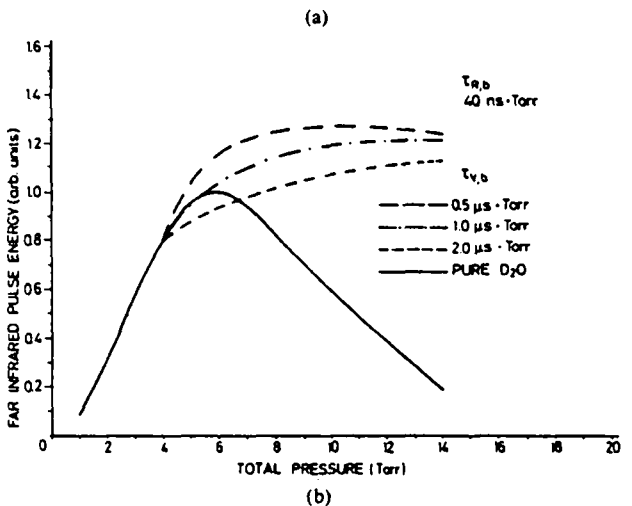
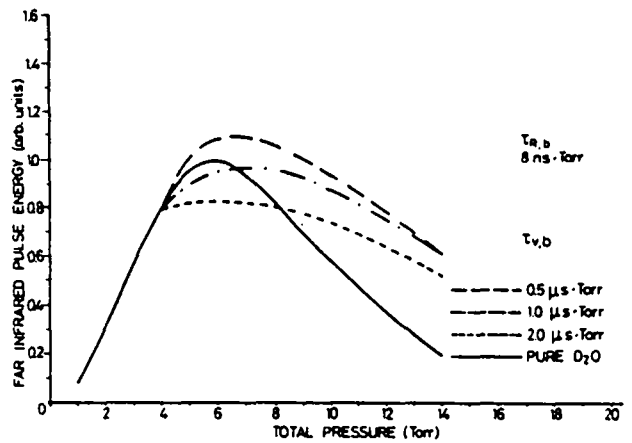


Fig. 3. Calculated FIR output energies as a function of total pressure for a mixture of buffer gas and 4.0 torr of  $D_2O$ . The buffer gas parameters are  $\tau_{v,b}$ : 0.5, 1.0, and  $2.0 \mu\text{s} \cdot \text{torr}$ ;  $\tau_{r,b}$ : 8 ns  $\cdot$  torr in (a), 40 ns  $\cdot$  torr in (b). The results for pure  $D_2O$  are shown for comparison (solid line).

## IV. EXPERIMENTAL

### A. Choice of Molecules

Several molecules have been investigated as a test for some of the selection guidelines given above. Table I lists the molecules together with their vibrational energy levels close to the  $\nu_2$  band of  $D_2O$  ( $1079 \text{ cm}^{-1}$ ) and their static electric dipole moments  $p_s$ .

The molecules that produced an increase (+) in FIR output energy when used as additives in a pulsed  $D_2O$  laser (i.e.,  $SF_6$ ,  $CF_4$ , and  $n$ -hexane) all satisfy the selection criteria and were studied in more detail. Sulphur hexafluoride ( $SF_6$ ) and carbon tetrafluoride ( $CF_4$ ) are spherical top molecules which possess neither permanent electric dipole nor quadrupole moments. The linear molecule  $n$ -hexane ( $C_6H_{14}$ ) has a large number of vibrational degrees of freedom with several vibrational bands in the region of interest. Both molecules  $C_6H_{14}$  and  $SF_6$  have already been reported as efficient buffer gases in a CW  $CH_3F$  laser [9], [10]. For each of the three molecules, absorption on the 9R(22) line of the  $CO_2$  laser was measured using the FIR laser tube as an absorption cell. The absorption of  $SF_6$  was

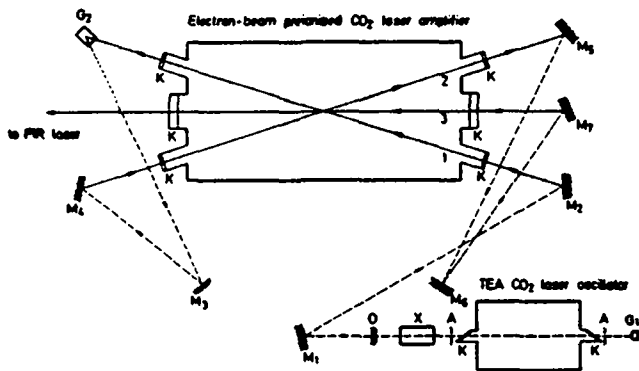


Fig. 4. Side view of CO<sub>2</sub> laser system. The oscillator and the beam paths shown by broken lines lie outside the plane of the figure.  $G_1$ : diffraction grating for wavelength selection,  $A$ : variable apertures for transverse mode control.  $K$ : KCl windows.  $X$ : low pressure CO<sub>2</sub> laser module for longitudinal mode control.  $O$ : ZnSe output coupler.  $M$ : plane metal mirrors.  $G_2$ : diffraction grating used to prevent parasitic oscillation on higher gain lines.

at least an order of magnitude lower than that of D<sub>2</sub>O, and the absorption of CF<sub>4</sub> [16], [17] and C<sub>6</sub>H<sub>14</sub> were negligible.

### B. Experimental Details

The CO<sub>2</sub> laser, used as an optical pump for the D<sub>2</sub>O laser, comprises a hybrid TEA laser oscillator operating in a single mode on the 9R(22) line and an electron-beam preionized amplifier, as represented in Fig. 4.

The oscillator is identical to that in an earlier publication [4], while the *e*-beam amplifier is now used without preamplifier in a more efficient triple-pass configuration. In order to achieve high gain on the 9R(22) line, a relatively CO<sub>2</sub>-rich gas mixture of CO<sub>2</sub>:N<sub>2</sub>:He = 4:1:1 is used at a total pressure of 2.3–2.6 atm. Between the first and second passages, a grating  $G_2$  with 150 rulings/mm is used in first order, to prevent parasitic oscillation on any line other than 9R(22) from propagating backwards into the oscillator. The total optical path length from the CO<sub>2</sub> laser oscillator to the FIR resonator is 65 m.

With careful adjustment of the time delay between the firing of the oscillator and the amplifier, the system is capable of producing single mode pulses of 1  $\mu$ s FWHM with energy up to 850 J.

The FIR laser (Fig. 5) comprises a 4.0 m long folded unstable resonator formed by a concave mirror ( $M_{cc}$ , radius of curvature 10.3 m, diameter 200 mm) and a convex mirror ( $M_{cv}$ , radius of curvature 2.3 m, diameter 42 mm). The resonator is folded by a wire grid ( $W$ ) which is 90 percent transmitting for the pump beam and 75 percent reflecting for the FIR. For this configuration, an effective output coupling of  $T = 0.95$  has been calculated. The pump beam from the CO<sub>2</sub> laser enters the tube via a 180 mm diameter KCl window ( $K$ ). The glass tube ( $T$ ) serves to confine the CO<sub>2</sub> laser radiation to the volume of the FIR resonator. The limiting aperture of the FIR laser is 200 mm. An off-axis paraboloidal mirror ( $M_p$ ) is used to collect and focus the FIR beam to a point outside the tube. Because the FIR resonator does not contain any mode se-

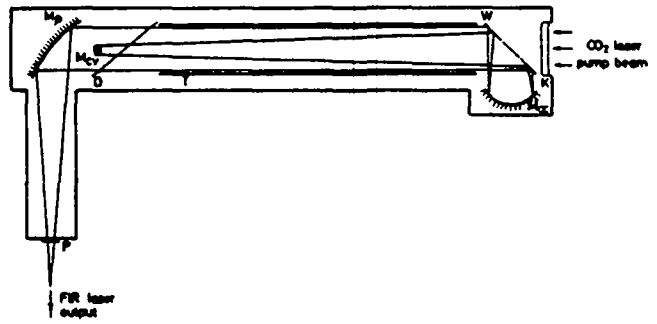


Fig. 5. Optically pumped FIR D<sub>2</sub>O laser.  $K$ : KCl window for input of CO<sub>2</sub> laser beam.  $W$ : Tungsten wire grid.  $M_{cc}$ : concave mirror.  $T$ : glass tube used to guide the pump beam.  $D$ : teflon sheet as beam dump for unabsorbed pump energy.  $M_{cv}$ : convex mirror.  $M_p$ : off-axis paraboloidal mirror.  $P$ : TPX window.

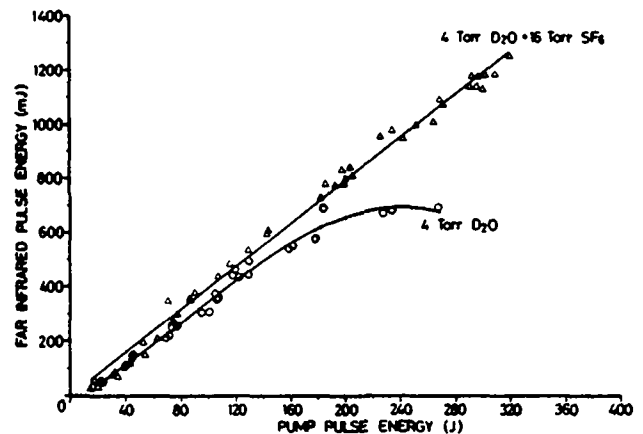


Fig. 6. FIR pulse energy as a function of pump pulse energy for (a) pure D<sub>2</sub>O,  $P = 4.0$  torr; (b) 4.0 torr of D<sub>2</sub>O and 16.0 torr of buffer gas.

lective elements, the laser pulses show modulation due to mode beating.

### C. Results

1) *Pump Saturation*: In Fig. 6, the FIR pulse energy is plotted versus the pulse energy of the CO<sub>2</sub> pump laser for operation at a filling pressure of 4.0 torr of D<sub>2</sub>O. Deviations from a linear relationship become noticeable at pump energies of about 150 J (energy densities of  $\sim 10$  kJ/m<sup>2</sup>). With the addition of 16.0 torr of SF<sub>6</sub> (upper curve), these saturation effects disappear. The influence of the buffer gas SF<sub>6</sub> on the absorption of the pump radiation is shown in Fig. 7. The fraction of unabsorbed pump pulse energy is plotted as a function of total pressure, with the D<sub>2</sub>O partial pressure kept fixed at 4.0 torr and SF<sub>6</sub> added. The pump beam absorption is clearly increasing with SF<sub>6</sub> pressure, as is expected from our model for a buffer gas that permits efficient vibrational deexcitation of the D<sub>2</sub>O molecules. The numerical code predicts a similar behavior (solid curve), although no attempt has been made to fit these experimental results. This observation seems to be at variance with the results presented in [10] for a CW CH<sub>3</sub>F laser. However, it should be noted that an increase in absorption, induced by the addition of buffer gas, can

TABLE I  
CANDIDATE BUFFER GAS MOLECULES

Molecule	Permanent dipole moment $p_p^*$	Vibrational* bands	Effect on FIR laser output
$\text{CH}_3\text{F}$	1.85 D	1048 $\text{cm}^{-1}$ 1196 $\text{cm}^{-1}$	-
$\text{CF}_4$	0	904 $\text{cm}^{-1}$ 1070 $\text{cm}^{-1}$ 1265 $\text{cm}^{-1}$	+
$\text{C}_2\text{H}_6$	0	949 $\text{cm}^{-1}$ 995 $\text{cm}^{-1}$ 1050 $\text{cm}^{-1}$ 1342 $\text{cm}^{-1}$	-
$\text{C}_2\text{H}_3\text{Cl}$	1.45 D	850-1050 $\text{cm}^{-1}$	-
$\text{SF}_6$	0	965 $\text{cm}^{-1}$ 1262 $\text{cm}^{-1}$ 1282 $\text{cm}^{-1}$	+
n-hexane $\text{C}_6\text{H}_{14}$	0	973-1166 $\text{cm}^{-1}$	+

\*Data from [14]-[16].

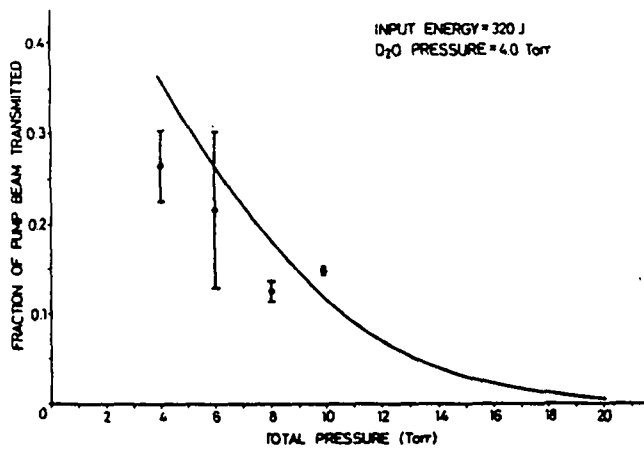
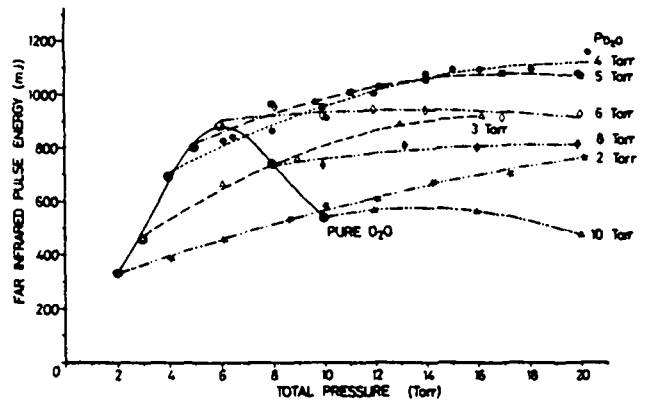


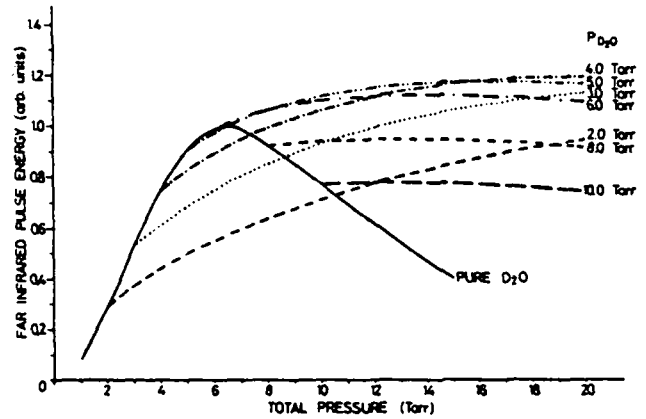
Fig. 7. Pump beam energy transmission through  $\text{D}_2\text{O}$  laser tube as a function of total pressure  $P_{\text{tot}}$  for fixed  $\text{D}_2\text{O}$  and varying  $\text{SF}_6$  pressure. The points represent average values over three laser shots, and the solid curve gives the results from the numerical simulation using the parameters of Table II.

only be expected if the vibrational bottleneck effect causes strong saturation of the pump transition, as is the case for the pulsed  $\text{D}_2\text{O}$  laser operated under the conditions described above. As already mentioned above, the absorption of the 9R(22) line of the  $\text{CO}_2$  laser in pure  $\text{SF}_6$  in this pressure range is small enough to be neglected.

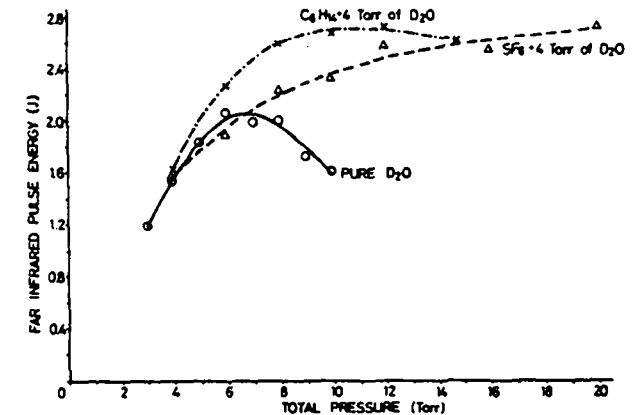
2) *FIR Pulse Energy*: The effects of the candidate buffer gases on the  $\text{D}_2\text{O}$  laser output were investigated by measuring the variation of pulse energy with total pressure for  $\text{D}_2\text{O}$  alone and for various mixtures of  $\text{D}_2\text{O}$  and buffer gas. Fig. 8(a) shows the results of such a set of measurements for the buffer gas  $\text{SF}_6$ . Each point is the average of at least three shots, and the curves are least square fits to the data. The points fitted by the solid curve in Fig. 8(a) show the



(a)



(b)



(c)

Fig. 8. FIR pulse energy as a function of total gas pressure. (a) Experimental results with an average of 320 J of pump pulse energy, using  $\text{SF}_6$  as buffer gas. (b) Results of the simulation code using the  $\text{SF}_6$  parameter values of Table II, and a pump energy of 320 J. (c) Comparison of experimental results for buffer gas additives  $\text{SF}_6$  and  $n$ -hexane at fixed  $\text{D}_2\text{O}$  pressure of 4.0 torr.

FIR pulse energies with pure  $\text{D}_2\text{O}$ . The other curves represent the pulse energy for a fixed  $\text{D}_2\text{O}$  partial pressure, as indicated, the total pressure being varied by progressively adding  $\text{SF}_6$ . The  $\text{CO}_2$  laser pump energy entering the  $\text{D}_2\text{O}$  laser was 320 J, in a  $1 \mu\text{s}$  long pulse. For an effective pumping beam area of  $A = 0.012 \text{ m}^2$ , the spatially averaged energy density is  $27 \text{ kJ} \cdot \text{m}^{-2}$ .

Fig. 8(b) shows results of the numerical simulation code

TABLE II  
SUMMARY OF RELAXATION TIME CONSTANTS

Parameter	Published or measured value	Best fit values	
		SF <sub>6</sub>	CF <sub>4</sub>
$\tau_{V,d}$	1.0 $\mu\text{s}\cdot\text{Torr}$	1.5 $\mu\text{s}\cdot\text{Torr}$	1.5 $\mu\text{s}\cdot\text{Torr}$
$\tau_{R,d}$	8 ns $\cdot\text{Torr}$	8 ns $\cdot\text{Torr}$	8 ns $\cdot\text{Torr}$
$\tau_{V,b}$	-	1.8 $\mu\text{s}\cdot\text{Torr}$	1.2 $\mu\text{s}\cdot\text{Torr}$
$\tau_{R,b}$	-	46 ns $\cdot\text{Torr}$	46 ns $\cdot\text{Torr}$

produced by adjusting parameter values to obtain good agreement with the experimental results for SF<sub>6</sub>. Apart from a constant scaling factor for the FIR pulse energy, there is good qualitative agreement between the results given in Fig. 8(a) and (b), which confirms the model of the D<sub>2</sub>O-buffer gas interaction. The parameter values for SF<sub>6</sub> and CF<sub>4</sub> as obtained from the fitting procedure are summarized in Table II.

Because the model used in the simulation code is of necessity a simplification of the real laser system, for example, in its assumption of spatially uniform pumping, it is not reasonable to expect to obtain precise numerical values for the fitted parameters. Rather, the purpose of performing the fit is to obtain information about the relative values of the time constants.

The best fit value of the effective beam area  $A = 0.014 \text{ m}^2$  is in good agreement with the value  $0.012 \text{ m}^2$ , which was estimated with a large uncertainty from CO<sub>2</sub> laser burn marks on thermally sensitive paper. The parameter  $\tau_{R,d}$  was kept fixed at the published value of  $8 \text{ ns}\cdot\text{torr}$  [18]. The best fit value  $\tau_{V,d} = 1.5 \mu\text{s}\cdot\text{torr}$ , while somewhat larger than the published value of  $1.0 \mu\text{s}\cdot\text{torr}$  [5], is not unreasonable, given the limitations of the code.

The most interesting information obtained from the simulation comes from a comparison of D<sub>2</sub>O and buffer gas parameter values. It is found that the vibrational relaxation time constant for buffer gas-D<sub>2</sub>O collisions,  $\tau_{V,b}$ , is not very different from the value for D<sub>2</sub>O-D<sub>2</sub>O collisions,  $\tau_{V,d} = 1.5 \mu\text{s}\cdot\text{torr}$ . The difference between  $\tau_{V,b}$  values for SF<sub>6</sub> and CF<sub>4</sub> reflects the faster increase in FIR energy with increasing partial pressure for CF<sub>4</sub> than for SF<sub>6</sub>, at low partial pressures. The closeness of the values of  $\tau_{V,b}$  and  $\tau_{V,d}$  means that the buffer gases are about as effective as D<sub>2</sub>O itself in deexciting the  $\nu_2$  vibrational level of D<sub>2</sub>O.

In order to explain why, at D<sub>2</sub>O pressures near 4 torr, the addition of buffer gas is more beneficial to laser efficiency than the addition of further D<sub>2</sub>O, it is necessary to compare the rotational relaxation time constants  $\tau_{R,d}$  and  $\tau_{R,b}$ . We see that  $\tau_{R,b} = 46 \text{ ns}\cdot\text{torr}$  (for both SF<sub>6</sub> and CF<sub>4</sub>) is considerably larger than the corresponding D<sub>2</sub>O time constant  $\tau_{R,d} = 8 \text{ ns}\cdot\text{torr}$ . The addition of buffer gases therefore contributes much less to the detrimental rotational line broadening than would the addition of the same quantity of D<sub>2</sub>O. Since  $\tau_{V,d}$  and  $\tau_{V,b}$  are about equal, a higher relaxation rate is achieved via a sufficiently high partial pressure of the buffer gas.

Caution must be employed in interpreting the quoted values of  $\tau_{R,b}$ , since the fit is quite insensitive to the precise value. A reasonable fit of the model to the observed data can be obtained with a large range of values as long as the condition  $\tau_{R,b} \gg \tau_{R,d}$  is satisfied.

Fig. 8(c) shows a comparison of the performance of the D<sub>2</sub>O laser with SF<sub>6</sub> and *n*-hexane for a D<sub>2</sub>O pressure of 4.0 torr (which is not far from the optimum D<sub>2</sub>O pressure for both buffer gases). These results were obtained with a beam reducing telescope which increased both the CO<sub>2</sub> beam transport efficiency and the pump energy density in the D<sub>2</sub>O laser. The 2.6 J pulses are the most energetic that have been obtained from this laser. Higher pulse energies from a D<sub>2</sub>O laser have so far only been reported in [19]. The different pressure dependence for the two buffer gases indicates that *n*-hexane has smaller  $\tau_{V,b}$  and  $\tau_{R,b}$  than SF<sub>6</sub>.

3) *Pulse Shape*: Observation of the D<sub>2</sub>O laser pulse shape clearly shows the influence of the bottleneck effect. The accumulation of D<sub>2</sub>O molecules in the  $\nu_2$  vibrational state should be observable as a decrease in the energy conversion efficiency after a time of the order of one or two vibrational relaxation time constants.

In Fig. 9, the top and middle traces are measured CO<sub>2</sub> laser and FIR laser pulses, respectively. The bottom traces are calculated FIR pulse shapes with the actual CO<sub>2</sub> laser pulse as input. For the purpose of comparison to the numerical results, the modulation on the recorded FIR pulses due to mode beating has been filtered out. It can be seen that the FIR power (middle trace) falls more rapidly than the pump power (top trace), beginning about  $0.4 \mu\text{s}$  after the start of the pulse, for a laser operated with 4.0 torr of pure D<sub>2</sub>O. The  $0.4 \mu\text{s}$  delay in the onset of the dip is consistent with the estimated value of  $\tau_{V,d}/P_{\text{tot}}$ . The simulation code predicts an FIR pulse shape (bottom trace) which is in qualitative agreement with the observed pulse. The simulated pulse differs from the observed one mainly in having a smaller bottleneck dip. Addition of 4.0 torr of SF<sub>6</sub> [Fig. 9(b)] is seen to reduce the size of the bottleneck dip, and with 16.0 torr there is no evidence of it any more. In the latter case, the FIR pulse shape is essentially identical to that of the pump, in agreement with the theoretical predictions.

4) *Optimization of Buffer Gas Performance*: Noting that for near optimum partial pressure of D<sub>2</sub>O, the FIR pulse energy is almost independent of total pressure in the range above 10 torr (see Fig. 8), we determined the optimum D<sub>2</sub>O partial pressure in a more precise way. For this purpose the FIR pulse energy was measured as a function of D<sub>2</sub>O partial pressure for fixed total pressure, by varying the mixing ratio of D<sub>2</sub>O and buffer gas.

Fig. 10 shows the results of such measurements for SF<sub>6</sub> ( $P_{\text{tot}} = 17.0 \text{ torr}$ ) and CF<sub>4</sub> ( $P_{\text{tot}} = 12.0 \text{ torr}$ ), together with the curve predicted by the code using the parameter values for CF<sub>4</sub> (solid line). The results from the numerical code have been scaled in order to obtain the same peak height as in the experiment. It is seen that under the operating conditions employed, the optimum partial D<sub>2</sub>O pressure is between 3.5 and 3.8 torr for CF<sub>4</sub> and SF<sub>6</sub>. The

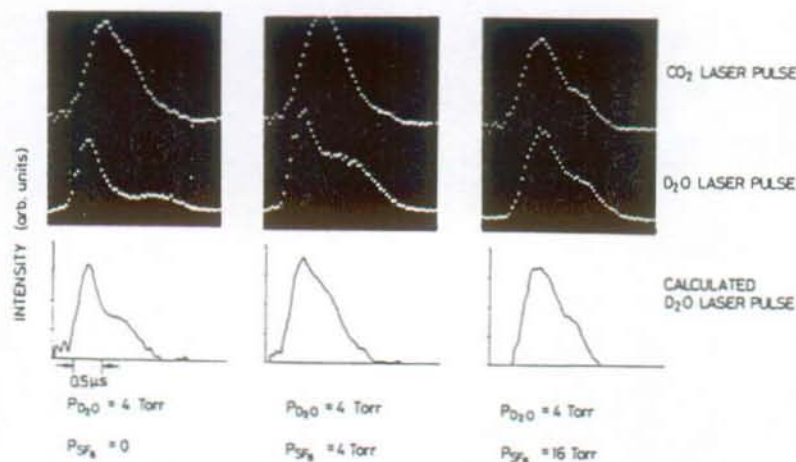


Fig. 9. Comparison of CO<sub>2</sub> and FIR laser pulse shapes. D<sub>2</sub>O pressure: 4.0 torr, SF<sub>6</sub> pressure: (a) 0 torr, (b) 4.0 torr, and (c) 16.0 torr. Top: CO<sub>2</sub> laser pulse, experimental result. Middle: FIR laser pulse, experimental result. Bottom: FIR laser pulse, from simulation code. For the observed pulses, the dots are individual samples taken by a digitizing oscilloscope.

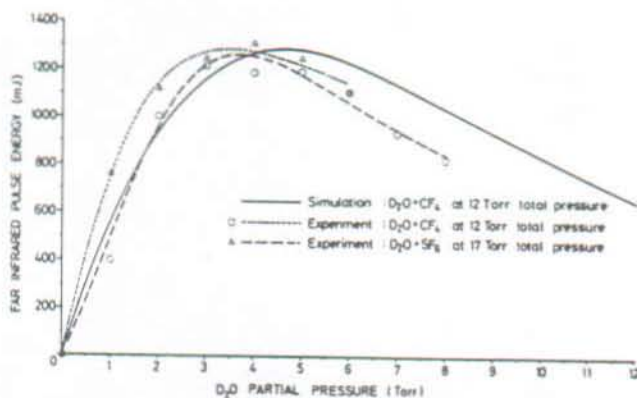


Fig. 10. Determination of optimum D<sub>2</sub>O partial pressure for operation with SF<sub>6</sub> and CF<sub>4</sub>. The total pressure was kept constant at 17.0 torr for the case of SF<sub>6</sub> and at 12.0 torr for CF<sub>4</sub>. The solid curve was calculated using the CF<sub>4</sub> parameter values of Table II, and has been scaled to give the same peak height as the experimental results.

code, while agreeing with the general form of the experimental curves, predicts a somewhat higher value.

Table III summarizes the improvements in FIR output energy with the three buffer gases.

### V. CONCLUSIONS

An experimental study supported by numerical simulations has been carried out to investigate the influence of buffer gas additives on output energy and pulse shape of an optically pumped D<sub>2</sub>O laser.

The molecules that were found to increase the pumping efficiency are characterized by near-resonant vibrational levels allowing fast vibrational energy exchange, and by lack of a permanent dipole moment to avoid broadening of the D<sub>2</sub>O rotational levels.

The experiments were performed using a single-mode CO<sub>2</sub> laser providing pump energies up to 850 J in 1 μs long pulses. Under optimum conditions, FIR emission of 2.6 J per pulse has been measured.

At pump energy densities which in pure D<sub>2</sub>O would lead

TABLE III  
IMPROVEMENTS IN PULSE ENERGY USING SF<sub>6</sub>, CF<sub>4</sub>, AND C<sub>6</sub>H<sub>14</sub>

Buffer gas molecule	SF <sub>6</sub>	CF <sub>4</sub>	C <sub>6</sub> H <sub>14</sub>
Maximum pulse energy (normalized)*	1.32	1.40	1.36
Optimum D <sub>2</sub> O partial pressure (Torr)	3.8	3.5	3.0

\*Note: Maximum pulse energy obtained with buffer gas additive divided by maximum energy with pure D<sub>2</sub>O.

to saturation caused by the vibrational bottleneck, an increase in pulse energy of up to 40 percent has been observed using SF<sub>6</sub>, C<sub>6</sub>H<sub>14</sub>, or CF<sub>4</sub> as a buffer gas additive. The observed dip in the FIR pulse shape during long pump pulses in pure D<sub>2</sub>O is filled in when buffer gas is added. This important effect permits long pulse operation.

As for the design of a D<sub>2</sub>O laser with specified output energy, the use of a buffer gas as a means to avoid pump saturation will considerably reduce the required laser volume.

### ACKNOWLEDGMENT

The authors gratefully acknowledge the advice of Dr. H. Van den Bergh in the selection of buffer gas molecules. They also thank Q. H. Do for his assistance during some of the experiments.

### REFERENCES

- [1] D. E. Evans, L. E. Sharp, W. A. Peebles, and G. Taylor, "Far-infrared super-radiant laser action in heavy water," *Opt. Commun.*, vol. 18, pp. 479-484, 1976.
- [2] R. J. Temkin, "Theory of optically pumped submillimeter lasers," *IEEE J. Quantum Electron.*, vol. QE-13, pp. 450-454, 1977.
- [3] P. Woskoboinikow, H. C. Pradde, W. J. Mulligan, D. R. Cohn, and B. Lax, "High-power tunable 385 μm D<sub>2</sub>O vapour laser optically pumped with a single-mode tunable CO<sub>2</sub> TEA laser," *J. Appl. Phys.*, vol. 50, pp. 1125-1127, 1979.

- [4] R. Behn, I. Kjelberg, P. D. Morgan, T. Okada, and M. R. Siegrist, "A high power D<sub>2</sub>O laser optimized for microsecond pulse duration," *J. Appl. Phys.*, vol. 54, pp. 2995-3002, 1983.
- [5] R. L. Sheffield, K. Boyer, and A. Javan, "Study of vibrational and rotational relaxations in D<sub>2</sub>O," *Opt. Lett.*, vol. 5, pp. 10-11, 1980.
- [6] D. Dangoisse, P. Glorieux, and J. Wascot, "Diffusion and vibrational bottleneck in optically pumped submillimeter lasers," *Int. J. Infrared, Millimeter Waves*, vol. 2, pp. 215-229, 1981.
- [7] P. K. Cheo, "Effects of CO<sub>2</sub>, He, and N<sub>2</sub> on the lifetimes of the 00<sup>0</sup>1 and 10<sup>0</sup>0 CO<sub>2</sub> laser levels and on pulsed gain at 10.6 μm," *J. Appl. Phys.*, vol. 38, pp. 3563-3569, 1967.
- [8] P. K. Cheo, "CO<sub>2</sub> lasers," in *Lasers*, vol. 3, A. K. Levine and A. J. DeMaria, Eds. New York: Dekker, 1971, pp. 148-167.
- [9] T. Y. Chang and C. Lin, "Effects of buffer gases on an optically pumped CH<sub>3</sub>F FIR laser," *J. Opt. Soc. Amer.*, vol. 66, pp. 362-369, 1976.
- [10] N. M. Lawandy and G. A. Koepf, "Energy-transfer-mechanisms in the CH<sub>3</sub>F-SF<sub>6</sub> optically pumped laser," *Opt. Lett.*, vol. 5, pp. 336-338, 1980.
- [11] J. D. Lambert, "Relaxation in gases," in D. R. Bates, *Atomic and Molecular Processes*. New York: Academic, pp. 783-806, 1962.
- [12] P. C. Pandey and S. L. Srivastava, "Collision broadening of C<sub>2</sub>H<sub>4</sub>O lines. I. Broadened by polar molecules," *J. Chem. Phys.*, vol. 57, pp. 3282-3286, 1972.
- [13] T. Okada, R. Behn, M. A. Dupertuis, P. D. Morgan, and M. R. Siegrist, "Numerical analysis of an optically pumped D<sub>2</sub>O far infrared laser," *J. Appl. Phys.*, vol. 54, pp. 2987-2994, 1983. Note: The numerical code has been modified to include reabsorption of the 385 μm emission by a rotational transition in the ground state of D<sub>2</sub>O.
- [14] *CRC Handbook of Chemistry and Physics*, 49th ed., R. C. Weast, Ed. Cleveland, OH: CRC Press, 1968.
- [15] G. Herzberg, *Molecular Spectra and Molecular Structure. Vol. 2: Infrared and Raman Spectra of Polyatomic Molecules*. Princeton, NJ: Van Nostrand, 1945.
- [16] *DMS Tables*, Inst. f. Spektrochemie u. Angewandte Spektroskopie, Dortmund, and Infrared Absorption Data Joint Committee, London, Eds. London, England: Butterworths.
- [17] J. J. Tice and C. Wittig, "CF<sub>4</sub> and NOCl molecular laser operating in the 16 μm region," *Appl. Phys. Lett.*, vol. 30, pp. 420-422, 1977.
- [18] S. J. Petuchowski, A. T. Rosenberger, and T. A. DeTemple, "Stimulated Raman emission in infrared excited gases," *IEEE J. Quantum Electron.*, vol. QE-13, pp. 476-481, 1977.
- [19] A. Semet, L. C. Johnson, and D. K. Mansfield, "A high energy D<sub>2</sub>O submillimeter laser for plasma diagnostics," *Int. J. Infrared, Millimeter Waves*, vol. 4, pp. 231-246, 1983.



R. Behn received the degree in physics in 1975 and the Ph.D. degree in 1980, both from the University of Stuttgart, Stuttgart, West Germany.

He is now with the Centre de Recherches en Physique des Plasmas, Lausanne, Switzerland, where his work is concerned with the development of FIR lasers and their applications to plasma diagnostics. At present he is mainly involved in the operation of an experiment to determine the ion temperature of a tokamak plasma by Thomson scattering using a pulsed FIR laser.



Marc-André Dupertuis was born in the Canton de Vaud, Switzerland, on May 10, 1956. He received the Diplôme d'ingénieur physicien in 1980 and the Ph.D. degree from the Ecole Polytechnique Fédérale de Lausanne, Lausanne, Switzerland, in 1985 for his thesis entitled "Theoretical study of pulsed far-infrared lasers and their multimode behavior."

His interests include quantum electronics, plasma physics, and computer modeling. He is currently working as a Research Fellow at the Research Institute for Theoretical Physics, Helsinki, Finland.

Dr. Dupertuis is a member of the Swiss Physical Society.



Ivar Kjelberg was born in Baerum, Norway, on January 13, 1955. He received the Diplôme d'ingénieur physicien from the Ecole Polytechnique Fédérale, Lausanne, Switzerland, in 1979.

In 1978 he spent three months as a student at CERN, Geneva, working on the ISOLDE project, and is currently working towards the Ph.D. degree at the Centre de Recherches en Physique des Plasmas, Lausanne, Switzerland. His major field of research is the development and use of far infrared lasers for an ion temperature measurement by collective Thomson scattering on the Lausanne TCA tokamak.

lective Thomson scattering on the Lausanne TCA tokamak.



Peter A. Krug was born in Sydney, Australia, on February 1, 1955. He received the B.Sc. (Hons.) and Ph.D. degrees from the University of Sydney, Sydney, Australia, in 1977 and 1983, respectively.

In 1982 he joined the Centre de Recherches en Physique des Plasmas, Lausanne, Switzerland, where he has been involved with the development of a far infrared laser diagnostic experiment to measure the ion temperature in the TCA tokamak by collective Thomson scattering.

Dr. Krug is a member of the Australian Institute of Physics and the Swiss Physical Society.



S. A. Salito was born in Geneva, Switzerland, on July 29, 1959. He received the Diplôme d'ingénieur physicien from the Swiss Federal Institute of Technology, Lausanne, Switzerland, in 1983.

He is currently working towards the Ph.D. degree at the Centre de Recherches en Physique des Plasmas, Lausanne, Switzerland. Apart from his participation in an FIR Thomson scattering experiment, he is investigating molecular absorption filters in the far infrared band.



Mark R. Siegrist received the diploma in physics from the University of Berne, Berne, Switzerland, in 1969, and the Ph.D. degree from the Australian National University, Canberra, Australia, in 1974.

In 1976 he joined the Centre de Recherches en Physique des Plasmas, Lausanne, Switzerland, where he became involved in the development of far infrared lasers for plasma diagnostics. He is currently leader of a project to determine the ion temperature in the TCA tokamak from collectively scattered far infrared radiation.

Dr. Siegrist is a member of the European Physical Society and the Optical Society of America.

## APPENDIX: E.

### TABLE OF SYMBOLS.

Electronic charge	$e$	$1.602 \cdot 10^{-19}$	C
Electron mass	$m_e$	$9.109 \cdot 10^{-31}$	kg
Proton mass	$m_i$	$1.673 \cdot 10^{-27}$	kg
Speed of light (in vacuo)	$c$	$2.998 \cdot 10^8$	m/s
Plank's constant	$h$	$6.626 \cdot 10^{-34}$	Js
Boltzmann's constant	$\kappa$	$1.380 \cdot 10^{-23}$	J/K
Avogadro's number		$6.022 \cdot 10^{23}$	part./mole
Permeability of free space	$\mu_0$	$4\pi \cdot 10^{-7}$	H/m
Permittivity of free space	$\epsilon_0$	$8.854 \cdot 10^{-12}$	F/m

1 eV =  $1.602 \cdot 10^{-19}$  J is equivalent to  $\kappa T$  for  $T = 11600$  K

1 Torr = 1 mm Hg contains  $3.54 \cdot 10^{22}$  part./m<sup>3</sup> at  $T = 273$  K

A	§3.1	Einstein spontaneous emission coefficient
A	§3.1.5	Beam area
$A\Delta\Omega$	§5.1	Beam étendue
$A, A_{12}, A_{23}$	§5.4	Diplexer signal amplitude
a	§2.3	Plasma minor radius
$a_e$	§1.7	Electron to ion thermal velocity ratio
B	§1.7.8	Magnetic field (vector)
B	§2.8	Bandwidth of spectral channel
$B_T$	§2.0	Toroidal magnetic field
dE	§3.1.5	Energy density of laser radiation
$dE_s$	§3.1.5	Saturation energy density
$E(\mathbf{x}, t)$	§5.1	Electromagnetic field
$F_{q0}$	§1.7	Normalized plasma velocity distribution
$F_{He}, F_{N2}$	§3.1.4	Mole fraction of gas species
f	§4.6	Focal length
$G_f$	§3.3.5	Calculated FIR transition absorption
$G_p$	§3.3.5	Calculated pump transition absorption

$g$	§2.3	Gaunt factor ( $g \approx 5$ in the FIR)
$g_i$	§3.1.6	Resonator parameter for mirror $i$
$I$	§1.2	Intensity of an electromagnetic wave
$I$	§5.5.1	Current
$I_b$	§5.9	Schottky diode bias current
$I_{f\text{-sat}}$	§3.3.5	FIR transition saturation intensity
$I_{p\text{-sat}}$	§3.3.5	Pump transition saturation intensity
$I_s$	§5.5.1	Schottky diode saturation current
$i$	§4.3	Imaginary value ( $\sqrt{-1}$ )
$i(t)$	§5.1	Current
$J$	§3.3	Angular quantum number
$J_0$	§4.3	Bessel function (first order)
$j$	§5.7	Imaginary value ( $\sqrt{-1}$ ) electric notation
$k$	§1.3	Wavenumber (vector)
$L$	§1.7	Linear extend of the scattering volume
$L$	§3.1.4	Length of laser cavity
$L_c$	§5.1	Mixer conversion loss
$L_o$	§5.9	Optical losses
$\ell$	§2.1	Harmonic frequency count
$\Delta\ell$	§5.4	Length of optical path (in the diplexer)
$M$	§3.1.3	Molecular gas weight in amu
$m_q$	§1.1	Mass of a particle
$N_D$	§2.0	Number of particles in a Debye cloud
$N_f$	§5.6.1	Noise figure
NEP	§2.5.1	Noise equivalent power
$n$	§4.9	Relative index of refraction
$n_q$	§1.4	Plasma density
OF	§4.6	Focusing distance of elliptic mirror
$P$	§1.2	Power (usually scattered power)
$P$	§3.1.3	Pressure
$P_B$	§2.4	Bremsstrahlung radiation power
$P_{BB}$	§2.4	Blackbody radiation power
$P_{ECE}$	§2.4	ECE radiation power
$dP$	§1.2	Scattered power density
$p$	§3.3	Gas pressure
$q$	§5.5.1	Charge of the electron (electric notation)
$R_{\perp}$	§4.9	Perpendicular intensity reflectance
$R_i$	§3.1.6	Radius of curvature of mirror $i$
$R_s$	§5.5.1	Schottky diode serial resistance



$r$	§2.7.1	Resolution parameter
$r$	§4.3	Radial distance
$r_1, r_2$	§5.4	Diplexer element amplitude reflectivity
$r_e$	§1.2	Classical electron radius
$S(\mathbf{k}, \omega)$	§1.7	Thomson scattering dynamic form factor
$S_q(\alpha)$	§2.3	Thomson scattering dynamic form factor
$S/N$	§2.6	Final signal to noise ratio
$s$	§2.5.1	Signal to noise ratio (pre integration)
$s_e$	§6.5	Standard error (statistical)
$T_a$	§5.1	Amplifier effective noise temperature
$T_d$	§5.9	Diplexer effective noise temperature
$T_m$	§5.1	Mixer effective noise temperature
$T_q$	§1.4	Plasma temperature
$T_s, T_{sys}$	§5.1	System effective noise temperature
$\Delta T_i / T_i$	§2.7.2	Relative error of ion temperature
$t$	§5.1	Time
$t_1, t_2$	§5.4	Diplexer element amplitude transmission
$U_1, U_2$	§4.3	Radiation field distribution
$U_{sf}$	§3.3.5	FIR transition saturation power density
$U_{sp}$	§3.3.5	Pump transition saturation power density
$V$	§1.7	Volume
$V$	§5.5.1	Voltage
$\mathbf{v}$	§1.3	Particle velocity (vector)
$v_q$	§1.4	Particle thermal speed
$W(\mathbf{x}_q)$	§1.7	Plasma dispersion function
$w$	§2.7.1	Gaussian radial beam waist ( $e^{-2}$ of intensity)
$x_q$	§1.7	Particle normalized frequency
$Y$	§5.6.1	Microwave signal quality factor
$Z$	§1.7	Particle charge
$Z$	§5.1	Electrical impedance
$Z_{eff}$	§1.7.6	Plasma effective charge
$z$	§3.1.5	Length parameter
$\alpha_0$	§3.1.5	Small signal gain
$\alpha$	§1.4	Thomson scattering electron parameter
$\alpha$	§4.9	Full cone angle
$\beta$	§1.7	Thomson scattering ion parameter
$\delta$	§4.9	Incident beam angle

$\epsilon(\mathbf{k},\omega)$	§1.7	Plasma dielectric function
$\eta$	§5.5.1	Schottky diode quality factor
$\Gamma_q(\mathbf{k},\omega)$	§1.7	Electron screening integral
$\theta$	§1.2	Scattering angle
$\Delta\theta$	§2.7.1	Angular extent
$\lambda$	§1.3	Wavelength
$\lambda_{\text{crit}}$	§2.1	Plasma cut-off wavelength
$\lambda_D$	§1.4	Debye length
$\lambda_f$	§2.7.1	Wavelength of scattering vector $\mathbf{k}$
$\nu$	§1.1	Frequency of an electromagnetic wave
$\nu_1 \nu_2^\ell \nu_3$	§3.1	Vibrational quantum numbers of the $\text{CO}_2$ molecule
$\nu_a$	§3.2.1	Axial resonator mode spacing
$\nu_e$	§1.6	Plasma electron frequency
$\nu_i$	§1.6	Frequency of the plasma ion acoustic wave
$\nu_l$	§3.2.1	Longitudinal resonator mode spacing
$\Delta\nu$	§2.2	Frequency width
$\Delta\nu_{\frac{1}{2}}$	§1.5	FWHM : full frequency width at half maximum
$\rho$	§3.1	Molecular dipole moment
$\rho$	§4.3	Radial distance
$\rho_p$	§3.3	Optical pumping rate
$\rho_q$	§1.7.8	Plasma Larmor radius
$\sigma_t$	§1.2	Thomson scattering cross section
$\tau$	§1.7	Time interval
$\tau_\ell$	§2.4	Optical depth
$\tau_r$	§3.3	Rotational level refill rate
$\tau_v$	§3.3	Vibrational level refill rate
$\Omega$	§1.2	Solid angle
$d\Omega$	§1.2	Element of solid angle
$\omega$	§1.3	Angular frequency
$\omega_{\text{ece}}$	§2.1	Electron cyclotron angular frequency
$\omega_{\text{pq}}$	§1.4	Plasma angular frequency

### Subscripts

o	$\lambda_o$	Incident
c	$T_c$	Cold
d	$\omega_d$	Doppler shifted
h	$T_h$	Hot

if	$\nu_{if}$	Intermediate frequency
lo	$E_{lo}$	Local oscillator
q	$m_e, m_i$	Charge type $q=e$ electrons, $q=i$ ions
s	$P_s$	Scattered
s	$E_s$	Signal

### Superscripts

o	$\tau_l^o$	Ordinary ray
e	$\tau_l^e$	Extraordinary ray
*	$E_{lo} \cdot E_{lo}^*$	Complex conjugate



## CURRICULUM VITAE

KJELBERG Ivar, born on the 13. of January 1955 in Bærum,  
Norway.

- 1961 - 65 First four years of primary school at Stabekk,  
Norway.
- 1965 - 68 Last three years of primary school at Versoix,  
Switzerland.
- 1968 - 70 Collège Moderne, Geneva.
- 1970 - 74 Collège de Genève (Voltaire), Maturité Fédérale type  
C (scientifique).
- 1974 - 79 Ecole Polytechnique Fédérale de Lausanne, section  
of Physics. Practical diploma done at the CRPP  
(Centre de Recherches en Physique des Plasmas) in  
Laser and Plasma Physics.
- 1977 Three months spent as summer student in the ISOLDE  
group at CERN, Geneva (the European Center for  
Nuclear Research).
- 1979 - 86 Assitant and Ph. D. student at the CRPP. Working on  
the devlopment of FIR lasers and a microwave hetero-  
dyne detection system for collective Thomson scat-  
tering on the TCA tokamak plasma. Specializing in  
experimental work, the design of mechanical and  
electronic equipment, and the development of soft-  
ware for the acquisition of experimental data.

**PUBLICATIONS:**

- [1] "On minimising reflection losses from laser windows", M.R. Green, I. Kjelberg, P.D. Morgan, M.R. Siegrist, R.L. Watterson, CRPP-EPFL report LRP 150-79 (1979).
- [2] "Preliminary results from a 66  $\mu\text{m}$  D<sub>2</sub>O laser having an unstable Reststrahlen resonator", M.R. Green, I. Kjelberg, P.D. Morgan, M.R. Siegrist, R.L. Watterson, CRPP-EPFL report LRP 151-79 (1979).
- "A 66  $\mu\text{m}$  D<sub>2</sub>O laser having an unstable Reststrahlen resonator", M.R. Green, I. Kjelberg, P.D. Morgan, M.R. Siegrist, R.L. Watterson, E. Akhmetov, J. Phys. D.: Appl. Phys., Vol. 13, pp. 1029-1042, (1980).
- [3] "Isolation between amplifiers in a TEA CO<sub>2</sub> laser using absorbing gases", M.R. Green, I. Kjelberg, P.D. Morgan, M.R. Siegrist, R.L. Watterson, M.A. Dupertuis, R. Duperré, J.L. Scartezzini, H. Van den Bergh, CRPP-EPFL report LRP 152-79 and J. Phys. D.: Appl. Phys., Vol. 13, pp. 1399-1404, (1980).
- [4] "Parametric study of an optically pumped far infrared oscillator" M.R. Siegrist, M.R. Green, P.D. Morgan, I. Kjelberg, R.L. Watterson, J. Appl. Phys., Vol. 51, pp. 3531-3535, (1980).
- [6] "A comparative study of D<sub>2</sub>O oscillators emitting at 385  $\mu\text{m}$ ", M.R. Green, I. Kjelberg, P.D. Morgan, M.R. Siegrist, R. Behn, CRPP-EPFL report LRP 190-81 and IEEE J. Quant. Elect., Vol. QE-19, pp. 222-232, (1983).
- [7] "A high power D<sub>2</sub>O laser optimized for microsecond pulse duration", R. Behn, I. Kjelberg, P.D. Morgan, T. Okada, M.R. Siegrist, CRPP-EPFL report LRP 213-82 and J. Appl. Phys., Vol. 54, pp. 2995-3002, (1983).

- [8] "Transport of far infrared beams for use in plasma diagnostics", M.R. Siegrist, I. Kjelberg, R. Behn, CRPP-EPFL report LRP 215-82, and Appl. Opt., Vol. 22, pp. 1318-1324, (1983).
- [9] "Buffer gases to increase the efficiency of an optically pumped far infrared D<sub>2</sub>O laser", R. Behn, M.A. Dupertuis, I. Kjelberg, P.A. Krug, S.A. Salito, M.R. Siegrist, IEEE J. Quant. Elect., Vol. QE-21, pp. 1278-1285, (1985).
- [10] "CRC-16 flies better in assembler", (note to the Editor) I. Kjelberg, IEEE Micro, Vol. 5, pp. 4 and 99, (1985).

#### Conferences attended:

- 3rd International Conference on Sub-millimeter Waves and their Applications, March 1978, University of Surrey, Guilford, England.
- 4th National Quantum Electronics Conference, Edinburgh, Scotland, September 1979.
- 5th International Conference on Infrared and Millimeter Waves, Würzburg, Germany, October 1980.  
"An unstable resonator D<sub>2</sub>O oscillator for 385  $\mu$ m", M.R. Green, I. Kjelberg, R. Behn, P.D. Morgan, M.R. Siegrist.
- Société Suisse de Physique, autumn 1980.  
"A study of strong far infrared laser emission from optically pumped molecules", I. Kjelberg, M.R. Green, P.D. Morgan, M.R. Siegrist.
- One week course on contacting Schottky diodes for microwave detection, Farran Research, Microelectric Research Centre, University College, Cork, Ireland, September 1981.

- Société Suisse de Physique, spring 1982.  
"System to measure plasma ion temperature on the TCA tokamak by Thomson scattering at  $385 \mu\text{m}$ ", I. Kjelberg, R. Behn, M.A. Dupertuis, P.D. Morgan, T. Okada, M.R. Siegrist.
- International conference on Plasma Physics, Lausanne, June 1984.  
"Preliminary results from a FIR Thomson scattering diagnostic on TCA, I. Kjelberg, R. Behn, M.A. Dupertuis, P.A. Krug, P.D. Morgan, A. Salito, M.R. Siegrist.
- Swiss DECUS Symposium, Lausanne, May 1984.
- Swiss DECUS Symposium, Lucerne, April 1986.

Contributions to papers presented at other conferences:

- "A high power D<sub>2</sub>O laser optimised for microsecond pulse duration", R. Behn, M.A. Dupertuis, I. Kjelberg, P.D. Morgan, M.R. Siegrist, 12th. International Conference on Quantum Electronics, München, Germany, June 1982.
- "The effect of buffer gases on the performance of a high power D<sub>2</sub>O laser", R. Behn, M.A. Dupertuis, I. Kjelberg, P.D. Morgan, M.R. Siegrist, 7th International Conference on Infrared and millimeter waves, Marseille, France, February 1983.
- "Iontemperaturmessung mittels Thomson-Streuung am TCA Tokamak: Entwicklungszustand des Projectes und neueste Resultate", M.R. Siegrist, R. Behn, M.A. Dupertuis, I. Kjelberg, P.A. Krug, Société Suisse de Physique, spring 1983



- "High energy D<sub>2</sub>O laser for collective Thomson scattering", R. Behn, Q.H. Do, I. Kjelberg, P.A. Krug, A. Salito, M.R. Siegrist, H. Weisen, Société Suisse de Physique, autumn 1983.
- "A High energy D<sub>2</sub>O laser for plasma diagnostics", R. Behn, I. Kjelberg, P.A. Krug, A. Salito, M.R. Siegrist, H. Weisen, 8th International Conference on Infrared and millimeter waves, Miami Beach, USA, December 1983.
- "Line and mode competition in an optically pumped multilevel system", R. Behn, M.A. Dupertuis, P.A. Krug, I. Kjelberg, S.A. Salito, M.R. Siegrist, Conference on the Trends in Quantum Electronics, Bucharest, Romania, September 1985.
- "Measurement of FIR D<sub>2</sub>O laser radiation collectively scattered by thermal fluctuations in a tokamak plasma", R. Behn, M.A. Dupertuis, I. Kjelberg, P.A. Krug, S.A. Salito, M.R. Siegrist, Conference on the Trends in Quantum Electronics, Bucharest, Romania, September 1985.
- "Observation of collective Thomson scattering of D<sub>2</sub>O laser radiation from a tokamak plasma", R. Behn, I. Kjelberg, P.A. Krug, A. Salito, M.R. Siegrist, 10th International Conference on Infrared and Millimeter Waves, Miami, USA, December 1985.
- "Erste Ergebnisse zur Kollektiven Thomson-Streuung an einem Tokamak Plasma mit Hilfe eines D<sub>2</sub>O Fern-infrarot Lasers", R. Behn, M.A. Dupertuis, I. Kjelberg, P.A. Krug, A. Salito, M.R. Siegrist, Société Suisse de Physique, spring 1985.
- "Thomson scattering at 385 micrometers as a means to measure the ion temperature of a Tokamak plasma", R. Behn, I. Kjelberg, P.A. Krug, S.A. Salito, M.R. Siegrist, International School of Plasma Physics "Piero

Caldirola", Course and Workshop on: "Basic and Advanced Fusion Plasmas Diagnostic Techniques", Varenna, Italy, 3-13. September 1986.

- "Progress towards Ion Temperature Measurements in TCA Tokamak by Collective Thomson Scattering of Far Infrared Laser Radiation", R. Behn, I. Kjelberg, P.A. Krug, S.A. Salito, M.R. Siegrist, 11th International Conference on Infrared and Millimeter Waves, Pisa, Italy, 20-24. October 1986.
  
- "Time Resolved Linewidth and Lineshape Measurements of an Optically Pumped Far Infrared D<sub>2</sub>O Laser", R. Behn, M.A. Dupertuis, I. Kjelberg, P.A. Krug, S.A. Salito, M.R. Siegrist, 11th International Conference on Infrared and Millimeter Waves, Pisa, Italy, 20-24. October 1986.